Technische Universität München
TUM School of Engineering and Design

TUΠ

Impact of hydropeaking on groundwater mixing: from laboratory experiments to field scale observations

Mónica Basilio Hazas

.

CONTENTS

When I was a child, my mom suggested me that I could become a water scientist.

At the time I didn't listened: I wanted to be volcanologist or paleontologist.

Later, medicine, biology and mathematics came across my mind,

but I finally did a bachelor's degree in chemical engineering.

It was until my master's when I discovered hydrology

and then worked on the topic during my PhD.

So, it took me a bit more than 20 years

to understand a basic rule of life:

my mom is always right!

…

To my family

ABSTRACT

The mixing of dissolved solutes in the groundwater is controlled by the characteristics of the subsurface and the boundary conditions of the system. This dissertation focuses on highly transient boundary conditions at the surface water – groundwater (SW-GW) interface inspired by the case of hydropeaking, river fluctuations caused by the operation of hydropower plants. In particular, it aims to understand how highly transient boundary conditions impact the groundwater flow field and how mixing mechanisms change accordingly. The investigation is carried out at three different spatial scales: laboratory, field, and regional. The laboratory scale consists of flow-through laboratory experiments accompanied by a model-based interpretation, and explores the transport mechanisms behind mixing enhancement in transient flows. The study at field scale involves the interaction between the transient boundaries and the heterogeneities of the aquifer. Specifically, it explores how this interplay affects the transport of a solute plume and the Okubo-Weiss field. The regional investigation takes the case of an aquifer traversed by different rivers affected by hydropeaking and analyses the weekly signal in the rivers and the groundwater fluctuations. The laboratory and field studies apply mixing metrics such as the breakthrough curves, plume perimeter and area, and the dilution index, as well as topological analysis using the Okubo-Weiss parameter. The results at laboratory scale show that transient boundary conditions similar to those generated by hydropeaking can enhance mixing processes and lead to dynamic areas of higher stretching and shearing, even in homogeneous porous media. Folding and stretching contribute to mixing enhancement; however, the flow topology can also control mixing dynamics, and internal dispersion and diffusion may play an important role in dilution processes. Additionally, the investigation provides experimental evidence that the size of a plume is associated with the dilution index and that the dilution rate is coherent with the effective Okubo-Weiss parameter. In heterogeneous aquifers, transport can be controlled by either the transient boundary conditions, the local hydraulic conductivity, or both, and SW-GW interactions can affect the fate of a solute plume, helping it or not to find preferential flow paths. Moreover, while the heterogeneous hydraulic conductivity field strongly influences the flow topology, the transient boundary conditions affect the temporal variability of the Okubo-Weiss field. The regional study, on the other hand, applies wavelet techniques to analyze and compare the impact of hydropeaking in the aquifer in two different hydrological years. Hydropeaking displays a stronger weekly signal during drought conditions, not only in the river fluctuations but also in the groundwater heads and the exchanged water between the rivers and the aquifer. Furthermore, maps based on the weekly signal reveal that the area of the aquifer affected by hydropeaking was similar in the two compared years; however, the impact is stronger during the drought conditions. Overall, the results of this dissertation can be applied to improve the modeling of contaminant plumes near highly fluctuating water bodies, the implementation of remediation strategies, and the decision-making processes for water managers dealing with areas influenced by hydropower production.

ZUSAMMENFASSUNG

Die Durchmischung von gelösten Stoffen im Grundwasser wird durch die Charakteristiken des Untergrundes und die Randbedingungen des Systems beherrscht. Diese Dissertation beschäftigt sich mit hochgradig instationären Randbedingungen an der Grenzfläche zwischen dem Oberflächenwasser und dem Grundwasser (SW-GW), angeregt durch den Fall des Hydropeaking, d. h. Flussschwankungen, die durch den Betrieb von Wasserkraftwerken verursacht werden. Insbesondere soll untersucht werden, wie sich hochgradig instationäre Randbedingungen auf das Grundwasserströmungsfeld auswirken und wie sich die Durchmischungsmechanismen entsprechend verändern. Die Untersuchung wird auf drei verschiedenen räumlichen Skalen durchgeführt: im Labor und auf Feld- und regionaler Ebene. Im Labormaßstab werden Durchfluss-Laborexperimente durchgeführt, die von einer modellbasierten Interpretation begleitet werden. Hierbei werden die Transportmechanismen untersucht, die der Verstärkung der Durchmischung in instationären Strömungen zugrunde liegen. Die Studie im Feldmaßstab befasst sich mit der Wechselwirkung zwischen den instationären Grenzen und der Heterogenität des Grundwasserleiters. Insbesondere wird untersucht, wie sich dieses Zusammenspiel auf den Transport einer gelösten Schadstofffahne und das Okubo-Weiss-Feld auswirkt. Die regionale Untersuchung befasst sich mit einem Grundwasserleiter, der von verschiedenen Flüssen mit Hydropeaking durchflossen wird, und analysiert das wöchentliche Signal in den Flüssen und die Grundwasserschwankungen. In den Labor- und Feldstudien werden Mischungsmetriken wie Durchbruchskurven, Fahnenumfang und -fläche und der Verdünnungsindex sowie eine topologische Analyse unter Verwendung des Okubo-Weiss-Parameters verwendet. Die Ergebnisse im Labormaßstab zeigen, dass instationäre Randbedingungen, ähnlich denen, die durch Hydropeaking erzeugt werden, Mischungsprozesse verstärken und zu dynamischen Bereichen mit höherer Dehnung und Scherung führen können, selbst in homogenen porösen Medien. Faltung und Dehnung tragen zur Verbesserung der Durchmischung bei; allerdings kann auch die Strömungstopologie die Durchmischungsdynamik steuern, und interne Dispersion und Diffusion können eine wichtige Rolle bei Verdünnungsprozessen spielen. Darüber hinaus liefert die Untersuchung experimentelle Belege dafür, dass die Größe einer Fahne mit dem Verdünnungsindex zusammenhängt und dass die Verdünnungsrate mit dem effektiven Okubo-Weiss-Parameter kohärent ist. In heterogenen Grundwasserleitern kann der Transport entweder durch die instationären Randbedingungen, die lokale hydraulische Leitfähigkeit oder durch beides gesteuert werden, und SW-GW-Wechselwirkungen können das Schicksal einer gelösten Fahne beeinflussen, indem sie dazu beitragen, dass diese bevorzugte Fließwege findet oder nicht. Obwohl das heterogene hydraulische Leitfähigkeitsfeld die Strömungstopologie stark beeinflusst, wirken sich die instationären Randbedingungen auf die zeitliche Variabilität des Okubo-Weiss-Feldes aus. In der regionalen Studie werden Wavelet-Techniken angewandt, um die Auswirkungen von Hydropeaking im Grundwasserleiter in zwei verschiedenen hydrologischen Jahren zu analysieren und zu vergleichen. Hydropeaking zeigen während der Trockenheit ein stärkeres wöchentliches Signal, nicht nur bei den Flussschwankungen, sondern auch bei den Grundwasserhöhen und dem Wasseraustausch zwischen den Flüssen und dem Grundwasserleiter. Außerdem, zeigen Karten, die auf dem wöchentlichen Signal basiert sind, dass die von Hydropeaking betroffene Fläche des Grundwasserleiters in den beiden verglichenen Jahren ähnlich groß war; die Auswirkungen sind jedoch während der Trockenheit stärker. Insgesamt können die Ergebnisse dieser Dissertation angewendet werden, um die Modellierung von Schadstofffahnen in der Nähe von stark schwankenden Gewässern, die Umsetzung von Sanierungsstrategien und die Entscheidungsfindung für Wasserwirtschaftsunternehmen im Umgang mit Gebieten, die von der Wasserkraftproduktion beeinflusst werden, zu verbessern.

ACKNOWLEDGEMENTS

SCIENTIFIC CONTRIBUTIONS

RESEARCH ARTICLES INCLUDED IN THIS DISSERTATION

Six research articles integrate this dissertation. Three of them are first-author manuscripts that have been peer-reviewed and published. Therefore, they are to be considered in the requirements for a cumulative dissertation. The other three articles consist of two co-author publications and a manuscript in preparation. They are included in order to complete the storyline of this dissertation. The two-coauthor manuscripts have also been peer-reviewed and published, and it is planned to submit the manuscript in preparation to a peer-review journal. The articles are listed according to the chapters of this dissertation rather than in a chronological order of submission and publication.

The publication Basilio & Chiogna (2022) was shortlisted as one of the finalists of the John F. Kennedy Student Paper Competition at the 39th IAHR World Congress organized by the International Association for Hydro-Environment Engineering and Research.

Title:	Mixing Enhancement Mechanisms in Aquifers Affected by Hydropeaking: Insights From Flow-Through Laboratory Experiments
Authors:	Ziliotto, F.[(1)], **Basilio Hazas, M.** [(2)], Rolle, M. [(3)], Chiogna, G. [(4)]
Journal:	Geophysical Research Letters (published)
DOI:	10.1029/2021GL095336
Contribution:	(1) Conceptualization, experimental design and execution, data processing, manuscript composition, review and editing. (2) Conceptualization, experimental design and execution, data processing, manuscript composition, review and editing. (3) Conceptualization, experimental design, review and editing. (4) Conceptualization, experimental design, review and editing.
Notes:	Co-author publication, Chapter 2
Title:	Relation between mixing and plume geometry in porous media under highly transient flow fields
Authors:	**Basilio Hazas, M.** [(1)], Ziliotto, F. [(2)], Lee, J. [(3)], Rolle, M. [(4)], Chiogna, G. [(5)]
Journal:	In preparation
DOI:	N/A
Contribution:	(1) Conceptualization, experimental design and execution, data processing, manuscript composition, review and editing. (2) Conceptualization, experimental design and execution, data processing, review and editing. (3) Software development, review and editing. (4) Conceptualization, experimental design, review and editing. (5) Conceptualization, experimental design, review and editing.
Notes:	Publication in preparation, Chapter 3

Title:	Linking mixing and flow topology in porous media: An experimental proof
Authors:	**Basilio Hazas, M.** [1], Ziliotto, F. [2], Rolle, M. [3], Chiogna, G. [4]
Journal:	Physical Review E (published)
DOI:	10.1103/PhysRevE.105.035105
Contribution:	(1) Conceptualization, experimental design and execution, data processing, manuscript composition, review and editing. (2) Data processing, review and editing. (3) Conceptualization, review and editing. (4) Conceptualization, experimental design, review and editing.
Notes:	First author publication (1/3), Chapter 4

Title:	Effects of Highly Transient Boundary Conditions on Groundwater Solute Transport
Authors:	**Basilio Hazas, M.** [1], Chiogna, G. [2]
Journal:	Conference Proceedings 39th IAHR World Congress (published)
DOI:	10.3850/IAHR-39WC252171192022763
Contribution:	(1) Conceptualization, experimental design and execution, data processing, manuscript composition, review and editing. (2) Conceptualization, experimental design, review and editing.
Notes:	First author publication (2/3), Chapter 5
	Shortlisted in the finalists of the John F. Kennedy Student Paper Competition.

Title:	Propagation of hydropeaking waves in heterogeneous aquifers: effects on flow topology and uncertainty quantification
Authors:	Merchán-Rivera, P. [1], **Basilio Hazas, M.** [2], Marcolini, G. [3], Chiogna, G. [4]
Journal:	International Journal on Geomathematics (published)
DOI:	10.1007/s13137-022-00202-9
Contribution:	(1) Conceptualization, experimental design and execution, data processing, manuscript composition, review and editing. (2) Conceptualization, experimental design, manuscript composition. (3) Conceptualization, experimental design, manuscript composition. (4) Conceptualization, experimental design, manuscript composition, review and editing.
Notes:	Co-author publication, Chapter 6

Title:	Drought Conditions Enhance Groundwater Table Fluctuations caused by Hydropower Plant Management
Authors:	**Basilio Hazas, M.** [1], Marcolini, G. [2], Castagna, M. [3], Galli, M. [4], Singh, T. [5], Wohlmuth, B. [6], Chiogna, G. [7]
Journal:	Water Resources Research (published)
DOI:	10.1029/2022WR032712

Contribution:	(1) Conceptualization, experimental design and execution, data processing, manuscript composition, review and editing. (2) Conceptualization, experimental design and execution, data processing, manuscript composition, review and editing. (3) Experimental design, data processing, review and editing. (4) Experimental execution, data processing and manuscript composition. (5) Manuscript composition, review and editing. (6) Review and editing. (7) Conceptualization, experimental design, manuscript composition, review and editing.
Notes:	First author publication (3/3), Chapter 7

RESEARCH ARTICLE NOT INCLUDED IN THIS DISSERTATION

Title:	Integration of Remote Sensing and Mexican Water Quality Monitoring System Using an Extreme Learning Machine
Authors:	Arias-Rodriguez, L. F., Duan, Z., Díaz-Torres, J. de J., **Basilio Hazas, M.**, Huang, J., Udhaya Kumar, B., Tuo, Y., Disse, M.
Journal:	Sensors (published)
DOI:	10.3390/s21124118

CONFERENCES AND ORAL PRESENTATIONS

Title:	Effects of hydropower plant management on groundwater table fluctuations: a regional-scale analysis on an Alpine Valley
Authors:	**Basilio Hazas, M.,** Chiogna, G., Marcolini, G., Singh, T., Wohlmuth, B.
Event:	TUM x IIT Bombay Research Forum 2022

Walking Together: Indo-German Dialogue on Common Risks and Shared Pathways to Sustainability |
| Place: | Munich, Germany / virtual |
| Date: | November 3rd, 2022 |

Title:	Perspectivas jóvenes de la seguridad hídrica
Authors:	**Basilio Hazas, M.**
Event:	IAHR Mexico Young Professionals Network

Precongreso 2022 – Aportaciones de la juventud hacia la seguridad hídrica - XXVI Congreso Nacional de Hidráulica |
Place:	virtual
Date:	October 26th, 2022
Note:	Panel discussion on water security. Participation includes discussion on the impacts of hydropeaking on groundwater and how they relate to water security

Title:	How do highly fluctuating rivers affect solute transport in the groundwater?
Authors:	**Basilio Hazas, M.** & Chiogna, G.
Event:	Graduate School of Engineering and Design - Technical University of Munich
	Doctoral Candidates' Day 2022
Place:	Munich, Germany
Date:	July 14th, 2022

Title:	A wavelet analysis of surface water − groundwater interaction in reaches affected by hydropeaking
Authors:	Chiogna, G., **Basilio Hazas, M.**, Marcolini, G., Singh, T., Wohlmuth, B.
Event:	International Association of Hydrological Sciences
	XIth IAHS Scientific Assembly (IAHS 2022)
Place:	Montpellier, France
Date:	29 May–3 Jun 2022

Title:	Effects of Highly Transient Boundary Conditions on Groundwater Solute Transport
Authors:	**Basilio Hazas, M.** & Chiogna, G.
Event:	International Association for Hydro-Environment Engineering and Research
	39th IAHR World Congress
Place:	Granada, Spain
Date:	June 21st, 2022
Note:	Presented in the session with the finalist of the John F. Kennedy Student Paper Competition

Title:	Effects of hydropeaking on groundwater mixing: from laboratory experiments to field scale observations.
Authors:	**Basilio Hazas, M.**, Ziliotto, F., Marcolini, G., Rolle, M. and Chiogna, G.
Event:	European Geosciences Union General Assembly
	vEGU21
Place:	virtual
Date:	2021

Title:	Análisis experimental de transporte de plumas en agua subterránea bajo condiciones de frontera transitorias
Authors:	**Basilio Hazas, M** Chiogna, G.
Event:	Casa Universitaria Franco-Mexicana (MUFRAMEX) and Consejo Nacional de Ciencia y Tecnología (CONACYT)
	Sustentabilidad de los paisajes de humedales mexicanos: sinergias para garantizar la integridad de los ecosistemas y el bienestar humano
Place:	virtual

Date:	November 24th, 2020
Title:	Experimental analysis of plumes transport and dilution processes under highly transient boundary conditions.
Authors:	**Basilio Hazas, M.**, Ziliotto, F., Rolle, M. and Chiogna, G.
Event:	International Society for Porous Media
	Interpore 2020
Place:	virtual
Date:	2020
Title:	Impact of hydropeaking on rivers and groundwater: the case of the Adige Basin
Authors:	**Basilio Hazas, M.** & Chiogna, G.
Event:	Casa Universitaria Franco-Mexicana (MUFRAMEX)
	8° Simposio Becarios Conacyt en Europa
Place:	Strasbourg, France
Date:	April 3-5th, 2019
Note:	Coordinator of the Round Table Towards the Sustainable Development Goals, Challenges and Opportunities in Mexico - Water
Title:	Impact of highly transient boundary conditions on groundwater flow field and its implication for mixing
Authors:	**Basilio Hazas, M.** & Chiogna, G.
Event:	Society for Industrial and Applied Mathematics
	SIAM Conference on Mathematical & Computational Issues in the Geosciences (GS19)
Place:	Houston, USA
Date:	March, 11-14th 2019

POSTERS

Title:	12.05 Uncertainties due to boundary conditions in predicting mixing in groundwater (UNMIX)
Authors:	**Basilio Hazas, M.**, Merchan-Rivera, P., Bittner, D., Rolle, M., Wohlmuth, B., Chiogna, G.
Event:	International Graduate School of Science and Engineering - Technical University of Munich
	IGSSE Forum 2022
Place:	virtual
Date:	May 16-18th, 2022
Title:	Trockenheit verstärkt Fluktuationen des Grundwasserspiegels durch den Betrieb von Wasserkraftwerken
Authors:	**Basilio Hazas, M.**, Singh, T., Marcolini, G., Wohlmuth, B., Chiogna, G.
Event:	Tag der Hydrologie (TdH 2022)

Place:	Garching, Germany
Date:	March 22-23rd, 2022
Title:	Impact of hydropeaking on groundwater flow and transport: a case study in the Adige Valley
Authors:	**Basilio Hazas, M.** & Chiogna, G.
Event:	4th Cargèse Summer School: Flow and Transport in Porous and Fractured Media
Place:	Cargèse, France
Date:	June 25th – July 7th, 2018
Title:	UNMIX – Uncertainties due to boundary conditions in predicting mixing in groundwater
Authors:	**Basilio Hazas, M.**, Merchan-Rivera, P., Bittner, D., Teixeira Parente, M., Mattis, S., Wohlmuth, B., Chiogna, G.
Event:	International Graduate School of Science and Engineering - Technical University of Munich IGSSE Forum 2018
Place:	Raitenhaslach, Germany
Date:	May 7-9th, 2018

DOCTORAL JOURNEY

FELLOWSHIPS AND AWARDS

Awarding institution:	International Association for Hydro-Environment Engineering and Research
Type of award:	Finalist of the John F. Kennedy Student Paper Competition
Year/Period:	2022
Awarding institution:	Society for Industrial and Applied Mathematics
Type of award:	SIAM Student Travel Award
Year/Period:	2019
Awarding institution:	Centre national de la recherche scientifique (CNRS) Summer School: Flow and Transport in Porous and Fracture Media
Type of award:	Selected attendant at summer school
Year/Period:	2018
Awarding institution:	Consejo Nacional de Ciencia y Tecnología (CONACYT)
Type of award:	Mexican fellowship for pursuing a PhD degree abroad

Year/Period: 2018-2020

DOCTORAL REPRESENTATION

Organization:	TUM Graduate Council
Position:	Deputy Speaker
Term:	2021
Organization:	International Graduate School of Science and Engineering
Position:	Doctoral candidate representative
Term:	2019-2021

CHAPTER 1

INTRODUCTION

From the settlements of early humans (Magill et al. 2016; Speth 1987) to the latest space exploration missions (Impey 2022), we have been in a constant search for water. Indeed, water was not only essential for the origin and evolution of life on Earth (Waltham 2019), but it also has played an important role in the development of our culture and history (Hosseiny et al. 2021), including the need for understanding water systems and developing water management strategies. For instance, the Mayas stored rainwater in the subsurface to cope with drought periods (Simms et al. 2012; Scarborough and Gallopin 1991), and the Persians excavated qanats, underground galleries that transported groundwater from higher to lower altitudes over long distances (Wilson 2012). Today, every human has the right to safe, acceptable, physically accessible, and affordable water (United Nations General Assembly 2018). In addition to its use for drinking and sanitation, water is involved in other human activities, such as agriculture, tourism, and energy production, and it is essential for the healthy conservation of the ecosystems.

Groundwater is by far the largest source of available freshwater, as it constitutes close to 97% of the liquid freshwater on the planet. Many terrestrial and aquatic ecosystems depend directly or indirectly on groundwater. For humans, groundwater provides about half of the world's drinking water, 40% of the irrigation water, and one-third of the water used in industry (Jakeman et al. 2016; Siebert et al. 2010). Despite this abundance, excessive water abstraction has led to groundwater depletion (Rodell et al. 2018) and contributes to aquifer salinization (Pauloo et al. 2021; Werner et al. 2013). Fertilizers, pesticides, oil spills, wastewater, and landfill leachates can also jeopardize groundwater systems as they infiltrate the soil and reach the saturated zone. Aquifers can also experience natural contamination, such as the geogenic occurrence of arsenic in different areas around the world (Podgorski and Berg 2020). Finally, external factors, including droughts (Song et al. 2018; Singh et al. 2019), peak flow events (Merchán-Rivera et al. 2021; Wallace et al. 2020), atmospheric conditions (Ahmadi et al. 2022), or land cover and land use changes (Bittner et al. 2018), can affect the groundwater flow and mixing processes in the aquifers.

Mixing is inefficient in porous aquifers, where low Reynolds numbers characterize the flow, and the structure and distribution of the pores often lead to incomplete mixing and mass-transfer limitations within the pore channels (Jiménez-Martínez et al. 2015; Rolle and Kitanidis 2014). Thus, mixing is often the critical step for many biogeochemical reactions and the efficiency of contaminant remediation strategies (Valocchi et al. 2019; Wright et al. 2017; Sole-Mari et al. 2020). For this reason, it is important to understand how mixing works and how it can be enhanced—in general, mixing in porous media results from the combined effect of molecular diffusion, advection and dispersion mechanisms at multiple spatial scales (Turuban et al. 2019; Dentz et al. 2022). At the pore-scale, the pore structure induces the formation of filaments that can elongate due to the main flow direction (de Anna et al. 2014), or that can fold and stretch due to chaotic flow patterns within the pore spaces (Souzy et al. 2020; Turuban et al. 2019). The elongation, folding and stretching of the filaments help to sustain chemical gradients and increase the interface available for diffusion (Heyman et al. 2020; Jiménez-Martínez et al. 2015). At the Darcy scale, the soil matrix and the boundary conditions of the system influence the groundwater flow and the transport of dissolved solutes. Here, mixing enhancement is often associated to spatial variabilities in the flow field. These variabilities can be caused by topographic features (Bandopadhyay et al. 2018), transient conditions (Sposito 2006; Kahler and Kabala 2016; Piscopo et al. 2013), or the heterogeneous structure of the soil matrix (de Barros et al. 2012; Ye et al. 2015a; Chiogna et al. 2015). In particular, heterogeneous conductivity fields can lead to flow focusing and defocusing (Dentz et al. 2016; Rolle et al. 2009; Werth et al. 2006), and anisotropies can produce streamlines with helical structures (Ye et al. 2015c; Ye et al. 2020; Cirpka et al. 2015).

Dynamic boundary conditions can create complex flow patterns and enhance the mixing of dissolved solutes (Trefry et al. 2019; Dentz and Carrera 2003; de Dreuzy et al. 2012; Piscopo et al. 2013). In fact, transient boundary conditions can fold and stretch the plume (e.g., (Neupauer et al. 2014); folding and stretching can then enlarge the plume's interface available for molecular diffusion and dispersion and thus increase dilution and mixing processes. Transient flows may result from natural phenomena or anthropogenic factors. Examples of natural phenomena are ocean tides (Wu et al. 2020; Geng et al. 2020; Wallace et al. 2020), peak discharge events (Guérin et al. 2019; Merchán-Rivera et al. 2021; Singh et al. 2020) and changes in evapotranspiration and infiltration rates (Cremer et al. 2016). Anthropogenic factors may include engineered pumping systems (Neupauer et al. 2014; Bagtzoglou and Oates 2007) or the operation of hydropower plants, which leads to an artificial river flow regime known as hydropeaking (Ferencz et al. 2019; Sawyer et al. 2009).

Hydropeaking is characterized by sharp and frequent fluctuations of the water level (Fette 2005) and poses highly transient boundary conditions to the surface water-groundwater (SW-GW) interface with important implications for groundwater flow and transport at multiple spatio-temporal scales. Hydropeaking affects hydraulic gradients, water exchange, biogeochemical cycles and thermal processes in the hyporheic zone (Hester et al. 2017; Cardenas et al. 2004; Song et al. 2018; Singh et al. 2019). At larger scales, it can influence the groundwater flow on riverine islands (Francis et al. 2010) and along the river floodplain (Song et al. 2020; Zachara et al. 2020). Concerning the temporal variability, even if the water fluctuations occur within minutes or hours (Casas-Mulet et al. 2015; Zolezzi et al. 2011), hydropeaking also reveals signals at the daily, weekly and yearly scales (Pérez Ciria et al. 2019; Pérez Ciria et al. 2020). This is important since the frequency also plays a role in the propagation of a fluctuating signal into the aquifer (Townley 1995; Sawyer et al. 2009) and thus a solute plume at a certain distance from the shore may be affected mainly by a specific frequency (Rizzo et al. 2020).

For all these reasons, this dissertation considers the case of hydropeaking in order to investigate with a multi-scale approach the impact of highly transient boundary conditions on the groundwater flow field and transport. The research starts with process understanding at laboratory scale, where spreading, plume dilution and mixing processes are analyzed, and ends with a three-dimensional model of a real aquifer affected by hydropeaking. This investigation will allow us to improve the modeling of the fate and transport of contaminants near riverine environments and raise awareness of the influence of surface water management practices on aquifers.

1.1 HYPOTHESIS AND OBJECTIVES

As mentioned at the end of the previous section, this dissertation aims to study the impact of highly transient boundary conditions on groundwater flow and mixing with a multi-scale approach. The main research question can be then posed as follows:

How do highly transient boundary conditions, in particular hydropeaking, impact the groundwater flow field at different spatio-temporal scales, and how do spreading, plume dilution and mixing processes change accordingly?

To answer this question, we considered six hypotheses covering the laboratory, field, and regional scales. These hypotheses are associated with one or more of the research articles included in this dissertation, as it will be described by the research storyline in section 1.2. While this section lists them to give the reader a better overview of the investigation, a deeper explanation will be developed in the research framework in section 1.3. The hypotheses are thus the following:

1. Highly transient boundary conditions can affect the flow field and enhance mixing beyond the SW-GW interface at multiple spatio-temporal scales. Therefore, a multi-scale approach is relevant to investigate the fate and transport of contaminants under transient conditions.

2. Experimental laboratory tests are an important tool for understanding mixing processes in aquifers under highly transient boundary conditions.

3. Highly transient boundary conditions at the SW-GW interface modify the topology of groundwater flow fields, thus enhancing mixing mechanisms.

4. Highly transient boundary conditions influence the groundwater flow in heterogeneous aquifers and are

able to create transient flow fields with different characteristic from steady-state heterogeneous flows.

5. The uncertainties associated with highly transient boundary conditions, such as hydropeaking, should be considered for predicting groundwater flow fields and mixing.
6. Multitemporal analysis techniques, such as the wavelet transform, help to study the impact of hydropeaking in the aquifer at a regional scale.

As it can be seen from the hypotheses, this research involves laboratory experiments, metrics to measure mixing, and groundwater models. Therefore, it is necessary to consider different tasks, including the experimental work, testing which metrics will be used to study mixing, modeling the experiments, and modeling heterogeneous aquifers at larger scales. These tasks can be organized into the following general objectives:

1. To perform experiments at laboratory scale of plume dilution under highly transient boundary conditions.
2. To characterize the topological and kinematic properties 2-D transient flow fields and identify relevant metrics to predict plume deformation and quantify dilution.
3. To perform a model-based interpretation of the experimental result using a validated numerical model and to investigate the capability of topological metrics to predict dilution and mixing.
4. To apply the results at field scale and determine mixing properties in a realistic case study by modeling two-dimensional heterogeneous, porous aquifers affected by hydropeaking.
5. To analyze SW-GW interactions in a complex river-aquifer system by modeling a real aquifer affected by hydropeaking.

Similar to the hypothesis, the general objectives are associated with one or more research articles included in the dissertation, where they are broken down into more specific objectives. For more clarity, the next section presents the research storyline and how the dissertation chapters are connected to the hypotheses and objectives.

1.2 GENERAL RESEARCH STORYLINE

In order to better understand how highly transient boundary conditions affect groundwater flow and solute transport in the aquifer, this investigation takes a multi-scale approach from laboratory experiments to field. Specifically, it considers three spatial scales (laboratory, field and regional scale) with time windows and resolutions that go from subdaily to seasonal analysis. The core part of the research is developed in chapters 2 to 7, which correspond to the six research articles included in the dissertation. These chapters are organized in the three spatial scales as follows:

Laboratory scale (Chapters 2 to 4):

The first chapters focus on gaining process understanding at laboratory scale by using a flow-through chamber experimental setup and the model-based interpretation of the results. The setup represents an aquifer cross-section in contact with two rivers affected by hydropeaking. This part of the dissertation explores mixing mechanisms under transient flows in a homogeneous porous medium to consider only the effect of the transient boundary conditions. Additionally, it compares different metrics for solute transport and mixing (plume geometry, dilution index, Okubo-Weiss parameter) and analyzes if and how these metrics are related.

Field scale (Chapters 5 and 6):

Chapters 5 and 6 incorporate heterogeneities of the hydraulic conductivity and analyses how their combined effect with the transient boundary conditions affects solute transport and mixing. Specifically, Chapter 5 upscales the experimental setup to the field scale by modeling the vertical cross-section of a heterogeneous aquifer affected by hydropeaking. The model is based on the Adige Valley, an aquifer traversed by multiple managed rivers, and compares different hydraulic scenarios and subdaily and daily time resolutions. Chapter 6, on the other hand, assumes uncertainty in the amplitude and phase of the hydropeaking waves. It uses a stochastic approach in a synthetic scenario to analyze the uncertainty in the propagation of hydropeaking waves into the groundwater heads and the topology of the flow.

Regional scale (Chapter 7):

Chapter 7 models a much larger section of the Adige Valley in three dimensions and applies wavelet analysis techniques to study how river fluctuations affect the groundwater level at regional scale. The study is at daily time resolution and focuses on the weekly periodicity of the hydropeaking signal. In addition, it compares the impacts of dam operation in a wet and a dry hydrological year.

Figure 1.1 displays a graphical summary of the research storyline. Table 1.1 shows an overview of the chapters and publications with their corresponding spatial scale and dimension, associated hypothesis, general objectives, and specific research question and objectives. Hypothesis 1 is not included in the table as it is implicit throughout the dissertation.
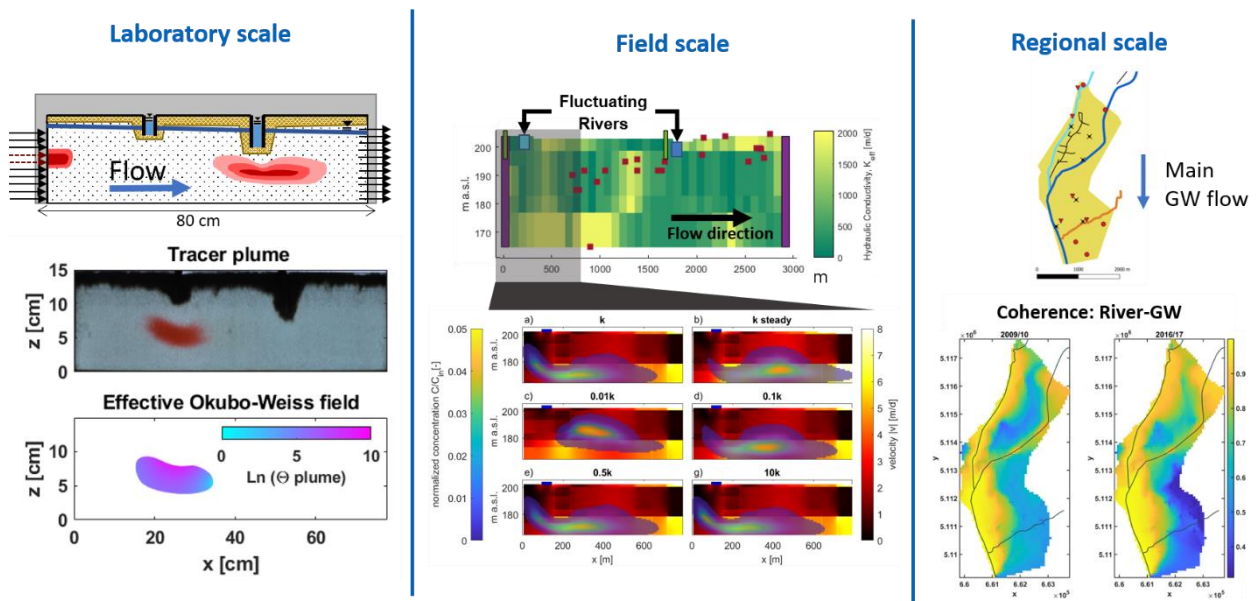
Figure 1.1: Multiscale approach used in the study of transient boundary conditions on groundwater flow and transport. Adapted from (Basilio Hazas et al. 2022b) for laboratory scale; (Basilio Hazas & Chiogna 2022) for field scale and (Basilio Hazas et al. 2022a) for regional scale.

CH	Publication	Scale & dimension	HO	Specific research question	GO	Specific objectives
2	Ziliotto et al. (2021) GRL	Laboratory scale Vertical cross-section	2	Can hydropeaking enhance plume mixing in the underlying aquifer?	1, 2	To design an experimental setup able to mimic the effect of hydropeaking in the subsurface. To develop a methodology for quantifying plume mixing in the experimental setup.
3	Basilio Hazas et al. In preparation	Laboratory scale Vertical cross-section	2, 3	Which are the main mechanisms for mixing enhancement under highly transient boundary conditions (i.e., hydropeaking)?	2, 3	To model the experiment and perform a model-based interpretation. To analyze the characteristics of the plume and their relation to plume mixing.
4	Basilio Hazas et al. (2022b), PRE	Laboratory scale Vertical cross-section	2, 3	What is the relation between flow topology and mixing under transient flow fields?	2, 3	To characterize the flow topology with the Okubo-Weiss parameter. To study the relation between mixing and flow topology under transient flow fields.
5	Basilio Hazas & Chiogna (2022), 39th IAHR Proceedings	Field scale Vertical cross-section	4	How does hydropeaking affect flow and mixing in a heterogeneous aquifer?	4	To model a cross-section of an aquifer affected by hydropeaking (Adige Valley). To study solute transport under different hydraulic scenarios.
6	Merchan-Rivera et al. (2022) GEM	Field scale Horizontal cross-section	4, 5	How do uncertainties in the boundary conditions affect the flow field and mixing?	4	To analyze the propagation of different hydropeaking waves into the aquifer and their effect on flow topology. To implement uncertainty in the hydropeaking waves within a stochastic framework.
7	Basilio Hazas et al. (2022a), WRR	Regional scale Three - dimensional	6	How does hydropeaking affect the aquifer at large scale?	5	To model an aquifer affected by hydropeaking (Adige Valley). To use wavelet analysis techniques to study surface water and groundwater interactions at large scale.

Table 1.1: Overview of the dissertation chapters (CH). Publications, scales and dimension, associated hypothesis (HO) and general objectives (GO), and specific research question and objectives.

1.3 RESEARCH FRAMEWORK

This section develops a broader literature review based on the hypothesis, providing additional context on mixing processes, transient boundary conditions, and hydropeaking. In addition, it explains how each chapter addresses the hypothesis.

1.3.1 MULTISCALE APPROACH TO STUDY TRANSIENT SW-GW INTERACTIONS AND MIXING PROCESSES

***Hypothesis 1:** Highly transient boundary conditions can affect the flow field and enhance mixing beyond the SW-GW interface at multiple spatio-temporal scales. Therefore, a multi-scale approach is relevant to investigate the fate and transport of contaminants under transient conditions.*

Just as mixing processes in porous media, SW-GW interactions also occur at multiple spatio-temporal scales. In the case of rivers, the extent of hyporheic flows and mixing can range from processes within the pores to flow paths of hundreds of meters (Boano et al. 2014; Hester et al. 2017) and can influence groundwater flow regimes at regional scales (Epting et al. 2018). The hyporheic zone presents larger and more variable head gradients than the deeper groundwater (Hester et al. 2017), and thus many studies on hydropeaking focus on this zone or its proximity (Cardenas et al. 2004; Sawyer et al. 2009; Schmadel et al. 2016; Singh et al. 2019). However, hydropeaking also affects the groundwater in riverine islands, river reaches, river corridors and flood plains (Francis et al. 2010; Yellen and Boutt 2015; Shuai et al. 2019; Zachara et al. 2016).

Temporal scales in SW-GW interactions can range from seconds to tens of years (Boano et al. 2014). Moreover, in the case of transient flows, the characteristics of the dynamic boundaries affect the aquifer's response. Fluctuations with low frequencies penetrate further distances into the aquifer, while high frequencies damp fast and do not propagate deeply (Townley 1995; Singh 2004; Trefry et al. 2019). This is relevant for hydropeaking, given it multitemporal scales (Pérez Ciria et al. 2020; Pérez Ciria et al. 2019). In this sense, the subdaily fluctuations could affect areas closer to the rivers, while the weekly fluctuations have the potential to impact at larger scales. The amplitude of the surface water fluctuations (tides included) also plays a role in the response of the groundwater heads, affecting also flow topology and mixing processes (Wu et al. 2020; Sawyer et al. 2009; Trefry et al. 2019).

To exemplify the multiple spatio-temporal scales of SW-GW interactions, Figure 1.2 shows the Townley number (Townley 1995) vs the tidal strength (Trefry et al. 2019) for flow-through experiments, for different coastal aquifers, and for aquifers connected to rivers affected by hydropeaking, as described in the Supporting Information of (Ziliotto et al. 2021). The Townley number ($\mathcal{T} = \omega L^2 D_{eff}^{-1}$) measures the response of an aquifer to a periodic signal and is directly dependent to the frequency of the SW fluctuations (ω) and characteristic length of the aquifer (L), and inversely proportional to the effective aquifer diffusivity (D_{eff}). Higher values of the Townley number indicate that the fluctuating signal dampens fast, and lower values are associated with deeper propagation into the aquifer. The tidal strength ($\mathcal{G} = g_p J^{-1} L^{-1}$) represents the ratio of the amplitude of the forcing signal (g_p) to the inland head gradient (J) and the length scale. Higher values indicate that the system has higher propensity to chaotic mixing structures.

The distributions of $\mathcal{T}$ and $\mathcal{G}$ for multiple SW-GW systems in Figure 1.2 reinforce the necessity of analyzing the effects of highly transient boundary conditions on groundwater flow and mixing with a multiscale approach. Therefore, this dissertation covers three spatio-temporal scales: laboratory scale with subdaily fluctuations (Chapters 2-4), field scale with subdaily and daily fluctuations (Chapters 5-6), and regional scale with weekly fluctuations (Chapter 7).
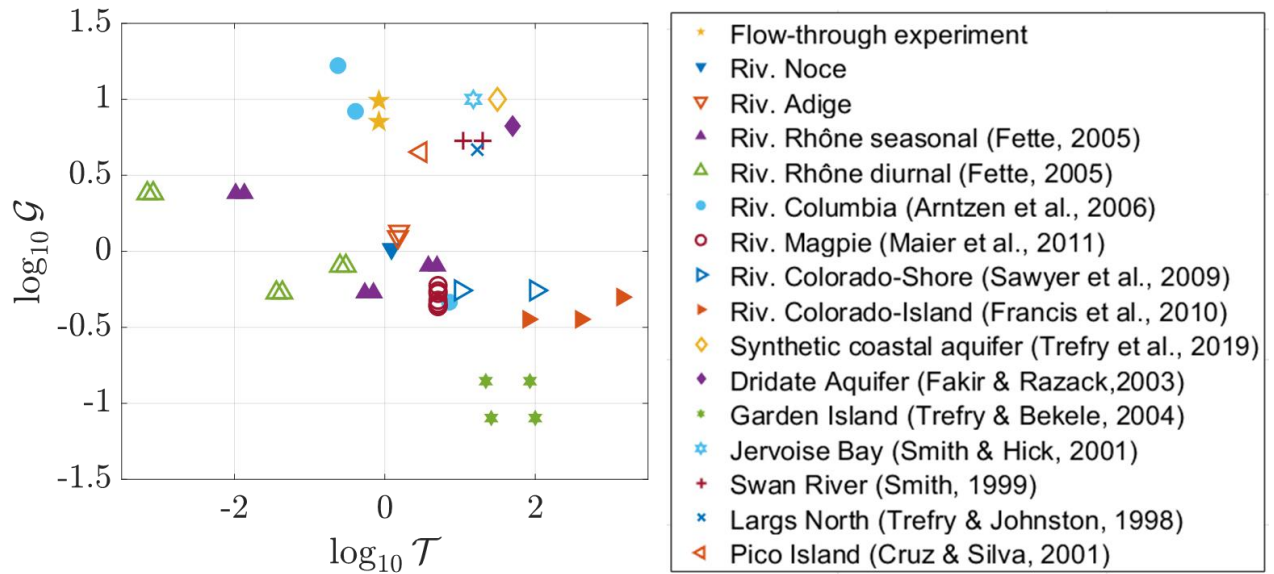
Figure 1.2: Logarithmic dimensionless Townley number ($\mathcal{T}$) and tidal strength ($\mathcal{G}$) for different SW-GW systems under transient boundary conditions. Adapted from the supporting information in Ziliotto et al. (2021).

1.3.2 LABORATORY EXPERIMENTS TO STUDY TRANSIENT FLOWS AND SW-GW INTERACTIONS

Hypothesis 2: Experimental laboratory tests are an important tool for understanding mixing processes in aquifers under highly transient boundary conditions.

Solute transport experiments can study mixing processes at different scales, including the pore scale (Souzy et al. 2020; Jiménez-Martínez et al. 2017), laboratory scale (Jaeger et al. 2009; Sprocati et al. 2021), and field scale (Cho et al. 2019). At the laboratory scale, experimental setups often consist of packed columns and flow-through chambers filled with a porous material. While packed columns are primarily for one-dimensional analysis (Cremer and Neuweiler 2019; Ahmadi et al. 2022), flow-through chambers allow to study flow and mixing processes in (quasi-) two (Castro-Alcalá et al. 2012; Rolle et al. 2009) and even three dimensions (Ye et al. 2016). Most of the flow-through chamber experiments studying solute transport and mixing have been performed under steady boundary conditions (e.g., Muniruzzaman & Rolle 2017; Muniruzzaman et al. 2014; Ye et al. 2015c; Castro-Alcalá et al. 2012; Rolle et al. 2009; Haberer et al. 2011; Santizo et al. 2020). Some studies, however, establish dynamic boundaries to account for the effect of an upwelling water table (Haberer et al. 2012) or ocean tides in coastal aquifers (Boufadel et al. 2006; Chang and Clement 2012). In the case of tidal effects, the dynamic boundaries have been implemented on the sides of the chambers, focusing mainly on the saltwater-freshwater interface (Chang and Clement 2012; Levanon et al. 2019), though some studies also have looked at the location of solute plumes (Boufadel et al. 2006). Compared to SW-GW interaction in coastal aquifers, physical models for studying river-aquifer interactions are new. Santizo et al. (2020) induced a hyporheic flow maintained partly by a water divider in order to study hyporheic processes. Hester et al. (2021) expanded their work and introduced transient conditions, which they created by changing the inflow in a lateral reservoir on the side of the hyporheic cell.

The cited literature exemplifies several experimental setups in the context of mixing processes, surface-water interaction and transient conditions. However, none of the previous studies have addressed the case of solute transport in the aquifer under highly transient boundary conditions. Chapter 2 targets this gap and thus introduces an experimental setup consisting on a flow-through chamber filled with a homogeneous porous medium connected to two water reservoirs on the top able to change their elevation and thus generate transient flows (Figure 1.3). The setup is representative of a vertical cross-section of an aquifer in hydraulic contact with two rivers (or with a meandering river) affected by hydropeaking and allows us to track the evolution of an injected conservative tracer.

7

In total, seven experiments were performed, considering steady and transient flows, different velocities and different fluctuation sequences. While the first five experiments are presented in Chapter 2, the remaining ones are introduced in Chapters 3 and 4. Table 1.2 summarizes their respective characteristics.
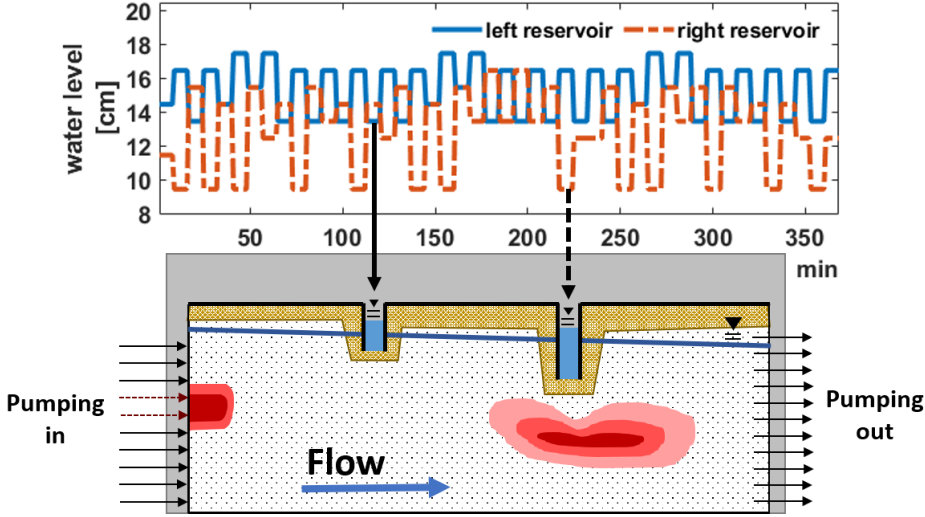
Figure 1.3: Experimental setup. Adapted from Basilio Hazas et al. (2022b).

No. experiment	Flow conditions	Averaged plume velocity*	Main phase shift
1	Steady state, no rivers	14 m/d	-
2	Steady state	14 m/d	-
3	Transient	14 m/d	In phase
4	Transient	14 m/d	Counter phase
5	Transient	14 m/d	Counter phase
6	Steady state	5 m/d	-
7	Transient	5 m/d	Counter phase

*The average plume velocity is rounded with respect to the mean velocity estimated for experiments no. 5 and no. 7, which are 14.09 ± 2.23 m/d and 4.97 ± 3.18 m/d, respectively. This is done for comparability in the analysis, since the pumping rates for the other experiments were the same.

Table 1.2: Summary of the different experiment configurations presented in Chapters 2 to 4.

1.3.3 TRANSIENT GROUNDWATER FLOW FIELDS AND MIXING ENHANCEMENT MECHANISMS

Hypothesis 3: *Highly transient boundary conditions at the SW-GW interface modify the topology of groundwater flow fields, thus enhancing mixing mechanisms.*

The topology of the flow can be analyzed using either Lagrangian or Eulerian approaches. The Lagrangian framework describes the fluid in terms of the trajectory of individual particles, whereas the Eulerian one looks at the instantaneous properties of the velocity field. Examples of Lagrangian approaches to quantify mixing enhancement are the Lyapunov exponents, associated with the divergence of a filament and stretching rates (Ottino 1990), and the methods based on the Cauchy Green tensor, which indicates the intensity and direction of the dominant flow deformation (Engdahl et al. 2014; Yoon et al. 2021). On the other hand, the Okubo-Weis function (Okubo 1970; Weiss 1991) is an Eulerian approach that distinguishes filamentary and vortex structures in two-dimensional flow fields. Positive values correspond to regions dominated by shearing and stretching forces (forming filaments), while negative values correspond to regions dominated by vorticity. In steady-state flows, regions with high Okubo-Weiss values also display mixing hotspots or high mixing probabilities (Engdahl et al. 2014; Wright et al. 2017). Furthermore, the effective Okubo-Weiss parameter (positive Okubo-Weiss values averaged over the area of a plume) shows a positive relation with the dilution of the plume (de Barros et al. 2012).

Previous studies on flow topology have theorized that ocean tides (Trefry et al. 2019; Wu et al. 2020) and engineered pumping systems (Bagtzoglou and Oates 2007; Piscopo et al. 2013; Neupauer et al. 2014; Sposito 2006) are able to generate chaotic advection, a flow regime with folding and stretching properties at low Reynold numbers and thus able to enhance mixing (Aref et al. 2017). While this dissertation does not focus on chaotic advection, it is worth noting that the surface water fluctuations in the flow-through experiments lead to a certain degree of plume folding and stretching. Moreover, the quantification of spreading and dilution showed evidence of mixing enhancement (Ziliotto et al. 2021). Therefore, the next objective is to study whether observed mixing processes are related to the flow topology generated by the implemented transient boundary conditions.

The dilution index (Kitanidis 1994) and the flux-related dilution index (Rolle et al. 2009) are common metrics for the quantification of mixing processes (e.g., Rolle et al. 2012; Rodríguez-Escales et al. 2017; Ballarini et al. 2014; Sprocati et al. 2021) and are based on the distribution of the concentration of the plume. The larger the dilution index, the solute is more uniformly distributed and occupies a larger area of the fluid, meaning that the peak concentration of a contaminant may be lower and thus less harmful for the environment (Kitanidis 1994). The dilution index can also be expressed in its logarithmic form, known as the Shannon entropy. Other methods to characterize solute transport are based on the breakthrough curves and the spatial moments of the plume (Rolle and Kitanidis 2014). The breakthrough curves allow to observe the evolution of the concentration at a specific location, the first spatial moment gives the location of the centroid of the plume, and the second spatial moment is a measure of the spreading and dispersion of the plume. The simultaneous use of these metrics helps to better understand the mechanisms for mixing enhancement in porous media (e.g., Muniruzzaman &Rolle 2017; Rolle et al. 2009; Rolle & Le Borgne 2019; Sprocati et al. 2021).

In order to analyze the flow topology of the experiments, it is necessary to solve the flow field using numerical simulations. Since mixing mechanisms are also investigated, it is necessary that the transport model uses parameters that properly upscale and reflect the physical mixing processes at the microscopic level. Therefore, the implemented parametrization of the transverse dispersion considers the non-linear relation to the flow velocity and dependence of molecular diffusion to the chemical species of the dissolved plume (Chiogna et al. 2010; Rolle et al. 2012; Delgado 2006; Ye et al. 2015c). This part of the investigation applies the mixing metrics mentioned in the previous paragraph, quantifies the geometrical characteristics of the plume (i.e., perimeter and area), and computes the effective Okubo-Weiss parameter. In addition, the dispersive fluxes, which depend on concentration gradients and the hydrodynamic dispersion, are also estimated and used to compute the spatially averaged flux components.

Chapter 3 deals with the implementation of the non-linear velocity-dependent transverse dispersion parametrization, the model calibration, the quantification of different mixing metrics, and the analysis of plume geometry, dilution index, and dispersive fluxes. Chapter 4 mainly focuses on the plume topology (Okubo-Weiss

field) and its relation to mixing (Shannon entropy). Figure 1.4 shows an example of the conservative tracer in the flow-through chamber, considering the original image, the plume concentration, the Okubo-Weiss field and the dispersive processes.
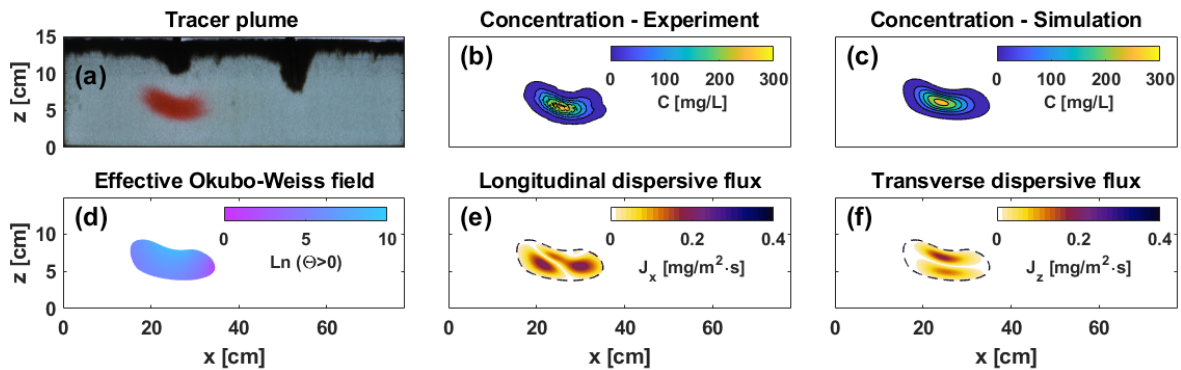
Figure 1.4: (**a**) Tracer plume, concentration distributions (C) from the (**b**) experiment and (**c**) model, (**d**) effective Okubo-Weiss field (Θ) over the plume area, and (**e**) longitudinal and (f) transverse dispersive fluxes (J_x and J_z) of the solute plume at time 109 minutes of the experiment 7 (Table 1.2). (a) and (d) are adapted from (Basilio Hazas et al. 2022b).

1.3.4 FLOW AND TRANSPORT IN HETEROGENEOUS AQUIFERS UNDER HIGHLY TRANSIENT BOUNDARY CONDITIONS

Hypothesis 4: *Highly transient boundary conditions influence the groundwater flow in heterogeneous aquifers and are able to create transient flow fields with different characteristics from steady-state heterogeneous flows.*

In Chapters 2 to 4, the analysis at laboratory scale of groundwater flow and transport is done on a homogeneous porous media. However, aquifers are heterogeneous, and coupling these heterogeneities to transient flows may reveal additional complexities with implications for mixing, as observed, for example, by Geng et al. (2020) in the transversal cross-section of a coastal aquifer.

Since the heterogeneities occur at different scales, the laws and parameters for mixing also change. An example is the upscaling of local processes into the macro scale (Dentz et al. 2011). Similarly, the laws for mixing in heterogeneous aquifers under transient flows are also different than those for steady-state flows (Rehfeldt and Gelhar 1992). For example, in steady flows, the transverse dispersion coefficients may remain in the order of magnitude of the local dispersion, but they evolve to the macroscopic dispersion coefficient under transient conditions (Dentz and Carrera 2003). This has been relevant for derivations of the effective dispersion tensor (de Dreuzy et al. 2012; Bolster et al. 2009; Dentz and Carrera 2003, 2005), which can be approached as the sum of the contribution of local dispersion, dispersion due to spatial heterogeneities, and the interaction between local dispersion, spatial heterogeneity and transient flows (Dentz and Carrera 2005).

At the field scale, the interaction between transient boundary conditions and heterogeneity has been studied under different approaches. Neupauer et al. (2014), for instance, applied an engineered pumping system to different hydraulic conductivity fields and observed that the degradation of a contaminant increased with the degree of heterogeneity. Wu et al. (2020) studied under which conditions tidal forcing would lead to chaotic regions in a Gaussian hydraulic conductivity field, depending on factors such as the amplitude of the fluctuations and the log-variance of the hydraulic conductivity. Modeling real study-sites, Wallace et al. (2020) and Song et al. (2018) studied the implications of a high-flow event and of hydropeaking (respectively) for biogeochemical reactions and thermal transport near the SW-GW interface.

Overall, there must be a link between the process understanding and its application on the field. Therefore Chapter 5 upscales the experimental setup of Chapters 2 to 4 by modeling a cross-section of a heterogeneous aquifer in contact with two rivers affected by hydropeaking. In particular, the model is based on a vertical cross-

section of the aquifer under the Adige Valley that is traversed by the Noce and the Adige rivers (Figure 1.5). The focus is to explore the interplay of the highly transient boundary conditions with the heterogeneity of the aquifer under different hydraulic scenarios (i.e., riverbed conductance) at the field scale, and to analyze how this affects conservative solute transport. Since the frequency of the fluctuations plays a role in their propagation into the aquifer, the simulations are at daily and hourly resolutions, which are representative of seasonal and sub-daily fluctuations.
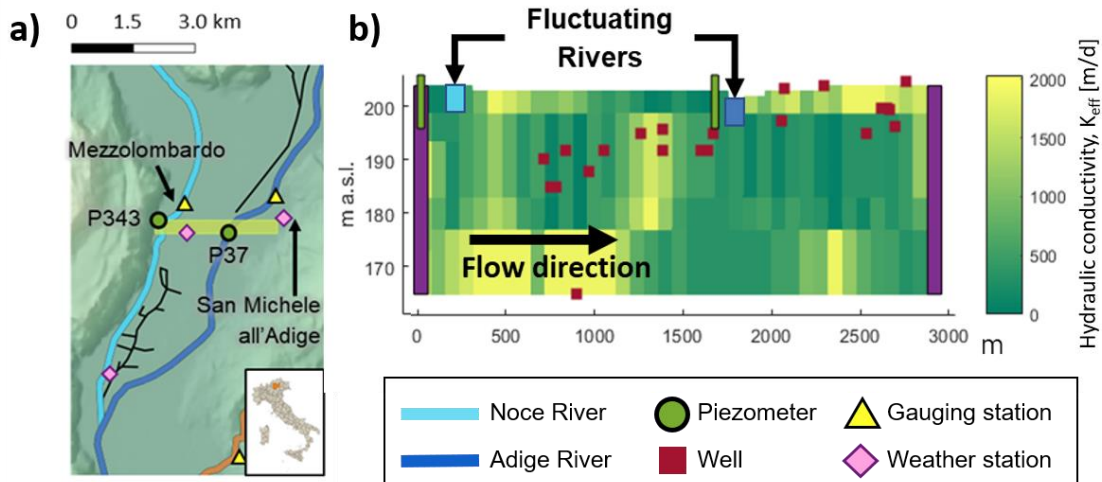
Figure 1.5: (**a**) Model domain and (**b**) vertical cross-section with heterogeneous hydraulic conductivity field. The area is the Adige Valley in Italy, which is traversed by different rivers affected by hydropeaking. Adapted from Basilio Hazas & Chiogna (2022)

1.3.5 UNCERTAINTY IN HIGHLY TRANSIENT BOUNDARY CONDITIONS

Hypothesis 5: The uncertainties associated with highly transient boundary conditions, such as hydropeaking, should be considered for predicting groundwater flow fields and mixing.

Models are simplifications of the natural world, and thus their accuracy may be hindered by several sources of uncertainty, which go from the measured data and model parameters, to the conceptualization of the problem and the equations used to represent different processes within the system (Anderson et al. 2015). These uncertainties propagate into the outputs and, depending on the purpose of the model, may have implications for the model calibration, forecasting, backcasting, or decision-making processes. In this sense, several works have thoroughly addressed sensitivity analysis and uncertainty quantification in environmental models (Pianosi et al. 2016; Teixeira Parente et al. 2019; Mattis et al. 2015; Beven and Binley 2014; Wu and Chen 2015; Merchán-Rivera et al. 2022b). Even in physical models such as our laboratory setups, where the inputs are typically known, it may be necessary to account for uncertainties. This was considered for example in the calibration of the flow-through experiments and mentioned in the Supporting Information for Chapter 4 (Appendix A.1). While this dissertation does not focus on methods for uncertainty quantification and sensitivity analysis, we consider that it is relevant to be aware that model uncertainties, particularly those associated with highly transient boundary conditions, may impact the analysis of groundwater flow and mixing processes.

Given the complex structure of the subsurface and data scarcity (e.g., few core drilling samples or hydrogeological measurements such as pumping tests and groundwater heads), most of the investigations related to uncertainty in the groundwater have focused on the heterogeneous properties of the aquifer (e.g., Nowak et al. 2010; Miller et al. 2018; Kitanidis 1986; Fu and Jaime Gómez-Hernández 2009). Other works included additional sources of uncertainty, such as precipitation and pumping rates (Vrugt et al. 2008; Xu et al. 2017) or the location and flux of a contaminant source (Mattis et al. 2015). Less attention has been paid to the

uncertainties related to surface water-groundwater interactions, especially under highly dynamic flows and extreme events (Merchán-Rivera 2022). For instance, river fluctuations due to hydropeaking depend on the operation of the hydropower plants, which in turn adapt to the energy market (Pérez Ciria et al. 2019; Chiogna et al. 2018a; Wagner et al. 2015) and the hydrological conditions of a specific season (Li and Pasternack 2021). Therefore, despite the typical periodicities of hydropeaking (Pérez Ciria et al. 2020), the occurrence, duration and amplitude of the peak events can change over time.

Chapter 6 centers its analysis on the propagation of different hydropeaking waves into a heterogeneous aquifer and how this affects mixing processes, described in terms of the Okubo-Weiss parameter (discussed in Chapter 4). The model remains at field scale, but it consists of a 2-dimensional horizontal section. The study is performed within a stochastic framework and, despite being a synthetic scenario, the frequency and amplitude of the fluctuations are inspired by those of the Noce River (Chapters 5 and 7). Figure 1.6 shows a scheme of the model boundaries and domain, the hydraulic conductivity field, and an example of the uncertain transient boundary conditions.
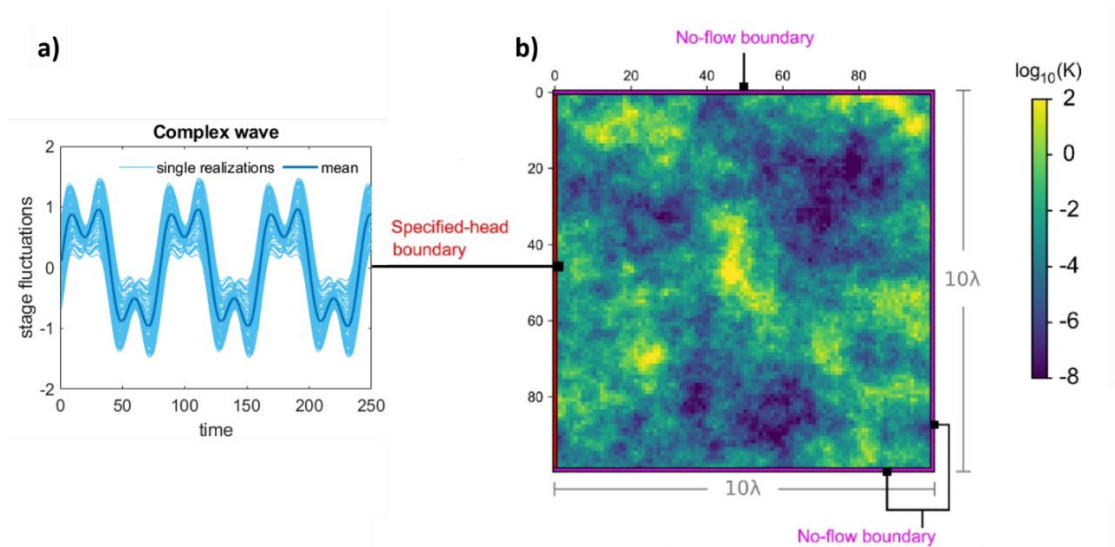
Figure 1.6: (**a**) Example of uncertain transient boundary conditions for the complex wave and (**b**) spatial domain and hydraulic conductivity field. λ is the correlation length used for generating the heterogeneous hydraulic conductivity field. Adapted from Merchán-Rivera et al. (2020).

1.3.6 MULTITEMPORAL ANALYSIS TO STUDY SW-GW INTERACTIONS AT REGIONAL SCALE

Hypothesis 6: Multitemporal analysis techniques, such as the wavelet transform, help to study the impact of hydropeaking in the aquifer at a regional scale.

Many investigations on hydropeaking and groundwater flow and transport at field scale consider systems with a single river (Shuai et al. 2019; Zachara et al. 2020; Song et al. 2020; Ferencz et al. 2019; Francis et al. 2010; Zachara et al. 2016). However, natural systems may have more complexities, as in the case of Alpine regions, where it is common that multiple dam-regulated rivers converge in relatively narrow valleys (Pérez Ciria et al. 2019). Furthermore, as mentioned in the introduction, hydropeaking has multiple periodicities (Pérez Ciria et al. 2019), with specific periods that control solute transport at larger scales (Rizzo et al. 2020). Overall, these reasons show the necessity for a more comprehensive analysis of hydropeaking and SW-GW interaction at large regional and multi-temporal scales. Nevertheless, such studies imply additional challenges. In fact, it would be computationally too expensive to process a regional model in a fine grid resolution able to capture solute transport features such as those observed in Chapters 2 to 5. Therefore, methods that imply only solving the flow field become relevant. However, it is also necessary to consider the dimensions of the model. For example, the

Okubo-Weiss parameter is currently defined for two-dimensional flow fields and has thus limitations in case of three-dimensional models [although a recent work has formulated an Okubo-Weiss type criterion for 3D axisymmetric flows using polar coordinates (Shivamoggi et al. 2022), its application to hydrogeological flows still needs to be studied].

Wavelet analysis techniques can be used to analyze the river and the groundwater head time series and thus offer an alternative approach for investigating the impact of hydropeaking on the aquifer. In fact, the continuous wavelet transform [CWT (Torrence and Compo 1998)] and the wavelet transform coherence [WTC (Grinsted et al. 2004)] have been applied to investigate non-stationary periodicities and identify correlations in multitemporal scales in different (hydro)geological systems (Tenorio-Fernandez et al. 2019; Lu et al. 2015), including in the context of SW-GW interaction (Chen et al. 2022; Song et al. 2018). The CWT detects the periodicities in a signal and determines the temporal scales and time frames at which such periodicities are dominant (Torrence and Compo 1998; Agarwal et al. 2016a; Pérez Ciria et al. 2019). The WTC looks at the correlation between two CWTs (Pérez Ciria et al. 2020) and can be understood as the local correlation coefficient of the time series in the time-frequency domain (Grinsted et al. 2004). In addition, the time-averaged wavelet spectrum and time-averaged coherent wavelet spectrum reveal the temporal scales at which the variability is more relevant.

Chapter 7 expands the vertical cross-section of Chapter 5 to the entire northern part of the Adige Valley in a three-dimensional model. The model covers three rivers differently affected by hydropeaking: the Noce, the Adige and the Avisio (Figure 1.7). However, instead of computing the solute transport, Chapter 7 applies wavelet analysis techniques to analyze the coherence between the river and the groundwater head fluctuations of the entire modeled aquifer. In particular, it focuses on the variability of 7 days, which is associated to the difference in energy production between the working days and the weekend (Chiogna et al. 2018a; Pérez Ciria et al. 2019; Majone et al. 2016). Furthermore, it introduces wavelet maps to analyze the weekly periodicity in the entire aquifer domain and compares wet and dry conditions.
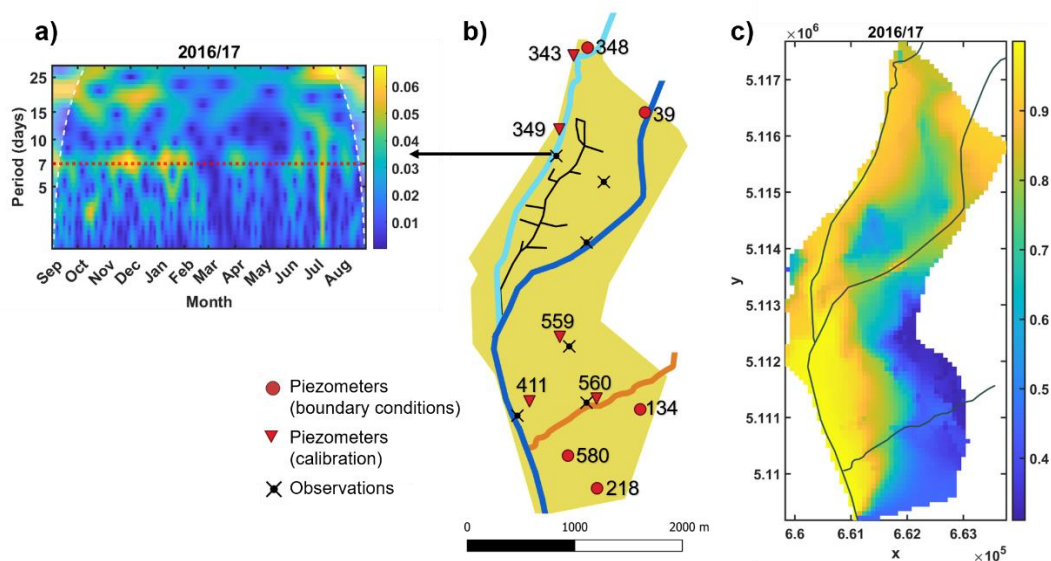
Figure 1.7: (**a**) CWT of the groundwater head time series at a selected observation point near the Noce River, (**b**) model domain for the Adige Valley, and (**c**) map of the time-averaged coherence wavelet spectrum at a period of seven days. The white shaded areas show the cone of influence. The dashed red line along the period of 7 days identifies the temporal scale focus of the present study. Warmer color indicates times and periods of intense power (in a) or areas of higher coherence between the river stage and groundwater heads (in b). Adapted from (Basilio Hazas et al. 2022a)

1.4 GOVERNING PRINCIPLES, METRICS AND EQUATIONS

While this section does not intend to be an exhaustive review of all the concepts and mathematical formulations included in the dissertation, it provides some principles and equations used for modeling flow and transport and quantifying mixing.

1.4.1 GROUNDWATER FLOW AND SOLUTE TRANSPORT

Flow in porous media is governed by the Navier-Stokes equation considering no slip and no flow boundary conditions at the grain-fluid interface. At the pore scale and low Reynolds numbers, the flow can be described by only solving the Stokes equation (e.g., Valocchi et al. 2019; Rolle and Kitanidis 2014):

$$\rho g \nabla h = \mu \nabla^2 \boldsymbol{v}$$
$$\nabla \cdot \boldsymbol{v} = 0$$

(1.1)

where $\rho[ML^{-3}]$ is the density of the fluid, $g\ [LT^{-2}]$ the acceleration due to gravity, $\nabla h\ [-]$ is the hydraulic head gradient, $\mu[ML^{-1}T^{-1}]$ the dynamic viscosity, and $\boldsymbol{v}[LT^{-1}]$ the velocity vector.

At the macroscopic scale, the flow can be described by the Darcy's law:

$$q = -\boldsymbol{K} \cdot \nabla h,$$

(1.2)

where $q\ [LT^{-1}]$ is the specific discharge, and $\boldsymbol{K}\ [LT^{-1}]$ corresponds to the hydraulic conductivity tensor.

Since this dissertation deals with the macroscopic description of flow and transport, the next equations presented here apply to this case. Therefore, the groundwater flow equation for transient flows with a constant density is computed through the combination of Darcy's law and the continuity equation:

$$S\frac{\partial h}{\partial t} = \boldsymbol{\nabla} \cdot (-\boldsymbol{K} \cdot \nabla h) + \boldsymbol{q'},$$

(1.3)

where $\boldsymbol{q'}\ [LT^{-1}]$ is a source/sink term, and $S\ [-]$ is the storage coefficient.

Fick's law defines the diffusive flux $\boldsymbol{J}[ML^{-2}T^{-1}]$ of a dissolved species as

$$\boldsymbol{J} = -\boldsymbol{D}\nabla C,$$

(1.4)

where $C[ML^{-3}]$ is the tracer concentration, and $\boldsymbol{D}[L^2T^{-1}]$ is the dispersion tensor.

Then the transport equation for a conservative tracer in the groundwater is described by the advection-dispersion equation:

$$\frac{\partial(nC)}{\partial t} = \nabla \cdot (n\boldsymbol{D}\nabla C) - \nabla \cdot (n\boldsymbol{v}),$$

(4)

where $n[-]$ is the porosity.

The dispersion tensor is composed by the longitudinal dispersion coefficient, D_L, and a transverse dispersion coefficient, D_T. Here we use a non-linear hydrodynamic transport model, where D_L and D_T are parametrized as follows:

The longitudinal dispersion coefficient is estimated using a linear, grain size (d_p) specific parametrization (Guedes de Carvalho and Delgado 2005; Muniruzzaman & Rolle 2017)

$$D_L = D_P + \frac{1}{2}d_P v$$

(1.5)

The transverse dispersion coefficient uses a grain size and compound-specific non-linear parameterization (Chiogna et al. 2010; Ye et al. 2015c)

$$D_T = D_P + D_{aq} \left(\frac{Pe^2}{Pe + 2 + 4\delta^2} \right)^{\beta},$$

(1.6)

where D_P $[L^2 T^{-1}]$ denotes the effective pore diffusion coefficient, Pe is the dimensionless grain Péclet number defined as $Pe = |v| d_p / D_{aq}$, $\delta [-]$ is the ratio between the length of a pore channel and its hydraulic radius, and $\beta [-]$ is an empirical exponent to capture the degree of incomplete mixing in pore channels. The effective pore diffusion coefficient approximated by $D_P = D_{aq}/\tau$, being $D_{aq} [L^2 T^{-1}]$ the aqueous pore diffusion coefficient, $\tau [-]$ is the tortuosity, which is posed equal to the inverse of the porosity (Boving and Grathwohl 2001; Grathwohl 1998). The values of β=0.5 and δ=5.37 are based on the compilation of transverse dispersion experiments presented in Ye et al. (2015c). An alternative and frequently used parametrization of the transverse dispersion at the field scale is to consider a variable that is linearly dependent of the longitudinal one, that is $D_T = k D_L$, where *k* commonly takes the value 0.1. This parametrization was used in Chapter 5.

Boundary conditions

The boundary conditions can be classified in three different types. The first type, or Dirichlet boundary conditions, consists of specified head boundaries where the groundwater head along the boundary is a known value. In the second type, or Neumann conditions, the derivative of the head at the boundary is known; therefore, this boundary is also called specified flow boundary. No flow conditions are a special case of Neumann conditions. Finally, the boundaries of the third type are the Robin boundaries, or head-dependent boundaries, which are a mixture of the first and the second boundary types.

The transient boundary conditions representing the fluctuating rivers can be considered as Robin boundary conditions. In such case, the implementation for a river reach can follow Harbaugh et al. (2000) as:

$$q_{riv} = c_{riv}(h_{riv} - h')$$

(1.7)

where q_{riv} $[L^3 T^{-1}]$ is the head-dependent flux, h_{riv} $[L]$ is the head of the river and $c_{riv} [L^2 T^{-1}]$ is the riverbed conductance. The value of $h'[L]$ depends on whether the river is in contact with the saturated aquifer. If it is connected, h′ is the head of the saturated cell; if disconnected, it takes the value of the bottom of the riverbed.

The Robin boundary conditions are used in most chapters of this dissertation, except in Chapter 6, where the transient boundary conditions are modeled as Dirichlet boundaries. This was done to consider only the effect of the groundwater fluctuations propagating into the aquifer without additional parametrizations, such as the riverbed conductance.

1.4.2 METRICS FOR MIXING

Breakthrough curves and vertical profiles

The evolution of the concentration in time or along the space can be analyzed through breakthrough curves and vertical profiles. The breakthrough curves (BTCs) show concentration changes in time at specific point of the domain. While this is typically done at the outlet of flow-through experiments, additional measurement points are established within the porous media domain. The vertical profiles show the concentration of the plume along a vertical line for a given time. These profiles are also drafted at the outlet and in the interior of the flow-through chamber. Figure 1.8 shows an example of a BTC and a vertical profile for a solute plume.
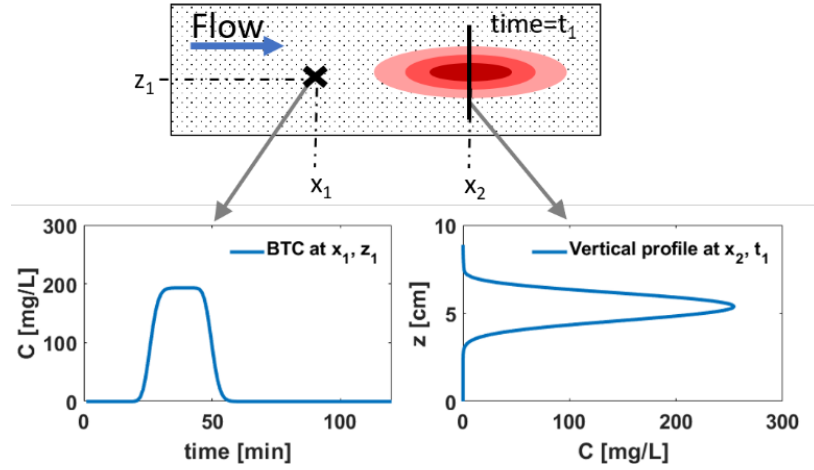
Figure 1.8: Schematics of a breakthrough curve (BTC) taken at the observation point (x_1, z_1) and a vertical profile along x_2 at time t_1 in a flow-through experiment.

Dilution index

The dilution index (Kitanidis 1994) quantifies the dilution of a conservative solute plume and for the continuous case is calculated as

$$E(t) = exp\left(-\int_V p\,(x,t)\ln\big(p\,(x,t)\big)\,dV\right) \tag{1.8}$$

where p(x,t) is the probability distribution function of the mass in the x-coordinate at time t.

$$p(x,t) = \frac{C(x,t)}{\int_V C\,(x,t)dV}, \tag{1.9}$$

being C the concentration of the plume and V the total volume of the domain. In its logarithmic form, the dilution index represents the Shannon entropy of the plume, ln E(t).

Spatial moments

The first and second spatial moments give, respectively, the location and spreading of the plume. The first spatial moment, α_i, indicates where is the centroid of the plume in the i-direction:

$$\alpha_i(t) = \int_V p\,(x,t)\,x_i\,dV \tag{1.10}$$

And the second spatial moment measures the spreading of the plume around the centroid:

$$\Delta_{ij}(t) = \int_V p\,(x,t)(x_i - \alpha_i)\big(x_j - \alpha_j\big)dV \tag{1.11}$$

where Δ_{xx} and Δ_{zz} are the longitudinal and transverse spreading, respectively.

Geometrical descriptors

The geometry of the plume is described in terms of its perimeter and area. The area, $A[L^2]$, is calculated by a spatial integration of the regions occupied by the plume

$$A(t) = \int H[C(x,t)]\,dA \tag{1.12}$$

where $H(y)$ is the Heaviside step function.

The perimeter is calculated following the Freeman method, which applies chain code algorithm (Freeman 1961). The chain code algorithm encodes the drawing direction of the contour of a figure in a sequence that allows to identify vertical, horizontal and diagonal directions. For an anisotropic rectangular grid, the perimeter is estimated as proposed in Chapter 3:

$$P = \Sigma(0 \; or \; 4) \times \Delta x \; + \; \Sigma(2 \; or \; 6) \times \Delta z \; + \; \Sigma(odd) \times \sqrt{\Delta x^2 + \Delta z^2} \tag{1.13}$$

where $\Sigma(0 \; or \; 4)$ are the total number of horizontal chain directions, $\Sigma(2 \; or \; 6)$ refers to the vertical chain directions, and $\Sigma(odd)$ corresponds to the diagonal chain directions.

1.4.3 FLOW TOPOLOGY

The topology of a two-dimensional flow field can be described by the partial derivatives of the velocity as follows:

$$\alpha = 2\frac{\partial v_x}{\partial x}, \qquad \sigma = \frac{\partial v_z}{\partial x} + \frac{\partial v_x}{\partial z}, \qquad \omega = \frac{\partial v_z}{\partial x} - \frac{\partial v_x}{\partial z}, \tag{1.14}$$

where $\alpha \; [T^{-1}]$ corresponds to stretching, $\sigma \; [T^{-1}]$ to shearing, and $\omega \; [T^{-1}]$ to vorticity. The Okubo-Weis parameter (Okubo 1970; Weiss 1991), Θ, is then computed by

$$\Theta = (\alpha^2 + \sigma^2) - \omega^2 \tag{1.15}$$

Thus, the Okubo-Weiss field differs regions where shearing and stretching dominate (positive values), from regions dominated by vorticity (negative values). Since the shearing and stretching forces are associated to areas of local mixing strength (e.g., Wright et al. 2017), global mixing properties are estimated using the effective Okubo-Weiss parameter (de Barros et al. 2012):

$$\Theta^e(t) = \frac{\sum \Theta(\boldsymbol{x}, t) H[\Theta(\boldsymbol{x}, t)] H[C(\boldsymbol{x}, t)] \Delta X \; \Delta Z}{\sum H[\Theta(\boldsymbol{x}, t)] H[C(\boldsymbol{x}, t)] \Delta X \; \Delta Z}, \tag{1.16}$$

where $\Theta(\boldsymbol{x}, t)$ and $C(\boldsymbol{x}, t)$ are the Okubo-Weiss function and tracer concentration estimated at time t over the space coordinates $\boldsymbol{x}$ [L], and $H(y)$ is the Heaviside step function.

CHAPTER 2

FLOW-THROUGH LABORATORY EXPERIMENTS TO STUDY HYDROPEAKING

Published as

Abstract

This study presents high-resolution flow-through experiments investigating transport processes in a laboratory setup mimicking an aquifer affected by hydropeaking (i.e., abrupt fluctuations in the river stage by the release or storage of water in reservoirs). Highly transient flow conditions were experimentally generated by sudden changes of the water level in two rivers in hydraulic contact with an unconfined aquifer. High-resolution image analysis and depth-resolved, high-frequency sampling at the outlet allowed monitoring the spatio-temporal evolution and the breakthrough of a dye tracer plume in the porous medium. The plume spreading and mixing were quantified by moment analysis and entropy based metrics of the scalar field. We show that hydropeaking strongly enhances spreading and mixing in the subsurface (up to 249.5% and 41.8% in these experiments) and demonstrate the relevance of considering highly transient flow regimes to properly capture transport and mixing-controlled biogeochemical reactions at the surface water - groundwater interface.

2.1 INTRODUCTION

Mixing of fluids is relevant in many fields of science and engineering over a large range of time and length scales (Aref et al., 2017; Kitanidis, 1994; Ottino, 1990; Rolle & Le Borgne, 2019; Valocchi et al., 2019). Mixing is strongly associated to stretching and deformation in the flow field (Ottino, 1990) and to the combined action of advection and diffusion mechanisms (Turuban et al., 2019). In geophysical flows, mixing affects biogeochemical cycles, mineral precipitation/dissolution, carbon sequestration, oil recovery, and surface water and groundwater contamination and remediation (e.g., Cardenas et al. 2004; Chiogna et al. 2012; Cil et al. 2017; Wallace et al. 2020; Zhang et al. 2010).

In porous media, mixing is often slow and incomplete thus constituting the overall rate-limiting step of many biogeochemical processes (Sole-Mari et al., 2020; Valocchi et al., 2019; Wright et al., 2017). Therefore, identifying the mechanisms that can enhance mixing is of great importance, in particular at the millimeter to meter scale where mixing-controlled reactions often occur in a very thin (bio)reactive fringe (Bauer et al. 2009; Hester et al. 2017; Rolle et al. 2013). At the pore scale, fingering structures (de Anna et al., 2014; Jiménez-Martínez et al., 2016) and chaotic advection (Heyman et al., 2020; Lester et al., 2013; Lester et al., 2016; Souzy et al., 2020; Turuban et al., 2019) enhance mixing and exert a key control on dispersion and reaction rates. At the Darcy scale, anisotropic (Chiogna et al. 2015; Ye et al. 2015c; Ye et al. 2018) and heterogeneous flow fields (e.g., de Barros et al., 2012; Dentz et al., 2016) enhance plume dilution and reactive mixing. Variability in the hydraulic conductivity fields (Rolle et al., 2009; Werth et al., 2006; Ye et al., 2015c), topographic features (Bandopadhyay et al., 2018) and transient conditions (e.g., de Dreuzy et al., 2012; Kahler & Kabala, 2016; Sposito, 2006; Piscopo et al., 2013; Trefry et al., 2019) lead to spatially variable flow fields.

Transient flow fields are important both in natural and engineered subsurface systems (Piscopo et al., 2013; Singh et al., 2020). For instance, in coastal aquifers, the combined effect of tides and regional groundwater flow impacts mixing and reactive processes (Geng et al., 2020; Trefry et al., 2019; Wu et al., 2020a), influencing salinity distributions and biogeochemical processes. Among engineered applications, in the field of groundwater remediation, transient flow fields have been proposed to enhance reactant delivery and contaminant degradation (Bagtzoglou and Oates 2007; Neupauer et al. 2014; Reising 2018; Rodríguez-Escales et al. 2017; Zhang et al. 2009). Transient flow fields and their effect on spreading, including the theoretical derivation of an effective dispersion tensor have been also analyzed in previous studies (de Dreuzy et al., 2012; Dentz & Carrera, 2003; Dentz & Carrera, 2005; Bolster et al., 2009). These studies focused on heterogeneous porous media and on the evolution of spreading towards an asymptotic behavior. Effective and macrodispersion coefficients were commonly expressed as a function of the heterogeneous properties of the porous medium. Our focus here is on mixing occurring in aquifer systems affected by hydropeaking in hydraulically connected rivers, where sudden fluctuations in river stage at the sub-daily scale are caused by the release or storage of water in artificial reservoirs. This hydrological regime leads to sharp and frequent fluctuations in the groundwater velocity field, altering the flux and solute exchange between the river and the aquifer and, in combination with the geomorphic features of the river, it plays an important role in physical, geochemical, thermal and biological processes in the hyporheic zone (Cardenas et al., 2004; Ferencz et al., 2019; Hester et al., 2013; Sawyer et al., 2009; Schmadel et al., 2016; Shuai et al., 2019; Song et al., 2018; Wu et al., 2018; Wu et al., 2020b). Hydropeaking affects sediment and solute transport in the river (Béjar et al. 2018; Pulg et al. 2016), as well as, biogeochemical cycles (Maavara et al. 2020) and riverine ecosystems (Gillespie et al. 2015; Hauer et al. 2017a). However, the experimental quantification of the impact of hydropeaking on solute transport, mixing, and mixing enhancement in the underlying aquifer has received little attention.

This work provides experimental evidence of the effects of hydropeaking on solute transport and mixing enhancement in porous aquifers. We adopt an approach based on multidimensional flow-through experiments, which have been increasingly used to investigate solute transport and mixing in steady-state flow fields (e.g.,

Castro-Alcalá et al. 2012; Haberer et al. 2015; Muniruzzaman & Rolle 2015, 2017; Simmons et al. 2002; Ye et al. 2015b). Conversely, fewer contributions have provided experimental evidence of the effect of transient boundary conditions on mixing (e.g., Boufadel et al., 2007; Cho et al., 2019; Zhang et al., 2009), particularly in the context of surface water-groundwater interaction (Santizo et al., 2020). We focus on groundwater plume spreading and mixing enhancement caused by fluctuating stages in two river transects in hydraulic contact with the aquifer. Such setup was inspired by the conditions typically encountered in the Alps, where multiple streams in the same plain are affected by the operation of different hydropower plants (Perez-Ciria et al., 2019) and it is also representative of a longitudinal cross section of a meandering or braided river affected by a hydropeaking wave. We perform the experiments in a quasi-two-dimensional flow-through chamber representing the vertical cross-section of an unconfined homogeneous aquifer. The homogeneous porous medium allowed us to study the impact of transient flows caused by hydropeaking on solute transport and mixing in isolation, avoiding mixing enhancement effects that occur in heterogenous porous materials (e.g., Rolle et al. 2009; Werth et al. 2006; Ye et al. 2015a). A dye tracer is injected in the setup in a series of five experiments considering both steady and transient flows. High-resolution monitoring of the spatio-temporal plume evolution is performed with a non-invasive imaging technique and by depth-resolved sampling and spectrophotometric measurements at the outlet of the setup. We quantify plume spreading and mixing, and their link with the highly fluctuating flow fields by analyzing breakthrough curves (BTCs), the second central spatial moments of the solute distribution, the dilution index and the flux-related dilution index.

2.2 EXPERIMENTAL SETUP

A quasi 2-D acrylic glass setup with inner dimensions of 77.9×15×1.1 cm^3 (length × height × width) was used as flow-through chamber (Figure 2.1). The experiments were performed in an unconfined homogenous porous medium made of glass beads with diameter in the range 1.0-1.5 mm (Sartorius AG, Germany).
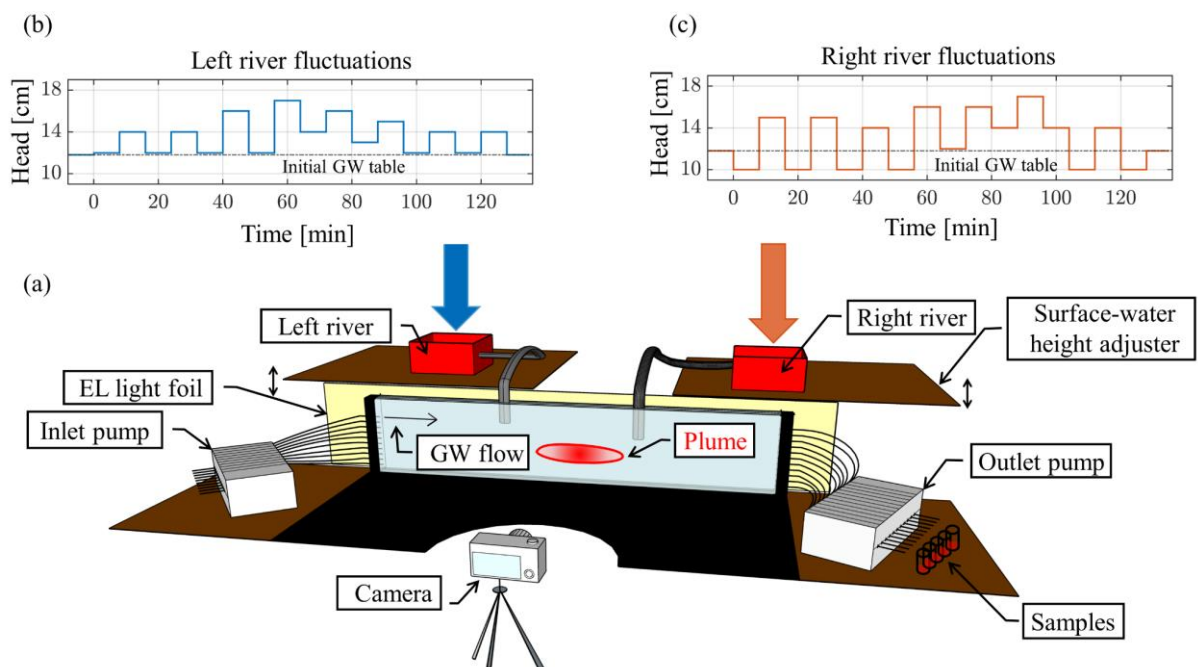

Figure 2.1: (**a**) Schematic illustration of the experimental setup, including the flow-through chamber, the inlet and outlet pumps, and the reservoirs placed above two surface-water height adjusters mimicking hydropeaking. (**b-c**) Hydrographs showing the fluctuations of the two rivers used in one of the transient flow experiments (Transient 1).

In the transient flow experiments, an additional layer of sand (d=0.5-0.8 mm, Euroquartz, Germany) was positioned on top of the glass beads to recreate the riverbed and the riverbanks. The riverbed bottoms of the two river transects were placed at different depths in the flow-through chamber to allow for both losing (left river) and variably losing/gaining conditions (right river), moreover the rivers have different widths and riverbed thickness as indicated in Table S1. The flow through system is equipped with 13 ports, equally spaced by a constant distance of 1.1 cm. Two high-precision multi-channel peristaltic pumps (IPC-N24, ColeParmer, United States) were connected to the lowest ten inlet and outlet ports to establish the flow in the aquifer. To generate transient flow conditions within the porous medium, two water reservoirs were connected to the top of the flow-through chamber with two semi-rigid tubes and placed on two surface-water height adjusters, which could be moved vertically to simulate an oscillating water head (Figure 2.1). An additional channel was considered at the outlet to avoid the overflow of the system due to the additional water from the losing conditions of the rivers in the transient experiments. The river stage fluctuations are shown in Figure 2.1.

In the experiments we consider river-aquifer interaction by changing the phase of the oscillations in the stage of the two rivers, the amplitude of the fluctuations, the river bottom location, the thickness of the sandy river bottom, and the width of the two rivers. The frequency of the oscillations is kept constant. In the transient experiments, the Townley number (i.e., ratio between the relative time scale of diffusion and the tidal forcing), and the tidal strength (i.e., ratio between the amplitude of the tidal forcing and the regional gradient) are typical for systems affected by hydropeaking (Francis et al., 2010; Sawyer et al., 2009; Pérez-Ciria et al. ,2019) and costal aquifers (e.g., Trefry et al., 2019) and are reported in the Supporting Information (Text S1, Table S1 and Figure S1). The grain Péclet number of the experiment is 566 and indicates advection-dominated conditions. During each experiment, a constant concentration C_0=300 mg/L of the red azo dye new coccine (CAS 2611-82-7, Sigma-Aldrich, United States) solution was injected from the two central inlet ports (fourth and fifth) for 24 minutes. This tracer is chemically stable and photostable and displays low scattering and no fluorescence (Jaeger et al., 2009). The plume movement and concentration were captured with optical imaging, using a Nikon D5000 camera (12 Megapixel resolution, 18-55 mm Nikon lens). Details about the optical calibration are provided in Text S2 and Figures S2-S3 (Supporting Information). We collected samples at the outlet ports every 4 minutes (~120 samples for each experiment) and measured the tracer concentration using a DR 3900 Spectrophotometer (Hach Lange, Germany). The collected samples were also used to validate the results obtained from the optical analysis and to calculate the flux-related dilution index. The spectroscopy calibration curve is shown in Figure S4.

We processed the raw images taken with the camera to quantify the concentration of the tracer using an algorithm based on the one presented by Jaeger et al. (2009). A comparison between raw photographs and post-processed images is shown in Figure 2.2 for four plume pictures at different time steps (Figures 2.2a-b) and the mapped concentrations (Figures 2.2c-d) under steady and transient flow conditions.

The photographs in Figure 2.2 highlight the difference in the plume shape between the steady and transient setups while the tracer plume moves through the porous medium. A deformed plume in the transient experiment (Figure 2.2b) is observed as a consequence of the interaction with the rivers. Besides capturing the evolving shape of the plume, the post-processed images (Figures 2.2c-d) allowed us to quantify the temporal evolution of solute concentrations, which is necessary for the analysis of spreading and mixing in each experiment.
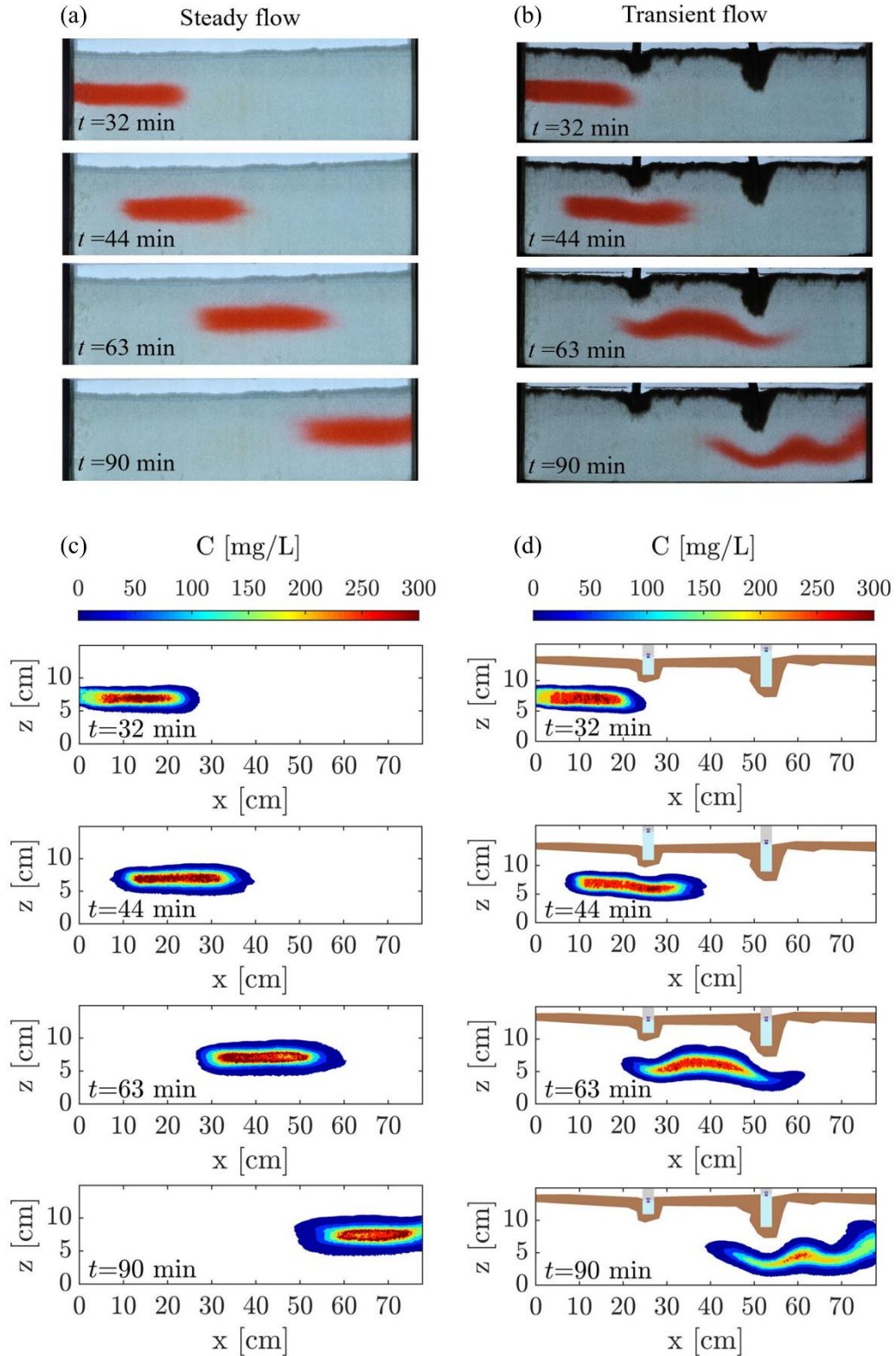
Figure 2.2: Photographs (**a-b**) and processed images (**c-d**) of the dye tracer plume at different time steps under steady and transient flow conditions.

A total of five flow-through experiments was performed. The first one was run under steady-state flow conditions without the river system. In the second experiment, the rivers were added to the previous setup, keeping the head of both rivers equal to the groundwater table to avoid any surface water - groundwater exchange. Finally,

three transient flow experiments were performed considering two time series of fluctuating river heads (Figure 2.1). In the first transient experiment, the head fluctuations in the left and right rivers were in-phase, while in the second one they were in counter-phase. In the third transient flow experiment, the river fluctuations in counter-phase were repeated by filling with sand the whole part of the flow-through chamber above the glass beads, to reduce the possible occurrence of water levels higher than the porous matrix and in this way lowering the centroid of the plume in the vertical direction after injection of the tracer solution (Figure S8). Details of the experimental settings, river fluctuations, and hydraulic and transport parameters are reported in Table S1.

2.3 EVALUATION OF PLUME SPREADING AND MIXING

We computed the spatial moments to analyze the distribution of the solute concentration in the porous medium and to quantify the spreading of the plume and its temporal evolution. The first spatial moment in the i- direction, α_i [L], is used to describe the location of the centroid of the plume and it is calculated as:

$$\alpha_i(t) = \int_V p\,(\boldsymbol{x}, t)\, x_i\, dV \qquad (2.1)$$

where x_i is the ith component of the spatial coordinates, t is a dimensionless time expressed in pore volumes (PV=(v t)/L, where v is the seepage velocity and L is the length of the flow-through chamber), and $p\,(\boldsymbol{x}, t)$ [L^{-3}] is the probability distribution of the location of the tracer at time t in the domain V:

$$p\,(\boldsymbol{x}, t) = \frac{c(\boldsymbol{x}, t)}{\int_V c\,(\boldsymbol{x}, t)\, dV} \qquad (2.2)$$

The second spatial moment $\boldsymbol{\Delta}_{ij}$ [L^2] is a second-order tensor and represents the mean square distance from the centroid of the plume. It gives information about the spreading of the plume and it is computed as:

$$\Delta_{ij}(t) = \int_V p\,(\boldsymbol{x}, t)(x_i - \alpha_i)(x_j - \alpha_j)dV \qquad (2.3)$$

A dimensionless second spatial moment is obtained by dividing the value of $\Delta_{ij}(t)$ by $\Delta_{ij}(t_p)$, where t_p is the time at which the tracer solution is completely injected in the flow-through setup. To evaluate mixing in porous media, we computed the dilution index (Kitanidis, 1994) and the flux-related dilution index (Chiogna et al., 2011; Rolle & Kitanidis, 2014). The dilution index $E(t)$ [L^3] is related to the Shannon entropy of the concentration of a plume and is a true measure of mixing that is expressed by the following equation:

$$E(t) = exp\left(-\int_V p\,(\boldsymbol{x}, t)\ln\big(p\,(\boldsymbol{x}, t)\big)\, dV\right) \qquad (2.4)$$

The dimensionless representation of the dilution index is called volumetric reactor ratio M and it is obtained by dividing the dilution index by the volume of the flow-through system. The flux-related formulation of the dilution index, $E_Q(\boldsymbol{x}, t)$, can also be used to characterize mixing in flow-through porous media. This metric quantifies how the mass flux of a solute is distributed over a given flow rate (Chiogna et al., 2011; Rolle et al., 2009) and it is calculated as (Rolle & Kitanidis, 2014):

$$E_Q(\boldsymbol{x}, t) = exp\left(-\int_A p_Q\,(\boldsymbol{x}, t)\ln\big(p_Q\,(\boldsymbol{x}, t)q_x(\boldsymbol{x}, t)\big)\, dA\right) \qquad (2.5)$$

where $q_x(\boldsymbol{x},t)$ [L/T] is the component of the specific discharge in the main flow direction, A [L^2] is the cross-sectional area normal to the main flow direction and $p_Q(\boldsymbol{x},t)$ is the flux-related probability density function of the concentration:

$$p_Q(\boldsymbol{x},t) = \frac{c(\boldsymbol{x},t)}{\int_A c(\boldsymbol{x},t)q_x(\boldsymbol{x},t)dA} \tag{2.6}$$

The dimensionless representation of the flux-related dilution index is obtained by dividing $E_Q(\boldsymbol{x},t)$ by the water flux through the system.

2.4 RESULTS AND DISCUSSION

The experiments performed in this study allowed investigating the dynamics of spreading and mixing of a plume affected by the transient fluctuations occurring in the river stage due to hydropeaking. Such fluctuations have an important impact both on the solute breakthrough at the outlet of the setup and on the concentration distribution within the porous medium.

2.4.1 BREAKTHROUGH CURVES
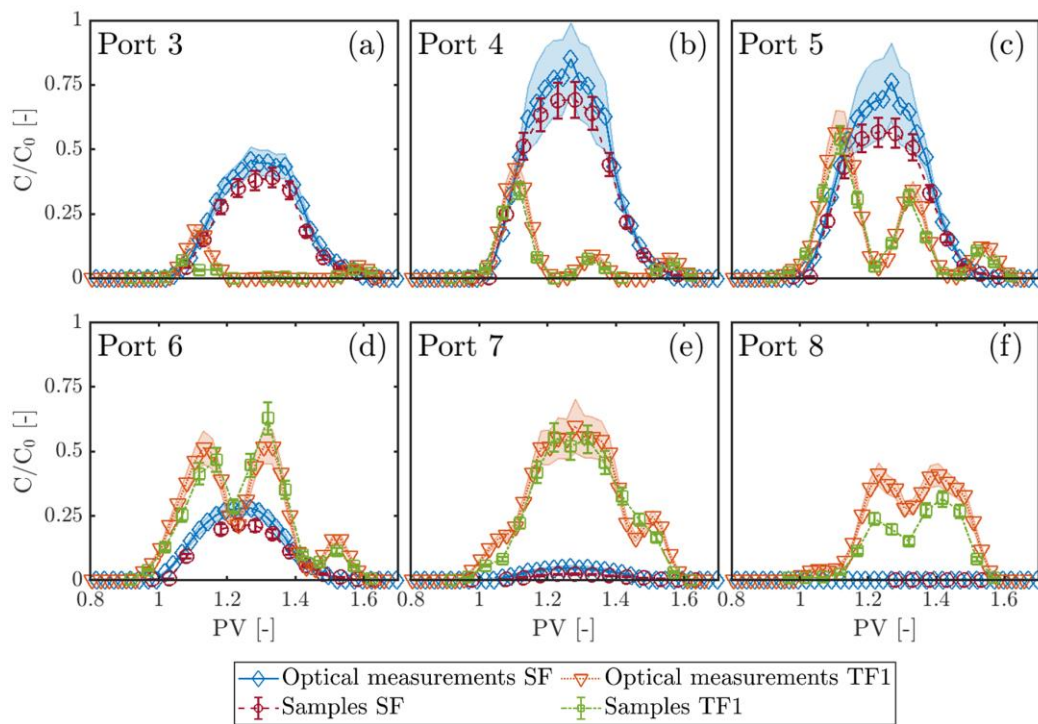
Figure 2.3: Breakthrough curves obtained from the results of the optical analysis and spectrophotometric measurements of the samples collected at different outlet ports in a steady flow (SF) and transient flow experiment 1 (TF1). The shaded areas represent the experimental uncertainty of the concentration estimated by image analysis.

The quantification of solute concentration at the outlet of the flow-through chamber allowed obtaining port-resolved (Figure 2.3) and integrated BTCs (Figure S6). The BTCs of new coccine at several outlet ports reported in Figure 2.3 show the results of transport under steady flow conditions and under the fluctuating conditions of

the transient flow 1 experiment. Similar results for the other transient experiments are reported in Figures S5 and S6, showing that considering both in-phase or counter-phase oscillations leads to multi-peaked BTCs.

In the steady flow field, the solute plume displays the typical bell-shaped concentration distribution at all ports, and the highest peak concentrations occur at ports 4 and 5, which are in line with the injection of the plume at the inlet. The breakthrough curves of the transient flow 1 experiment display more complex patterns. As observed in Figure 2.2, the transient flow, induced by the fluctuations in the river stage, leads to stretching and folding, enhanced spreading in the longitudinal and transverse directions, and also depth-dependent variations of the advective velocity. The part of the plume closer to the river is more affected by the change in the hydraulic head gradients and shows more pronounced deformation in the concentration distribution within the porous medium. The breakthrough curves measured in the transient experiments become multi-modal, especially in the core of the plume (ports 4, 5, 6, and 7); normalized concentrations higher than 0.5 occur now at three ports (ports 5, 6 and 7) at three distinct times (1.12 PV, 1.32 PV and 1.28 PV respectively) and we can observe strong fluctuations in the concentration values measured at the same port at different times. Besides the concentration values of the measured breakthrough curves, the river stage fluctuations also impact the time at which peak concentrations are reached. The first peak concentration occurs earlier in the transient experiment than the single-peak displayed in the steady flow experiment. In fact, the mean velocity increases due to the local reduction of the thickness of the saturated porous medium induced by the presence of the rivers (this effect is clearly visible in the breakthrough curves measured for the steady flow experiment with rivers in Figure S5). Moreover, positive and negative fluctuations around the mean flow velocity caused by changes in the river stage can both accelerate and decelerate the plume movement (depending on its location in the system), increase spreading in the longitudinal direction, and influence local dispersion by sharpening concentration gradients and by affecting the magnitude of the hydrodynamic dispersion coefficients. We provide further details and data about solute breakthrough in the Supporting Information, including the port-resolved breakthrough curves for all experiments (Figure S5), the depth-integrated breakthrough curves (Figure S6), and the evolution of the vertical spatial profiles at the outlet for the steady flow and the transient flow experiment 1 (Figure S7). Considering the location of the first central moment on the vertical direction through the comparison between Transient 2 and Transient 3 experiments, we can observe that the multi-modal shape of the BTCs is more pronounced in plumes that flow closer to the river boundary (Figures S5 and S8).

2.4.2 PLUME SPREADING, MIXING, AND MIXING ENHANCEMENT

The normalized second moments in the longitudinal and transverse directions, $\Delta_{xx}(t) / \Delta_{xx}(t_p)$ and $\Delta_{zz}(t) / \Delta_{zz}(t_p)$, respectively, and the volumetric reactor ratio M for all flow-through experiments were computed based on the results of the image analysis (Figures 2.4a-c). The flux-related reactor ratio, M_Q (Figure 2.4d), was calculated from the collected samples at the outlet using the flow rate measured at each port and the samples' solute concentrations determined by spectrophotometric analysis. These quantities were calculated to analyze and quantify the impact of the rivers' fluctuations on plume spreading, mixing, and mixing enhancement. In addition to the experimental results of the steady flow experiment, we computed the analytical solution of the 2-D advection-dispersion equation considering a pulse input of a tracer from a line source (Text S3). Even if the analytical solution requires some simplifications in comparison to the experimental setup, it describes very well the steady flow experiment without rivers, validating the evidence collected in the steady flow experiments and allowing the quantification of local longitudinal and transverse dispersion coefficients ($D_{l,sf} = 1.02 \times 10^{-7}$ m^2/s and $D_{t,sf} = 8.0 \times 10^{-9}$ m^2/s).
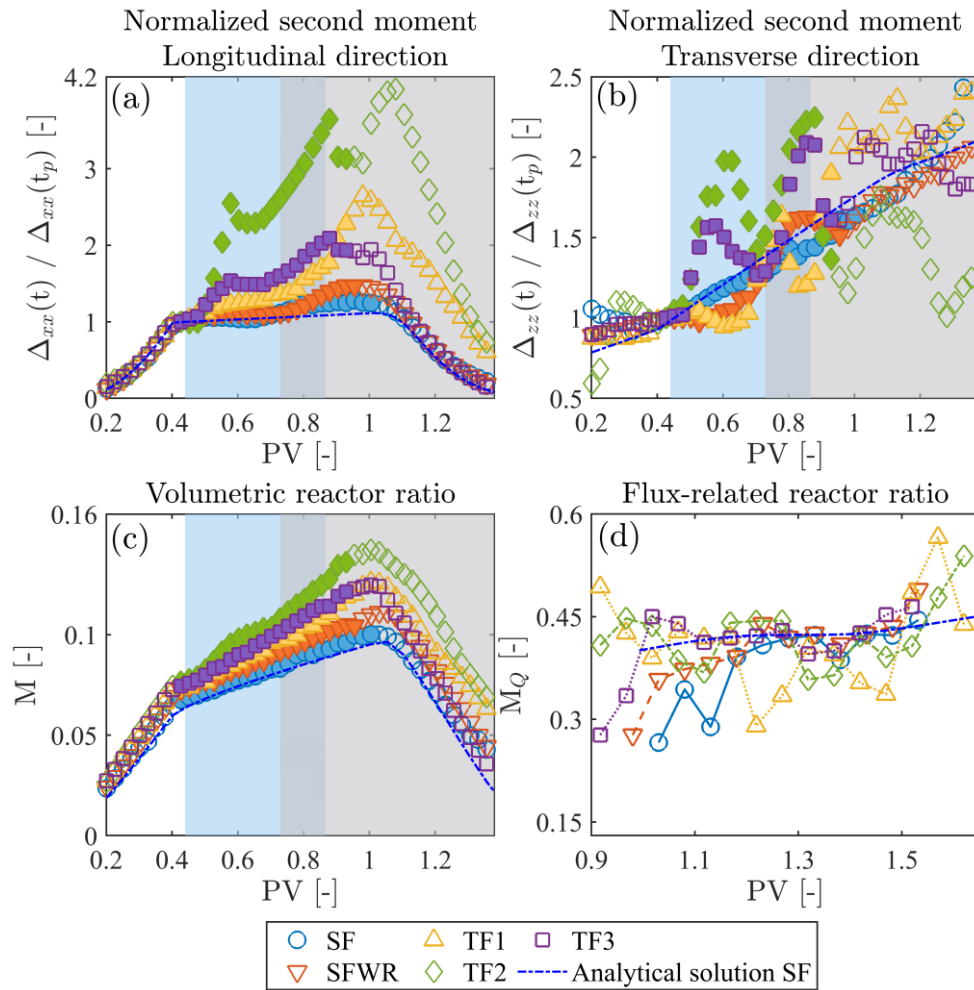
Figure 2.4: Second spatial moments normalized by $\Delta_{ij}(t_p)$, where t_p is the time at which the tracer solution is completely injected in the flow-through setup, obtained from the optical analysis for all the experiments (**a-b**). Volumetric reactor ratio M obtained from the optical analysis for all the experiments (**c**). The filled markers indicate the time during which the tracer solution is completely injected in the flow-through setup. The light blue area ( ) indicates the time spent by the plume under the left river, while the grey area ( ) indicates the time spent under the right river. Panel (**d**) shows the flux-related reactor ratio obtained from the spectrophotometric analysis of the samples collected at the outlet of the setup.

Figures 2.4a-b show that the spreading in the longitudinal and transverse directions is more pronounced in the transient flow experiments than in the steady flow ones. The spreading in the longitudinal direction increases following almost a monotonic trend for all the experiments. However, we can observe the different effect of a loosing river (left river) in comparison to a loosing/gaining river (right river). The increase in longitudinal spreading is reduced under loosing conditions since the longitudinal flow velocity of the plume decreases. If loosing/gaining conditions are variably present, longitudinal spreading decreases/increases due to the river acting as a source/sink term for the flow. On the contrary, the spreading in the transverse direction fluctuates strongly in accordance with the squeezing and the stretching of the plume caused by the oscillations in the rivers' water table. The highest and fastest increase in spreading occurs below the river on the right, where the shape of the plume significantly changes. The downstream river is located deeper than the one upstream and is characterized by stage fluctuations with a larger amplitude. Therefore, the closer the plume is to the surface water-groundwater interface and the larger the fluctuations, the larger is the expected effect of hydropeaking on spreading. For instance, the comparison between transient 2 and transient 3 experiments close to the left

26

river shows that the amplitude in the fluctuations of Δ_{zz} is related to the distance of the centroid of the plume to the river (Figure S8). Comparing the differences in the timing of the peaks in Δ_{zz}, we can appreciate the effect of the phase shift between the oscillations in transient 1 (in-phase), and transient 2 and transient 3 (counter-phase) experiments. Moreover, during transient flow conditions, local transverse dispersion, which is nonlinearly dependent on the groundwater flow velocity (Chiogna et al., 2010), may have an additional effect on enhancing spreading in the vertical direction (Figure 2.4b). Even if mixing cannot be described by the second moments only, a correlation between spreading in the vertical direction and mixing can be observed. In fact, the dilution index increases faster under transient flow than in steady flow conditions (Figure 2.4c). As observed, the spatial variability of the flow velocity leads to changes of plume shape, enhances solute spreading, affects local dispersion coefficients, and all these processes result in enhancement of plume dilution. Finally, we observe that the hydropeaking-induced fluctuations impact the distribution of the solute mass flux over the water flux (Figure 2.4d). The flux-related reactor ratio integrates both the impact on solute distribution by diffusive-dispersive processes at the plume fringe as well as the changing water flux due to the hydraulic connection of the rivers with the underlying aquifer. Overall, the fluctuations cause a distribution of the solute over a larger flow rate in particular at early and late times (i.e., 0.92 PV < t < 1.12 PV and 1.47 PV < t < 1.62 PV, respectively) when higher values of flux-related reactor ratio are reached. This behavior is explained by the fact that plumes in the transient experiments are more elongated than in the steady flow experiments and the forward and backward fringes of the plume are more diluted. Spreading and mixing enhancement show very dynamic patterns, which are illustrated in Figures S9, S10 and S11 (Supporting Information). The sole presence of the rivers leads to some increase of Δ_{xx} and Δ_{zz} (i.e., 20.4% and 49.8%, respectively) as shown in Figures S9-S10, and only to a slight mixing enhancement of 4.8% at the outlet of the system (Figure S11). All transient flow experiments show significant spreading enhancement (Δ_{xx} from 63% to 105.6% and Δ_{zz} from 81.9% to 249.5%) and mixing enhancement ranging from 23.7% to 41.8% at the end of the system, with respect to the steady flow experiment. More specifically, the spreading enhancement only due to hydropeaking (i.e. compared with the steady flow with rivers experiment) ranges from Δ_{xx} 44.7% to 78.8% and from Δ_{zz} 38.7% to 209.6%, and the mixing enhancement ranges from 13.2% to 29.7% at the outlet of the flow-through chamber. In the transient flow experiment 1, we observe the smallest maximum enhancement in lateral spreading (i.e., 81.9%) and consequently the smallest mixing enhancement (23.7%). Conversely, when Δ_{zz} reaches its maximum value in the transient flow experiment 2 (249.5% at 0.43 PV), we observe a variation in the slope of the volumetric reactor ratio (Figures 2.4 b-c) and the highest increment (+41.8%) is reached at the outlet of the system (Figures S10-S11). These results show a positive correlation between plume deformation quantified through lateral spreading and mixing enhancement. In particular, from the analyzed setups we can observe that the distance of the plume to the riverbed and the amplitude of the fluctuations are key factors controlling mixing and spreading, whereas the phase shift between the fluctuations of the two rivers and the thickness of the sand layer play a minor role. Finally, Figure S12 shows that our system does not reach an asymptotic value in the effective dispersion coefficient as, for example, in Dentz and Carrera (2005), de Dreuzy et al. (2012) and Bolster et al. (2009) due to the local impact of the river fluctuations and their high frequency. In our experiment, the system remains in non-equilibrium conditions and the mean values of both longitudinal and transverse effective dispersion coefficients, normalized by $D_{l,sf}$ and $D_{t,sf}$, vary with the river fluctuations.

2.5 CONCLUSIONS

The laboratory investigation performed in this study provides first experimental evidence of the effects of dynamic river fluctuations, mimicking hydropeaking conditions, on solute transport and concentration distribution in the subsurface. The experimental outcomes, obtained by combining high-resolution imagining techniques and conventional depth-resolved sampling and spectrophotometric analysis, show that hydropeaking generates multi-modal, fluctuating breakthrough curves. Our results also show a significant spreading and mixing enhancement when comparing the transient flow with the steady flow experiments. Moreover, the unique

dataset collected in this experimental investigation can be used in future studies to test theoretical works on plume dispersion in porous media, as well as the capabilities of numerical models to accurately describe flow and transport under transient conditions. The rivers' fluctuations enhance spreading in the longitudinal direction and cause the spreading in the vertical direction to strongly fluctuate because of the squeezing and the stretching of the plume. Even if spreading cannot univocally describe mixing, the link between the spreading in the vertical direction and mixing enhancement is evident. In fact, when the plume is more deformed and consequently diffusive/dispersive fluxes occur over a larger area, mixing is also enhanced. These findings are opposite to the observations in heterogeneous media, where mixing enhancement is mainly caused by flow focusing: in regions of high hydraulic conductivity contrast, streamlines are squeezed and the area available for diffusive/dispersive fluxes decreases (i.e., a reduction in transverse spreading), however the solute distributes effectively over a larger water flux. Indeed, the main mixing enhancement in the setup considered in this study is due to an increase in plume spreading and to changes in the local dispersion coefficient caused by the highly transient boundary conditions. Our outcomes show the importance of considering hydropeaking, and more generally transient conditions at the surface water-groundwater interface, as an important factor for subsurface solute transport.

CHAPTER 3

RELATION BETWEEN MIXING AND PLUME GEOMETRY IN POROUS MEDIA

In preparation as

Abstract

Highly transient boundary conditions affect mixing of dissolved solutes in the groundwater. An example of these transient boundary conditions occurs at the surface water-groundwater interface, where the water level in rivers can change rapidly due to the operation of hydropower plants, leading to a regime known as hydropeaking. Inspired by this phenomenon, this work studies at laboratory scale the effects of fluctuating surface water bodies on solute transport in aquifers. We performed flow-through experiments at different velocities and under steady and transient flow conditions where a conservative tracer was injected in the system and its concentration measured via optical imaging methods. The experimental results were quantitatively interpreted with numerical simulations implementing a non-linear velocity-dependent dispersive transport model. We estimated plume dilution by computing the dilution index and its evolution as well as two key geometrical metrics of the transient plumes: the perimeter and the area. We further investigated mixing enhancement interpreting it through the analysis of spatially distributed dispersive fluxes. The results show that despite a good correlation between the plume perimeter and the dilution index, the plume area is a better proxy for analyzing dilution enhancement, as most of the dispersive fluxes occur within the plume. We also observe that the imposed transient boundary conditions enhance both longitudinal and transverse dispersive fluxes, with the latter contributing the most to the mixing enhancement of the plume.

3.1 INTRODUCTION

Describing mixing in porous aquifers is complex since it results from multiple processes at different scales (Dentz et al. 2011; Rolle and Le Borgne 2019; Marçais et al. 2022). At the pore scale, solutes can follow different pathways and velocities due to the structure and distribution of the porous media. This behavior can induce incomplete mixing (Le Borgne et al. 2011; Rolle and Kitanidis 2014; Jiménez-Martínez et al. 2016), filamentary structures in reactive fronts (de Anna et al., 2014) and chaotic advection in the pores (Souzy et al. 2020; Turuban et al. 2019; Lester et al. 2013; Lester et al. 2016). The variability in the flow field leads to stretching, folding and elongation of dissolved solutes, and therefore to a longer interface for molecular diffusion. At the continuum scale, hydrodynamic dispersion couples the effect of aqueous diffusion and pore velocity variability to describe solute dispersion. Its lower limit is molecular diffusion reduced by a tortuosity factor, and as the velocity increases, hydrodynamic dispersion increases due to mechanical dispersion pores (Souzy et al. 2020; Turuban et al. 2019; Lester et al. 2013; Lester et al. 2016). Local hydrodynamic dispersion at the fringes of a dissolved contaminant plume plays an important role in mixing and degradation in aquifer systems (Cirpka et al., 2012; Rolle et al., 2013; Valocchi et al., 2019; Wright et al., 2017). Therefore, many researchers have looked for a proper description of the longitudinal and transverse hydrodynamic dispersion coefficients based on experimental, theoretical and numerical modelling approaches (Delgado 2006; Hochstetler and Kitanidis 2013; Hochstetler et al. 2013; Scheidegger 1954).

At larger scales, mixing can be enhanced due to heterogeneities in the soil matrix, which lead to a wide range of groundwater flow velocities and to the formation of complex patterns with flow focusing and defocusing (Dentz et al., 2016; Rolle et al., 2009; Werth et al., 2006). Moreover, anisotropies in three-dimensional porous media can cause helical streamlines in groundwater flows (Bakker & Hemker, 2002) and lead to higher mixing rates (Chiogna et al., 2014; Chiogna et al., 2015; Cirpka et al., 2015; Ye et al., 2015a; Ye et al., 2020). Transient boundary conditions can also alter the groundwater flow field, generally yielding a mixing enhancement both considering time-varying regional flow boundaries (de Dreuzy et al., 2012; Dentz & Carrera, 2005; Goode & Konikow, 1990; Kinzelbach & Ackerer, 1986; Trefry et al., 2019; Wu et al., 2020) and engineered flow fields (Bagtzoglou & Oates, 2007; Cho et al., 2019; Neupauer et al., 2014; Neupauer et al., 2020; Piscopo et al., 2013; Rodríguez-Escales et al., 2017; Sposito, 2006; Zhang et al., 2009). For instance, theoretical works on heterogeneous porous media show that both the longitudinal and the transverse effective dispersion coefficients increase under fluctuating boundary conditions, whereas under steady-state flows, the transverse effective dispersion coefficient is similar to the local dispersion coefficient (Cirpka & Attinger, 2003; Dentz & Carrera, 2003, 2005).

At larger scales, mixing can be enhanced due to heterogeneities in the soil matrix, which lead to a wide range of groundwater flow velocities and to the formation of complex patterns with flow focusing and defocusing (Dentz et al. 2016; Rolle et al. 2009; Werth et al. 2006). Moreover, anisotropies in three-dimensional porous media can cause helical streamlines in groundwater flows (Bakker and Hemker 2002) and lead to higher mixing rates (Chiogna et al. 2015; Ye et al. 2020; Chiogna et al. 2014; Ye et al. 2015a; Cirpka et al. 2015). Transient boundary conditions can also alter the groundwater flow field, generally yielding a mixing enhancement both considering uniform time-dependent boundaries (Kinzelbach and Ackerer 1986; Goode and Konikow 1990; de Dreuzy et al. 2012; Dentz and Carrera 2005) and engineered flow fields (Bagtzoglou and Oates 2007; Cho et al. 2019; Neupauer et al. 2014; Piscopo et al. 2013; Rodríguez-Escales et al. 2017; Sposito 2006; Trefry et al. 2019; Wu et al. 2020; Zhang et al. 2009; Neupauer et al. 2020). For instance, theoretical works on heterogeneous porous media show that both the longitudinal and the transverse effective dispersion coefficients increase under fluctuating boundary conditions, whereas under steady-state flows, the transverse effective dispersion coefficient is similar to the local dispersion coefficient (Dentz and Carrera 2003, 2005; Cirpka and Attinger 2003).

Dynamic boundaries at the surface water-groundwater interface may be caused by natural phenomena such as ocean tides (Geng et al. 2020; Trefry et al. 2019; Wallace et al. 2020; Wu et al. 2020), peak discharge events

(Guérin et al. 2019; Gu et al. 2008; Singh et al. 2019; Singh et al. 2020; Merchán-Rivera et al. 2021) and seasonal fluctuations such as snow melting (Huntington and Niswonger 2012; Zaremehrjardy et al. 2022), or by anthropogenic causes, such as the operation of hydropower plants that leads to a river hydrological regime known as hydropeaking (Pérez Ciria et al. 2019; Casas-Mulet et al. 2015; Hauer et al. 2017b). The fluctuations in the water level and the characteristics of the bed geomorphology (Cardenas et al. 2004; Bandopadhyay et al. 2018; Gomez-Velez et al. 2014; Wu et al. 2018) affect physical and biogeochemical processes, including hyporheic exchange, nutrient cycling or arsenic mobilization (Hester et al. 2017; Boano et al. 2014; Schmadel et al. 2016; Gu et al. 2012). Hydropeaking, in particular, is a highly transient boundary condition because the changes in the river stage are abrupt and occur within a few minutes or hours. The impacts of hydropeaking on hyporheic flow and mixing have been widely studied using different approaches, including numerical models (e.g., Gomez-Velez et al. 2017; Singh et al. 2019; Singh et al. 2020; Schmadel et al. 2016; McCallum and Shanafield 2016; Ferencz et al. 2019), laboratory experiments (Santizo et al. 2020) and field-based investigations (e.g., Arntzen et al. 2006; Schmadel et al. 2017; Derx et al. 2010). The effect of hydropeaking on the groundwater in farther areas from the river has been investigated to a lesser extent despite its relevance for the correct estimation of energy and mass fluxes. For instance, Francis et al. (2010) observed that hydropeaking in the Colorado River leads to changes in the groundwater flow field in a riverine island. Moreover, works conducted in the Columbia River corridor have shown that hydropeaking may extend hundreds of meters from the shore (Zachara et al. 2013) and affect solute transport along the shoreline and the flood plain (Zachara et al. 2016; Song et al. 2020; Rizzo et al. 2020). And recently, Merchán-Rivera et al. (2022a) showed the impact of different hydropeaking waves on flow topology and hence on mixing.

In the present work, we aim to investigate the effect of highly transient surface water-groundwater boundary conditions on solute transport at laboratory scale. To this end, we perform flow and transport modeling to quantitatively interpret the outcomes of previous transient and steady- experiments (Ziliotto et al. 2021; Basilio Hazas et al. 2022b) and a new steady-state experiment with the aim of exploring the relation between mixing and plume geometry. The numerical simulations are performed with the widely used software MODFLOW (Boyce 2020; Harbaugh et al. 2000) and MT3D-USGS (Bedekar et al. 2016b), with a non-linear parameterization of transverse dispersion implemented in the transport simulator. We consider two different groundwater flow velocities and both steady and transient flow conditions. Specifically, we focus on the relation between the dilution index (Kitanidis 1994) and the geometrical characteristics of the plume (i.e., perimeter and area). The laboratory setup allows us to investigate at high spatial and temporal resolution the impact of transient flow conditions at the surface water/groundwater interface on solute transport and mixing while avoiding the influence of additional mixing enhancement mechanisms such as flow focusing or helical flows which may occur in heterogeneous anisotropic natural aquifers.

3.2 MATERIALS AND METHODS

3.2.1 EXPERIMENTAL SETUP

The experimental setup consists of a quasi two-dimensional flow-through system that represents a vertical cross-section of a homogeneous, unconfined aquifer in contact with two surface water bodies. The water level in the water bodies changes emulating two rivers affected by hydropeaking (Figure 3.1). The chamber, with inner dimensions of 77.9×15×1.1 cm (length × height × width), is homogeneously filled with glass beads [1.0-1.5 mm diameter, hydraulic conductivity $1.27×10^{-2}$ m/s – (Rolle et al. 2009)] and connected to a pumping system that generates the groundwater flow. The pumping system includes 10 inlet ports (numerated from top to bottom) and 11 outlet active ports. We inject for 24 minutes a conservative color tracer using two of the central inlet ports (Ports 4 and 5), and as it moves through the chamber, we track its concentration changes at high temporal and spatial resolution using a digital camera (Nikon D5000) with image processing techniques. In addition, we

measure its concentration at the outlet using spectroscopy techniques. Further details on the experimental setup are found in Ziliotto et al. (2021).
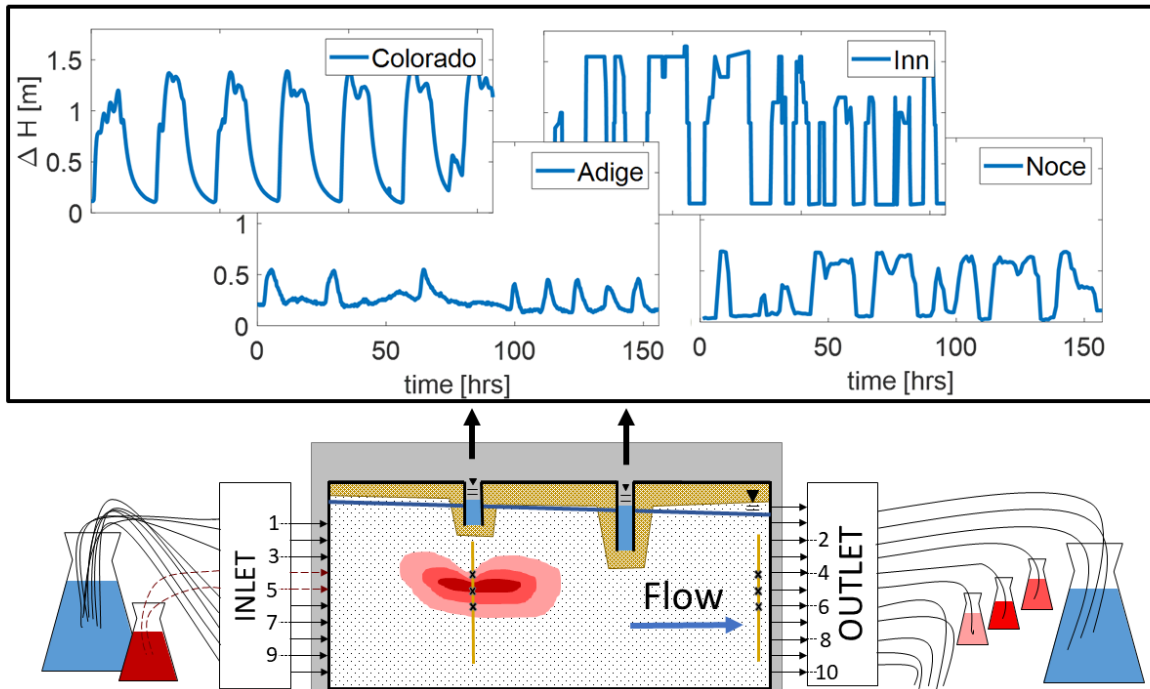
Figure 3.1: Sketch of the experimental setup (not at scale) representing an unconfined aquifer in hydraulic contact with two rivers affected by hydropeaking. A sand layer (yellow, darker area) on the top of the chamber represents the sediment material of the riverbanks. The crosses (black) and vertical lines (yellow) represent the location of the 6 observation points. The top panel shows examples of hydropeaking time series for different rivers.

This study focuses on two transient flow experiments at different pumping rates. In the first case, the pumping rate is set up to 0.456 ± 0.025 mL/min, which leads to an average plume velocity of 14.09 ± 2.23 m/d. In the second case, the flow rates at the ports are set up to 0.138 ± 0.009 mL/min, leading to an average seepage velocity of 4.97 ± 3.18 m/d in the transient case. Through the variability around the average seepage velocities, the effect of river fluctuations on the flow field is accounted. For the sake of simplicity, the velocities will be referred to as 14 m/d and 5 m/d henceforth, respectively.

3.2.2 FLOW MODEL

The model consists of 450,300 cells, corresponding to 1,140 columns ($\Delta x = 0.068\ cm$), and 395 layers with two different vertical discretizations: a coarse one ($\Delta z_c = 0.080\ cm$) and a refined one ($\Delta z_f = 0.027\ cm$). The refined layers are located from z=2.326 cm and z =10.722 cm which is the zone through which the tracer moves. This discretization allows us to adequately model the observed multiple peaks in the breakthrough curves. The transient groundwater flow equation at the Darcy scale with a constant density is computed through the combination of Darcy's law and the continuity equation:

$$\boldsymbol{\nabla} \cdot (\boldsymbol{K} \cdot \nabla h) + \boldsymbol{q}' = S \frac{\partial h}{\partial t} \qquad (3.1)$$

where K $[LT^{-1}]$ is the hydraulic conductivity tensor, ∇h $[-]$ the hydraulic head gradient, q' $[LT^{-1}]$ is a source/sink term, and S $[-]$ is the storage coefficient. Under unconfined conditions $S = S_s b$, S_s $[L^{-1}]$ is the specific storage and b $[L]$ is the thickness of the confined cell; in the unsaturated zone, the storage is equal to the specific yield ($S = S_y$).

We solve the groundwater flow equation with the One Water Hydrologic Flow Model MODFLOW-OHWM (Boyce et al. 2020), a version based on MODFLOW-2005 that unifies different packages and solvers in a single executable file. In particular, we use the Newton-Raphson solver NWT (Niswonger et al. 2011), which can account for the non-linearity in the solutions due to drying and rewetting cycles especially when the water level is moving across different layers. As convergence criteria we use a tolerance error up to 0.6 % as suggested in the literature (Anderson et al. 2015)

The flow-through system is simulated as an unconfined aquifer. The flux entering and leaving the system through the ports is treated as a Neumann boundary condition and therefore simulated using the Well Package (McDonald and Harbaugh 1988) in the cells corresponding to the location of the inlet and outlet ports. Each well had assigned the flow rate measured in the corresponding channel of the pumping system. The other cells on the left and right boundaries and the bottom of the model are treated as no-flow boundaries. The hydraulic conductivity is divided into two zones: one for the area occupied by the glass beads and another one for the sand.

The rivers are simulated as Robin boundaries using the River Package (McDonald and Harbaugh 1988). The equation to estimate the water flow q_{riv} $[\mathrm{L}^3\mathrm{T}^{-1}]$ through the river reach is written as

$$q_{riv} = c_{riv}(h_{riv} - h') \tag{3.2}$$

where h_{riv} $[\mathrm{L}]$ is the head of the river; $h'[\mathrm{L}]$ is the head of the saturated cell if the river is in contact with the aquifer, or the bottom of the riverbed if the aquifer and the river are disconnected; and $c_{riv}[\mathrm{L}^2\mathrm{T}^{-1}]$ is the riverbed conductance, which is considered a fitting parameter of the model.

3.2.3 TRANSPORT MODEL

The transport of conservative solutes in the groundwater can be described by the advection-dispersion equation:

$$\frac{\partial C}{\partial t} = \nabla \cdot (\boldsymbol{D}\nabla C) - \nabla \cdot (vC) \tag{3.3}$$

where $C[ML^{-3}]$ is the tracer concentration, $\boldsymbol{D}$ $[L^2T^{-1}]$ is the dispersion tensor, and v $[LT^{-1}]$ is the effective pore velocity. The transport simulations are calculated with MT3D-USGS (Bedekar et al. 2016a), which is coupled to MODFLOW-NWT.

We modified the source code to implement a non-linear hydrodynamic transport model. In this case, the longitudinal dispersion coefficient is based on a linear, grain size specific parametrization (Guedes de Carvalho and Delgado 2005; Muniruzzaman & Rolle 2017):

$$D_L = D_P + \frac{1}{2}d_P v \tag{3.4}$$

and for the transverse dispersion coefficient we use a grain size and compound specific non-linear parameterization (Chiogna et al. 2010; Rolle et al. 2012)

$$D_T = D_P + D_{aq}\left(\frac{Pe^2}{Pe + 2 + 4\delta^2}\right)^\beta \tag{3.5}$$

where $D_P [L^2 T^{-1}]$ is the effective pore diffusion coefficient approximated by $D_P = D_{aq}/\tau$, being $D_{aq} [L^2 T^{-1}]$ the aqueous pore diffusion coefficient, τ [-] is the tortuosity, which is posed equal to the inverse of the porosity n (Boving and Grathwohl 2001; Grathwohl 1998), d_p [L] is the grain size and Pe is the dimensionless grain Péclet number equal to $Pe = |v| d_p / D_{aq}$. The constant δ $[-]$ is the ratio between the length of a pore channel and its hydraulic radius, and the empirical value of $\beta [-]$ captures the degree of incomplete mixing in pore channels. Based on the compilation of transverse dispersion experiments by Ye et al. (2015c), $\beta = 0.5$ and $\delta = 5.37$.

To verify the new implementation of the non-linear transverse dispersion coefficient in MT3D-USGS, we compare the linear and the non-linear numerical results of the solute transport under a steady flow field for both a continuous and a point injection. Details of the comparison can be found in the Supporting Information, Text S1 and Figures S1-S5.

3.2.4 PLUME ANALYSIS

To compare the experimental data with modeling results, we post-process the images obtained in the laboratory experiments (e.g., Figure 3.2a at t=64 min for the transient experiment at the velocity of 14 m/d) and use an optical calibration curve to estimate the concentration distribution within the plume as shown in Figure 3.2b. Based on the limit of detection of the optical method, we use a threshold of 5 mg/L in the calculations. This limit does not affect the interpretation of the results, since the same value is applied also to the results of the numerical simulations for consistent comparisons.

3.2.4.1 BREAKTHROUGH CURVES AND VERTICAL PROFILES

The advantage of the optical measurements with respect to the spectroscopy analysis performed with the samples collected at the outlet of the system is that one can compare the experimental results not only at the outlet, but also within the porous medium. We established 6 observation points shown in Figure 3.1, which in the longitudinal direction correspond to the areas below the first river and the outlet of the system, and in the z-coordinate correspond to the heights of the 5th, 6th and 7th inlet ports (top to bottom). We use these points to estimate breakthrough curves (BTCs) of the plume for the simulations and the experiments. For the vertical profiles, we consider the entire optical measurements and simulation results along the vertical axis of the observation points (Figure 3.1).

3.2.4.2 DILUTION INDEX

The plume dilution is quantified using the dilution index (Kitanidis 1994). This metric is mathematically described as the exponential of the Shannon entropy and it measures the uniformity of the mass distribution within the porous medium. For the continuous case, the dilution index is calculated as:

$$E(t) = exp\left(- \int_V p\,(\boldsymbol{x}, t) \ln\big(p\,(\boldsymbol{x}, t)\big) dV \right) \tag{3.6}$$

where p is the probability distribution of the mass in the *x*-coordinate at time *t*. Since we estimate the dilution index for a three-dimensional domain, *E* has units of volume.

3.2.4.3 PLUME PERIMETER AND AREA

To calculate the area and the perimeter of the tracer plume, we first convert the estimated concentrations to a binary image. All concentrations above the detection threshold are set to 1, and those below the threshold are set to 0. To remove the noise we use a standard technique in image processing called image opening (Serra 1982). An example of the resulting binary image is shown in Figure 3.2c.

We use image analysis techniques built in MATLAB to delineate the perimeter of the plume as shown in Figure 3.2d, and then apply the Freeman chain code algorithm (Freeman 1961). The Freeman algorithm encodes the drawing direction of a contour for a rectangular array considering a neighborhood of 8 pixels (Figure 3.2e). Each even chain unit represents a vertical or horizontal direction in the obtained sequence, while an odd unit represents a diagonal direction, as shown in Figure 3.2f. According to the Freeman method, in a unit squared grid, the curve length can be determined as $perimeter = even + odd\sqrt{2}$. For our case where the grid is anisotropic, we estimate the plume perimeter, P [L], as follows:

$$P = \Sigma(0 \ or \ 4) \times \Delta x + \Sigma(2 \ or \ 6) \times \Delta z + \Sigma(odd) \times \sqrt{\Delta x^2 + \Delta z^2} \tag{3.7}$$

where $\Sigma(0 \ or \ 4)$ and $\Sigma(2 \ or \ 6)$ are the total number of chain directions that assigned to 0 or 4 (horizontal) and 2 or 6 (vertical) along the plume boundary, respectively.

The area A [L^2] is calculated considering the spatial integration of the binary image contained within the plume's perimeter:

$$A(t) = \int H_5[C(\boldsymbol{x},t)] \ dA \tag{3.8}$$

where $H_5[C(\boldsymbol{x})]$ is a step function for concentrations higher than the threshold of 5 mg/L.
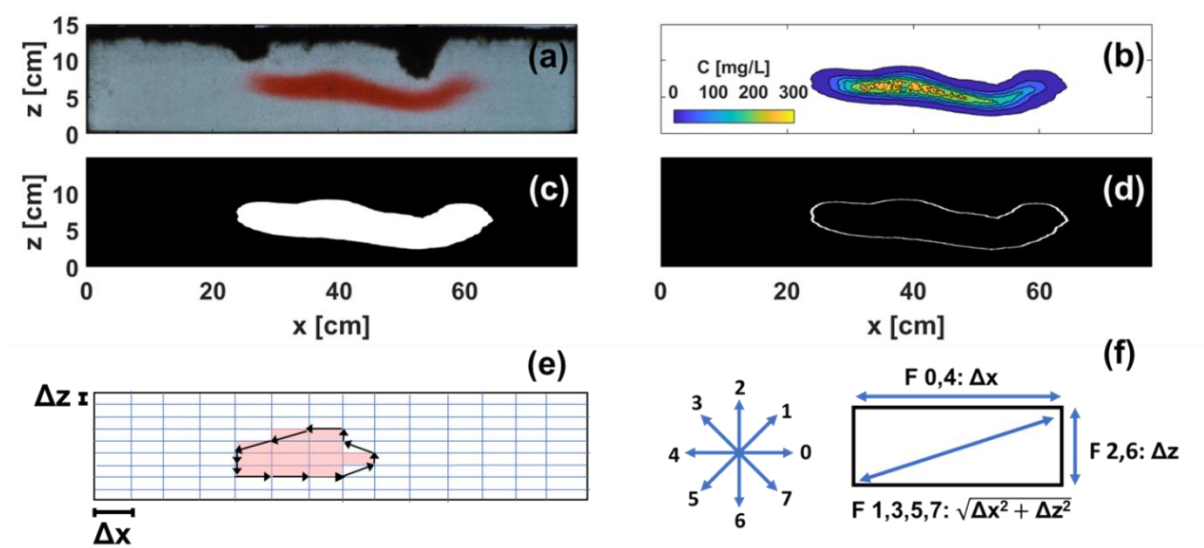
Figure 3.2: Snapshot of the plume in the porous medium at the velocity of 14 m/d under transient conditions at t=64 min: (**a**) raw image, (**b**) concentration distribution, (**c**) binary image, (**d**) plume perimeter; (**e**) schematic of the Freeman chain, and (**f**) chain directions and computation of the Freeman method.

3.2.4.4 SPATIAL MOMENTS

The first spatial moment, α_i, represents the location of the centroid of the plume in the i-direction, and it is defined as:

$$\alpha_i(t) = \int_V p\,(\boldsymbol{x},t)\, x_i \ dV \tag{3.9}$$

The second central spatial moment measures the spreading of the plume around the centroid, and is computed by

$$\Delta_{ij}(t) = \int_V p\,(\boldsymbol{x}, t)(x_i - \alpha_i)(x_j - \alpha_j)dV \qquad (3.10)$$

Δ_{xx} and Δ_{zz} correspond to the longitudinal and transverse spreading, respectively.

3.2.4.4 DISPERSIVE FLUXES

Following Fick's law, the diffusive flux J $[ML^{-2}T^{-1}]$ of a dissolved species is defined as follows:

$$\boldsymbol{J} = -\boldsymbol{D}\nabla C \qquad (3.11)$$

The longitudinal and the transverse components of the dispersion flux can be written using the longitudinal and transverse dispersion parametrizations from Equations 3.4 and 3.5:

$$J_x = -D_{xx}\frac{\partial C}{\partial x}, \quad where \quad D_{xx} = \frac{1}{2}d_P\frac{v_x^2}{|v|} + D_{aq}\left(\frac{Pe^2}{Pe + 2 + 4\delta^2}\right)^\beta \frac{v_z^2}{|v|} + D_P \qquad (3.12a)$$

$$J_z = -D_{zz}\frac{\partial C}{\partial z}, \quad where \quad D_{zz} = \frac{1}{2}d_P\frac{v_z^2}{|v|} + D_{aq}\left(\frac{Pe^2}{Pe + 2 + 4\delta^2}\right)^\beta \frac{v_x^2}{|v|} + D_P \qquad (3.12b)$$

Additionally, we compute the spatially averaged absolute flux in the i-direction within the space occupied by the plume by

$$|J_i(t)| = \frac{\int |J_i(t)|\,H_5[C(\boldsymbol{x}, t)]\,dA}{A(t)} \qquad (3.13)$$

3.2.4.5 MODEL CALIBRATION AND SENSITIVITY ANALYSIS

The hydraulic conductivity, porosity of the glass beads and the grain size of the porous material were already estimated by Rolle et al. (2009), while the aqueous diffusion coefficient was fixed as in Ziliotto et al. (2021). These values are given in the Supporting Information (Table S2). On the other hand, the unknown parameters are the hydraulic conductivity of the river bank sand layer, specific storage, specific yield, vertical anisotropy of glass beads and sand, pumping rate multiplier, riverbed conductances, and river head addends (See Table S3).

The sensitivity analysis and model calibration for the unknown model parameters have been performed in terms of the root mean square error:

$$RMSE = \sqrt{\frac{1}{N}\sum_{i=1}^{N}(X_M - X_E)^2} \qquad (3.14)$$

where N is the number of observations, X_E are the experimental results, and X_M are the model results. We consider specifically the RMSE for concentration distributions at selected time steps (41, 61, and 81 min at v=14 m/d, and 110, 166, and 200 at v=5 m/d, which exemplify the plume below the first river, in the middle of the chamber and below the second river, respectively), for the breakthrough curves in the locations described in Section 2.4.1, as well as the dilution index, the plume moments, the plume perimeter, and the plume area.

The range of the specific storage, the specific yields, and the hydraulic conductivity of the sand are determined based on the characteristics of the porous medium. For the imposed river heads and the inflow and outflow pumping rates we considered the range given by the experimental uncertainty in these measurements. The ranges are given in the Supporting Information (Table S3).

We evaluate a total of 1500 Monte Carlo realizations to identify the most sensitive parameters and to choose the best model parameters for both the steady-state and the transient experiments at v=14 m/d and v=5 m/d.

Among all simulations we excluded the cases where the tracer left the domain through the rivers as well as the simulations that did not show any plume deformation.

In general, the model was sensitive to the riverbed conductance, the specific yield, the hydraulic conductivity of the sand, and the vertical anisotropy of both the sand and the glass beads, in particular under transient conditions. The calibrated flow model parameters are presented in the Supporting Information (Table S3). The model performance and the RMSE values are discussed in Text S2 and Table S4.

3.3 RESULTS AND DISCUSSION

The experimental results and their model-based interpretation are presented in the following sections starting with the solute spatial distribution, followed by the breakthrough curves, the dilution index, and the plume perimeter and area. Finally, the model results are used to illustrate the spatial and temporal distribution of dispersive fluxes in the flow-through system and their impact in the observed plume dynamics.

3.3.1 PLUME EVOLUTION UNDER TRANSIENT CONDITIONS

Figure 3.3 presents the concentration distributions observed in the experiment (Figures 3.3a, 3.3d, and 3.3g), the model results (Figure 3.3b, 3.3e, and 3.3h), and the difference between the two (Figures 3.3c, 3.3f, and 3.3i) for the transient flow experiment at v=14 m/d. In addition, the timeseries of the applied river fluctuations is shown in Figure 3.3j. The displayed concentration distributions correspond to the times marked in the river stage time series (i.e., 41, 61, and 81 min). Alterations in the flow field can lead to plume folding and stretching, in which case the plume would deviate from its original shape. Here, both the experiments and the numerical simulations exhibit a clearly deformed plume. For instance, at the end of the experiments at v=14 m/d, the plume exhibits "w"-shaped appearance (Figures 3.3g and 3.3h). On the contrary, under steady flow conditions (Supporting Information, Figure S6), the plume passing below the rivers results in "u"-shaped appearance due to the deformation caused by the presence of the river and tends to recover its original shape shortly after. The additional plume deformation observed in the transient case is due to the fluctuating river boundaries. The imposed head in the two reservoirs alternatively speeds up and slows down only the front or the rear part of the plume. As different parts of the plume experience different velocities at the same time step, the plume folds and stretches.

Figure 3.3: (**a-i**) Concentration distribution under transient flow conditions at 14 m/d. The columns correspond to the experimental images (left), the simulation results (center) and their difference (right). The rows correspond to 41 (top), 61 (center) and 81 (bottom) minutes. (**j**) Fluctuations of the river stages in the experiment.

Analogous to Figure 3.3, the tracer distribution of the v=5 m/d transient experiment and the applied river fluctuations are displayed in Figure 3.4. The selected times for the plume visualization are at 110, 166, and 200 min. Here, even if the transient flow conditions lead to a higher plume deformation than under steady-state flow conditions (see Supporting Information, Figure S7), the plume is much less deformed than that at v=14 m/d (Figure 3.3). For instance, the plume is less elongated since the imposed head in the two reservoirs affects almost uniformly the entire plume sampling a less heterogeneous velocity field than that at v=14 m/d. This in turn leads to a smaller deformation in the shape of the plume than the plume deformation in the v=14 m/d experiment.
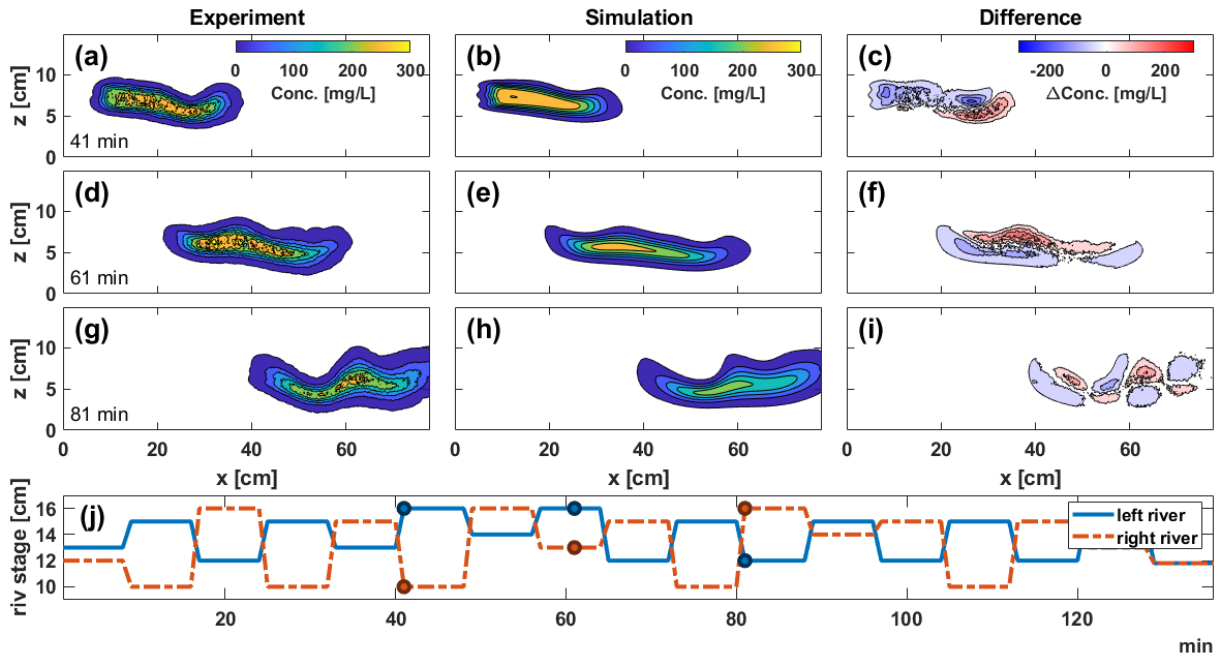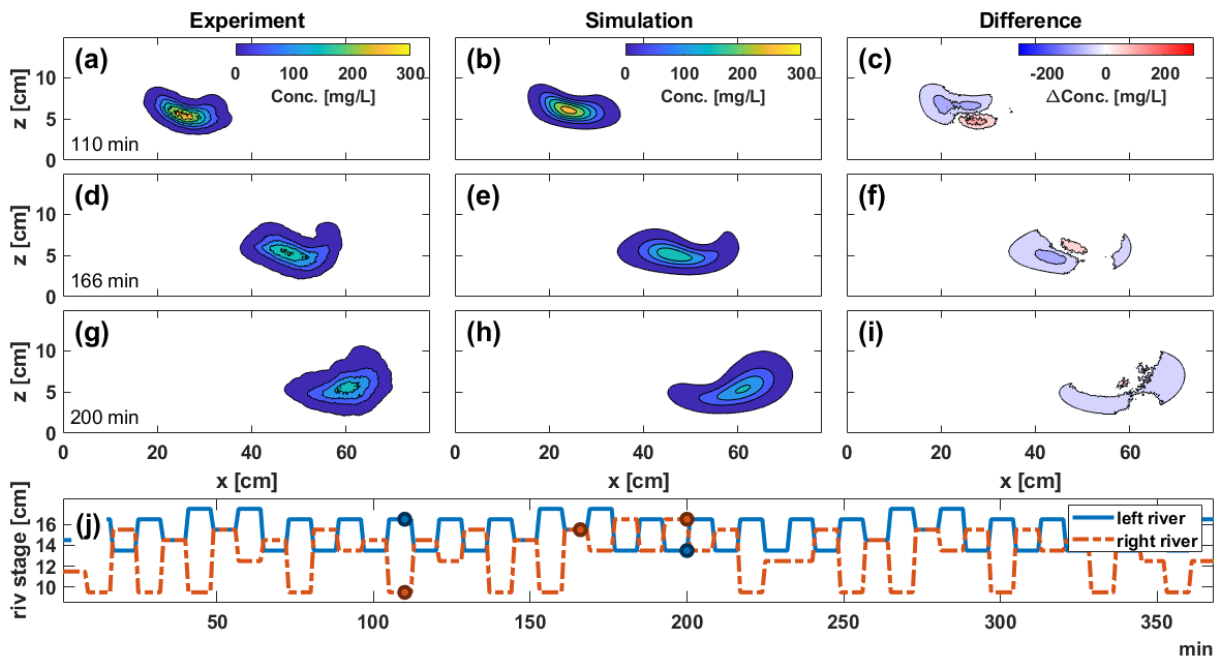

Figure 3.4: (**a-i**) Concentration distribution under transient flow conditions at 5 m/d. The columns correspond to

the experimental images (left), the simulation results (center), and their difference (right). The rows correspond to 110 (top), 166 (center), and 200 (bottom) minutes. (**j**) Fluctuations of the river stages in the experiment.

The effect of the transient boundary conditions on the plume deformation is also observed in the BTCs, both in the experimental and in the numerical results. Figure 3.5 depicts selected breakthrough curves (below the first river and at the outlet, for elevations corresponding to ports 5, 6, and 7) for the transient flow cases. At v=14 m/d, the BTC at the elevation of port 5 shows a bimodal pattern below the first river whereas it evolves towards a more bell-shaped curve at the outlet (Figure 3.5a). The opposite behavior characterizes the BTCs of ports 6 and 7 (Figure 3.5b-c). On the contrary, the BTCs in the steady flow experiment (Supporting Information, Figure S8) remained bell-shaped, even when passing below the rivers. These observations might suggest that the transient head-dependent flow boundaries contribute to the deformation of the solute plume by folding and stretching mechanisms. This is consistent with the observations in Nissan et al. (2017), where changes in the flow velocity were associated with multi-peaked BTCs. Moreover, these findings add evidence that a tracer moving through homogeneous porous media in a flow-through configuration can also experience folding or stretching under fluctuating boundary conditions. At v = 3 m/d, no obvious multimodal peaks are detected in the breakthrough curves (Figure 3.5d-f). In fact, instead of an evident folding or stretching, the plume is mainly translated up and down by the river fluctuations, similarly to the conditions described by de Dreuzy et al. (2012).
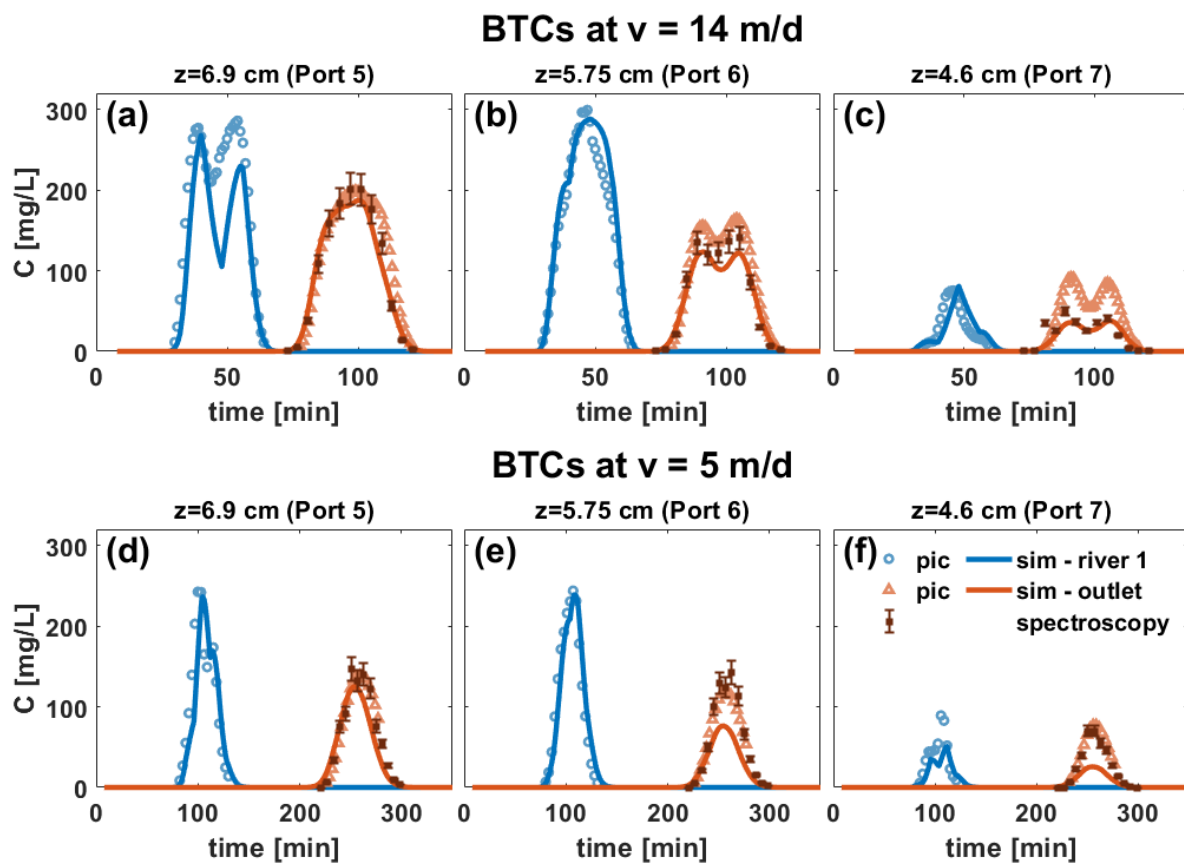
Figure 3.5: Observed (symbols) and simulated (lines) breakthrough curves for the transient flow experiments at v=14 (**a-c**) and 5 (**d-f**) m/d.

Figure 3.6 shows the vertical profiles of the transient plumes below the first river and at the outlet at t=50 min and t=101 min for the experiment at v=14 m/d (Figure 6a-b), and at t=104 and t=254 minutes for the experiments at 5 m/d (Figure 6c-d). The observation times were chosen when about half of the BTCs in Figure 3.5 passed the observation points. In general, the plume profile is more spread at the outlet (Figure 6b and 6d) due to the flow focusing below the first river and to the transverse dispersion. In all cases, the maximum concentration is located

approximately between the locations of ports 5 and 6 in the experimental setup. Since the injection was done in ports 4 and 5, this reflects a change of the plume location. For comparison purposes, Figure S9 of the Supporting Information presents the vertical profiles for the steady-state flow experiment. In general, the numerical simulations capture the experimental observations at the different locations reasonably (Supporting Information, Text S2).
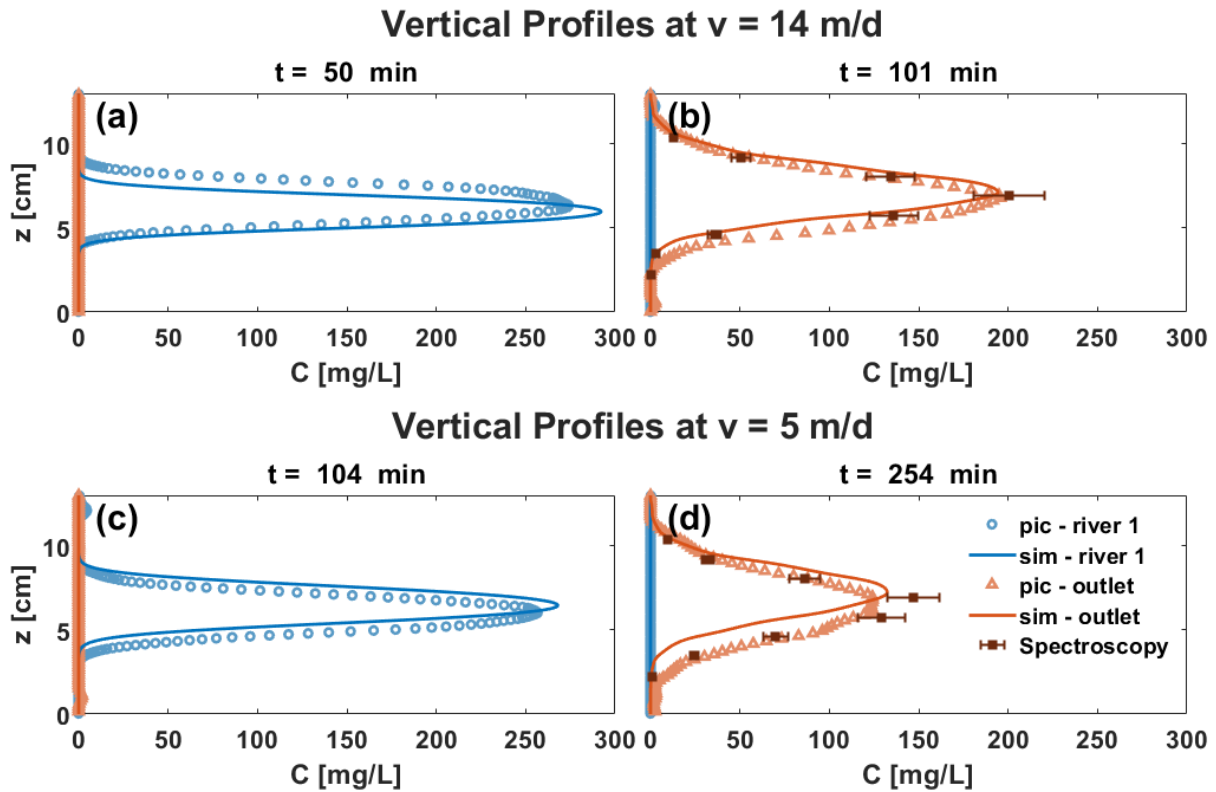
Figure 3.6: Vertical profiles in the experiments (symbols) and simulations (lines) at 14 m/d (**a**,**c**) and 5 m/d (**b**,**d**) for the transient flow.

3.3.2 PLUME MIXING

The dilution index can be understood as a measure of how well the concentration is distributed in the porous medium. For a conservative tracer, the dilution index monotonically increases and a higher value implies that the tracer occupies a larger volume in the system. On the other hand, the plume perimeter is an indicator of the interface available for diffusive/dispersive fluxes. Figure 3.7, illustrates the temporal evolution of the dilution index, the plume perimeter and the area for the steady-state and the transient flow experiments at both v=14 m/d and v=5 m/d, considering only the time window in which the entire plume was located inside the flow-through chamber. This time corresponds to the intervals 39-72 min at v=14 m/d, and 58-210 min at v=5 m/d. As expected, the tracer plumes show a monotonic increase of the dilution index in both experiments, as well as an increment of its perimeter and area. However, the increment differs between the steady and the transient scenarios. For instance, the dilution, perimeter, and area reach higher values in the transient scenarios than those in the steady-state scenarios, in particular at v=14 m/d. At v=5 m/d, even if both steady and transient experiments reach a similar perimeter, the increment seems faster under transient conditions. In general, even in the simple case of steady flows, dispersion will increase both the entropy and the second moment of the plume. As the interface available for diffusion increases, dilution increases as well, leading to a positive correlation between the plume and its perimeter.
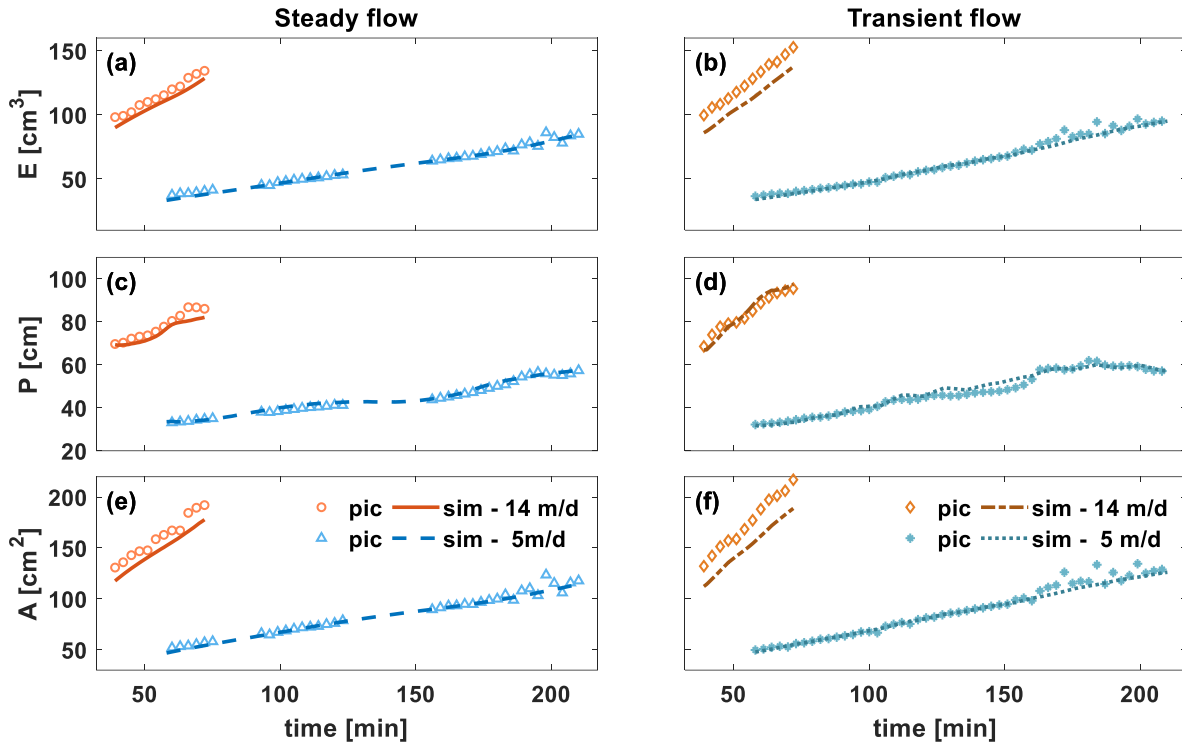
Figure 3.7: (**a-b**) Dilution index, (**c-d**) perimeter and (**e-f**) area of the experiments and the simulations.

To quantify the relation between the perimeter of the plume and the dilution index, we compute their correlation and confirm a high correlation both in the simulations and in the laboratory experiments (R^2=0.94 and R^2=0.98, respectively). To expand the analysis of how they interact, Figure 3.8a-b displays the normalized dilution index vs. the normalized perimeter from the experiments and the model simulations. The normalization is performed by the initial state of the plume described in the previous paragraph (t=39 min and 58 min at v=14 m/d and 5 m/d, respectively). The results suggest that the dilution is not monotonically increasing with the perimeter despite its positive correlation and, in particular, for large values of the dilution index, the two quantities appear to be uncorrelated.

On the other hand, we observe a stronger correlation between the normalized area of the plume and the normalized dilution index (R^2=0.99). In fact, Figure 8c-d shows that the ratio between both normalized quantities is constant and even close to the identity relation, where $E/E_0 = A/A_0$. This suggests that in a quasi 2D setup, the normalized area can be a good proxy for the normalized dilution index, allowing the quantification of mixing and mixing enhancement from experiments less sensitive to the optical calibration procedure. Furthermore, this relation confirms experimentally that the dilution index is a representative metric of the space occupied by a solute tracer.
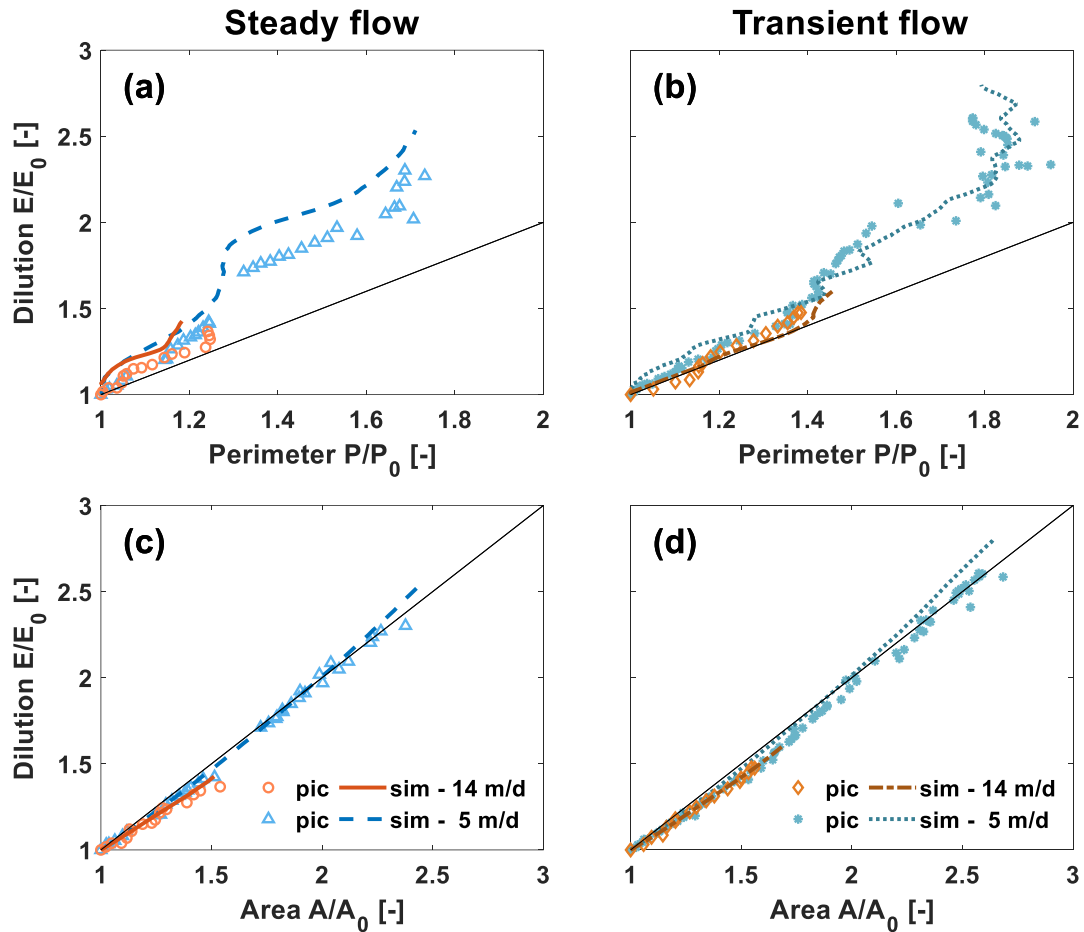
Figure 3.8: Normalized dilution index vs normalized perimeter (**a-b**) and normalized area (**c-d**) for the experiments and simulations. Thin black line marks the identity line ($E/E_0 = A/A_0$).

Regarding mixing enhancement, although at v=14 m/d the dilution index and the dimensions of the plume are larger than at v=5 m/d (Figure 3.7), the normalized area, normalized perimeter, and normalized dilution index reached much higher values at the slower velocity (Figure 3.8). For instance, at v=14 m/d, P/P_0 increases by between 25% and 50%, and the increase in A/A_0 and E/E_0 is by 50% in both steady and transient flow conditions. At v=5 m/d, the normalized perimeter increased by almost 100%, and the normalized area and normalized dilution index increase almost up to 300%. In addition, higher values of perimeter, area, and dilution were reached under transient boundary conditions (Figures 3.8b and 3.8d) compared to those under steady flows (Figures 3.8a and 3.8c). In fact, the plume deformation (i.e., folding and stretching) caused by the transient boundary conditions enhance the plume perimeter, which allows more area for diffusion processes and thus leads to higher mixing. However, as mentioned in the previous paragraph, the perimeter is not monotonically increasing with the dilution index.

3.3.3 DISPERSIVE FLUXES

The deviation of the normalized perimeter vs. the normalized dilution index from the one-to-one relationship suggests that at certain moments the dominating mixing processes are not taking place at the outer boundary of the plume, but within it. Several factors such as the size of the plume and its deformation, the concentration gradients, and both the bulk and local velocity, would determine the spatial distribution of the dominating dilution processes. In fact, the velocity affects directly the dispersion tensor, which together with the local concentration gradients have an effect on the dispersive fluxes.

To better analyze the spatial and temporal distribution of the dispersive fluxes, Figure 3.9 depicts the maps of its longitudinal and transverse components at selected times. The results show that the largest solute dispersive fluxes happen rather within the plume than at the outer plume edges. The plume displays marked hotspots where the dispersive fluxes reach predominantly higher values. These hotspots are close to locations with large plume deformation. For instance, near the rivers where the plume is squeezed due to the hydraulic head differences in the vertical direction, but is elongated in the perpendicular direction of the compressing force. Other particularly important areas for dispersive fluxes are at the opposite ends of the plume for the longitudinal flux component, and throughout the plume's length for the transverse flux component.
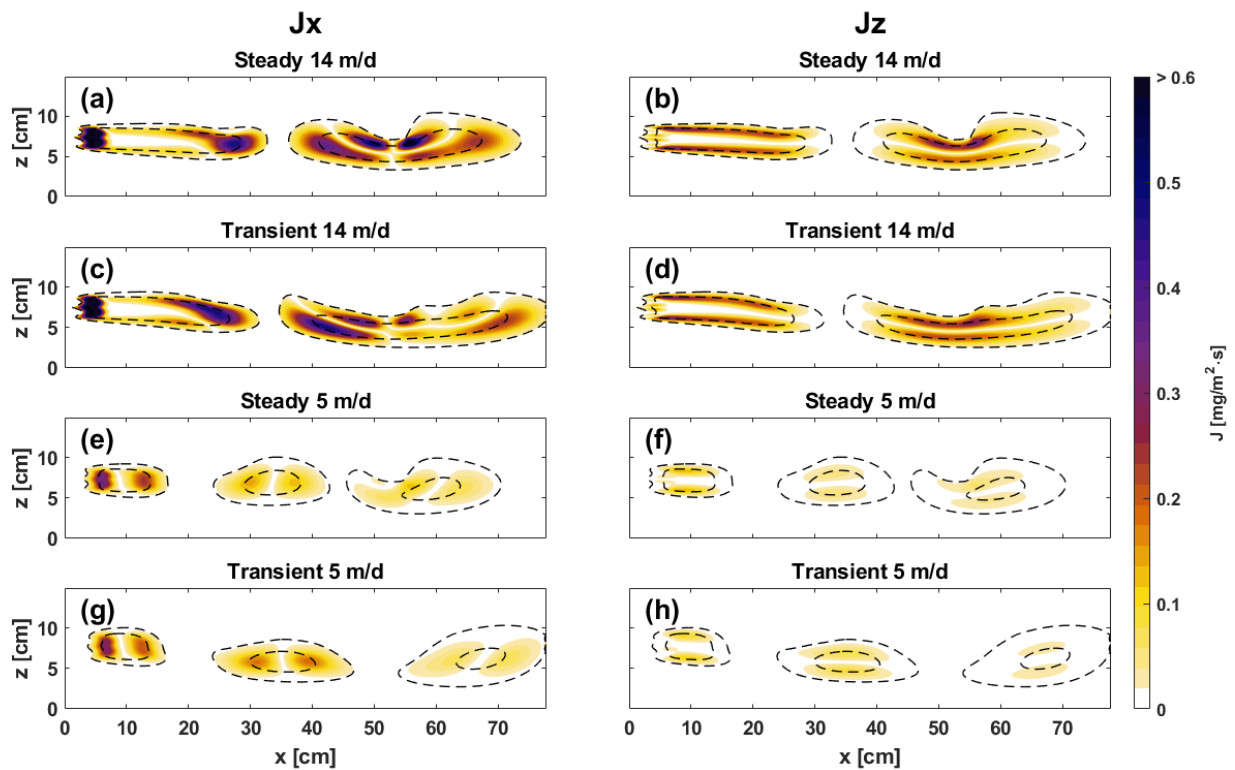
Figure 3.9: Maps of flux components in the longitudinal (left) and transverse (right) directions corresponding to (**a-d**) $t = 37$ and 77 min in the experiment at v=14 m/d, and to (**e-h**) $t = 60, 140$ and 220 min in the experiment at v=5 m/d. The dotted contour lines represent the perimeter of the plume (thresholded at 5 mg/L) and the concentration of 100 mg/L.

For a better overview of the role of the transient boundary conditions in the dispersive fluxes, Figure 3.10 shows the time evolution of the spatially averaged absolute flux within the plume. Although the longitudinal dispersion coefficient is almost one order of magnitude larger than the transverse one, the dispersive flux in the transverse direction is on the same order of magnitude as the longitudinal one. In particular, the enhancement due to the transient flows is stronger for the dispersive fluxes in the transverse direction than the enhancement of dispersive fluxes in the longitudinal direction. Therefore, it is noted that the dispersive flux in the transverse direction contributes to the enhancement of dilution under the transient boundary conditions.
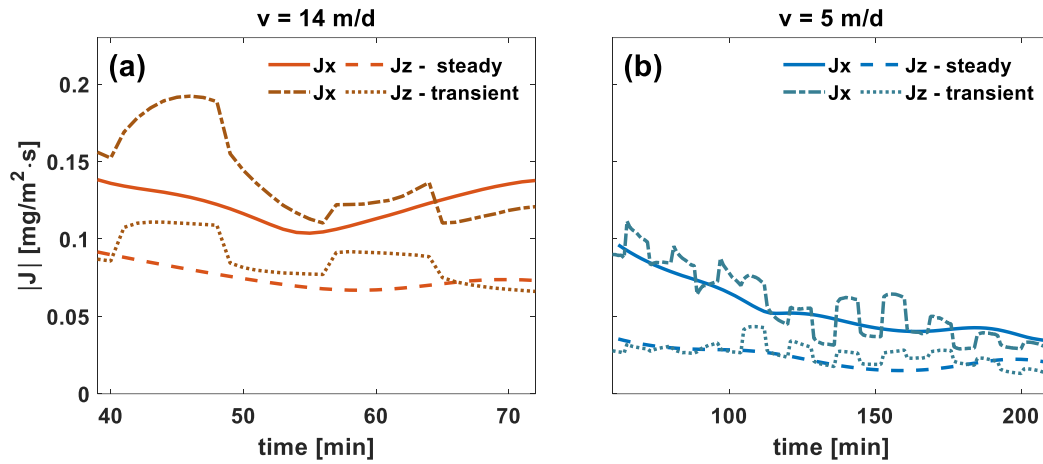
Figure 3.10: Spatially averaged flux components in the longitudinal and transversal direction corresponding at (**a**) v=14 m/d and (**b**) v=5 m/d.

3.5 CONCLUSIONS

In this work, we studied the effect of transient boundary conditions on solute mixing in an experimental setup mimicking two highly fluctuating rivers (i.e., hydropeaking) hydraulically connected to an unconfined aquifer. We presented a combined approach based on flow-through experiments and numerical flow and transport simulations. We considered transport of a dissolved color tracer at two different velocities under steady and transient flow conditions. The results showed that the plume deformation was larger under transient flow conditions compared to the steady flow conditions. This was particularly evident at higher velocity, where the plume was effectively stretched and folded by the river dynamic. This deformation also affected the shape of the breakthrough curves at different locations within the porous medium and at the outlet of the flow-through setup.

In an attempt to characterize mixing and to link it to different geometrical descriptors of the tracer plumes, we computed the dilution index, the plume perimeter and area, and their evolution in the different experimental and modeling scenarios. At v=14 m/d, where advection was strongly dominant, the ratio between the normalized dilution index and the normalized perimeter was found close to one for both the steady and transient flows. At v=5 m/d, dispersion processes had a greater impact on plume dilution and mixing, as shown by the normalized dilution index higher than the normalized perimeter. Although the perimeter is an indicator of the area available for diffusive/dispersive mass transfer between the plume and the surrounding groundwater and showed a good correlation with the dilution index, the perimeter did not monotonically increase with dilution, moreover it also showed some decrease, in particular at later times. Instead, we found a better relation between the area of the plume and the dilution index, expressed as $E/E_0 = A/A_0$. This relation experimentally confirmed that the dilution index is indeed a measure associated with the spatial dimensions of the plume, and it suggested that in a quasi 2-D setup, the area can be used as a proxy for dilution when concentration measurements are not available. Our results also show that under certain conditions, dispersion processes are not always dominant at the outer fringes of the plume, but they can be dominated by the local concentration gradient and the local velocity within the plume. In fact, most of the mass transfer occurred within the plume in our setup.

Future research should study the interplay between highly transient boundary conditions and heterogeneity and its impact on solute transport in porous media. In particular, the relation among geometrical properties of the plume and its mixing behavior, as well as the magnitude, spatial location and temporal evolution of hydrodynamic dispersive fluxes should be investigated in more complex heterogeneous setups and under transient flow conditions.

CHAPTER 4

LINKING MIXING AND FLOW TOPOLOGY IN POROUS MEDIA

Published as

Abstract

Transport processes in porous media are controlled by the characteristics of the flow field which are determined by the porous material properties and the boundary conditions of the system. This work provides experimental evidence of the relation between mixing and flow field topology in porous media at the continuum scale. The setup consists of a homogenously packed quasi 2D flow-through chamber in which transient flow conditions, dynamically controlled by two external reservoirs, impact the transport of a dissolved tracer. The experiments were performed at two different flow velocities, corresponding to Péclet numbers of 191 and 565, respectively. The model-based interpretation of the experimental results shows that high values of the effective Okubo-Weiss parameter, driven by the changes of the boundary conditions, lead to high rates of increase of the Shannon entropy of the tracer distribution and, thus, to enhanced mixing. The comparison between a hydrodynamic dispersion model and an equivalent pore diffusion model demonstrates that despite the spatial and temporal variability in the hydrodynamic dispersion coefficients, the Shannon entropy remains almost unchanged because it is controlled by the Okubo-Weiss parameter. Overall, our work demonstrates that under highly transient boundary conditions, mixing dynamics in homogeneous porous media can also display complex patterns and is controlled by the flow topology.

4.1 INTRODUCTION

Theoretical studies have shown that flow topology may have a strong influence on dilution and mixing processes (Chiogna et al. 2014; Lee and Kang 2020; Ottino 1990; Turuban et al. 2018; Danish et al. 2016; Le Borgne et al. 2013). For instance, radial flows (Brau et al. 2017; Comolli et al. 2019; Neupauer et al. 2020), convective transfer (Budroni et al. 2019; Hidalgo et al. 2012) and vortex structures (Lee and Kang 2020; Sen et al. 2020) can control reaction dynamics. At low Reynolds numbers, mixing is often slow but it can be enhanced by transient flow conditions with important applications in fields such as biology, medicine, and engineering (Aref et al. 2017; Bagtzoglou and Oates 2007; Sundararajan and Stroock 2012; Stroock et al. 2002; Villermaux et al. 2008; Zhang et al. 2009; Rodríguez-Escales et al. 2017; Clemente et al. 2019). Particularly complex is the case of mixing processes in porous media and microchannels, where flow dynamics and mixing are further complicated by the complex topological structure of the pore space (de Anna et al. 2013; Jiménez-Martínez et al. 2016; Souzy et al. 2020; Lester et al. 2018; Turuban et al. 2019; Heyman et al. 2020; Dentz et al. 2011; Hernandez-Aguirre et al. 2022). At the continuum scale, heterogeneities and anisotropies in the porous material (Chiogna et al. 2015; Werth et al. 2006; Ye et al. 2020), or external forcing, like applied voltages (Shang et al. 2015), moving objects like artificial cilia (Toonder et al. 2008) or prisms (Ortega-Casanova and Lai 2018) within microchannels, source-sink pulses (Di Dato et al. 2018; Neupauer et al. 2014; Piscopo et al. 2013; Cremer et al. 2016; Cremer and Neuweiler 2019; Mays and Neupauer 2012) and periodic boundaries (Trefry et al. 2019; Rizzo et al. 2020; Goode and Konikow 1990; Phelan et al. 2008; Rehfeldt and Gelhar 1992), can lead to heterogeneous flow fields, which in turn can generate a wide range of stretching and folding behaviors (Dentz et al. 2016; Chiogna et al. 2015; Ye et al. 2015b), affect dispersion (de Dreuzy et al. 2012; Kinzelbach and Ackerer 1986) and enhance mixing (Rolle and Le Borgne 2019; Ye et al. 2015a; Sprocati et al. 2021).

Mixing processes are often enhanced when the interface of a solute with the surroundings enlarges, thus increasing diffusive and dispersive fluxes (Neupauer et al. 2014). Therefore, the quantification of mixing in porous media can be approached by analyzing the evolution of the concentration distribution of a solute plume, using for example the dilution index (Kitanidis 1994). The dilution index measures the state of dilution of a system, where a larger number indicates that a solute is more uniformly distributed and occupies a larger volume of the fluid. This index can be expressed in its logarithmic form as the Shannon entropy of the spatial distribution of the solute concentration. Other approaches to quantify mixing are based on the relation between flow topology and plume deformation. In this sense, a topological analysis can be done through the Okubo-Weiss function (Okubo 1970; Weiss 1991), commonly used in fluid mechanics to distinguish filament from vortex structures in two-dimensional flow fields and with applications in the study of turbulence (Perlekar et al. 2011; Kadoch et al. 2011) and vortex stability (Hurst et al. 2016), as well as in geophysical fluids (Casella et al. 2011; Geng et al. 2020; Roullet and Klein 2010), cellular flows (Blanch-Mercader et al. 2018), and germ spread (Li et al. 2016). Positive Okubo-Weiss values correspond to filament structures, which are found in regions where shear and stretching forces dominate over vorticity, causing hyperbolic motion in the fluid (Weiss 1991), and are associated with mixing hot-spots (de Barros et al. 2012). Negative Okubo-Weiss values indicate values of dominating vorticity. De Barros et al. (2012) identified a relation between the evolution of the Shannon entropy and the effective Okubo-Weiss parameter (defined as the average positive Okubo-Weiss value over the plume area) in a heterogeneous steady-state flow. Wright et al. (2017) found that reaction hot-spots in a 2D idealized heterogeneous porous medium were associated with the regions where the Okubo-Weiss parameter was highest, and Engdahl et al. (2014) obtained a positive correlation between the Okubo-Weiss field and the maximum increase of the collocation density, understood as the likelihood that reactive particles will occupy the same space.

Both numerical (e.g., de Barros et al. 2012; Kitanidis 1994; Dentz et al. 2016; Wright et al. 2017; Turuban et al. 2019; Engdahl et al. 2014) and experimental studies (e.g., Ye et al. 2015b, 2016; Souzy et al. 2020; Rolle et al. 2009) investigating flow topology and mixing in porous media generally consider steady-state flow conditions. Most research including time dependent flows has been theoretical (for example, uniform fluctuating boundaries

- de Dreuzy et al. 2012; Goode and Konikow 1990; Trefry et al. 2019), or dipole and quadrupole configurations (Sposito 2006; Neupauer et al. 2014), with only a few exceptions based on experimental data (Ziliotto et al. 2021; Cho et al. 2019). For instance, some works have focused on how fluctuating flow fields generate chaotic advection (Mays and Neupauer 2012; Neupauer et al. 2014; Piscopo et al. 2013; Trefry et al. 2019; Sposito 2006) and affect dispersion coefficients (Goode and Konikow 1990; Kinzelbach and Ackerer 1986; Rehfeldt and Gelhar 1992; Dentz and Carrera 2003, 2005; Bolster et al. 2009; de Dreuzy et al. 2012) with an overall increase in dispersion, spreading, and mixing. In this contribution, we use experimental data from a quasi 2D flow-through chamber subject to two time-dependent boundary conditions to analyze the dilution of a solute tracer. The chamber is packed with a homogeneous porous medium in order to isolate the effect of the transient flow field. We performed experiments at two different flow velocities and considering different fluctuations of the dynamic boundaries. Image analysis was employed to quantify the evolution of spreading and mixing of the dye color tracer in the transient flow field. The model-based interpretation of the experimental results allows us to identify the relation between the dynamics of solute mixing under transient flows, quantified through the temporal change of the plume entropy, and the topology of the flow.

4.2 MATERIAL AND METHODS

4.2.1 FLOW-THROUGH EXPERIMENTS

Figure 4.1a shows a sketch of the experimental setup. The quasi-two-dimensional flow-through chamber has inner dimensions of 77.9×15×1.1 cm^3. 10 inlet and 11 outlet ports on the left and right side of the system, respectively, are equally spaced by 1.1 cm and are connected to two high-precision multi-channel peristaltic pumps (IPC-N24, ColeParmer, United States). Each port injects/extracts 7.6×10^{-9}± 4.17×10^{-10} m^3/s, creating fixed flux boundary conditions on the left/right side. The system is water saturated and filled with a homogeneous porous medium consisting of glass beads with particle diameter d_p=1-1.5 mm (mean 1.25 mm), with an average hydraulic conductivity of 1.27×10^{-2} m/s and a porosity of 0.4. A wet packing procedure, consisting in progressively rising and maintaining the water level above the porous medium, was applied to avoid air entrapment (Haberer et al. 2012). The chamber is filled on the top with a finer sand layer [yellow color in the Fig. 1(a)] to avoid the occurrence of preferential flow. Two water reservoirs are connected to the flow-through chamber, at a distance of approximately one third and two thirds of the chamber length, and act as head-dependent flux boundaries. The water level in the reservoirs oscillates every 8 minutes generating transient flow fields [see water level in Fig 1(a)]. We call this interval of time τ. To study dilution and mixing processes, we injected a conservative tracer (New Coccine, CAS 2611-82-7, Sigma Aldrich, United States) from t_{i_1}=8 min to t_{i_2}=32 min and tracked the tracer plume across the chamber using a digital camera – Nikon D5000 [Fig. 1(b)]. From the recorded pictures, we estimated the concentration of the plume at high spatial and temporal resolution (60 pictures per hour and 135 ppi) following a similar process used by Jaeger et al. (2009). A full description of the flow-through chamber configuration and the optical calibration of the images can be found in Ziliotto et al. (2021).

In this study, we present two experiments in which the pumping rates established a predominantly horizontal flow with different grain (Pe) numbers defined as $Pe = |v| d_p / D_{aq}$ [-], where v [LT^{-1}] is the average pore water velocity, and D_{aq} [L^{2}T^{-1}] is the aqueous diffusion coefficient that for the tracer new coccine at 20°C is equal to 3.6×10^{-10} m^2/s (Jaeger et al. 2009). The Péclet number in the two flow-through experiments is $Pe = 191.0 \pm 63.4$ and $Pe = 565.1 \pm 63.5$, respectively. For the sake of simplicity, we refer to these two flow-through experiments as Pe200 and Pe570.
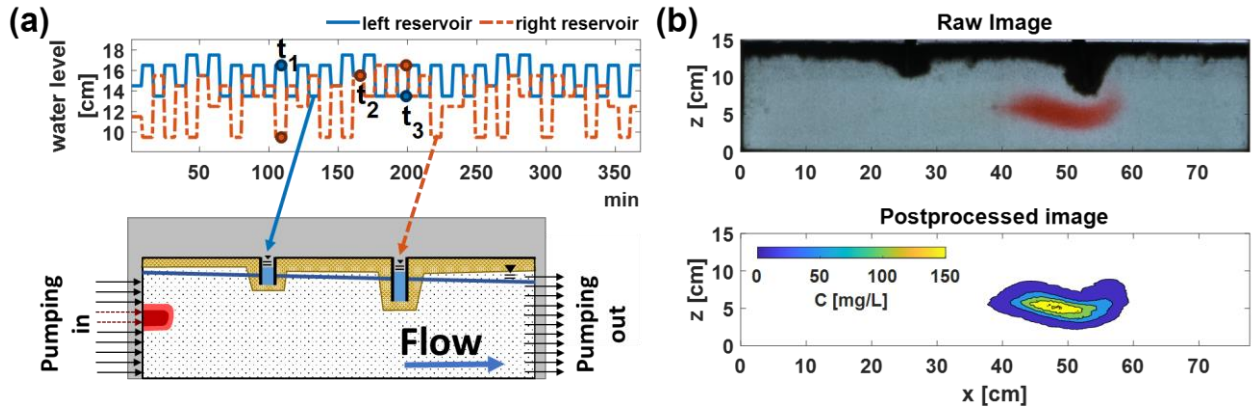
Figure 4.1: (a) Sketch of the flow-through experimental setup with fluctuations in the water level of the reservoirs applied in the experiment Pe200, where times t_1 (109 min), t_2 (166 min) and t_3 (199 min) correspond to the times showed in the flow and transport analysis of Fig. 4.2 and Fig. 4.3. **(b)** Tracer plume observed, as raw and post-processed images, at t=170 min for the experiment Pe200.

4.2.2 FLOW AND TRANSPORT MODELING

To obtain a quantitative interpretation of the experiments, we run flow and transport simulations and validate them with the tracer observations. The model also allows us obtaining a fully resolved velocity field, considering as boundary conditions the measured inlet and outlet pumping rates at each port of the flow-through chamber, as well as the fluctuating hydraulic heads in the reservoirs.

The transient flow equation is derived combining Darcy's law with the continuity equation over a representative elementary volume, yielding:

$$S \frac{\partial h}{\partial t} = \nabla \cdot (\boldsymbol{K} \cdot \nabla h) + \boldsymbol{q}',$$

(4.1)

where $\mathbf{K}\,[\mathrm{LT^{-1}}]$ is the hydraulic conductivity tensor, $\nabla h[-]$ the hydraulic head gradient, $\boldsymbol{q}'[\mathrm{LT^{-1}}]$ is the source/sink term and $S\,[-]$ is the storage coefficient. The flow simulations are solved with the finite difference model Modflow MF-OWHM (Boyce et al. 2020), considering a discretization of the two-dimensional domain of 1140 columns ($\Delta \mathrm{x} = 0.068$ cm) and 395 layers ($\Delta z_{min} = 0.027$ cm). The time-dependent boundary conditions are treated as a head-dependent flux. The finite differences equations are solved with a Newton-Raphson formulation capable of handling model cells that are drying and rewetting as a consequence of the oscillations in the water level (Boyce et al. 2020).

The transport equation for a conservative tracer is described by the advection-dispersion equation:

$$\frac{\partial (nC)}{\partial t} = \nabla \cdot (n\boldsymbol{D}\nabla C) - \nabla \cdot (n\boldsymbol{v}),$$

(4.2)

where $C[\mathrm{ML^{-3}}]$ is the tracer concentration, $n[-]$ is the porosity, and $\boldsymbol{D}[\mathrm{L^2 T^{-1}}]$ is the dispersion tensor. The transport simulations are calculated with a modified version of MT3D-USGS (Bedekar et al. 2016b) that implements a linear, grain size (d_p) specific parameterization for the longitudinal dispersion coefficient (Guedes de Carvalho and Delgado 2005; Muniruzzaman & Rolle 2017):

$$D_L = D_P + \frac{1}{2} d_P v,$$

(4.3)

and a non-linear, grain size and compound specific parameterization for the transverse dispersion coefficient (Chiogna et al. 2010; Ye et al. 2015c):

48

$$D_T = D_P + D_{aq} \left(\frac{Pe^2}{Pe + 2 + 4\delta^2} \right)^{\beta},$$
(4.4)

where $D_P = D_{aq}n \; [L^2T^{-1}]$ denotes the pore diffusion coefficient, $\delta[-]$ is the ratio between the length of a pore channel and its hydraulic radius, and $\beta[-]$ is an empirical exponent to capture the degree of incomplete mixing in pore channels. We use values of β=0.5 and δ=5.37 based on the compilation of transverse dispersion experiments presented in Ye et al. (2015c).

We refer to the dispersion model described by Eqs. 4.3 and 4.4 as hydrodynamic dispersion model ($D_T D_L$).

Additional simulations were performed considering only the velocity-independent pore diffusion term from Eqs. 4.3 and 4.4, but designed to reach the same dilution as the hydrodynamic dispersion model under the same velocity field. This was done by using a larger equivalent pore diffusion coefficient. To distinguish this model from the previous one, we identify it as equivalent pore diffusion model ($D_{P,eq}$).

4.3 FLOW TOPOLOGY AND MIXING METRICS

4.3.1 OKUBO-WEISS PARAMETER

The topology of a two-dimensional flow field can be described in terms of stretching $\alpha \; [T^{-1}]$, shear $\sigma \; [T^{-1}]$, and vorticity $\omega \; [T^{-1}]$. Following de Barros et al. (2012) and Okubo (1970), these quantities are defined by partial derivatives of the velocity field as follows:

$$\alpha = 2\frac{\partial v_x}{\partial x}, \qquad \sigma = \frac{\partial v_z}{\partial x} + \frac{\partial v_x}{\partial z}, \qquad \omega = \frac{\partial v_z}{\partial x} - \frac{\partial v_x}{\partial z},$$
(4.5)

where x an z are the components in the horizontal and vertical directions, respectively. The Okubo-Weiss parameter $\Theta \; [T^{-2}]$ is then calculated as (Okubo 1970; Weiss 1991):

$$\Theta = (\alpha^2 + \sigma^2) - \omega^2 .$$
(4.6)

Therefore, positive values indicate areas where shear and stress dominate, while negative values characterize vorticity dominating zones. While this parameter can be used to study local mixing-strength in porous media (de Barros et al. 2012; Geng et al. 2020; Wright et al. 2017), we focus on global mixing properties and therefore also calculate the effective Okubo-Weiss function $\Theta^e(t)$ following de Barros et al. (2012):

$$\Theta^e(t) = \frac{\sum \Theta(\mathbf{x},t)H[\Theta(\mathbf{x},t)]F_5[C(\mathbf{x},t)]\Delta X \, \Delta Z}{\sum H[\Theta(\mathbf{x},t)]F_5[C(\mathbf{x},t)]\Delta X \, \Delta Z},$$
(4.7)

where $\Theta(\mathbf{x},t)$ and $C(\mathbf{x},t)$ are the Okubo-Weiss function and tracer concentration estimated at time t over the space coordinates $\mathbf{x}$ [L], $H(y)$ is the Heaviside step function and $F_5(y)$ is a step function for concentrations higher than 5 mg/L, which is the limit of detection of the imaging method for the solute concentrations in the flow-through experiments. The computation of the Okubo-Weiss function and, thus, of the effective Okubo-Weiss parameter requires the computed fully resolved flow-field.

4.3.2 DILUTION INDEX

The pictures from the experiment and the conservative transport model provide qualitative and quantitative data of the tracer plume distribution, its concentration, and its temporal evolution in the domain. Using this

information, it is possible to quantify the dilution of the tracer plume in both the experiments and the simulations based on the dilution index, $E(t)$, which is defined as in Kitanidis (1994)

$$E(t) = \exp\left[-\int_V p\,(\boldsymbol{x},t)\,ln\,p(\boldsymbol{x},t)\,dV]\right],$$

(4.8)

where $p(\boldsymbol{x},t)\,[L^{-3}]$ is defined as the concentration of the solute tracer normalized by its total mass and is a probability density function:

$$p(\boldsymbol{x},t) = \frac{C(\boldsymbol{x},t)}{\int_V C\,(\boldsymbol{x},t)dV},$$

(4.9)

being *V* is the total volume of the domain. The dilution index is commonly interpreted as the exponential of the Shannon entropy of the plume, ln E(t) (Kitanidis 1994).

In addition, we compute the rate of increase of the entropy $d \ln E\,(t)/dt$, which is a measure of the kinetics of dilution and represents how quickly the plume occupies a progressively larger volume as it is transported in the porous medium.

4.4 RESULTS AND DISCUSSION

4.4.1 FLOW FIELD ANALYSIS

To analyze the impact of the fluctuating boundaries on the flow field, Figure 4.2 shows maps of the simulated velocities at selected times t_1=109, t_2=166 and t_3=199 min. These three timesteps correspond to three different water level conditions in the reservoirs (Fig. 4.1a) leading to three different velocity fields. At t_1, the hydraulic head of the left reservoir is 6 cm higher than the right reservoir. This accelerates the fluid motion in the horizontal direction, in particular in the area between both reservoirs (Figs. 4.2a, 4.2g). It also shows that for this time step, the water flows from the left reservoir towards the saturated porous medium, while the opposite occurs for the right reservoir (Fig. 4.2d). At t_2, the water level in both reservoirs is similar and although in both cases the water flows in the porous medium, the changes in the velocity field are smaller than at t_1. At t_3, the hydraulic head of the right reservoir is higher than the one of the left reservoir. The velocity in the mean direction of the flow decreases in the area between both reservoirs (Figs. 4.2c, 4.2i). In the vertical direction, we observe a flow reversal of the water compared to t_1. In this case, water flows from the saturated porous medium to the left reservoir, and from the right reservoir in the saturated porous medium (Fig. 4.2f). Overall, we observe that the variations in the velocity field in our system directly result from the oscillating boundaries.
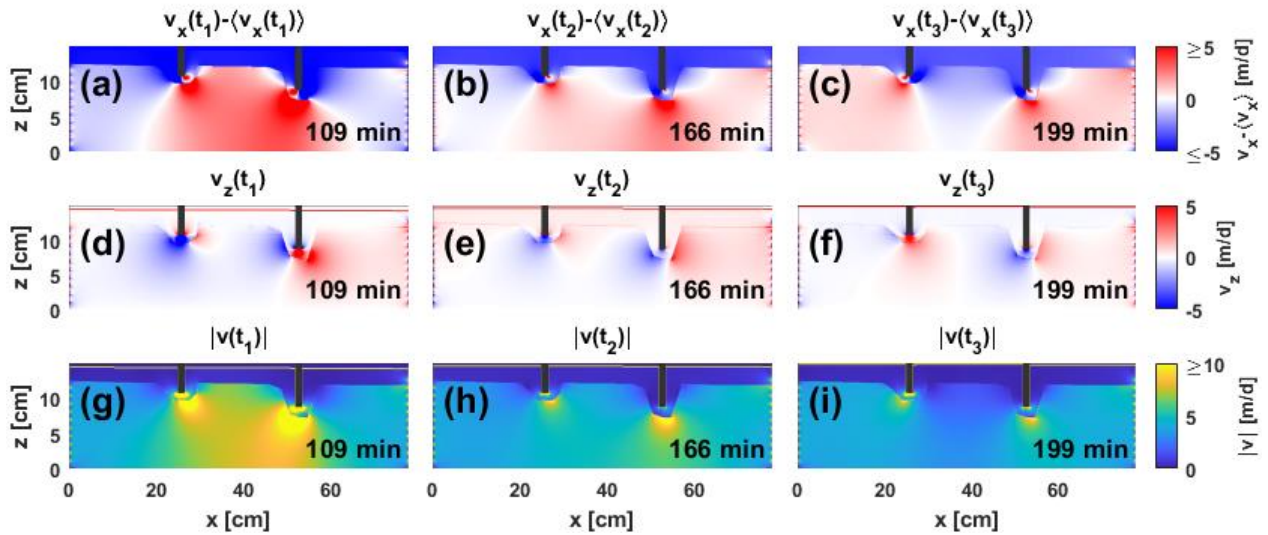
Figure 4.2: Linear average velocity field in the (a)-(c) horizontal and (d)-(f) vertical direction; and (g)-(i) magnitude of the velocity field for three selected times for the experiment Pe200 [the selected times are marked in Fig. 4.1(a)].

Figures 4.3a-c and 4.3d-f show, respectively, the images of the tracer plume and the maps of the Okubo-Weiss parameter $\Theta(x)$ for the selected times. For all velocity fields, the Okubo-Weiss value is mainly positive (over 97 % of the active cells), indicating that strain and stretching are dominating in the system over vorticity. A reason may be the homogeneity of the porous medium. In fact, also Geng et al. (2020), who simulated transient groundwater flows subject to tidal boundaries, observed that vorticity regions were only present in simulations with heterogeneous hydraulic conductivity fields. In our setup, the regions closer to the reservoirs and the zones with a change in the longitudinal velocity field display higher $\Theta(x)$ values. On the contrary, between the reservoirs the $\Theta(x)$ seems to be lower (Fig. 4.3d) even if the v_x is higher (Fig. 4.2a), meaning that the change in the velocity field is the main controlling factor for the observed stretching. In addition, to visualize how the topology of the flow field affects the plume in our setting, (Figures 4.3g-i) show the effective Okubo-Weiss values. Here we can notice that the part of the plume passing below the fluctuating reservoir displays the highest effective Okubo-Weis values.
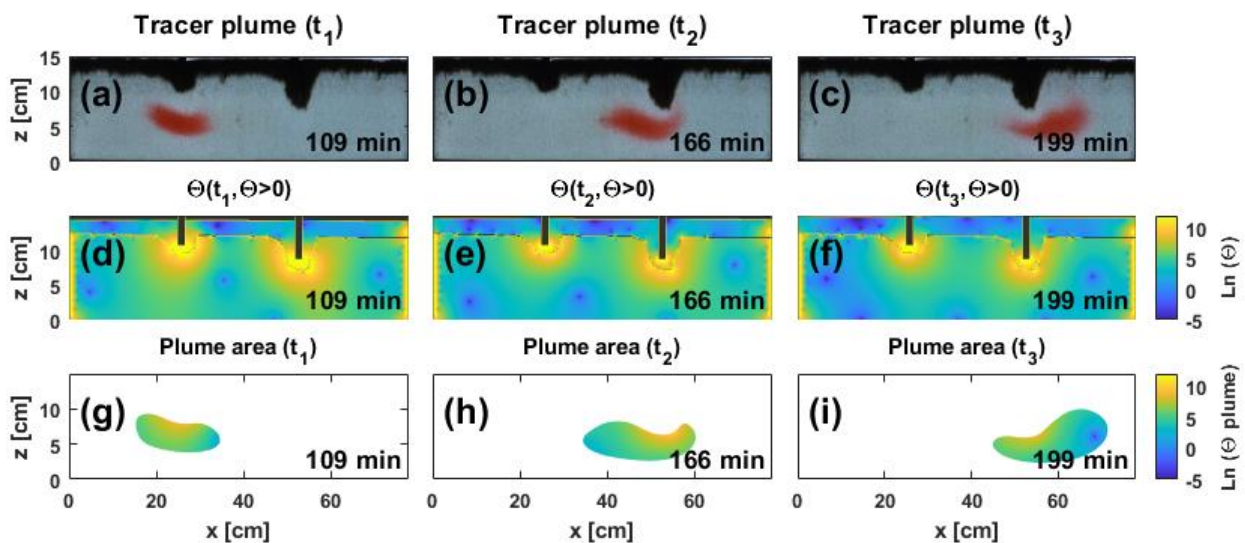
Figure 4.3: (**a-c**) Images of the tracer plume; (**d-f**) natural logarithm of the positive Okubo-Weiss field; and (**g-i**) local value of the Okubo-Weiss parameter in the area of the solute plume for the three different times for the experiment Pe200 shown in Fig. 4.1(a).

4.4.2 Solute transport analysis

Since the duration of the injection between the two experiments was kept constant, the experiment performed at Pe570 had more injected mass than the experiment at Pe200 and thus it reaches larger values of the dilution index. To make the result comparable, we normalized the value of the Shannon entropy by the simulated entropy of the plume at t_p, which represents the time when the tracer plume was completely injected in the system. We will refer to this entropy value as initial entropy. Figure 4.4 shows the modeled and measured Shannon entropy of the tracer plume normalized by its initial entropy in both flow-through experiments. In this and in the following figures, we show the time as the dimensionless quantity t/τ. Despite the slightly overestimation of the normalized entropies during some time intervals, we observe that there is a good agreement between the simulations and the experiment (root mean square error is 0.025 and 0.004 for Pe200 and Pe 570, respectively). This comparison helps us to validate our model results. The normalized entropy in both cases is increasing monotonically. Despite the larger volume of the plume at Pe570, the normalized entropy at Pe200 reaches higher values. This is partly because both plumes dilute at a very similar speed - in fact, the lines of the normalized entropy are almost superposed- and, as the plume at Pe200 spends more time in the domain, it has more time for dilution.
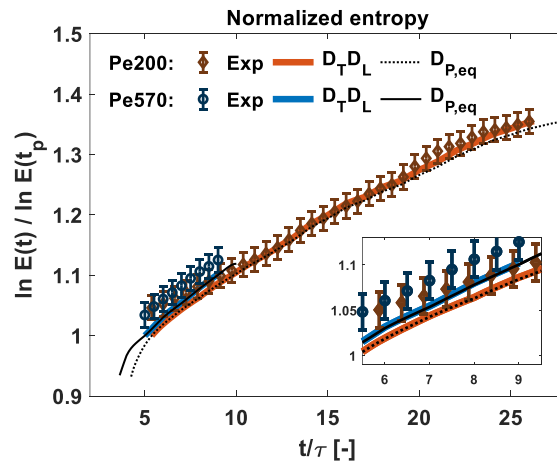
Figure 4.4: Normalized entropy at Pe200 and Pe570 in the experiment and the hydrodynamic dispersion model ($D_T D_L$) for the entire time series in which the tracer plume was completely inside the flow-through chamber. Error bars indicate experimental uncertainty. Thin lines correspond to the equivalent pore diffusion model ($D_{P,eq}$).

We investigate first the relation between the effective Okubo-Weiss parameter and the rate of increase of the entropy by wavelet coherence (Fig. 4.5). The wavelet coherence can be interpreted as the local correlation coefficient between the time series in the time-frequency domain (Grinsted et al. 2004). In the coherence plot, the color code represents the value of the coherence that can change in time (*x*-axis) and depending on the period (*y*-axis). Here, $\ln \Theta^e (t)$ and $d \ln E(t)/dt$ are coherent, in particular starting from $t/\tau=13$, which corresponds to the time at which the centroid of the plume passes below the first reservoir. Special attention is focused at the period of 16 minutes, where the right pointing arrows between 13 and 20 in the wavelet coherence indicate that $\ln \Theta^e (t)$ and $d \ln E(t)/dt$ are in-phase. After 20, the two timeseries start losing phase, although they remain coherent.
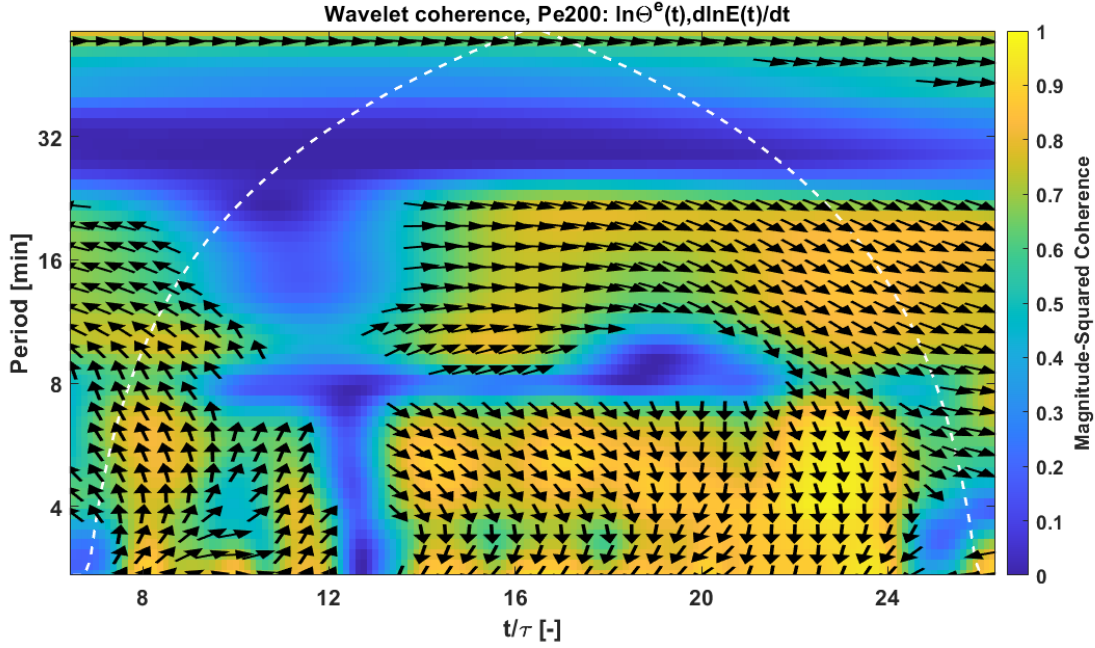
Figure 4.5: Squared-wavelet coherence between effective Okubo-Weiss and the rate of increase of the Shannon entropy for Pe200. Dashed lines represent the cone of influence.

In general, the relation between both metrics can also be seen in the time series of both the effective Okubo-Weiss parameter (Fig. 4.6a), right axis] and the entropy rate of increase (Fig. 4.6a, left axis), where both metrics display square-waves with a period of 16 minutes resulting directly from the fluctuations in the transient boundary conditions. In fact, by comparing fluctuations of the reservoirs (Fig.4.1a) with the Okubo-Weiss parameter, it is possible to observe that the crest of the wave of $\ln \Theta^e(t)$ corresponds to the times at which the water level of the left reservoir is higher than the right one. This can be explained because the stress imposed on the system is higher, in particular as the reservoir fluctuations are in counter-phase.

In the experiment at Pe570, the dilution rate and the effective Okubo-Weiss parameter also show a square wave behavior and are almost in phase (Fig. 4.6b). However, due to the shorter duration of the experiment, we cannot perform a wavelet coherence analysis since the period of 16 minutes is outside the cone of influence.
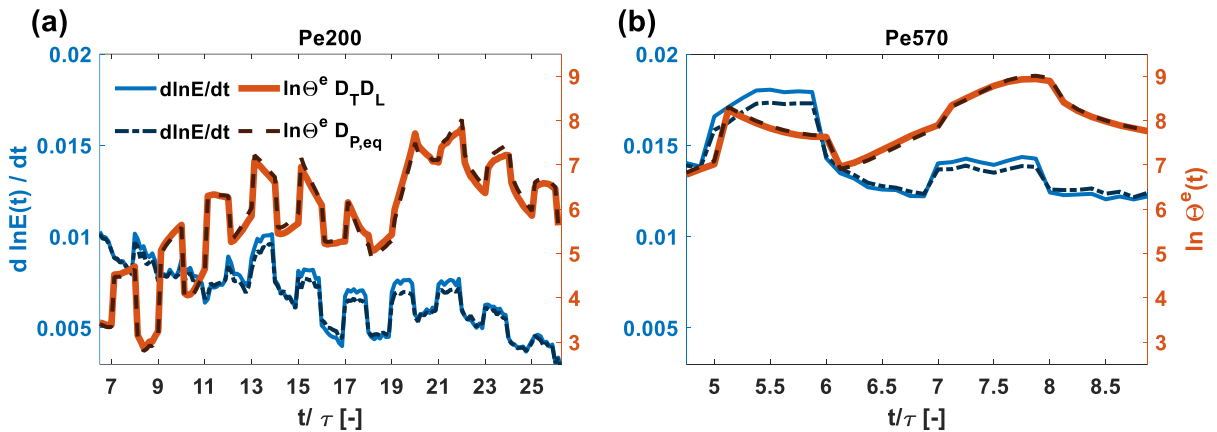
Figure 4.6: Rate of increase of the entropy (left axis) and effective Okubo-Weiss (right axis) considering the hydrodynamic dispersion ($D_T D_L$) and the equivalent pore diffusion ($D_{P,eq}$) simulations for Pe200 (**a**) and Pe570 (**b**), respectively.

The oscillations observed in $d\ln E/dt$ are more affected by the dynamics of the flow field in the area between both water reservoirs. Mixing enhancement, therefore, occurs mainly in the area between the reservoirs, as seen in Figures 4.3d-f. At Pe200, the fluctuations in $d\ln E/dt$ are stronger once the centroid of the plume travels below the first reservoir at t/τ =12.75. Then, they become weaker after the plume passes the second reservoir at approximately t/τ=25, even if the effective Okubo-Weiss parameter is high and its oscillations are strong. This result can be explained by the fact that, at the beginning and at the end of the flow-through system, the flow field is dominated by the fixed flux boundary conditions established through the pumps, and therefore the influence of the transient reservoir boundaries on plume deformation is less pronounced.

Besides the changes in the flow topology, a variable flow field also impacts the local dispersion coefficient, which ultimately affects mixing. In the physical experiment we cannot eliminate the effect of variable velocity on hydrodynamic dispersion. To confirm that mixing enhancement is controlled by the effective Okubo-Weiss parameter, we performed numerical simulations using the equivalent pore diffusion model (see Fig. 4.4, black lines). The effective pore diffusion coefficients were 20 and 30 times larger than D_p for Pe200 and Pe570, respectively. In Figures 4.6(a) and 4.6(b) we observe that even if we exclude the effect of the variable flow field on the hydrodynamic dispersion tensor, both $d\ln E/dt$ and Θ^e remain basically unchanged. Figures 4.7a-f and 4.7h-m show the spatial variability of the local hydrodynamic dispersion normalized by the aqueous diffusion coefficient at different selected times, as well as the mean value of the normalized local dispersion for both $D_T D_L$ and $D_{P,eq}$ at the Pe200 and Pe570. Overall, we observe in Figure 4.7g and 4.7n that the normalized mean local dispersion within the plume is changing according to the reservoir fluctuations in the hydrodynamic dispersion model, while in the pore equivalent model, the normalized mean local dispersion within the plume is much smaller. This confirms that the topology of the flow field is the dominant process controlling mixing in this kind of transient flow fields. If the Okubo-Weiss field would not control mixing, the entropy rate would not be fluctuating in the equivalent pore diffusion model, or the order of magnitude would be smaller. To the best of our knowledge, the results of this study provide first experimental evidence of the relation between Okubo-Weiss parameter and plume dilution in porous media.

Finally, the spatial and temporal variations in the local dispersion offer some additional insights in the physics of the experiment. For instance, the spatial variability of local dispersion is controlled by the velocity field which, as shown in Figure 4.2, has a higher magnitude near the reservoirs. In addition, the spatial averages of the longitudinal and transverse dispersion coefficients within the plume are also changing depending on the distance of the centroid of the plume from each reservoir. The longitudinal dispersion coefficient in Figure 4.7 ranges over several units within the plume surface. However, peak values are concentrated in small areas. This can also explain why processes controlling plume deformation, driven by shearing and stretching and acting over the entire plume, exert a stronger control on mixing than the enhancement in local dispersive processes occurring at very specific locations and for short time.
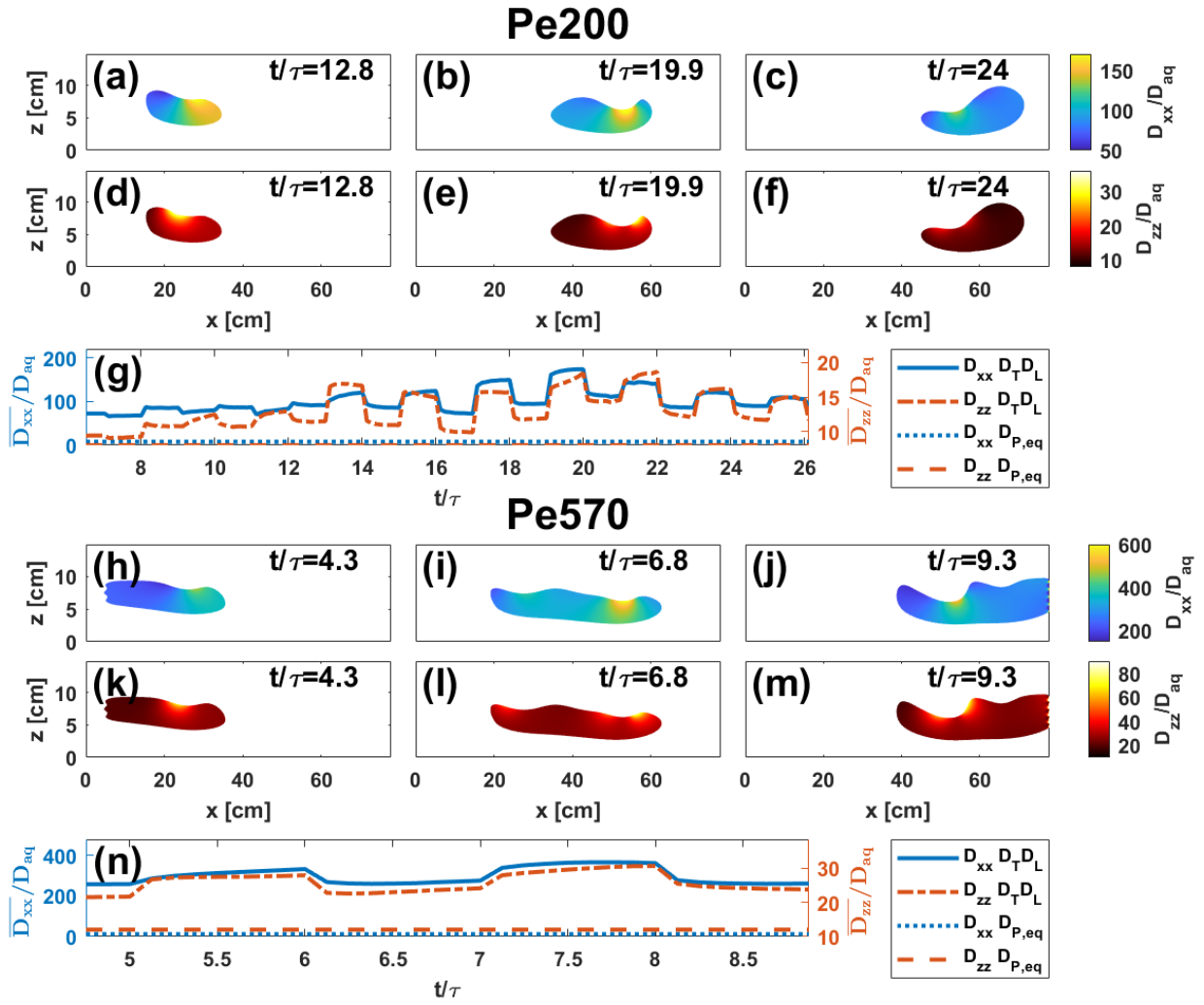
Figure 4.7: (a-f) Longitudinal and transverse local dispersion (D_{xx} and D_{zz}, respectively) experienced by the plume undergoing hydrodynamic dispersion in the porous medium, $D_T D_L$, at Pe200. **(g)** Mean of the longitudinal and transverse local dispersion (left and right axis, respectively) considering hydrodynamic dispersion and the equivalent pore diffusion model at Pe200. **(h-m)** and **(n)** are the same as (a-f) and (g) but for Pe570. Results are normalized by the aqueous diffusion coefficient.

4.5 CONCLUSIONS

In conclusion, the rate of increase of the entropy of a plume is coherent and highly dependent on the topology of the transient flow field. The model-based interpretation of the performed high-resolution laboratory experiments demonstrates that the effective Okubo-Weiss parameter is the main factor controlling the growth rate of the entropy of a solute plume and thus represents a good proxy for mixing. In the experiments, the variability in the flow field is caused by highly transient boundary conditions, showing that not only heterogeneous permeability fields may display complex mixing dynamics in porous media. Acknowledging the importance of the flow topology to quantify mixing and to understand mixing processes in porous media is relevant for both natural and engineered systems. In particular, our findings can be applied in mixing dynamics for the design of packed bed reactors, and for studying geophysical flows and groundwater aquifers connected to oscillating surface water bodies (e.g., tidal sea level fluctuations and regulated rivers). Moreover, considering that mixing-controlled reactions are commonly encountered in porous media, we envision future research

investigating reactive solute transport based on the analysis of the flow field topology. This will facilitate the understanding of the fate and transport of chemicals, nutrients, and energy fluxes in subsurface formations and at the interface between different environmental compartments.

Chapter 5

Effects of hydropeaking on groundwater solute transport

Published as

Abstract

Spreading, dilution and mixing processes in the groundwater are influenced not only by the heterogeneous properties of the porous media but also by the boundary conditions. Although less studied than the heterogeneity of the soil matrix, highly transient boundary conditions can often occur in the field and can also enhance mixing in Darcy flows. In this work, we focus on surface water-groundwater interaction, in particular on rivers affected by hydropeaking, an artificial flow regime with sharp and frequent water level fluctuations resulting from the operation of hydropower plants. To study how hydropeaking can affect the groundwater flow field and thus mixing in the subsurface, we modeled a cross-section of the Adige Valley, in Italy, where two Alpine rivers, the Noce and the Adige, are differently affected by hydropeaking. We performed two-dimensional flow and transport simulations using a calibrated model, and investigated different scenarios, considering both sub-daily and seasonal fluctuations. We characterized the flow field applying different topological and kinematic indicators and show their relation to mixing processes in the subsurface. Our results show that hydropeaking and hence the management of hydropower plants have a major effect on groundwater solute transport.

5.1 INTRODUCTION

Natural groundwater systems may be connected to fluctuating surface water bodies, water sinks and source terms which lead to transient boundary conditions. These conditions, together with the heterogeneous properties of the porous media, affect spreading, mixing and dilution processes in the aquifers (Rolle and Le Borgne 2019). While some transient boundary conditions are due to natural factors, such as ocean tides (Trefry et al. 2019; Geng et al. 2020) and seasonal fluctuations as occurs in rivers controlled by glacier melting (Pérez Ciria et al. 2019), others changes are caused by anthropogenic factors, including engineered pumping systems (Neupauer et al. 2014; Cho et al. 2019) and water management, in particular hydropeaking, an artificial flow regime characterized by changes in the water level due to the operation of hydropower plants (Ferencz et al. 2019; Arntzen et al. 2006).

Several works have shown the effects of hydropeaking on the hydrological cycle and sediment transport (Bruno et al. 2009; Fette et al. 2007), the physicochemical characteristics of the water (Hauer et al. 2017b; Zolezzi et al. 2011), and the interaction with hyporheic water (Singh et al. 2019; Sawyer et al. 2009; Song et al. 2018), with mostly negative impacts for riverine ecosystems (Casas-Mulet et al. 2021; Bejarano et al. 2018). Beyond the hyporheic zone, hydropeaking can cause variations in the groundwater level in river corridors and riverine islands (Francis et al. 2010; Song et al. 2020), and influence the transport of dissolved solutes near the shore (Zachara et al. 2016). More recently, an experimental study at laboratory scale by Ziliotto et al. (2021) has shown that hydropeaking has the potential to enhance the dispersion and spreading of a conservative plume moving below two rivers in a homogenous aquifer.

Understanding mechanisms behind mixing enhancement is relevant because mixing is slow in porous media and reactions are often incomplete (Valocchi et al. 2019; Wright et al. 2017), thus hindering the degradation of contaminants in the groundwater. In general, variations in the magnitude and direction of the velocity can increase mechanical dispersion, stretching and folding therefore enhancing mixing (Neupauer et al. 2020; de Anna et al. 2014). While these velocity variations are generally due to heterogeneities and anisotropies in the porous media (Ye et al. 2020; Cirpka et al. 2015), they can also be caused by transient boundary conditions (Dentz and Carrera 2005; de Dreuzy et al. 2012; Piscopo et al. 2013)). In fact, injection-extraction systems (Sposito 2006; Neupauer et al. 2014) and tidal forcing (Trefry et al. 2019; Wu et al. 2020) can generate transient flow fields with a complex and chaotic mixing dynamics.

The interaction between transient boundary conditions and heterogeneity and their effect for solute transport has been studied for different groundwater scenarios; for instance, de Dreuzy et al. (2012) for uniform fluctuations, Neupauer et al. (2014) for engineered systems, and Geng et al. (2020) for coastal aquifers. In terms of river-aquifer systems, Cardenas et al. (2004) analyzed the effect of heterogeneity in the hyporheic zone with its geometry, and Song et al. (2018) studied the impact of hydropeaking on the thermal regime and the biogeochemical reactions of a heterogenous cross-section of the hyporheic zone. In this work, we aim to study the interaction between river stage fluctuations and the heterogeneity of an aquifer, considering the conductivity of the river bed. For this, we model a cross-section of an aquifer located in an Alpine valley that is traversed by two rivers differently affected by hydropeaking, and perform flow and transport simulations with seasonal (daily resolution) and sub-daily (hourly resolution) fluctuations. We explore therefore, the effects of such fluctuations on a conservative tracer plume by analyzing its spatial distribution and dilution index, under different hydraulic scenarios.

5.2 METHODOLOGY

5.2.1 STUDY AREA AND MODEL

We study the aquifer under the Adige Valley (north of Italy), in particular the area between Mezzolombardo and San Michele all'Adige (Figure 5.1a). The valley is composed by loose sediments from the alluvial fan formations of the Adige River and its tributaries, and to the east and west is bordered by calcareous dolomitic mountains. Originally a wetland, the area has a high demand of groundwater for irrigation of vineyards (Castagna et al. 2015). As in most Alpine catchments, its hydrological regime is characterized by snow and glacier melting in spring, however it is heavily impacted by hydropeaking (Chiogna et al. 2016).
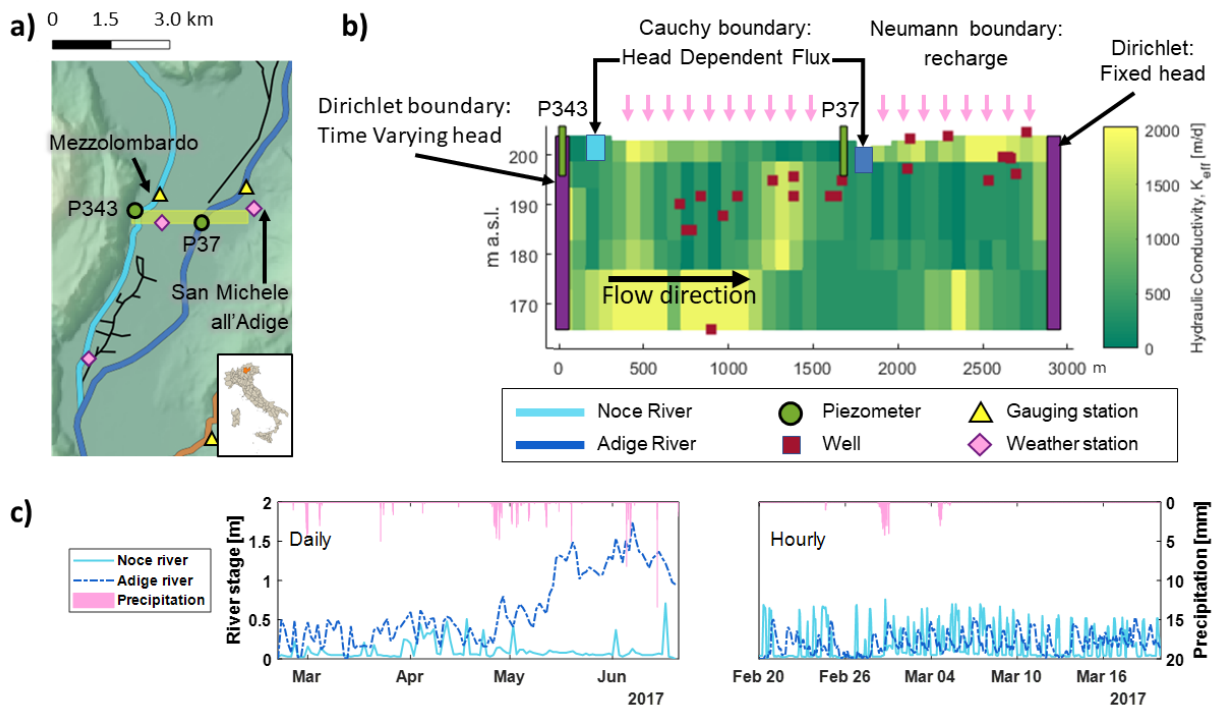
Figure 5.1: (**a**) Modeled area in the Adige Valley; (**b**) model and hydraulic conductivity of the cross section; and (**c**) hydrograph at daily and hourly timescales with precipitation.

Figure 5.1b shows the modeled vertical cross-section of the Adige Valley, which is traversed by the Adige River and the Noce River, a tributary of the Adige. The model origin is at long= 661636.44 and lat=5117317.54 (WGS84 – UTM 32N). The bottom of the unconfined aquifer is at 164 m a.s.l. and the topographical elevation of the surface varies from 204 to 209 m a.s.l. From west to east, the model extends of approximately 3120 m. The model is therefore discretized in 780 columns of $\Delta x = 4$ m and 80 layers of $\Delta z = 1$ m. Overall, we follow the methodology used in Castagna et al. (2015) to model a larger section of the Adige Valley, and we consider the hydraulic conductivity field which is used by the Geological Survey of Trento. The left and right sides of the cross-section are Dirichlet boundary conditions. On the left, we use the measurements of the piezometer P343 to implement a time variant specified head, and on the right, we apply a constant head. This boundary is far from the areas close to the highly transient boundary conditions (i.e., rivers) and it does not affect significantly the transient model.

On the top of the model, we apply Cauchy boundary conditions to implement the aquifer's recharge, which is computed after a leakage model based on soil saturation moisture (Laio et al. 2001; Rodriguez-Iturbe et al. 2001). Precipitation data was obtained from the meteorological stations at Mezzolombardo (Meteotrentino 2022) and

San Michele all'Adige (3BMeteo 2022). Precipitation at Mezzolombardo aggregated for daily steps is shown in the top axis of Figure 1c. Evapotranspiration and irrigation were obtained from (Galli 2019). We assign the recharge to each cell after the Thyesen polygon method. Cauchy boundary conditions were also applied to introduce the pumping wells. In fact, the cross-section contains several pumping wells, which location, use and maximum allowed pumping rate were provided by the Geological Survey of Trento. The rivers are implemented as Neumann boundary conditions, or head-depending flux. To estimate the river stage, we collect hourly data from the gauging stations of Mezzolombardo Ponte Rupe and San Michele all'Adige, provided by the Dam Office of the Autonomous Province of Trento (Provincia Autonoma di Trento - Ufficio Dighe 2017). We calculate the stage at the model area using the Chézy equation under the assumption of a rectangular channel and that the river flow is constant between the gauging stations and the area of interest. We consider a model at daily resolution to consider weekly and seasonal fluctuations, and a model at hourly resolution to account for sub-daily fluctuations. The daily resolution simulation is from February 20th to May 20th, 2017, while the hourly resolution simulation is for a one-month period, from February 20th to March 20th of the same year. The hydrograph of the Noce and the Adige rivers for both daily and hourly models is shown in Figure 5.1c.

5.2.2 MODEL CALIBRATION AND SYNTHETIC SCENARIOS

We calibrate the specific yield and the vertical hydraulic conductivity of both the Noce and the Adige riverbeds, and adjust the bottom of the riverbed at the Adige. For this, we use a Montecarlo approach and apply as objective functions the mean average error (MAE), and root mean squared error (RMSE), and the Nash-Stutcliffe coefficient (NSE). Piezometer P37 is used as calibration point. We calibrate the model at daily resolution (MAE=0.05, RMSE=0.07, NSE=0.98 and validate it with the hourly resolution (MAE=0.02, RMSE=0.03, NSE=0.85). In addition to the calibrated model, we simulate synthetic scenarios to account for the broad range of values in the hydraulic conductivity of the riverbed (Tang et al. 2015), as well as the case of a steady river stage. Therefore, we consider the cases of the vertical hydraulic conductivity k of the river as follows: 0.01k, 0.1k, 0.2k, 0.5k and 10k for the transient models, and k for the steady state simulation, where k is the calibrated hydraulic conductivity. For comparability purposes between the simulations at daily and hourly resolution, the steady state simulation uses the mean groundwater and river heads of the hourly model (February 20th - March 20th, 2017).

5.2.3 GROUNDWATER FLOW AND TRANSPORT EQUATIONS

The groundwater flow equation for a representative volume can be described by a combination of the Darcy's law with the continuity equation

$$S\frac{\partial h}{\partial t} = \nabla \cdot (\boldsymbol{K} \cdot \nabla h) + \boldsymbol{q}' \tag{5.1}$$

where $\mathbf{K}\,[LT^{-1}]$ corresponds to the hydraulic conductivity tensor, $\nabla h\,[-]$ is the hydraulic head gradient, $\boldsymbol{q}'[LT^{-1}]$ accounts for the source and sink, and $S\,[-]$ is the storage coefficient. We solve the groundwater flow equation with the finite differences code MODFLOW-OWHM (Boyce 2022). Specifically, we apply the Newton-Raphson solver (Niswonger et al. 2011), which is recommended for cases with water table fluctuations across different layers.

The rivers were implemented using the river package of MODFLOW. As mentioned earlier, the model is calibrated for the vertical hydraulic conductivity k of the river beds. This parameter is introduced in the river package through the riverbed conductance, defined as

$$C = \frac{\Delta x \Delta y k}{M}, \tag{5.2}$$

where Δx and Δy are the length and width of the cell occupied by the river, and M is the thickness of the riverbed. We assume a thickness of 1 m in order to calculate the vertical hydraulic conductivity k from the calibrated riverbed conductance.

The transport of solutes is solved by the advection-dispersion equation (ADE). For a conservative tracer, the advection-dispersion equation is written as

$$\frac{\partial(nC)}{\partial t} = \nabla \cdot (n\mathbf{D}\nabla C) - \nabla \cdot (n\mathbf{v}), \tag{5.3}$$

being $C\,[\mathrm{ML^{-3}}]$ the tracer concentration, $n\,[-]$ the porosity, and $\mathbf{D}\,[\mathrm{L^2T^{-1}}]$ the dispersion tensor. We solve the ADE using MT3D-USGS (Bedekar et al. 2016a). The dispersion tensor uses a longitudinal dispersion coefficient, D_L, while the transverse dispersion coefficient is parametrized as $D_T = 0.1D_L$.

5.2.4 DILUTION INDEX

We use the dilution index (Kitanidis 1994) to evaluate mixing for the solute concentrations estimated with the ADE. The dilution index is understood as the exponential of the entropy of the system, defined by

$$E(t) = \exp\left[-\int_V p\,(\mathbf{x},t)\,\ln p(\mathbf{x},t)\,dV]\right], \tag{5.4}$$

where $p\,(\mathbf{x},t)$ is the mass probability density function of the concentration at the coordinates $\mathbf{x}$, at time t in a system of volume V, and it is calculated by

$$p(\mathbf{x},t) = \frac{C(\mathbf{x},t)}{\int_V C\,(\mathbf{x},t)dV}, \tag{5.5}$$

Higher values of the dilution index correspond to a better dilution of the system.

5.3 RESULTS AND DISCUSSION

5.3.1 RIVER FLUCTUATIONS AND GROUNDWATER HEADS

We start the analysis with the model at daily resolution, which requires a simulation time much lower than the model at hourly resolution (less than a third), and in the area of the Noce River. In addition to the field observations, we added observation points for the simulated groundwater heads below the river and 25 m before the first river cell. During most of the simulated period, the estimated river head of the Noce is higher $(0.15 \pm 0.15 \text{ m})$ than the measured groundwater head at piezometer 343, located 95 m to the left of the river. Compared to the groundwater head below the river, the Noce is 0.06 ± 0.03 m higher, indicating that the Noce River is feeding the aquifer. On the side of the Adige River, the estimated river head is 0.36 ± 0.06 m lower than the groundwater head at piezometer 37 (85 m from the river), and the groundwater level below the riverbed is 0.01 ± 0.008 m higher than the river head, indicating that at the studied cross-section, the aquifer is feeding the river, and the groundwater flows towards the Adige.
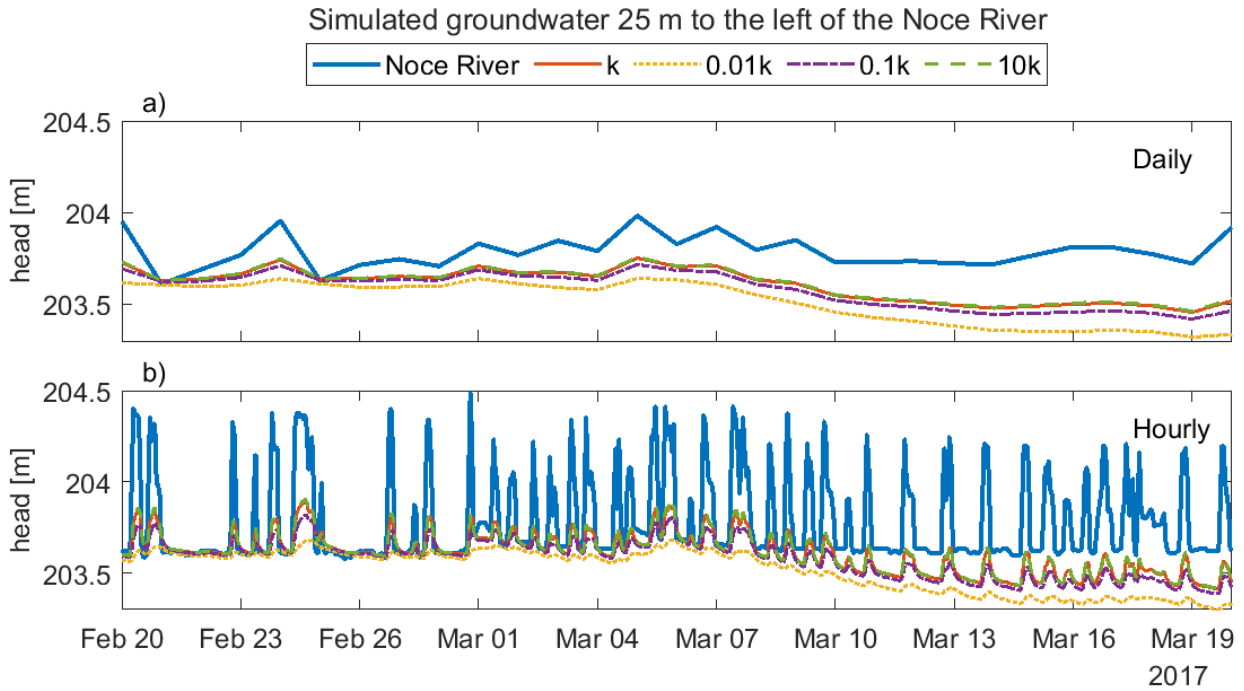
Figure 5.2: River fluctuations and simulated groundwater heads for the model at (**a**) daily and (**b**) hourly resolution for calibrated and synthetic scenarios during one month.

As a comparative example of the simulated groundwater heads in the calibrated model and selected synthetic scenarios, we show in Figure 5.2a the case for the daily observation points placed 25 m to the left of the Noce River during the period from February 20th to March 20th, 2017. We also included the estimated river head at the cross-section. The simulated groundwater levels are highly dependent on the boundary conditions, as it is noticeable in particular after March 7th, when the groundwater head drops. However, it is also possible to observe changes in the groundwater due the river fluctuation, as the tough in February 21st or peaks in February 24th and March 5th, in particular for k and 10k.

5.3.2 INTERPLAY OF HYDRAULIC CONDUCTIVITY, RIVER FLUCTUATIONS AND RIVERBED CONDUCTANCE

In order to study how solute transport is affected by hydropeaking in a heterogenous aquifer cross-section, we prepared the transport simulation in the seasonal model and considered a conservative tracer representing a contaminant plume with an initial rectangular shape 28 m length, 3 m wide and with a centroid placed 40 m to the left of the Noce River and 10 m below its riverbed. Its initial concentration is 100 $[M/L^3]$.

As the plume starts moving, it is pushed towards the bottom of the aquifer due to the combined effect of the river stage higher than the groundwater and the hydraulic conductivity field. In fact, the hydraulic conductivity below the Noce is lower compared to the region below the tracer plume, forming therefore a preferential path in the vertical direction enhanced by the vertical component of the velocity. Once the plume reaches the bottom of the aquifer, it moves to the right direction through the area with high hydraulic conductivity (Figure 5.1b between 164 and 175 m a.s.l. and 0 and 1000 m in the longitudinal direction). The plume distribution and its concentration at the end of the simulation is seen in Figure 5.3a (left colorbar), the magnitude of the velocity field is shown as background (right colorbar), and the blue rectangle on the top indicates the location of the Noce river.
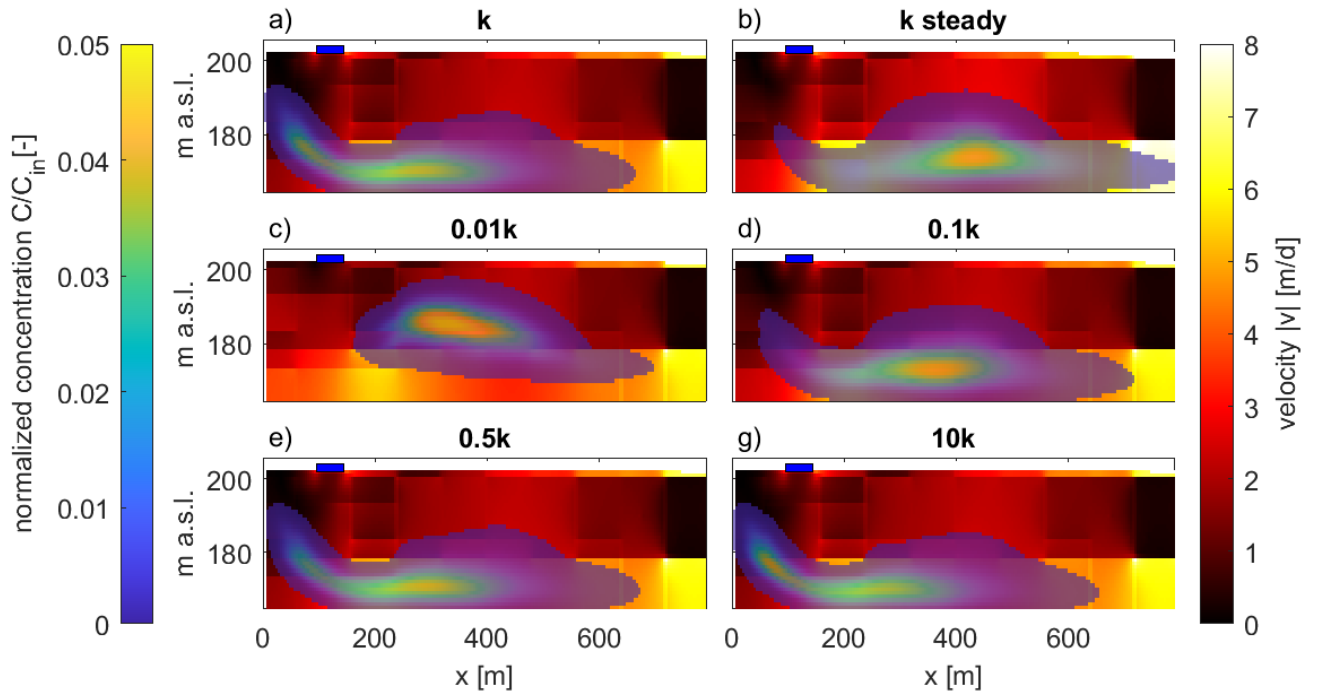
Figure 5.3. Magnitude of the velocity field and solute tracer distribution after 121 days for the calibrated transient model (**a**) and the synthetic scenarios (**b-g**).

The final plume distribution for the steady state simulation and the 0.01,0.1k,0.5k and 10 k scenarios is shown in Figures 3b-3g. These scenarios allow us to analyze the interplay of the heterogeneous conductivity field with the riverbed conductance and the river fluctuations. All the plumes have a hat/cap shape due to the fact that where the plume has a larger longitudinal dispersion in the area of higher velocity at the bottom of the aquifer. But they can also be grouped in different behaviors. For instance, the plumes of k, 0.5 k and 10 k (Figures 5.3a, 5.3e and 5.3g, respectively) look very similar at the first sight, and the simulated heads, compared below the river and at distances 25 and 40 m before the river, do not show a significant variation. However, the peak concentration of the plume is slightly different. In 0.5k, the peak is between 200 and 400 m, while in 10 k, the peak is between 50 and 100 m. In k, the concentration displays two local maxima in those two locations. A possible explanation is the interplay between the regional flow direction (to the right) and the feeding river that generates locally a flow in the opposite direction, that is, from the river to the left boundary. When k is higher, more water is exchanged between the river and the groundwater and the flow velocity towards the left boundary is higher, pushing the plume backwards.

The plumes k steady and 0.1k look similar to each other (Figures 5.3b and 5.3d). Like the first described group, they also move towards the bottom of the aquifer, but the peak concentration is not as stretched as for the former three cases and it arrives further, around 380 m for 0.1k and 400 m for the steady state. A reason why k steady reaches a farther distance than 0.1k is that it is does not experience the fluctuations that can increase the flow direction backward and therefore delay the plume. The most different final tracer distribution is encountered for the case 0.01k (Figure 5.3c), which does not reach the bottom of the aquifer. Here, the magnitude of the velocity field below the Noce River is also different from the other cases. Due to the low riverbed conductance, the vertical velocity is not pushing the plume to the bottom of the aquifer and the plume moves rather horizontally. This case is representative for a clogged riverbed.

While the final plume distribution is different when the hydraulic conductivity of the riverbed varies in orders of magnitude, it is interesting to observe that the variations in the groundwater head at 25 from the river are minimal (e.g., Figure 5.2a). In fact, assuming that the results for k are a measured groundwater head, MAE $\leq$ 0.021, RMSE$\leq$ 0.024 and NSE>0.9 for the scenarios $\geq$ 0.1k for the four months simulated period. Only the

scenario of 0.01k gave poor statistical values. With respect to the calibration point, the riverbed conductance of the Noce river is less sensitive than the river bed conductance of the Adige river. Considering that the conductivity of the river bed can change significantly over short distance, it is important to be aware of the different possible scenarios and the low model sensitivity to the groundwater heads, in particular when modeling solute transport in a regional model under highly transient boundaries in this heterogeneous aquifer.

5.3.3 SENSITIVITY OF DILUTION INDEX AT DAILY AND HOURLY RESOLUTION

We extend the previous analysis of solute transport to the Adige river and to the simulations at hourly resolution by estimating the dilution index. As mentioned earlier, the hourly resolution accounts for the subdaily fluctuations typical of rivers under hydropeaking. First of all, we place an initial solute concentration near the Adige River at the same relative distance as the plume near the Noce River. Here, the plume moves towards the river and starts leaving the system after 15 days. To keep only the period in which the tracer is present only in the aquifer and for comparison purposes, we present in Figure 5.4 the dilution index for both time resolutions and both rivers during the first 15 days. Despite the differences found in the location and distribution of the tracer concentration in section 3.2, the dilution index reaches similar values for all the transient simulated scenarios (Figure 5.4a), only the steady state scenario displays a different dilution. The hourly simulations (Figure 5.4c), on the contrary, show a broader range of the dilution index. The lowest final dilution value is the same as in the daily simulation: the steady state scenario. However, the dilution index after 15 days increases as the vertical hydraulic conductivity of the Noce Rive increases. Considering hourly resolution rather than a daily one may be particularly important when analyzing contaminant plumes. For instance, a daily resolution model may show that a plume has already diluted to no-harmful concentrations, while the same model but at hourly resolution may reveal that the peak concentrations are still dangerous for the environment.

Similar to the analysis of the Noce, we compared the scenarios with the simulated head 25 m to the left of the Adige River for the hourly simulations (Figure 5.2b). The different riverbed conductances of the transient simulations are not sensitive to the groundwater head in that point (MAE<0.031, RMSE<0.032 and NSE>0.99), except for 0.01k (MAE=0.19, RMSE=0.21 and NSE=0.75), where the groundwater head is higher than the other cases, since less water from the aquifer goes into the river. At the calibration point, it is possible to notice changes in the simulated groundwater head, showing that the groundwater head propagation is also sensitive to the hydraulic conductivity of the riverbed. Unlike the plume near the Noce that is affected by the subdaily river fluctuations, the behavior of the dilution index of the plume near the Adige river is controlled by the advection forces leading the plume towards the river (Figures 5.4b and 5.4d). In fact, the dilution index looks almost the same for all transient scenarios and the steady state model, except for 0.01k. In this case, the low riverbed conductance leads to a lower velocity of the aquifer water feeding the river. Similar to the Noce, the hourly resolution also leads to larger values of the dilution index, and it increases the difference between the higher and lowest dilution value (0.01k in this case).

Overall, our results emphasize both the necessity to account for sub-daily fluctuations rather than using the mean daily values when studying solute transport in highly transient systems and the heterogeneous response of surface water – groundwater interaction in two rivers, both affected by hydropeaking under similar hydrological and geological conditions.
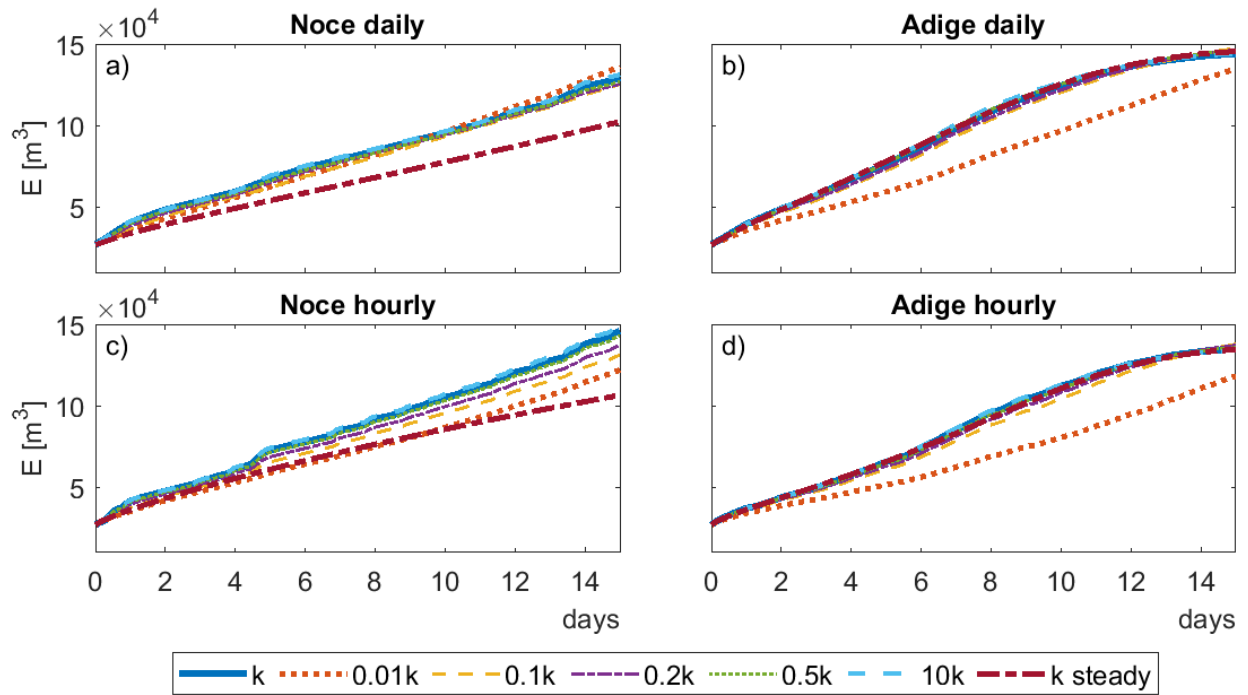
Figure 5.4: Dilution index for both rivers for the hourly and daily simulations during the first 15 days.

5.4 CONCLUSIONS

In this work, we modeled an aquifer cross-section of an Alpine valley differently impacted by two rivers affected by hydropeaking. We performed simulations at daily scale to consider seasonal fluctuations, and at hourly resolution to consider the effect of sub-daily fluctuations. We compared scenarios with different hydraulic conductivity of the river bed by analyzing variations in the groundwater head, the distribution of a tracer plume and the dilution index. Our results show that in a natural system, the interplay between the river fluctuations, and of the hydraulic conductivity of the aquifer and of the river bed can lead to a complex transport dynamic. In particular, the effect of sub-daily river stage fluctuations can be a relevant to correctly quantify the dilution index of a plume passing close to the river.

CHAPTER 6

UNCERTAINTY IN HYDROPEAKING WAVES: EFFECTS ON FLOW TOPOLOGY

Published as

Abstract

Topological flow properties are proxies for mixing processes in aquifers and allow us to better understand the mechanisms controlling transport of solutes in the subsurface. However, topological descriptors, such as the Okubo-Weiss metric, are affected by the uncertainty in the solution of the flow problem. While the uncertainty related to the heterogeneous properties of the aquifer has been widely investigated in the past, less attention has been given to the one related to highly transient boundary conditions. We study the effect of different transient boundary conditions associated with hydropeaking events (i.e., artificial river stage fluctuations due to hydropower production) on groundwater flow and the Okubo-Weiss metric. We define deterministic and stochastic modeling scenarios applying four typical settings to describe river stage fluctuations during hydropeaking events: a triangular wave, a sine wave, a complex wave that results of the superposition of two sine waves, and a trapezoidal wave. We use polynomial chaos expansions to quantify the spatiotemporal uncertainty that propagates into the hydraulic head in the aquifer and the Okubo-Weiss. The wave-shaped highly transient boundary conditions influence not only the magnitude of the deformation and rotational forces of the flow field but also the temporal dynamics of dominance between local strain and rotation properties. Larger uncertainties are found in the scenario where the trapezoidal wave was imposed due to sharp fluctuation in the stage. The statistical moments that describe the propagation of the uncertainty highly vary depending on the applied boundary condition.

6.1 INTRODUCTION

Mixing plays a critical role in describing solute transport in aquifers (de Anna et al., 2014; Rolle and Le Borgne, 2019). Understanding mixing-limited reactions in the subsurface is particularly relevant to recognize biogeochemical transformations (Boisson et al. 2013; Kang et al. 2019; Pinay et al. 2015), operate and design engineering remediation techniques (Cho et al. 2019; Mays and Neupauer 2012; McCarty and Criddle 2012; Neupauer et al. 2014), and understand hyporheic processes (Boano et al., 2014). A variety of methods have been developed to understand the transport dynamics in the subsurface and the effect that heterogeneous hydraulic properties have on spreading, dilution, and reactive mixing, (Valocchi et al., 2019). However, transport simulations are often computationally expensive and the quantification of uncertainties may result in a very time-consuming exercise (Lykkegaard et al. 2021; Smith 2013). The relation between topological flow properties and mixing processes in aquifers (Bresciani et al. 2019; de Barros et al. 2012) and porous media (de Anna et al., 2014; Engdahl et al., 2014; Wright et al., 2017) provides an interesting alternative to the solution of the transport problem. One advantage of investigating such relations is that the calculation of topological features of the flow field requires only the solution of the flow problem, which is much cheaper from the computational point of view than the solution of the flow and transport equations.

A topological quantity known as the Okubo-Weiss metric (Okubo, 1970; Weiss, 1991) was shown to be a good proxy for mixing potential (de Barros et al., 2012; Wright et al., 2017). This metric is commonly used in geophysics to identify filament from vortex structures (Casella et al. 2011; Roullet and Klein 2010) and characterize them in terms of dominant forces of the flow field, such as vorticity, shear strain, and normal strain de Barros et al., (2012) and Wallace et al., (2021). Still, the quantification of such topological descriptors of the flow field is affected by the uncertainty that is caused by the heterogeneous nature of the aquifer (Geng et al., 2020; Valocchi et al., 2019). Significant efforts have been made to quantify the uncertainty affecting the predictions of solute concentration values caused by the generally unknown hydraulic conductivity field (Moslehi and Barros 2017; Nowak et al. 2010). However, in this work, we assume the hydraulic conductivity field as properly characterized and well known in order to focus on a different source of uncertainty, which did not receive comparable attention in the literature, i.e., highly transient boundary conditions.

In fact, transient boundary conditions can also be uncertain and affect the estimation of the topological properties of the flow field and, consequently, the understanding of mixing and transport processes in aquifers (Hester et al., 2021; Ziliotto et al., 2021). This is particularly the case of the aquifer area close to surface water bodies (Dudley-Southern and Binley 2015; Merchán-Rivera et al. 2021; Santizo et al. 2020; Singh et al. 2020). In this work, we focus on a river reach that is affected by hydropeaking, i.e., sudden changes in the hydraulic head of the river caused by the operation of hydropower plants. Such fluctuations display some typical periodicity (Pérez Ciria et al., 2020) and modify the natural hydrological behavior and hydraulic conditions of the streams (Meile et al. 2011; Hauer et al. 2017b), which can impact the hyporheic zone (Sawyer et al., 2009; Singh et al., 2019) and propagate to the groundwater (Francis et al., 2010; Song et al., 2020). Moreover, since hydropeaking may depend on hydrological conditions (Li and Pasternack, 2021) and the dynamic behavior of the energy market (Chiogna et al., 2018; Pérez Ciria et al., 2019; Wagner et al., 2015), the stream head fluctuations entail uncertainty related to the peak amplitude and the temporal occurrence of the event.

The question that we aim at answering in this work is to what extent the shape and the uncertainty of hydropeaking waves affect the topology of the groundwater flow field quantified through the Okubo-Weiss parameter. To achieve our aim, we define one single realization of a two-dimensional heterogeneous aquifer and build modeling scenarios based on four typical settings for the stream fluctuations of the boundary conditions: a triangular wave, a sine wave, a complex wave (realized as the superposition of two sine waves), and a trapezoidal wave (Ferencz et al., 2019; Li and Pasternack, 2021; Sawyer et al., 2009). Moreover, we apply polynomial chaos

expansion (Xiu and Karniadakis 2002) to quantify the uncertainty due to the oscillatory boundaries and quantify the mean and standard deviation of the temporal and spatial values of the Okubo-Weiss metric.

The paper is structured as follows. Section 6.2 presents the synthetic case study, the deterministic and stochastic modeling scenarios, the polynomial chaos expansion method, and the topological metric that we use to describe the flow field. In Section 6.3, we present and discuss the results and findings related to the groundwater flow and the Okubo-Weiss metric and the quantification of the spatiotemporal uncertainty. We conclude this work in Section 6.4 by restating major findings and discussing the environmental implications of our results.

6.2 METHODS

6.2.1 GROUNDWATER FLOW EQUATION

The governing equation of the two-dimensional transient groundwater flow in a heterogeneous, isotropic, and unconfined aquifer can be written as

$$\frac{\partial}{\partial x}\left(K_x h \frac{\partial h}{\partial x}\right) + \frac{\partial}{\partial y}\left(K_y h \frac{\partial h}{\partial y}\right) = s_y \frac{\partial h}{\partial t} \pm Q \,, \tag{6.1}$$

where h is the hydraulic head [L], K_x and K_y are values of the hydraulic conductivity along the x and y coordinate axis [LT^{-1}], s_y is the specific yield of the porous medium [-], and Q describes the volumetric flux from source and sink terms [LT^{-1}] (Anderson et al. 2015; Bear 1979). The initial conditions and Dirichlet boundary conditions can be denoted as

$$h(x, y, 0) = h_0(x, y), \qquad x, y \in \Lambda, \tag{6.2}$$

$$h(x, y, t) = h_1(x, y, t), \qquad x, y \in \partial\Lambda, \tag{6.3}$$

respectively, where $h_0(x, y)$ is the initial hydraulic head [L] in the domain in the flow region Λ; $h_1(x, y, t)$ is the known hydraulic head value of the boundary head [L], and $\partial\Lambda$ denotes the boundary region (Bear and Cheng 2010; Cheng and Cheng 2005).

6.2.2 MODEL DESCRIPTION

In our system, we consider a two-dimensional unconfined aquifer with lognormal heterogeneous isotropic hydraulic conductivity field $g(x) = \ln[K(x)]$ defined by the geometric mean $\mu_g = 1 \times 10^{-3}$ m/s, the geometric standard deviation $\sigma_g = 1.5$ m/s and the correlation length $\lambda = 10$ m, equivalent to porous medium formed by sands and gravels (Coduto 1999). The area of the squared domain is $\mathcal{L}_1 \times \mathcal{L}_2 = 10\lambda \times 10\lambda$ with cell size $0.1\lambda \times 0.1\lambda$ (see **Figure 6.1**b). The distance between the ground surface and the bottom of the aquifer is $z = d(-z/2, z/2)$, the reference datum is the middle point $z_0 = 0$. The initial groundwater level conditions h_0 are set to a uniform water level in the domain, which matches the reference datum, so that $h_0 = z_0$ (see **Figure 6.1**c) and any simulation output h represents the relative movement of the groundwater head with respect to z_0. The time discretization of the simulation is τ/T, where T represents the simulation time length, and it is related to the wave frequency f such that $f = 1/(80\tau)$.
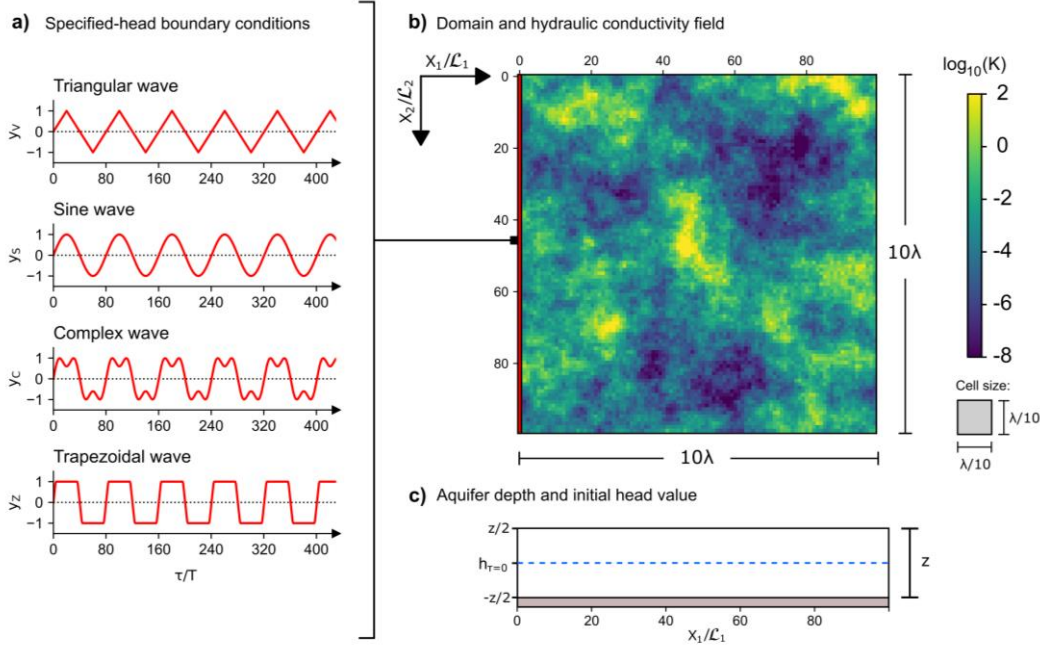
Figure 6.1: Model description: (**a**) wave-shaped time-variant specified head boundary conditions, (**b**) spatial domain and hydraulic conductivity field, and (**c**) aquifer depth and initial groundwater head conditions

The discontinuous release of water from hydropeaking events tends to follow a periodicity. Hence, the stage fluctuation in the stream can be described by a periodic function $y(t + F) = y(t)$, where $F = 1/f$ is a nonzero value defined as the period [T]. We introduce the periodic waves as specified-head boundary conditions, i.e., Dirichlet boundary conditions (Bear and Cheng, 2010), by fixing head values at the left border of the domain. The wave-shaped time series of heads represent the stream stage and the values at the boundary are time-dependent and updated as the simulation progresses. This setup assumes that the stage changes for the entire river reach considered simultaneously (i.e., no hydraulic model is used to describe the wave propagation along the reach) and strong connectivity between surface water and groundwater. These assumptions are consistent, for example, with the study of Sawyer (2009) focusing on the Colorado River in Texas. The top, bottom and right boundaries are defined as no-flow boundaries. We define the following periodic functions (see **Figure 6.1**a) to represent the effect of the hydropeaking on the left boundary conditions:

- Triangular wave:

$$y_V(t) = 4Af \left| \left\{ \left(t - \frac{1}{4f}\right) \bmod \left(\frac{1}{f}\right) \right\} - \frac{1}{2f} \right| - A \,, \tag{6.4}$$

- Sine wave

$$y_S(t) = A \sin(2\pi f(t - p)) \,, \tag{6.5}$$

- Complex wave:

$$\begin{aligned} y_C(t) &= y_S^\alpha(t) + y_S^\beta(t) \\ &= A_\alpha \sin(2\pi f_\alpha(t - p_\alpha)) + A_\beta \sin\left(2\pi f_\beta(t - p_\beta)\right) \,, \end{aligned} \tag{6.6}$$

- Trapezoidal wave

$$
y_Z(t) := \begin{cases} -A, & \text{if } y_V^*(t) < A; \\ A, & \text{if } y_V^*(t) > A; \\ y_V^*(t), & \text{otherwise,} \end{cases}
$$

(6.7)

$$
y_V^*(t) = 4b_Z A f \left| \left\{ \left(t - \frac{1}{4f} \right) \bmod \left(\frac{1}{f} \right) \right\} - \frac{1}{2f} \right| - b_Z A .
$$

(6.8)

Then, $y_V(t)$, $y_S(t)$, $y_C(t)$ and $y_Z(t)$ represent the time-variant specified-head boundaries for the triangular, sine, complex and trapezoidal wave scenario, respectively, t is the evaluation time step, A is the amplitude of the wave, p is the phase shift and f is the frequency. We shaped the trapezoidal wave using the stepwise function $y_Z(t)$ to remove the values that exceed the minimum and maximum limits defined by A, which depends on the outcomes of a triangular function $y_V^*(t)$. A coefficient b_Z is introduced to this triangular function to extend the amplitude A, which will determine the interval between minimum and maximum stage to be equal to $4/b_Z$ given the slope of the trapezoid legs with base angles $\theta = \arctan(4b_Z A f)$. The complex waveform is the result of combining two different sine waves ($y_S^\alpha(t)$ and $y_S^\beta(t)$) shaped by two different amplitudes (A_α and A_β), two phase shifts (p_α and p_β) and two frequencies (f_α and f_β).

6.2.2.1 DETERMINISTIC PROBLEM

As starting point, we want to observe the responses of the aquifer and the flow field topology assuming that all model inputs are known. Hence, there are four deterministic scenarios of one single deterministic transient flow problem, each applying one of the wave-shaped boundary conditions. The complex wave is defined by $A_\beta = 2A_\alpha/5$, $p_\beta = 3p_\alpha$ and $f_\beta = 3f_\alpha$ to satisfy symmetry relations between the periodic waves to match maximum (i.e., wave crest), minimum (i.e., wave through), temporal axis interceptions, and lag between two events. The trapezoidal wave is shaped considering $b_Z = 6$, so that the interval between minimum and maximum is equivalent to $1/12f$.

The spatial and temporal distribution of the groundwater heads and the Okubo-Weiss are analyzed with two-dimensional arrays. We are also interested in the variability of the groundwater head and the Okubo-Weiss metric at a certain distance $x_1/\mathcal{L}_1$ from the transient boundary conditions. Hence, we compute the variance in time at each discrete cell, and then the arithmetic mean of the variance relative to the distance $x_1/\mathcal{L}_1$. For simplicity we call $c_t^{i,j}$ the output of interest (i.e., groundwater heads or Okubo-Weiss metric) at a discrete cell with row i, and column j, at the time t, and follow

$$
\sigma_{i,j}^2 = \frac{1}{T} \sum_{t=1}^{T} \left(c_t^{i,j} - \mu_c^{i,j} \right)^2 , \qquad \mu_c^{i,j} = \frac{1}{T} \sum_{t=1}^{T} c_t^{i,j} ,
$$

(6.9)

where $\mu_c^{i,j}$ is the mean of the output of interest at a discrete cell $\{i,j\}$ along all the evaluation time T. Then, the arithmetic mean of the variances at the distance $x_1/\mathcal{L}_1$ can be computed along column $j \approx x_1/\mathcal{L}_1$, such that,

$$
\bar{\sigma}_j^2 = \frac{1}{n_i} \sum_{i=1}^{n_i} \sigma_{i,j}^2 ,
$$

(6.10)

being n_i the number of the discrete rows.

6.2.2.2 STOCHASTIC PROBLEM

We consider the amplitude A and phase p as uncertain parameters and we assume them as mutually independent random variables. On one hand, A represents the maximum water level in the stream, which fluctuates due to the variable discharges from the power plant, which in turn depends on market and seasonal

conditions. The uncertainty is defined from a minimum and maximum stage fluctuation that follows a uniform distribution $A \sim \mathcal{U}(a_A, b_A)$, where $a_A = 0.9$ and $b_A = 1.1$. On the other hand, p represents the shift in the stage signal. This random variable then introduces the temporal uncertainty due to changes in the gate management, turbine control and discharge duration. The random variable p is uniformly distributed, such that $p \sim \mathcal{U}(a_p, b_p)$. The parameters a_p and b_p describe the phase difference and relates the offset with f using a factor o_p, so that $a_p = -1/(o_p f)$ and $b_p = 1/(o_p f)$. This arrangement simplifies the application at multiple hydropeaking scale events (e.g., sub-daily, daily, and weekly) because any shift in the phase is a ratio of the periodicity. In our problem setup, we set $o_p = 8$, which is equivalent to a phase difference of $1/8f$.

In the case of the complex wave, the problem increases to 4 stochastic dimensions given that it is formed by the superposition of two sine waves $y_S^\alpha(t)$ and $y_S^\beta(t)$. Like in the deterministic problem, we keep the proportional relations between the two waves $y_S^\alpha(t)$ and $y_S^\beta(t)$ that form the complex wave and the random variables that are assumed mutually independent. Hence, two random variables $A_\alpha \sim \mathcal{U}(a_A^\alpha, b_A^\alpha)$ and $A_\beta \sim \mathcal{U}(a_A^\beta, b_A^\beta)$ represent the amplitudes, where $a_A^\alpha = a_A$, $b_A^\alpha = b_A$, $a_A^\beta = 2a_A^\alpha/5$ and $b_A^\beta = 2b_A^\alpha/5$. Also, two random variables $p_\alpha \sim \mathcal{U}(a_p^\alpha, b_p^\alpha)$ and $p_\beta \sim \mathcal{U}(a_p^\beta, b_p^\beta)$ represent the phase differences, where $a_p^\alpha = a_p$, $b_p^\alpha = b_p$, $a_p^\beta = a_p^\alpha/3$ and $b_p^\beta = b_p^\alpha/3$.

Scenario	Triangular wave	Sine wave	Complex wave	Trapezoidal wave
a) Deterministic				
Amplitude	$A = 1$	$A = 1$	$A_\alpha = 1$, $\quad A_\beta = \dfrac{2A_\alpha}{5}$	$A = 1$
Phase	$p = 0$	$p = 0$	$p_\alpha = 0$, $\quad p_\beta = 3p_\alpha$	$p = 0$
Frequency	$f = \dfrac{1}{80}$	$f = \dfrac{1}{80}$	$f_\alpha = \dfrac{1}{80}$, $\quad f_\beta = 3f_\alpha$	$f = \dfrac{1}{80}$
Trapezoid shape coefficient	–	–	–	$b_Z = 6$
b) Stochastic				
Amplitude	$A \sim \mathcal{U}(0.9, 1.1)$	$A \sim \mathcal{U}(0.9, 1.1)$	$A_\alpha \sim \mathcal{U}(0.9, 1.1)$, $\quad A_\beta \sim \mathcal{U}\left(\dfrac{2(0.9)}{5}, \dfrac{2(1.1)}{5}\right)$	$A \sim \mathcal{U}(0.9, 1.1)$
Phase	$p \sim \mathcal{U}\left(-\dfrac{1}{8f}, \dfrac{1}{8f}\right)$	$p \sim \mathcal{U}\left(-\dfrac{1}{o_p f}, \dfrac{1}{o_p f}\right)$	$p_\alpha \sim \mathcal{U}\left(-\dfrac{1}{o_p f_\alpha}, \dfrac{1}{o_p f_\alpha}\right)$, $\quad p_\beta \sim \mathcal{U}\left(-\dfrac{1}{3o_p f_\beta}, \dfrac{1}{3o_p f_\beta}\right)$	$p \sim \mathcal{U}\left(-\dfrac{1}{o_p f}, \dfrac{1}{o_p f}\right)$
Frequency	$f = \dfrac{1}{80}$	$f = \dfrac{1}{80}$	$f_\alpha = \dfrac{1}{80}$, $\quad f_\beta = 3f_\alpha$	$f = \dfrac{1}{80}$
Trapezoid shape coefficient	–	–	–	$b_Z = 6$
Phase coefficient	$o_p = 8$	$o_p = 8$	$o_p = 8$	$o_p = 8$

Table 6.1: Parameters used in the construction of the transient boundary conditions: (**a**) deterministic scenarios, and (**b**) stochastic scenarios.

In this work, we represent the dynamic system of the groundwater heads and flow topology as stochastic processes with uncertain boundary conditions using generalized polynomial chaos expansions. The statistical moments computed with the expansions and explained in the following section are also analyzed computing their arithmetic mean, analogous to Eq. 6.10. A summary of the specific parameters used in the deterministic and stochastic scenarios can be found in **Table 6.1**.

6.2.3 POLYNOMIAL CHAOS EXPANSION

6.2.3.1 STOCHASTIC FORMULATION

Let $(\Omega, \mathcal{F}, P)$ be a probability space, where Ω is a sample space, $\mathcal{F}$ is a σ-algebra on Ω, and P is a probability measure on Ω. Consider a function $u(t, x, \boldsymbol{\Phi})$ on the probability space $(\Omega, \mathcal{F}, P)$, where $\boldsymbol{\Phi} = [\Phi_1, \dots, \Phi_d] : \Omega \to \mathbb{R}$ is a random vector with a finite set of d mutually independent random variables with marginal probability density functions $\{\rho_{\Phi_i}(\varphi_i), i = 1, \dots, d\}$, and $\{t, x\}$ represent the deterministic temporal and spatial dependencies with a finite temporal horizon $t \in [0, T]$ within the spatial domain $\mathcal{D} \subset \mathbb{R}^2$ formed by fixed grid points $x = (x_1, x_2)$. Since each parameter $\Phi_i(\omega) : \Omega \to \mathbb{R}$ is associated to a density $\rho_{\Phi_i}(\varphi_i)$ and $\omega \in \Omega$ is a realization in the underlying probability space, we reformulate the problem in the image probability space $(\Gamma, \mathcal{B}(\Gamma), \rho_{\boldsymbol{\Phi}}(\varphi) d\varphi)$, where $\Gamma = \prod_{i=1}^d \Phi_i(\Omega)$ is the sample space for the range of Φ_i, $\mathcal{B}(\Gamma)$ is the Borel σ-algebra on Γ, and $\rho_{\boldsymbol{\Phi}}(\varphi)$ is the joint density associated with $\boldsymbol{\Phi}$, described by

$$\rho_{\boldsymbol{\Phi}}(\varphi) = \prod_{i=1}^d \rho_{\Phi_i}(\varphi_i). \tag{6.11}$$

The output function is then a random process $u(t, x, \boldsymbol{\Phi}) : [0, T] \times \mathcal{D} \times \Gamma \to \mathbb{R}$ with a finite variance. Following the generalized Cameron-Martin theorem (Cameron and Martin 1947), we can represent it as an infinite series expansion of polynomials, which can be truncated to order K, such that

$$\begin{aligned} u(t, x, \boldsymbol{\Phi}) &= \sum_{\boldsymbol{\kappa}=0}^{\infty} \hat{u}_{\boldsymbol{\kappa}}(t, x) \boldsymbol{\Psi}_{\boldsymbol{\kappa}}(\boldsymbol{\Phi}) \\ &\approx \sum_{\boldsymbol{\kappa}=0}^{K} \hat{u}_{\boldsymbol{\kappa}}(t, x) \boldsymbol{\Psi}_{\boldsymbol{\kappa}}(\boldsymbol{\Phi}), \end{aligned} \tag{6.12}$$

where $\hat{u}_{\boldsymbol{\kappa}}(t, x)$ are deterministic expansion coefficients, $\boldsymbol{\Psi}_{\boldsymbol{\kappa}}(\boldsymbol{\Phi})$ represent the multivariate orthogonal polynomial basis function, and $\boldsymbol{\kappa} = \{\kappa_1, \dots, \kappa_d\} \in \mathbb{N}_0^d$ is a multi-index of non-negative integers of size d to identify the degree of the polynomials for the input variable Φ_i. To achieve n order of polynomials, K can be optimally defined by $[(n + d)!/n! \, d!] - 1$ (Smith 2013; Xiu 2010), or by using experimental designs, such as the empirical rule $K = (d - 1) \times (n + 1)$ (Sudret 2008), to reduce the computational demand of the experiment. In this research, we define $K = 9$ and $n = 3$ for the triangular, sine and trapezoidal stochastic scenarios. The expansions in the complex scenario are calculated considering $K = 9$ and $n = 2$.

The orthogonal basis $\boldsymbol{\Psi}_{\boldsymbol{\kappa}}$ must be accordingly specified to $\rho_{\Phi_i}(\varphi_i)$ (Xiu and Karniadakis 2002). In this work, the uncertain input parameters associated to the boundary conditions $\boldsymbol{\Phi}$ are considered random variables uniformly distributed in the interval $[a, b]$, denoted by $\Phi_i \sim \mathcal{U}(a, b)$. An appropriate basis is formed by the family of Legendre polynomials, which are an orthogonal basis with respect to the weight function $\rho_{\Phi_i}(\varphi_i) = 1/2$ for all normalized $\varphi_i \in [-1, 1]$. Given the assumption that the random variables are mutually independent, the multivariate Legendre polynomial basis function $\boldsymbol{\Psi}_{\boldsymbol{\kappa}}(\boldsymbol{\Phi})$ can be defined as the tensor product of the associated univariate orthogonal polynomials ψ_{κ_i}, such that

$$\mathbf{\Psi_\kappa}(\mathbf{\Phi}) = \prod_{i=1}^{d} \psi_{\kappa_i}(\varphi_i) \,, \tag{6.13}$$

which satisfies orthonormality conditions given that

$$
\begin{aligned}
\mathbb{E}\big[\psi_{\kappa_i}, \psi_{\tau_i}\big] &= \int_\Gamma \psi_{\kappa_i}(\varphi_i)\psi_{\tau_i}(\varphi_i)\rho_{\Phi_i}(\varphi_i)d\varphi_i \\
&= \langle \psi_{\kappa_i}, \psi_{\tau_i} \rangle_\rho \\
&= \delta_{\kappa_i \tau_i} \,,
\end{aligned}
\tag{6.14}
$$

where $\langle \cdot, \cdot \rangle$ denotes the inner product of the sequence of two polynomials $\{\psi_{\kappa_i}, \psi_{\tau_i}\}$ of degree κ_i and τ_i in the ith variable, $\delta_{\kappa_i \tau_i}$ represents the Kronecker delta. The deterministic coefficients $\hat{u}_\kappa(t, x)$ can be approximated by exploiting the orthonormality of the basis function and projecting $u(t, x, \mathbf{\Phi})$ onto each basis function $\mathbf{\Psi}_k(\mathbf{\Phi})$ to obtain the representation

$$\hat{u}_\kappa(t, x) = \langle u(t, \mathrm{x}, \mathbf{\Phi}), \mathbf{\Psi_\kappa}(\mathbf{\Phi}) \rangle_\rho = \int_\Gamma u(t, x, \mathbf{\Phi})\mathbf{\Psi_\kappa}(\mathbf{\Phi})\rho_\mathbf{\Phi}(\varphi)d\varphi \,. \tag{6.15}$$

6.3.2 *PSEUDOSPECTRAL COLLOCATION APPROACH*

We use the pseudospectral approach as a solution technique to estimate multidimensional integral that describes $\hat{u}_\kappa(t, x)$. It is a discrete collocation method that relies on quadrature techniques to calculate $\hat{u}_\kappa(t, x)$ at selected quadrature nodes $\mathbf{g^q} = \{g_1^{q_1}, \dots, g_d^{q_d}\} \in \mathbb{R}$ defined on Γ with the associated weights $w_\mathbf{q} = \{w_{q_1}, \dots, w_{q_d}\} \in \mathbb{R}$. Therefore, the deterministic solvers that describe the groundwater flow and the topological responses of the aquifer are not modified (i.e., non-intrusive spectral projection) because it is only required to evaluate $u(t, x, \mathbf{g^q})$ at the given $\mathbf{g^q}$. We employ Gaussian quadrature rules (Golub and Welsch 1969) over a full tensor product grid to distribute $\mathbf{g^q}$ according to the probability density functions $\rho_{\Phi_i}(\varphi_i)$. Using Q to represent the quadrature integration, the extension of the univariate Gaussian quadrature yields to the summation over all possible combinations over m_i nodes

$$
\begin{aligned}
Q[u(t, x, \cdot)] &= \big(Q_{m_1} \otimes \dots \otimes Q_{m_d}\big)[u(t, x, \cdot)] \\
&= \sum_{q_1=1}^{m_1} \dots \sum_{q_d=1}^{m_d} u\big(t, x, g_1^{q_1}, \dots, g_d^{q_d}\big) w_{q_1} \dots w_{q_d} \,,
\end{aligned}
\tag{6.16}
$$

that can be recast for the sake of simplicity to the multi-index approximation

$$\hat{u}_\kappa(t, x) \coloneqq Q[u(t, x, \cdot)\mathbf{\Psi_\kappa}(\cdot)] = \sum_{\mathbf{q}=1}^{M} u(t, x, \mathbf{g^q})\mathbf{\Psi_\kappa}(\mathbf{g^q})w_\mathbf{q} \,, \tag{6.17}$$

where the total number of grid points is $M = m^d$ given that we opt for $m_1 = \dots = m_d = m$.

The expected value of $u(t, x, \mathbf{\Phi})$ can be estimated from the polynomial chaos coefficients $\hat{u}_0(t, x)$, given that

$$\mu = \mathbb{E}[u(t,x,\boldsymbol{\Phi})] \approx \mathbb{E}\left[\sum_{\kappa=0}^{K} \hat{u}_{\kappa}(t,x)\boldsymbol{\Psi}_{\kappa}(\boldsymbol{\Phi})\right]$$

$$= \hat{u}_0(t,x)\mathbb{E}[\boldsymbol{\Psi}_0(\boldsymbol{\Phi})] + \sum_{\kappa=1}^{K} \hat{u}_{\kappa}(t,x)\mathbb{E}[\boldsymbol{\Psi}_{\kappa}(\boldsymbol{\Phi})] \tag{6.18}$$

$$= \hat{u}_0(t,x).$$

Similarly, the variance $\sigma^2 = \mathbb{V}[u(t,x,\boldsymbol{\Phi})]$ and the standard deviation $\sigma = \sqrt[2]{\mathbb{V}[u(t,x,\boldsymbol{\Phi})]}$ are quantified following

$$\sigma^2 = \mathbb{V}[u(t,x,\boldsymbol{\Phi})] = \mathbb{E}[(u(t,x,\boldsymbol{\Phi}) - \mathbb{E}[u(t,x,\boldsymbol{\Phi})])^2]$$

$$\approx \mathbb{E}\left[\left(\sum_{\kappa=0}^{K} \hat{u}_{\kappa}(t,x)\boldsymbol{\Psi}_{\kappa}(\boldsymbol{\Phi}) - \hat{u}_0(t,x)\right)^2\right]$$

$$= \mathbb{E}\left[\left(\sum_{\kappa=1}^{K} \hat{u}_{\kappa}(t,x)\boldsymbol{\Psi}_{\kappa}(\boldsymbol{\Phi})\right)^2\right] \tag{6.19}$$

$$= \sum_{\kappa=1}^{K} \hat{u}_{\kappa}^2(t,x)\boldsymbol{\Psi}_{\kappa}.$$

6.2.4 OKUBO-WEISS

We consider a flow deformation metric based on a two-dimensional velocity gradient tensor, ϵ

$$\epsilon(t) = \nabla v(x,y,t), \tag{6.20}$$

where $v(x,y,t)$ is the velocity at the space coordinates x and y at time t and it is estimated with the calculated head gradient by solving **Error! Reference source not found.**.

The Okubo-Weiss function (Okubo, 1970; Weiss, 1991) is defined by

$$\xi = -4\det(\epsilon), \tag{6.21}$$

which in the horizontal plane with coordinates x and y is written as

$$\xi = -4\det\begin{bmatrix} \dfrac{\partial v_x}{\partial x} & \dfrac{\partial v_x}{\partial y} \\ \dfrac{\partial v_y}{\partial x} & \dfrac{\partial v_y}{\partial y} \end{bmatrix}. \tag{6.22}$$

We take the definition used by Okubo (1970) for stretching deformation $\hat{\alpha}$, vorticity $\hat{\omega}$, and shear deformation $\hat{\sigma}$

$$\hat{\alpha} = \frac{\partial v_x}{\partial x} - \frac{\partial v_y}{\partial y}, \qquad \hat{\omega} = \frac{\partial v_y}{\partial x} - \frac{\partial v_x}{\partial y}, \qquad \hat{\sigma} = \frac{\partial v_y}{\partial x} + \frac{\partial v_x}{\partial x}. \tag{6.23}$$

By substituting Equation 6.23 into Equation 6.22, and following de Barros et al. (2012), in which for a two-dimensional transport scenario $\frac{\partial v_x}{\partial x} = -\frac{\partial v_y}{\partial y}$, and therefore stretching deformation $\hat{\alpha} = 2\frac{\partial v_x}{\partial x}$, the deformation tensor can be then rewritten as

$$\epsilon = \frac{1}{2}\begin{pmatrix} \hat{\alpha} & \hat{\sigma} - \hat{\omega} \\ \hat{\sigma} + \hat{\omega} & -\hat{\alpha} \end{pmatrix},$$
(6.24)

and the Okubo-Weiss function ξ [1/T^2] is calculated by

$$\xi = (\hat{\alpha}^2 + \hat{\sigma}^2) - \hat{\omega}^2 \,.$$
(6.25)

Positive Okubo-Weiss values, $\xi > 0$, correspond to regions where shear and stretching forces dominate, and are associated to mixing hotspots (Engdahl et al., 2014; Wright et al., 2017). On the other hand, negative values, $\xi < 0$, correspond to regions dominated by vorticity and local mixing potential is low.

6.3 RESULTS AND DISCUSSION

6.3.1 DETERMINISTIC SCENARIOS

Figure 6.1 shows the spatial effect of the waveform on the groundwater heads at specific time steps $\tau/T \in \{60,80,86,100\}$. Steeper hydraulic gradients are observed in the trapezoidal wave, which significantly impact the flow field magnitude. These gradients occur in the trapezoidal wave due to two reasons. First, this wave exposes longer intervals of constant head at the wave crest and wave through. Second, the trapezoidal wave presents a sharp fluctuation from minimum to maximum stage. Furthermore, the behavior of the sine scenario is very similar to the triangular one. As expected, the porous medium acts as a damper that gradually moderates the propagation of groundwater head signals, converting all of them to sinusoidal patterns after travelling a certain distance and later vanishing them (see **Figure 6.2**). The dampening depends on the value of the hydraulic conductivity in accordance with the analytical solution for the head response in the semi-infinite aquifer presented by Singh (2004) and Sawyer et al., (2009) for the case of a homogeneous porous medium.

The outcomes from the deterministic scenarios show some remarkable differences in the mean variance of the groundwater heads and the Okubo-Weiss. In Figure 6.3a, we observe a larger $\bar{\sigma}_h^2$ from the trapezoidal wave scenario, followed by the complex wave scenario, which is also very similar to the sine one. This occurs due to the flux variations and the groundwater gradient differences among the cases. We also observe that the behavior of the four scenarios is very similar after $x_1/\mathcal{L}_1 = 40$ and that $\bar{\sigma}_h^2 \to 0$ after $x_1/\mathcal{L}_1 = 60$. Figure 6.3b shows the mean variance in the results of the Okubo-Weiss metric. We see that ξ may vary by several orders of magnitude depending on the wave used as boundary condition. Similar to $\bar{\sigma}_h^2$, we see larger variations in $\bar{\sigma}_\xi^2$ in the trapezoidal and complex scenarios.
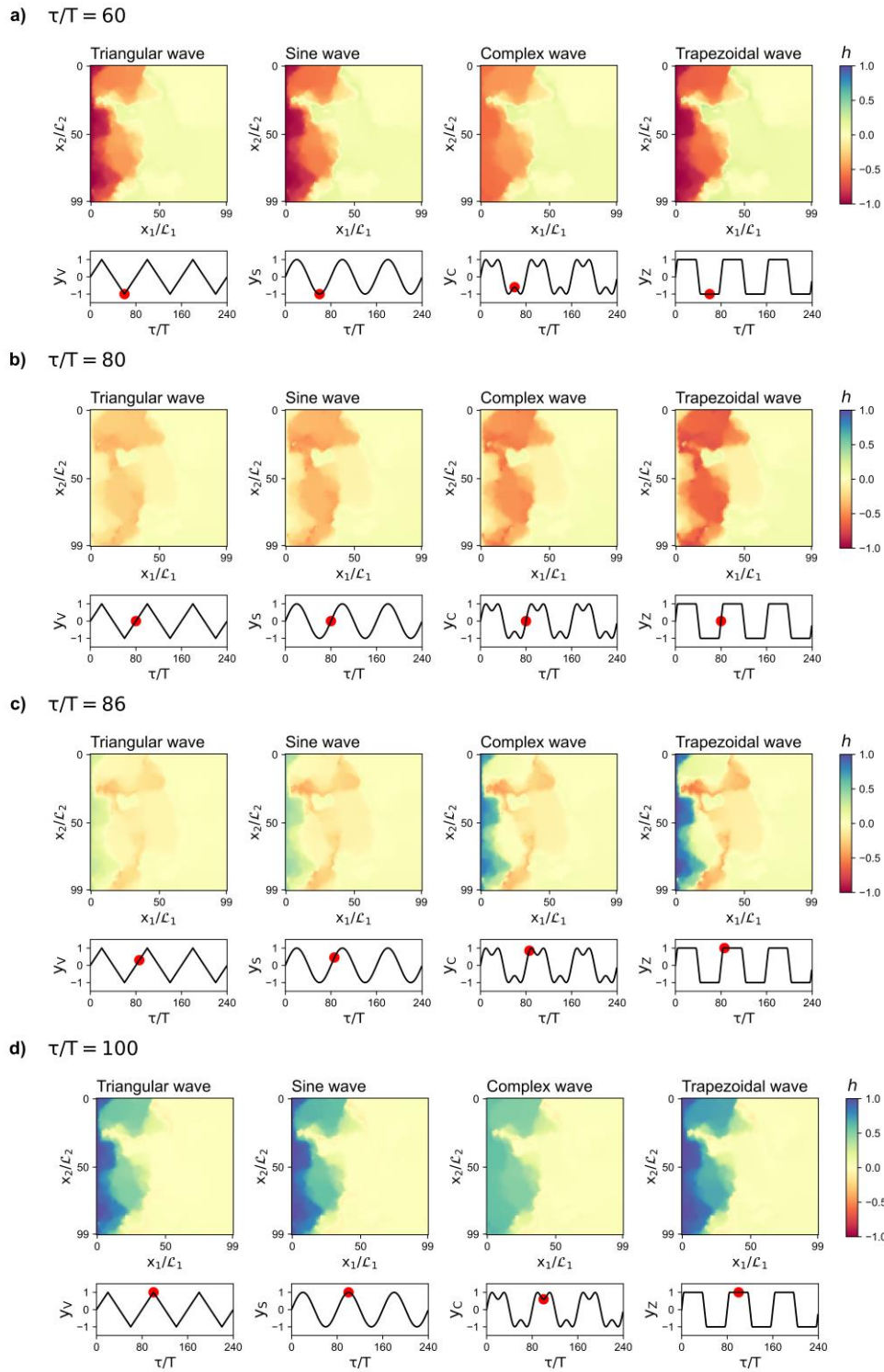
Figure 6.1: Groundwater head responses at different time steps: (**a**) τ/T=60, (**b**) τ/T=80, (**c**) τ/T=86, and (**d**) τ/T=100. The colored maps show the distribution of the groundwater heads, and the graph plot shows the imposed boundary conditions. The red dots show the time steps at which the snapshots were taken.

We show the spatial and temporal pattern of the Okubo-Weiss metric in **Figure 6.4**. We observe regions where the Okubo-Weiss metric is very high $\xi > 0.1e^{-6}$, when the flow is dominated by stretching and strain and very low $\xi < -0.1e^{-6}$, when vorticity dominates. These regions correspond to areas of high hydraulic conductivity and high conductivity contrasts (see **Figure 6.1**b), where also flow focusing may occur. Hence, the location of these spots is fully controlled by the configuration of heterogeneous field in all the scenarios. In temporal terms,

the most remarkable discrepancies in ξ among the four scenarios occur during the sharp ramp upwards and the sharp drop of the trapezoidal wave. In a lower magnitude, this is also visible in the complex wave. Highest positive and lower negative values of ξ are found in these two scenarios. Furthermore, it is possible to observe cells changing from positive ξ to negative ξ, and vice versa, in all the scenarios. This can be observed before and after the apexes of the trapezoidal wave (**Figure 6.4**b and **Figure 6.4**c), the peak of the triangular wave (**Figure 6.4**c and **Figure 6.4**d), the local maximum and local minimum of the complex wave (**Figure 6.4**b and **Figure 6.4**c). This swap of dominance is transitory and can be repeatedly observed in all the scenarios at critical points of the wave-shaped boundaries, such as stationarity points (i.e., constant value), inflection points, local maxima, and local minima. This could occur due to flow reversal caused by the deacceleration of the transient boundary signal into the aquifer. Overall, this behavior gives evidence of the waveform's role in the temporal dynamics of the topology of the flow field.
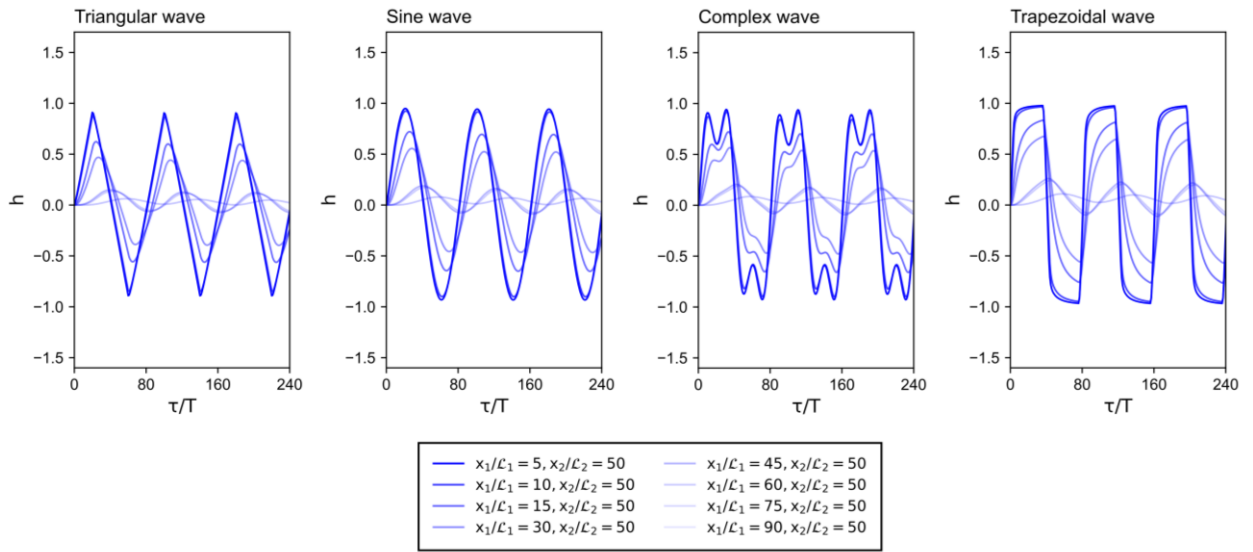
Figure 6.2: Dampening of the head signals from the different scenarios. The groundwater head values are extracted at various distances from the wave-shaped boundaries, $x_1/\mathcal{L}_1 \in \{5,10,15,30,45,60,75,90\}$, at the middle of the domain $x_2/\mathcal{L}_2 = 50$
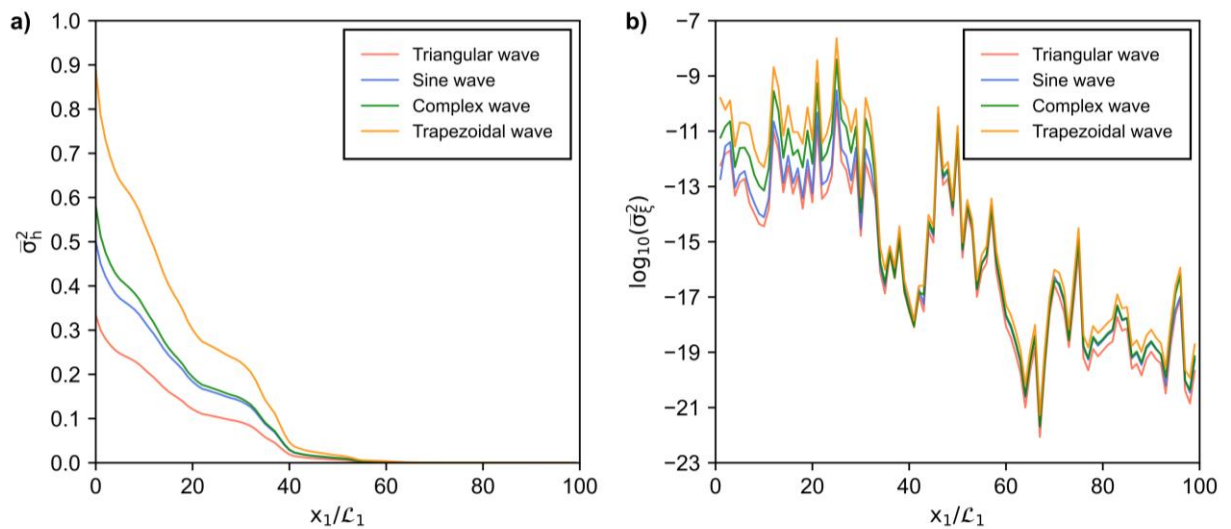
Figure 6.3: Spread of deterministic results at different distances $x_1/\mathcal{L}_1$ from the boundary conditions: (**a**) mean variance of the groundwater heads $\bar{\sigma}_h^2$, and (**b**) logarithm of the mean variance of the Okubo-Weiss $\bar{\sigma}_\xi^2$
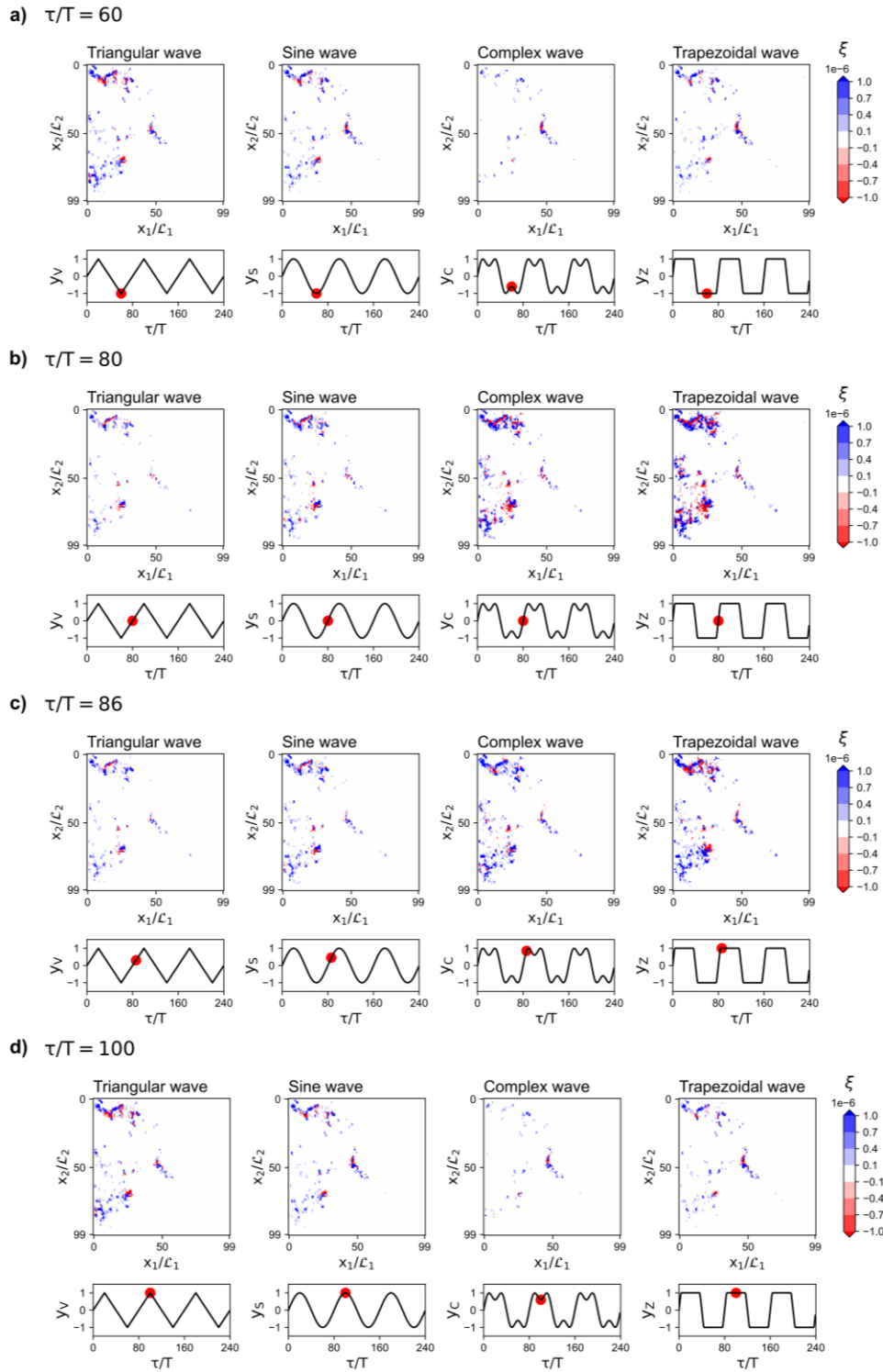
Figure 6.4: Okubo-Weiss values at different time steps: (**a**) $\tau/T = 60$, (**b**) $\tau/T = 80$, (**c**) $\tau/T = 86$, and (**d**) $\tau/T = 100$. The colored maps show the distribution of the groundwater heads, and the graph plot shows the imposed boundary conditions. The red dots show the time steps at which the snapshots were taken.

6.3.2 STOCHASTIC SCENARIOS

The uncertainty in the amplitude and phase of the waves propagates in the groundwater head following different patterns (see **Figure**). The results of μ_h are similar to the results of h in the deterministic scenarios. Regarding the standard deviation, in **Figure**a, we see at $\tau/T = 60$ that all scenarios present similar snapshots, with slightly higher σ_h close to the left boundary for the triangular wave. In contrast, in **Figure**b, a significant difference in σ_h can be observed at $\tau/T = 80$ in the complex and trapezoidal wave as compared to the triangular and sine waves. This time step corresponds to the change between low and high river stage.
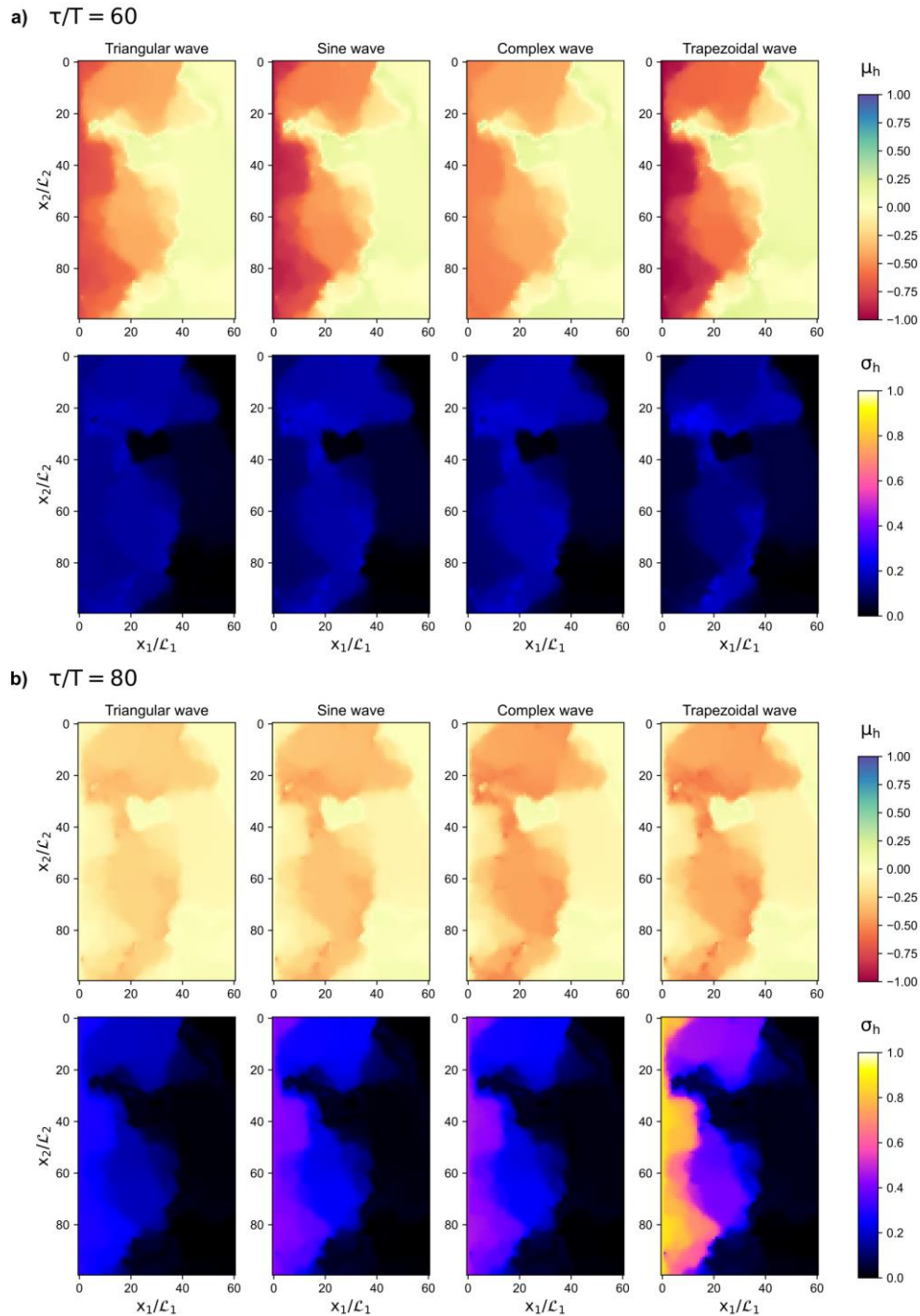
Figure 6.5: Propagation of the uncertainty into the groundwater head responses represented by the expected value μ_h and the standard deviation σ_h into the groundwater head responses at (**a**) $\tau/T = 60$, and (**b**) $\tau/T = 80$

We also computed the probability density functions from the output expansions of the groundwater heads. The results are shown in **Figure 6.5**. We observe small uncertainties at high and low values of the groundwater heads, which are depicted by the high occurrence values in the probability density functions, when $\tau/T = 60$ and $\tau/T = 100$ (see **Figure 6.5**a and **Figure 6.5**c). Larger uncertainties are observed when $\mu_h \approx 0$, when $\tau/T = 80$ (see **Figure 6.5**b). These behaviors occur in all the scenarios. However, two peaks of high probability are observed in **Figure 6.5**b in the trapezoidal scenario due to the rapid fluctuation of the heads in the transient boundary conditions. The trapezoidal scenario also shows the smallest uncertainty at $\tau/T = 60$ and $\tau/T = 100$, because of the low influence of the phase uncertainty in the points where the heads in the boundaries are constant (i.e, minimum and maximum).
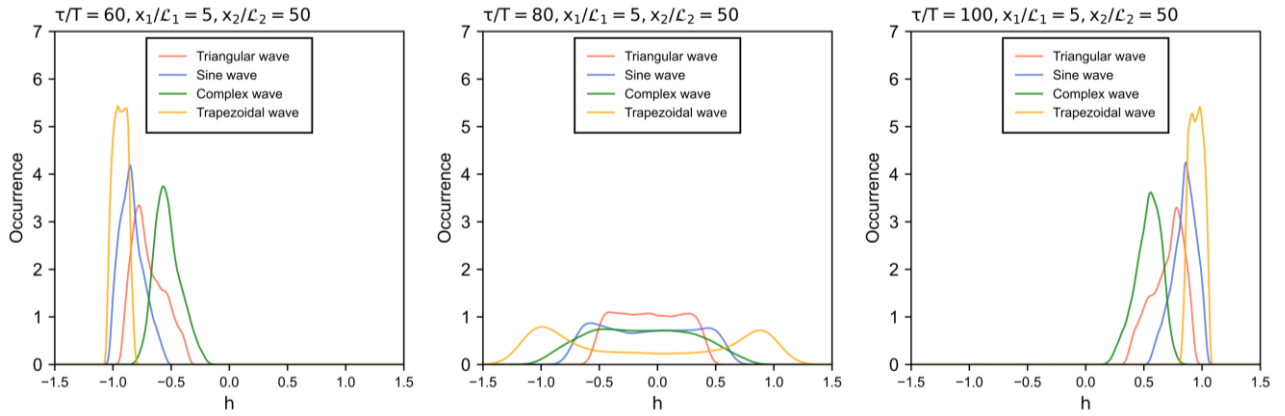

Figure 6.5: Posterior probability density functions of the groundwater heads at $\tau/T \in \{60, 80, 100\}$ at specific location $x_1/\mathcal{L}_1 = 5$ and $x_2/\mathcal{L}_2 = 50$

The influence of the uncertain transient boundary conditions is also reflected in the Okubo-Weiss values shown in **Figure 6.6**. As expected, the spots with large uncertainty appear in the regions with high hydraulic conductivity contrast and large hydraulic conductivity. Specifically, we allocate large uncertainties in the complex and trapezoidal scenarios at $\tau/T = 80$ (**Figure 6.6**b). This is a consequence of the large uncertainty in the groundwater heads observed previously (**Figure**b), which occur due to the effect of the phase shift over the sharp movements in the boundary conditions. The steepness of the slopes in these waves creates a wide range of variability when we introduced the offset uncertainty. Moreover, the magnitude of the μ_ξ values vary depending on the scenario, finding larger values in the trapezoidal and complex scenarios. Similar to the outcomes of the deterministic scenarios, the results of μ_ξ also reveal spots with variable dominances of the deformation and rotational forces of the flow field.

The responses of both h and ξ, as well as the statistics that define their uncertainty, follow periodic patterns. To evaluate the average behavior of the statistics of h and ξ at a certain distance from the boundaries and their differences, we chose a relatively close distance to the stream, at distance $\lambda/2$ (i.e., $x_1/\mathcal{L}_1 = 5$), where the propagation of the signal is clear. We computed the arithmetic means of the uncertainty statistics at a distance $x_1/\mathcal{L}_1 = 5$, which are shown in **Figure 6.7**. We see that $\bar{\mu}_h$ is highly fluctuating in the trapezoidal and the complex scenario. Moreover, according to the interval $[\bar{\mu}_\xi - \bar{\sigma}_\xi, \bar{\mu}_\xi + \bar{\sigma}_\xi]$, the trapezoidal scenario exhibits the highest uncertainty in ξ, followed by the complex wave. The results also indicate that it is more likely to find rotation properties dominating in the flow field under the trapezoidal scenario conditions than to find them under the conditions of the other scenarios. On the other hand, we see smaller variability of $\bar{\sigma}_h$ and $\bar{\sigma}_\xi$ in the sine wave scenario, showing a similar spread in the outputs along the whole simulation period. While the behavior of the triangular wave is similar to the sine wave, the complex wave is comparable with the trapezoidal wave.
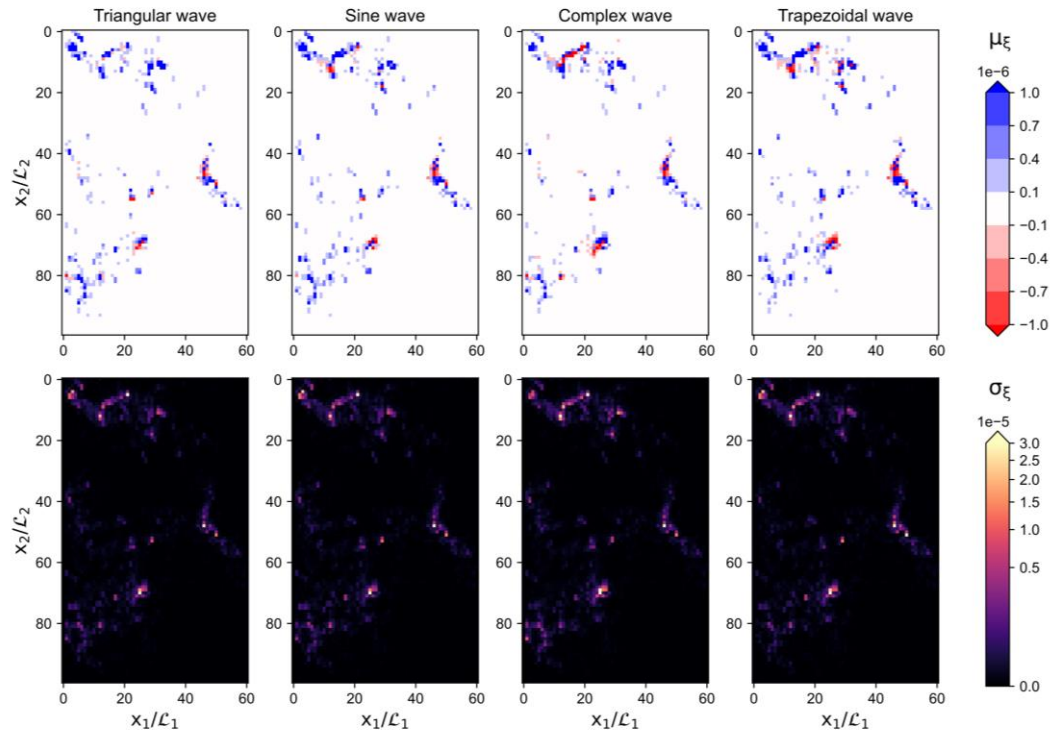
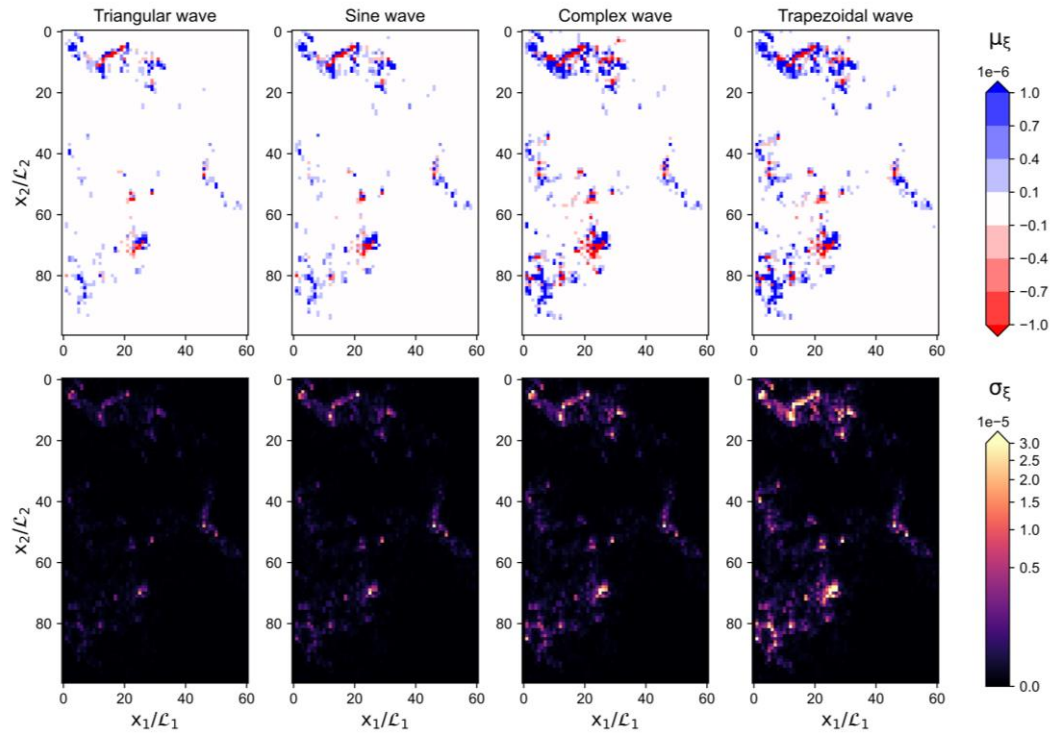**Figure 6.6:** Propagation of the uncertainty into the Okubo-Weiss metric represented by the expected value μ_h and the standard deviation σ_h into the groundwater head responses at different times.
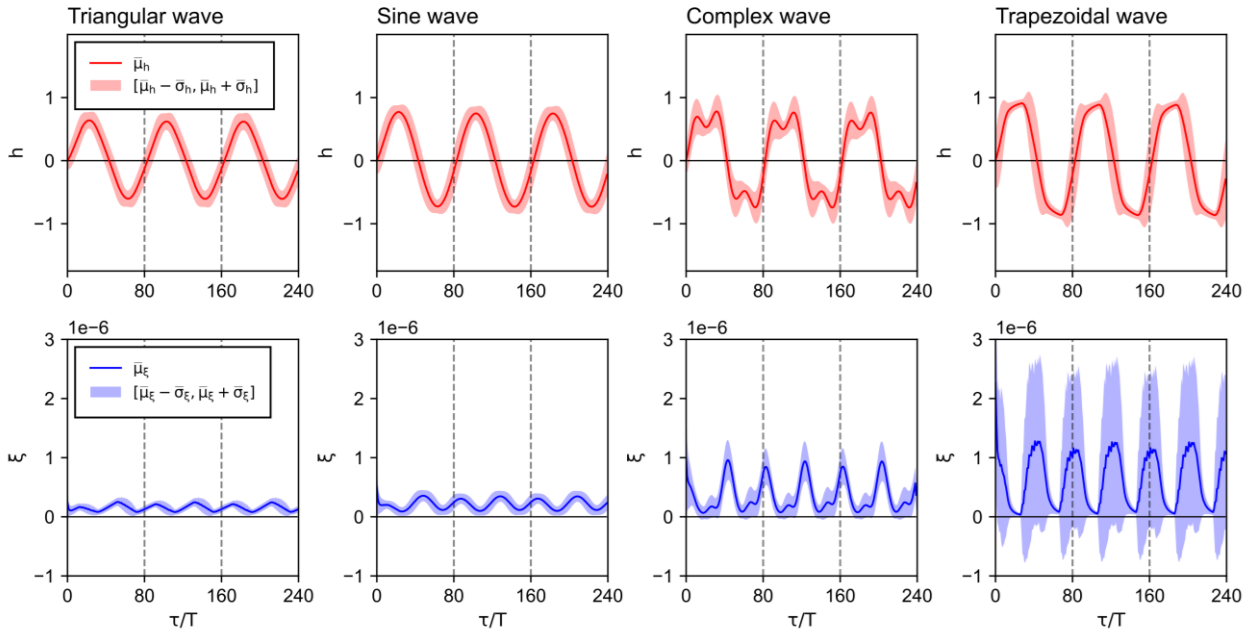
Figure 6.7: Uncertainty propagation into the groundwater heads and the Okubo-Weiss metric at a distance $\lambda/2$ from the boundary conditions ($x_1/\mathcal{L}_1 = 5$): (**a**) mean expected value of the groundwater heads and interval $[\bar{\mu}_h - \bar{\sigma}_h, \bar{\mu}_h + \bar{\sigma}_h]$, and (**b**) mean expected value of the Okubo-Weiss metric and interval $[\bar{\mu}_\xi - \bar{\sigma}_\xi, \bar{\mu}_\xi + \bar{\sigma}_\xi]$.

Overall, our results from the deterministic and stochastic scenarios show that wave-shaped boundary conditions can influence not only the magnitude of the deformation and rotational forces of the flow field (i.e., shear, stretching, and vorticity) but also the temporal dynamics of dominance between local strain and rotation properties. Although our results show that their location is determined by the areas with high hydraulic conductivity contrast, as can be seen in **Figure 6.1**b, we provide evidence that the mixing potential in these areas is significantly affected by highly transient boundary conditions. This occurs due to the variety of hydraulic gradient responses as a consequence of the highly fluctuating head boundary conditions. To observe in detail the temporal variation and the two-dimensional distribution of the groundwater heads, the Okubo-Weiss values, and the statistical moments that describe the uncertainty, we refer to a series of videos included as part of the Supplementary Material of this research.

6.4 CONCLUSIONS

We studied the effect of the periodic stage conditions due to hydropeaking events on the groundwater flow topology in terms of the Okubo-Weiss metric. We imposed Dirichlet boundary conditions in the form of wave-shaped specified-heads with four types of waveforms: triangular, sine, complex, and trapezoidal. The formulation of the system considers a deterministic solution of the heterogeneous hydraulic conductivity field for all the scenarios. The first part of our analysis was done assuming no input uncertainty over the four waves that define the transient boundary conditions. The second part of the study approached the problem as a stochastic system with uncertainty in the parameterization of the transient boundary conditions. Here, the wave amplitude and phase were considered uncertain and treated as mutually independent random variables. These variables introduced the uncertainty related to unknown fluctuations in the discharge volume and discharge duration and temporal uncertainty due to energy market demands and powerplant management. The application of polynomial expansions and pseudo-spectral collocation method allowed us to estimate the statistical moments

(i.e., mean, and standard deviation) of the outputs of interest (i.e., groundwater heads and Okubo-Weiss metric). The method was convenient to extract the required spatial and temporal detail with low computational effort.

One of the main messages that the Okubo-Weiss metric can provide us is the identification of reaction hotspots. The spatial distribution of the Okubo-Weiss responses is fundamentally controlled by the hydraulic conductivity. In accordance, our results show that their location is determined by the areas with high hydraulic conductivity contrast. However, we also provide evidence that the mixing potential in these areas is significantly affected by the highly transient boundary conditions. The magnitude and temporal behavior of this topological indicator of mixing significantly vary according to the impose boundary conditions. Different highly transient boundary conditions influenced in different degree the temporal dynamics of dominance between local strain and rotation properties and the magnitude of the deformation and rotational forces of the flow field. Therefore, given the dynamic responses of the flow field to the time-variant head boundary conditions, the detailed temporal characterization of this metric is important to reliably predict, for instance, mixing-driven reactions.

The evaluation of hydropeaking impacts on subsurface flow requires to characterize the management of the surface water system and the intensity of the impact (e.g., shape, amplitude, and periodicity of the wave). Hence, we think it is essential to estimate hydropeaking effects on flow and transport processes in aquifers using a stochastic approach, not only due to the essential uncertainty in the aquifer heterogeneity but also due to the uncertain stream stages. The statistical moments that describe the propagation of the uncertainty show a periodic behavior and a varying degree of uncertainty depending on the applied wave-shaped boundary. Further work should focus on the characterization of real hydropeaking events to explicitly acknowledge the inherit uncertainty of these systems and its effect in the estimation of topological descriptors.

Chapter 7

Wavelet analysis on surface water - groundwater

interactions

Abstract

Management of hydropower plants strongly influences streamflow dynamics and hence the interaction between surface water and groundwater. As dam operations cause variations in river stages, these can result in changes in the groundwater level at multiple temporal scales. In this work, we study the case of an Alpine aquifer, where weekly fluctuations are particularly pronounced. We consider an area with four river reaches differently impacted by reservoir operations and investigate the influence of these rivers on the common aquifer. Using continuous wavelet transform and wavelet coherence analysis, we show that weekly fluctuations in the groundwater table are particularly pronounced in dry years, in particular in the winter season, although the area of the aquifer impacted by dam operations remains almost unchanged. We thus observe that in Alpine catchments, surface water-groundwater interaction is sensitive to the conditions determined by a specific hydrological year. We also investigate the influences of the river-aquifer water fluxes and show that under dry conditions hydropeaking mainly affects their temporal dynamics. Our observations have significant consequences for predicting nutrient and temperature dynamics/regimes in river-aquifer systems impacted by hydropower plant management.

7.1 INTRODUCTION

Montanari et al. (2015) stated that "The interaction between human and water systems needs to be analyzed from new perspectives to develop a comprehensive picture of the inherent feedbacks and coevolving processes and scenarios." One of the most prominent examples of such interaction is hydropower production and the feedback processes that it generates on the natural environment (Hauer et al. 2017a), including sediment transport (Béjar et al. 2018; Hauer et al. 2019), biological process in the riverine environment (Bejarano et al. 2018; Bruno et al. 2009; Person 2013), the hydrological cycle (Shuai et al., 2019; Yellen & Boutt, 2015), biogeochemical processes (Graham et al. 2019), energy cycle (Wu et al., 2020), and surface water – groundwater interaction (Sawyer et al., 2009; Shuai et al., 2017). For instance, hydropeaking, i.e., sharp fluctuations in the river stage caused by the management of storage hydropower plants, has important consequences on flow and transport processes in rivers. Furthermore, it can also influence the aquifers even 100 km downstream from the hydropower dam (Ferencz et al., 2019) and tens of meters far from the river (Sawyer et al., 2009; Zachara et al., 2016; Zachara et al., 2020), including riverine islands (Francis et al., 2010).

Surface water-groundwater interaction is affected by the morphological characteristics of the riverbed (Schmadel et al., 2017; Singh et al., 2019; Wu et al., 2018) and the subsurface (Shuai et al., 2019), as well as by seasonal hydrological variability. For example, hydropeaking is stronger during dry periods (Li & Pasternack, 2021) or more in general low flow conditions (Chiogna et al. 2018a). In this sense, Song et al. (2018) illustrated how the effect of dam operations on the aquifer system depends on drought conditions of the catchment using numerical simulations. They also showed that to describe surface water-groundwater interaction it is important to consider the complex feedback between hydrological processes and water management.

Several studies have focused on surface water-groundwater interaction under altered streamflow conditions in different regions, such as the Colorado River (Francis et al., 2010; Sawyer et al., 2009), and the Deerfield River (Boutt and Fleming 2009; Yellen and Boutt 2015) in the USA, the Cockburn River in Australia (McCallum and Shanafield 2016; Welch et al. 2013), the Danube River in the Austrian part (Derx et al. 2010), and the Lundesokna River in Norway (Casas-Mulet et al., 2015), as well as synthetics models (e.g., Ferencz et al., 2019; Schmadel et al., 2016). These studies have addressed mainly the hydrological and geochemical interaction between surface water and the hyporheic zone or its proximity. At larger spatio-temporal scales, recent works in the Columbia River analyzed the effect of the river fluctuations on exchange flows and contaminant plumes along the river reach (Shuai et al., 2019) and the river corridor (Rizzo et al., 2020; Song et al., 2020; Zachara et al., 2016; Zachara et al., 2020). Little research on surface water-groundwater interaction has been done on Alpine aquifers, with exceptions such as Fette et al. (2007) who studied the upper Rhône River. In Alpine catchments, variability with a period of seven days is particularly relevant for hydrological studies focusing on water management because it represents the lower energy production typically occurring over weekends (Chiogna et al., 2018; Majone et al., 2016; Pérez Ciria et al., 2019). Furthermore, this periodic signal can propagate in the aquifer farther than the sub-daily fluctuations (Sawyer et al., 2009; Singh, 2004).

The aim of our work is to analyze the impact of fluctuations caused by dam operations on the groundwater considering the propagation of the weekly signal and its evolution in time and to observe how this changes in two different hydrological years (i.e., a wet and a dry year). Specifically, we study the Adige Valley aquifer, which is affected by several rivers impacted by hydropower operations. This area represents a typical scenario in Alpine catchments, where multiple regulated rivers can converge in relatively narrow valleys (Pérez Ciria et al., 2019).

In this paper, we develop a transient groundwater flow model to capture the aquifer's response to streamflow alterations with a weekly periodicity since observations with high spatio-temporal resolution are hardly available for large (i.e., greater than 10km^2) aquifers. We compare two different hydrological conditions corresponding to the hydrological years 2009/10 and 2016/17. The first one represents a typical year in terms of temperature and

precipitation. The latter is characterized by a drought caused by the lack of winter precipitation, which leads to low summer streamflow conditions (Chiogna et al. 2018b). We introduce the use of wavelet maps to analyze the coherence between weekly signal in the rivers and the whole modeled aquifer. The variability in the environmental and hydrological conditions encountered in this case study helps to validate this methodology for its application to other scenarios.

Wavelet analysis is a powerful tool to investigate non-stationary periodicities in hydrological time series. It has been applied to study time series in different (hydro)geological systems (Lu et al., 2015; Song et al., 2020; Tenorio-Fernandez et al., 2019; Wright et al., 2015), and more recently in the context of surface water-groundwater interaction to study hyporheic exchange flows (Chen et al. 2022). In this study, we apply the continuous wavelet transform (Torrence & Compo, 1998) and the wavelet coherence analysis (Grinsted et al., 2004) for three river discharge time series of the Adige catchment with different degrees of alteration under the same climatic and geologic conditions. As most of the large scale studies on surface water-groundwater interaction focus on a single river-aquifer system (Zachara et al., 2016; Song et al., 2018, Ferencz et al., 2019; Francis et al., 2010), this is one of the first works including such complex hydrological system where multiple impacted rivers exchange water with the same aquifer.

The manuscript is organized in the following way: Section 7.2 describes the study area and the used dataset. Section 7.3 introduces the modeling approach. In Section 7.4, we describe the continuous wavelet transform and wavelet coherence analysis, and explain how we apply them to create the wavelet maps. Section 7.5 shows through a wavelet transform analysis how the aquifer is affected by water management and the consequences on the surface-water groundwater flux exchange in a wet and a dry year. In Sections 7.6 and 7.7, we discuss the implication of our results and, finally present the conclusions of our research study, respectively.

2.2 STUDY AREA

The study site is located within the Adige catchment, in the northeast of Italy. It covers an area of about 30 km², which includes the Adige aquifer in the north of Trento (Figure 7.1). The area is traversed by the Adige River and two important tributaries: the Noce River and the Avisio River. These rivers, in particular the Noce and the Adige, are impacted by the operation of hydropower plants. In fact, the Adige catchment provides water for 34 hydropower plants and approximately 1050 small hydropower plants are distributed within the river basin (Chiogna et al., 2016). The region's climate is sub-alpine, composed of dry winters, snowmelt in spring, and humid summers leading to well-suited conditions for hydropower production in the Adige River basin (Chiogna et al., 2016; Perez Ciria et al., 2019). The long-term mean annual precipitation is 1022 mm (Castagna et al., 2015), and the mean seasonal temperature in the valley varies between -4°C in winter and 29 °C in summer.
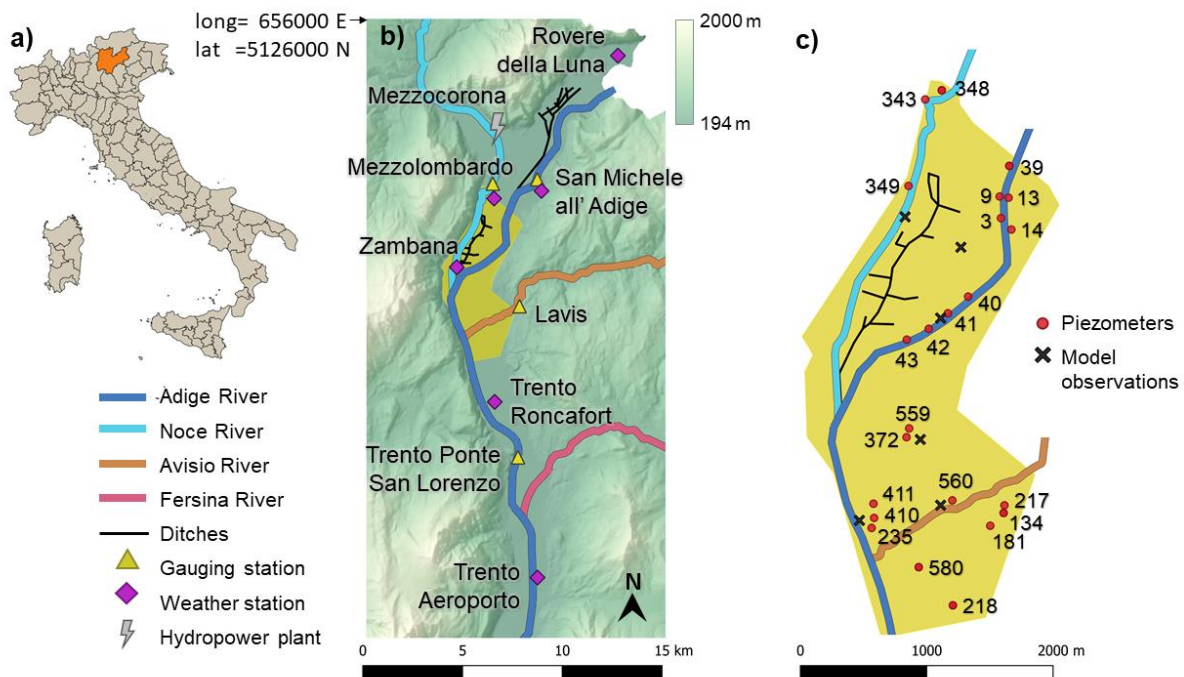
Figure 7.1: (**a**) Map of Italy with Trentino highlighted; (**b**) close-up to the Adige Valley with the modeled area highlighted in yellow and (**c**) modeled area, also depicting the locations of piezometers and model observations used in the presented study.

The geology of the Adige Valley is characterized by a multilayer aquifer system of sandy-gravelly material, interconnected with sandy-silty layers in-between (Autorità di Bacino del Fiume Adige 2007). The main shallow phreatic aquifer is a semiconfined aquifer with a maximum thickness that varies between 50 and 60 meters (Autorità di bacini distrentualle delle Alpi Orientali 2010; Viesi et al. 2016). Quaternary deposits present in the valley mainly consist of fine material, and lateral and alluvial fans from the tributaries of the Adige River, composed of sandy-gravelly material with a hydraulic conductivity between 10^{-3} m/s and 10^{-5} m/s (Autorità di bacino distrettuale delle Alpi Orientali, 2010). The aquifer is recharged by lateral springs corresponding to the Noce and Avisio Fans (Castagna et al., 2015). The shallow aquifer close to the Avisio Fan has a maximum depth of 20 meters, and its depth reaches 6 - 7 meters in areas close to the Adige River. The maximum depth of the shallow aquifer located in the Piana Rotaliana, where the Noce River flows, is about 17 m, while it reaches a very shallow depth (up to 1 m) in Nave San Rocco (Autorità di Bacino del Fiume Adige, 2007). The resulting system is very complex, with a multi-aquifer water circulation. This is mainly because the impermeable bed layers are irregular, which results in interconnections between different aquifers (Viesi, 2016). Also, it is important to consider that the Adige Valley is included in carbonate massifs which contribute to lateral recharges for the aquifers (Autorità di bacino distrettuale delle Alpi Orientali, 2010; Viesi, 2016).

Snow and glacier melting control the natural recharge of the Adige aquifer, although human activity, such as hydropower production and agriculture, also play a significant role in the aquifer dynamics (Castagna et al., 2015; Chiogna et al., 2016). The aquifer is exploited by 2070 wells spread along the whole valley, with pumping rates that vary seasonally according to agricultural needs (Beretta 2011; Castagna et al. 2015). Moreover, five well fields extract water for the drinking water supply system of the city of Trento. The most important well field is located in the Avisio Fan, with a mean extraction rate of 208 l/s (Castagna et al., 2015). Finally, since the area used to be a wetland, a network of ditches (Figure 7.1c) is present in the reclaimed zones. The water into the ditches naturally flows into the rivers, but when these have high levels, dewatering pumps are activated in order to preserve the land from floods. The ditches are also used to distribute water for irrigation during dry periods through the combined use of gates and inflow from the Noce River.

7.2.1 DATA COLLECTION AND RIVER CHARACTERISTICS

Groundwater head data is collected in collaboration with the Geological Survey of the Autonomous Province of Trento. These data series include 16 manual and 2 automatic measurement points for the period September 2009-August 2010 and 16 manual and 4 automatic measurement points for the period September 2016-August 2017 (Figure 7.1c). Manual data is measured about every three months, while automatic data about every six hours.

We obtain daily precipitation and temperature data from September 2009 to August 2010 and from September 2016 to August 2017 from the Meteorological Survey of the Autonomous Province of Trento (www.meteotrentino.it) and from 3Bmeteo (www.3bmeteo.com) at the meteorological stations in San Michele all' Adige, Roveré della Luna, Trento (Aeroporto), Zambana - Idrovora, Mezzolombardo - Maso delle Part and Trento - Roncafort (see Figures 7.1b and 7.2). It is noteworthy to observe the significantly lower precipitation in 2016-2017 compared to 2009-2010, particularly for October-March (see also Chiogna et al. 2018b). For example, in that period, the cumulative precipitation decreased around 20% and 30% in the stations of Roncafort and Zambana, respectively.

For the river discharges, we use collected data in the gauging stations of San Michele all'Adige (Adige River, northern part), Trento Ponte San Lorenzo (Adige River, southern part), Lavis (Avisio River) and Mezzolombardo (Noce River) by the Dams Office of the Province of Trento (www.floods.it). The location of the gauging stations is shown in Figure 7.1b. River discharges at the Adige San Michele gauging station were not available for the 2016/2017 year, and therefore a rating curve has been reconstructed considering river stages and discharges in the hydrological year 2009/10. With a mean streamflow of 46 m³/s at Mezzolombardo, the Noce River streamflow is highly variable due to the proximity of the Mezzocorona hydropower plant, about 9.3 Km upstream from its confluence with the Adige River (Figure 7.1b). In general, the Noce River basin (basin area of 1360 km²; main course length of 105 km) is highly impacted by hydropower production at different locations (Chiogna et al., 2016; Majone et al., 2016). The northern part of the Adige River reach shows less variability in the river stage than the Noce river since the operation of hydropower plants is located several kilometers upstream (Chiogna et al. 2018a; Pérez Ciria et al. 2019). However, in the southern part of the Adige River (mean of 212 m³/s at the Ponte San Lorenzo gauging Station in Trento), it is possible to observe the effect of the waves propagating from the Noce River (Pérez Ciria et al., 2019; Zolezzi et al., 2009). Finally, although the Avisio River (mean water discharge of 23.5 m³/s at Lavis) is also exploited for hydropower production, it does not display sharp and regular river stage fluctuations in the study area. Therefore, we consider this river reach as a non-impacted by hydropeaking.

The maximum allowed abstraction rates of all wells present in the study area are provided by the Geological Survey of the Province of Trento. We use these values to calculate the average daily pumping rates used in the model.

This work seeks to establish a proof of concept on how reservoir and hydropower plant operations can affect Alpine aquifers depending on the frequency of water release as well as on the season and on the wet/dry conditions of a specific hydrologic year. Therefore, we apply a single realization of the hydraulic conductivity field (see Supporting Information Figure S1) rather than multiple realizations. Such conductivity field was obtained from the estimations of Castagna et al. (2015) and had the minimum mean absolute error when compared to the available observations. We acknowledge, however, that hydraulic conductivity is an important source of uncertainty that has to be considered for further studies where uncertainty quantification is relevant.

7.3 NUMERICAL MODEL

The Adige aquifer is modeled with MODFLOW-2005 (Harbaugh 2005), which is a modular finite-difference flow model that solves the groundwater flow equation. We apply the transient groundwater flow model developed by Castagna (2017), based on the calibration of the steady-state model version (Castagna et al., 2015), which is currently the official model applied by the Geological Survey of the Autonomous Province of Trento for their investigations. The transient model assumes the same hydrological parameters as the stationary model, while the forcing factors (river stage, precipitation, evapotranspiration, transient boundary conditions and pumping rate of wells) are transient. The spatial grid of the model (x * y * z) is 80 m * 80 m * 5 m. The model includes 8 layers, 107 rows and 50 columns, and the total area of active cells is approximately 18 km² (Figure 7.1c).

We analyse two time periods: the first one is from September 2009 to August 2010 and corresponds to a wet year; the second one is from September 2016 to August 2017 and represents a dry year. While variability in the operation of hydropower plants also occurs at the subdaily scale (Zolezzi et al., 2011; Perez Ciria et al., 2019), we consider a daily temporal resolution since it allows us to describe the seven days' periodicity in the aquifer, which is the focus of this work.

The time series of four piezometers are used to define the boundary conditions of the groundwater model, implemented as Time-Variant Specified-Head (CHD) Package (Harbaugh, 2005). These piezometers are: piezometer 348 for the north side close to the Noce River, piezometer 39 for the north side close to the Adige River, piezometer 134 for the south-east side, and piezometers 218 and 580 for the south-west part in the hydrological years 2009/10 and 2016/17, respectively (Figure 7.1c). This change in the modeling of the two hydrological years is needed due to the available data. We present an extended description of the head boundary conditions in the Supporting Information Text S1.

To implement the river-groundwater interaction, we apply the river (RIV) package (Harbaugh, 2005). The flow between surface water and groundwater q_{riv} [L³/T] is modelled according to the following equation (Harbaugh, 2005):

$$q_{riv} = C_{riv}(H_{riv} - h) \text{ if } h > R_{bot} \tag{7.1}$$

$$q_{riv} = C_{riv}(H_{riv} - R_{bot}) \text{ if } h \leq R_{bot}$$

where C_{riv} [L²/T] is the hydraulic riverbed conductance, H_{riv} [L] is the water stage of the river, h [L] is the groundwater head simulated by MODFLOW below the river reach cell, and R_{bot} [L] is the bottom of the riverbed. q_{riv} is positive if the water flows from the river to the aquifer, and negative if vice versa. The values of H_{riv} are obtained in the output of a hydraulic simulation performed with the Software HEC-RAS (U. S. Army Corps of Engineers 2016), which is calibrated and validated based on the collected daily river discharge (section 7.2.1). Figure 7.2 (left axis) displays the computed daily river stages for the years 2009/10 and 2016/17 in the cells close to the model observation points near the rivers (Figure 7.1c).

Hydraulic parameters (riverbed conductance, hydraulic conductivity, and river bottom) were estimated in Castagna et al. (2015) and Castagna (2017) using the inversion of hydraulic head data by applying the Particle Swarm Optimisation (PSO) Algorithm (Robinson & Rahmat-Samii 2004). The calibration process is found in Castagna et al. (2015), and additional details on the generation of the heterogeneous hydraulic conductivity field appears in Text S2.
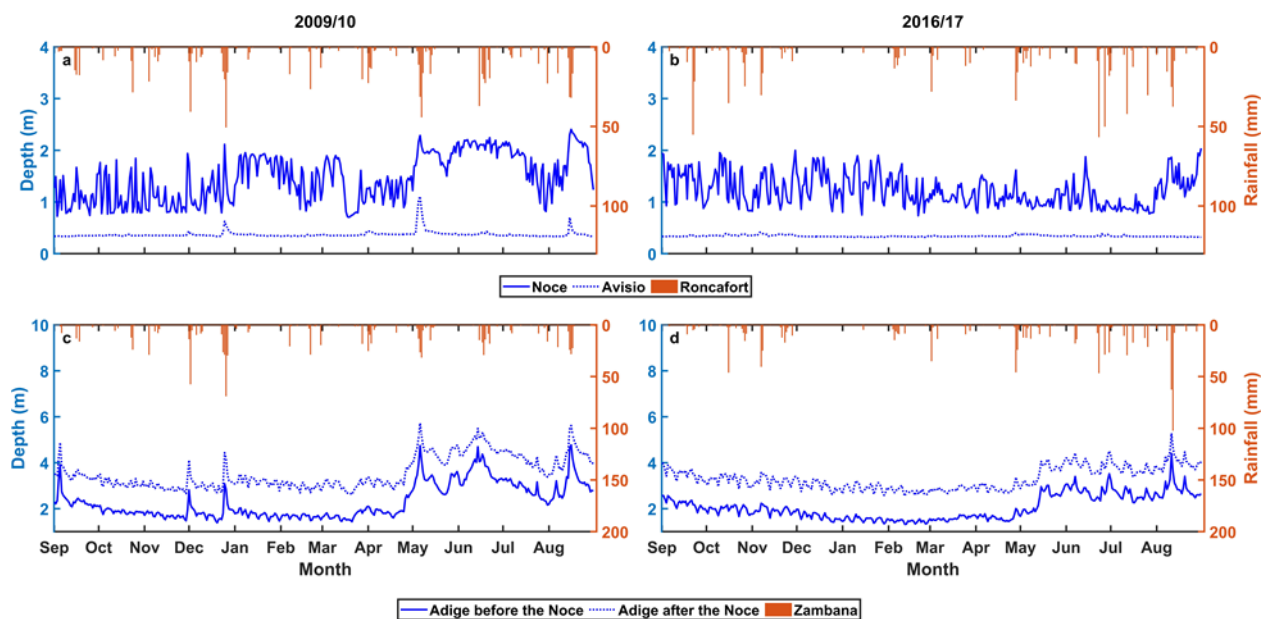
Figure 7.2. Depiction of river depth (m) time series for the Noce River (**a**, **b**), the Avisio River (**a**, **b**) and the Adige River before and after the confluence with the Noce river (**c,d**) for the years 2009/10 and 2016/17 (blue, left y-axis). Rainfall (mm) time series recorded in Roncafort (**a**, **b**) and Zambana (**c**, **d**) stations (orange, right y-axis).

The infiltration into the saturated zone is implemented using the Recharge (RCH) package (Harbaugh, 2005), which assigns values to each grid cell of the shallowest layer. In order to estimate the recharge to the aquifer, we apply the leakage model (Rodríguez-Iturbe & Porporato 2007) used in Castagna et al. (2015). This model considers that recharge depends not only on the precipitation, but also on irrigation, evapotranspiration and the soil characteristics (e.g., soil moisture). For the precipitation, we used the daily rainfall values collected by the meteorological stations (Figure 1b). The wavelet power spectrum of these time series is provided in the SI (Figure S2) and shows that high power is present during the events and propagates over several temporal periods as already observed for example by Schaefli et al. (2007) and Bittner et al. (2021). The irrigation rate is obtained based on the observations of Toller (2002). To calculate the evapotranspiration we follow the Thornthwaite Method (Chen et al., 2005; Sacratees, 2017). The soil characteristics are based on the work by Laio et al. (2001). We use the Voronoi triangulation as spatial aggregation method and therefore we assigned irrigation and precipitation to the model cells according to Thiessen polygons. Finally, we set the leakage to zero in urban areas. A complete description of the leakage model and the estimation of irrigation and evaporation rates are found in the Supporting Information (Text S3 and S4, respectively).

The well withdrawals provided by the Geological Survey of the Province of Trento are inserted into the model as punctual discharge rates, by applying the Well (WEL) package (Harbaugh, 2005). The pumping rates were calculated depending on the monthly irrigation demand and applied as daily average values. Further details about the implementation of extraction wells are provided in the Supporting Information (Text S5). The implementation of the ditches network was also done using the river package. Additional details are found in the Supporting Information (Text S6).

The model results are compared to head data available for continuous monitoring data collected in piezometers 349 and 411 in 2009/2010 and in piezometers 343, 349, 559 and 560 in 2016/17. The R^2 obtained is 0.997 and 0.991 for the two hydrological years respectively. Moreover, the results are compared with manual data provided by the Geological Survey of Trento and collected at the piezometers available in the study area (Figure 1c). Considering also these manual data, R^2 is 0.987 for the year 2009/10 and 0.990 for the year 2016/17.

7.4 WAVELET ANALYSIS

The goal of the continuous wavelet transform (CWT) analysis is the detection of periodicity in a signal and the determination of the temporal scales and time period at which they are dominant (Agarwal et al. 2016a; Agarwal et al. 2016b; Pérez Ciria et al. 2019; Torrence and Compo 1998). The CWT is defined as the convolution of a continuous signal with a scaled and translated version of the mother wavelet function $\psi(t)$. In the case of a discrete sequence x_n with a time step δt, where n indicates the localized time index, the CWT is approximated as:

$$W_n(s) = \sum_{n'=0}^{N-1} x_{n'} \psi^* \left(\frac{(n'-n)\delta t}{s} \right), \tag{7.2}$$

where $(*)$ indicates the complex conjugate, n' is the time variable, s is the wavelet scale and N is the number of points in the time series (Torrence & Compo, 1998). In the present work, the Morlet mother wavelet function is chosen for its good compromise between time and frequency resolution (Grinsted et al. 2004; Pérez Ciria and Chiogna 2020; Schaefli et al. 2007). It is defined as

$$\psi(t) = \pi^{-1/4} e^{i\omega t} e^{-t^2/2}, \tag{7.3}$$

where t is the dimensionless time and ω is the dimensionless angular frequency. In our calculations ω is set to 6 (Grinsted et al., 2004), since this number provides a good balance between time and frequency localization, while the scale value s in Eq. 7.2 is a fractional power of 2. Since the analyzed time series have a finite length, the wavelet analysis is affected by edge effects. The area where these effects become important is defined as the cone of influence (Torrence & Compo, 1998).

7.4.1 WAVELET TRANSFORM COHERENCE

The wavelet transform coherence (WTC) allows us investigating the local correlation between two CWTs (Pérez Ciria & Chiogna, 2020). It is defined as (Torrence and Webster 1999):

$$R_n^2(s) = \frac{|S[s^{-1}W_n^{XY}(s)]|^2}{S[s^{-1}|W_n^X(s)|^2]S[s^{-1}|W_n^Y(s)|^2]}, \tag{7.4}$$

where S is the smoothing operator, given by $S(W) = S_{scale}\{S_{time}[W_n(s)]\}$, while S_{scale} denotes smoothing with respect to scales s and S_{time} smoothing in time. WTC varies between 0 (uncorrelated) and 1 (fully correlated). This definition is similar to that of the correlation coefficient and the WTC can be interpreted as a localized correlation coefficient in the time-frequency space (Grinsted et al., 2004). We further consider two additional metrics to evaluate the model performance. The first one is the mean coherence between model and continuously available groundwater head data (in 2009/10 piezometers 349 and 411, and in 2016/17 piezometers 343,349,559 and 560) computed over the entire simulation time and all periods. The second one is the mean coherence between model and continuously available groundwater head data computed over the entire simulation time and only the seven-days period (Chiogna et al. 2018a). In both cases, we obtain a mean coherence value of 0.7

7.4.2 WAVELET MAPS

Continuous wavelet transform informs about the strength of a periodic signal for a specific periodicity and a specific time. Beside this information, we are interested in quantifying the average behavior of the groundwater table during the year and hence we compute the normalized time-average of the wavelet spectrum $\overline{W_n(s)}$, as

$$\overline{W(s)} = \frac{\left(\frac{1}{N}\sum_{n=0}^{N-1}|W_n(s)|^2\right)}{\sum_s\left(\frac{1}{N}\sum_{n=0}^{N-1}|W_n(s)|^2\right)}. \tag{7.5}$$

In order to visualize the spatial variability of this value for the 7-days period, we create the matrix $\overline{W(7)}$, where each element corresponds to the normalized time-averaged wavelet spectrum of the hydraulic head in the corresponding cell of the domain for a weekly signal:

$$\overline{W^{ij}(7)} = \frac{1}{N}\sum_{n=0}^{N-1}W_n^{ij}(7), \tag{7.6}$$

where the superscript ij refers to the cell (i,j) in the model, $W_n^{ij}(7)$ corresponds to the value of the wavelet spectrum for the hydraulic head at the time step n and for the period of 7 days.

We apply a similar procedure for the wavelet coherence. In this case, each element of the matrix $\overline{C(7)}$, corresponds to the average of the coherence wavelet between the river stage and the hydraulic head computed for each cell over time at a 7-days period,

$$\overline{C^{ij}(7)} = \frac{1}{N}\sum_{n=0}^{N-1}R_n^{2\,ij}(7), \tag{7.7}$$

giving hence a sort of mean coherence correlation along the year. The wavelet analysis and related elaborations have been performed with the Software MATLAB R2020b.

7.5 RESULTS

7.5.1 VARIABILITY IN THE RIVER STAGES

We analyze the influence of hydropower plant operations in the rivers by computing the continuous wavelet transform of the river stage time series shown in Figure 7.2, where the withe shaded area represents the cone of influence.

The continuous wavelet transforms presented in Figure 7.3 show considerable variations in high power regions across the river stage time series of the two hydrological years (2009/10 and 2016/17, respectively) for the Noce, Avisio, and Adige before and after the confluence with the Noce.
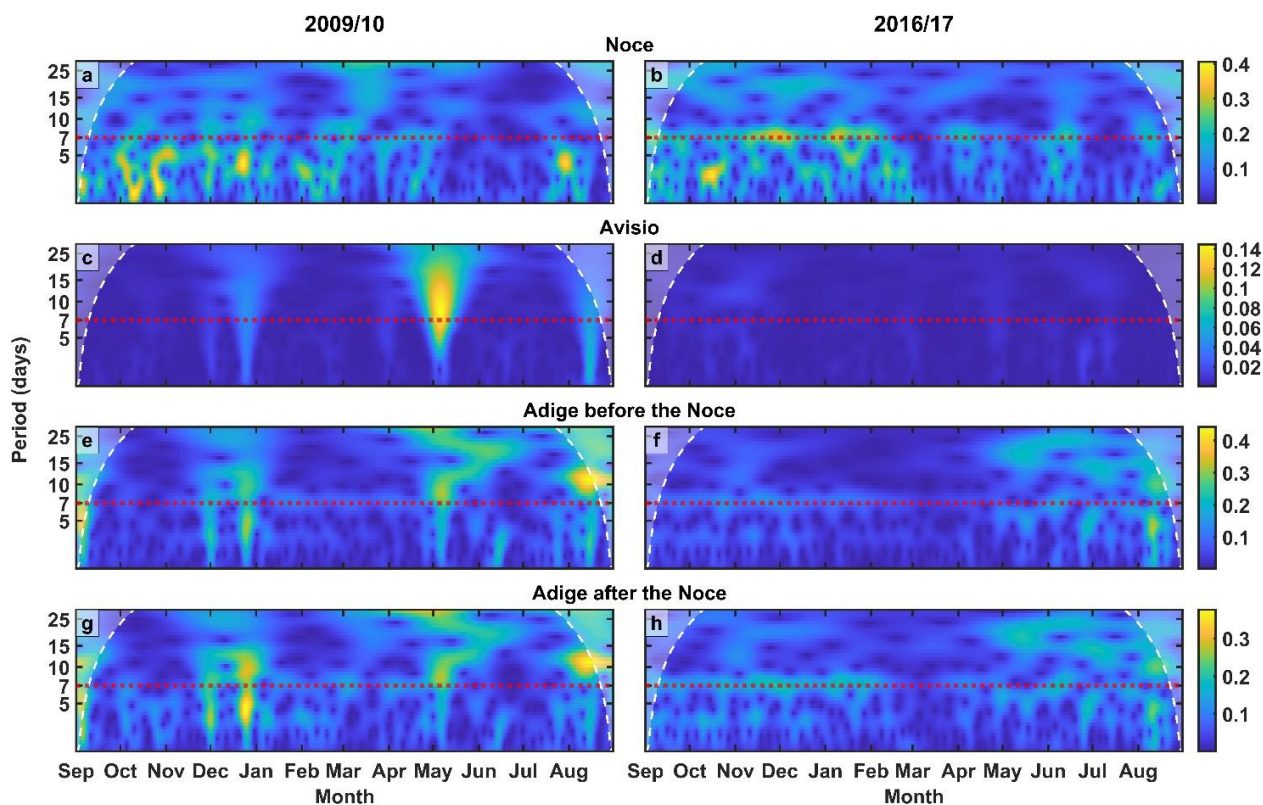
Figure 7.3: Continuous wavelet transform of the river's stage time series. Warmer color indicates times and periods of intense power. The white shaded areas show the cone of influence. The dashed red line along the period of 7 days identifies the temporal scale focus of the present study.

A light (yellow) color indicates times and periods of intense signal. The red dashed line in Figure 7.3 helps to identify the level of 7-days periodicity. Therefore, a higher intensity along this dashed line is an indicator of weekly streamflow alteration associated to low energy production during weekends (i.e., low stage in the affected rivers during the weekends and high stage during the week). In addition, high powers spreading over different levels of periodicity at a specific time are an indicator of intense precipitation events, as also observed by Schaefli et al. (2007). In our study area, large precipitation events generate a peak in the power spectrum from periods of 2 days until about 15 days as it can observed for example for the events occurred on December 1st 2009, December 25th 2009 and May 6th 2010. However, time series over longer periods may show coherence between precipitation and groundwater fluctuations that are not associated to specific rainfall events (e.g., Dountcheva et al. 2020)

The Noce River displays a peak in the power spectrum at the weekly scale typical for Alpine rivers affected by storage hydropower plant management (Chiogna et al. 2018a; Pérez Ciria et al. 2019) stronger during the wintertime, i.e. under low flow conditions, for both the hydrological years. We can also observe that the signal is stronger and more persistent in the snow scarce year 2016/17 (Chiogna et al. 2018b) than in 2009/10 since it extends to the spring period due to the lack in groundwater recharge due to snowmelt. Moreover, since the river stage is determined mainly by the hydropower plant operation, we do not observe significant impact of precipitation events in the power spectrum. High power values at the weekly period are also present in the whole analyzed segment of the Adige, even though it is stronger after the confluence with the Noce River. Furthermore, the Adige stage time series display peaks in the power spectrum induced by the precipitation events of December 2009 and May 2010, since the river stage is not only influenced by hydropower plant operation. These signals are also observed in the Avisio River, where we do not detect the 7-days periodicity due to surface water management operations.

7.5.2 VARIABILITY IN THE SIMULATED GROUNDWATER HEADS

To analyze the temporal variability of the groundwater table, we select six representative locations in the computational domain, indicated in Figure 7.1c. Four points are distributed in the domain to capture the behavior of the aquifer close to the rivers (close to the Noce River, close to the Avisio River, close to the Adige River before its confluence with the Noce and close to the Adige River after its confluence with the Noce), while two points represent the aquifer not influenced by the rivers (between the Adige and the Noce rivers and between the Adige and the Avisio rivers).

Figure 7.4 shows time series of the groundwater head at the six selected locations within the computational domain for the two considered hydrological years of 2009/10 and for 2016/17. We can observe that close to the Noce River (Figure 7.4a) the groundwater level displays rapid fluctuations of small amplitude throughout the year. This result contrasts with the observations for the groundwater head simulated close to the Avisio River, where the hydraulic head smoothly varies during the year, with higher water table in spring and summer when groundwater recharge occurs (Figure 7.4b). Far from surface water bodies, i.e., between the Adige and the Noce rivers (Figure 7.4e) and between the Adige and the Avisio rivers (Figure 7.4f) the aquifer behaves similar to the point close to the Avisio River. Particularly interesting are the results obtained for the Adige River where the surface water fluctuations in the riverhead of the Adige River before the confluence with the Noce are not strong enough to clearly propagate into the aquifer (Figure 7.4c). However, the impact of the Noce River on the Adige River is evident also in the aquifer and in fact after the confluence with the Noce also the aquifer close to the Adige River is characterized by fluctuations caused by surface water management (Figure 7.4d). Noteworthy is the reduced or even absent groundwater head increase in 2016/17 in the spring/summer period due to the lack of intense precipitation events as well as of snow melt occurred in that season.

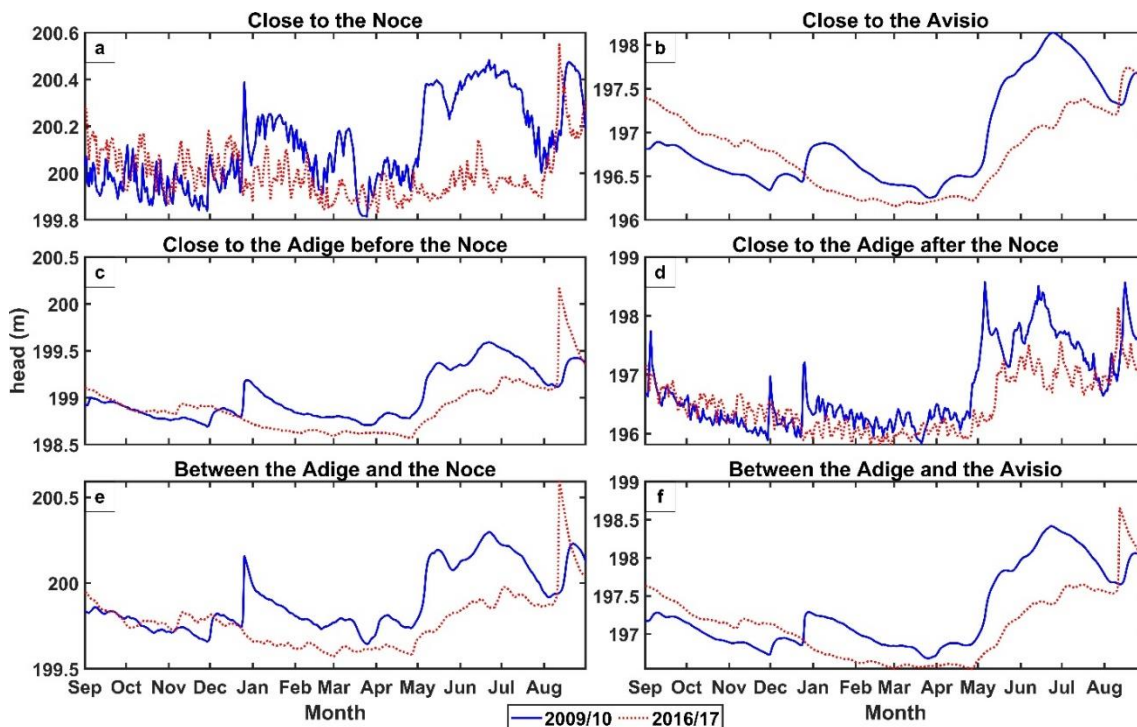**Figure 7.4:** Simulated groundwater heads [m] at six selected locations (see Figure 7.1c) namely (**a**) close to the Noce, (**b**) close to the Avisio, (**c**) close to the Adige before the Noce, (**d**) close to the Adige after the Noce, (**e**) between the Adige and the Noce, and (**f**) between the Adige and the Avisio for the hydrological years 2009/10 (blue solid line) and 2016/17 (red dotted line).

We calculate the normalized time-averaged wavelet power spectrum according to Eq. 7.5 (Figure 7.5) in order to analyze the overall behavior of each period integrated over time. For the groundwater observation points close to a river, we include in the figure the time-averaged wavelet power spectrum for the respective river depth, that is, the Noce River (Fig. 7.5a), the Avisio River (Fig 7.5b), and the Adige River [Figs 7.5(c-d)]. In such locations, we see that the behavior of the time-averaged wavelet power spectrum is similar between the river and the groundwater [Figure 7.5(a-d)], in particular in case of the Noce and Adige rivers. With respect to the different hydrological years, we can observe that in 2016/17 the period of 7 days displays a sharp peak for the Noce and the Adige after the Noce observation points (Figure 7.5a and 7.5d), while the Adige before the Noce, the Avisio and the points far from the influence of the rivers display a broad peak at about 15 days (Figures 7.5b-c, 7.5e-f) which can be associated mainly to recharge processes due to precipitation or their overlap with the signal caused by surface water management. In the year 2009/10, the weekly peak is less evident also for the Noce and the Adige after the confluence due to the more intense and frequent precipitation events in that year, since they generate very high power values over several periods. To see how the weekly signal changes over the time, we additionally show the weekly wavelet coherence between the groundwater at the selected locations and the closest river in Figure S3 of the Supporting Information. This analysis however provides only a partial representation of the complexity of the interaction between surface water and groundwater in this system, since it does not allow us to investigate the non-stationarity in the power spectrum.
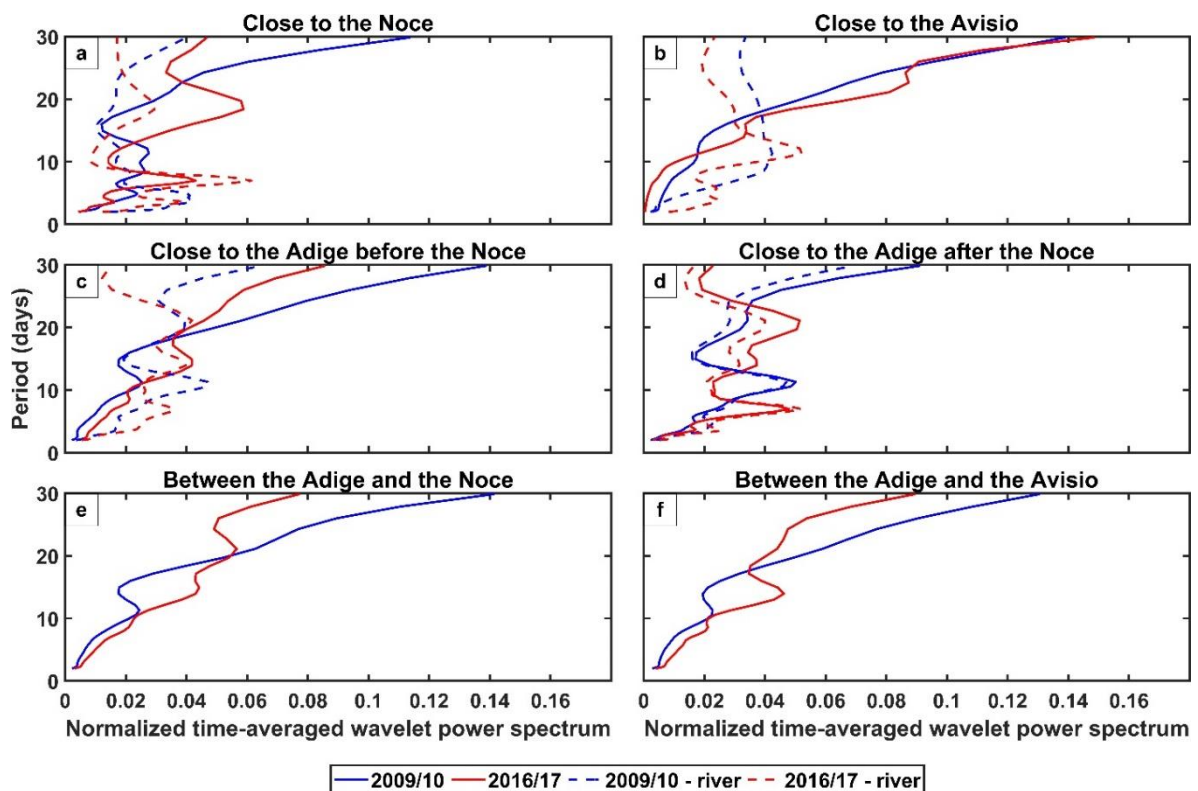
Figure 7.5: Normalized time-averaged spectrum of the groundwater estimated at six selected locations (see Figure 7.1c), namely (**a**) close to the Noce, (**b**) close to the Avisio, (**c**) close to the Adige before the Noce, (**d**) close to the Adige after the Noce, (**e**) between the Adige and the Noce, and (**f**) between the Adige and the Avisio for the hydrological years 2009/10 (blue solid line) and 2016/17 (red solid line). (a-d) also shows the normalized time-averaged spectrum for the river depth closest to the observation points for the years 2009/10 (blue dashed line) and 2016/17 (red dashed line). In (a) river refers to the Noce, in (b) river refers to the Avisio, and in (c-d) river refers to the Adige.

Figure 7.6 presents the wavelet power spectrum of the groundwater heads at the four selected locations closer to the rivers. The observation point close to the Noce River has the highest power at the period of 7 days for both hydrological years (Figure 7.6a and 7.6b). In particular, during the autumn and winter months, signal persistence in 2016/17 is higher than in 2009/10. Therefore, we can observe that the weekly wavelet signal is stronger in the aquifer during low flow periods. The low flow periods can be caused by the typical lack of groundwater recharge in the autumn and winter months, or due to a particularly dry winter, which - since the catchment is snow dominated - leads to little snow accumulation and thus to a lack of spring recharge (as for the 2016/17 year). This explains why the normalized time-averaged wavelet spectrum displays a sharper peak at a weekly period in 2016/17 than in 2009/10 (Figure 7.5a). The Avisio River does not display the 7-days periodicity neither in the river (Figure 7.3c-d) nor in the groundwater (Figures 6c and 6d). Despite the weekly signal present in the Adige River before its confluence with the Noce (Figure 7.3e-f), the groundwater near the river (Figures 7.6e and 7.6f) does not show this periodicity. This is most likely due to the interplay between the forcing signal and the hydraulic properties of the riverbed and the aquifer. Close to the Adige after the Noce, the continuous wavelet spectrum of the groundwater (Figure 7.6g and 7.6h) behaves similar to the groundwater near the Noce. However, the values in the power spectrum at the period of 7 days are smaller. This periodic signal has an anthropogenic nature and it is caused by the impact of water management for hydropower production on the river stage. Overall, the analysis of the continuous wavelet power spectrum and the normalized time-averaged wavelet power spectrum confirm the distinct difference between wet and dry years.
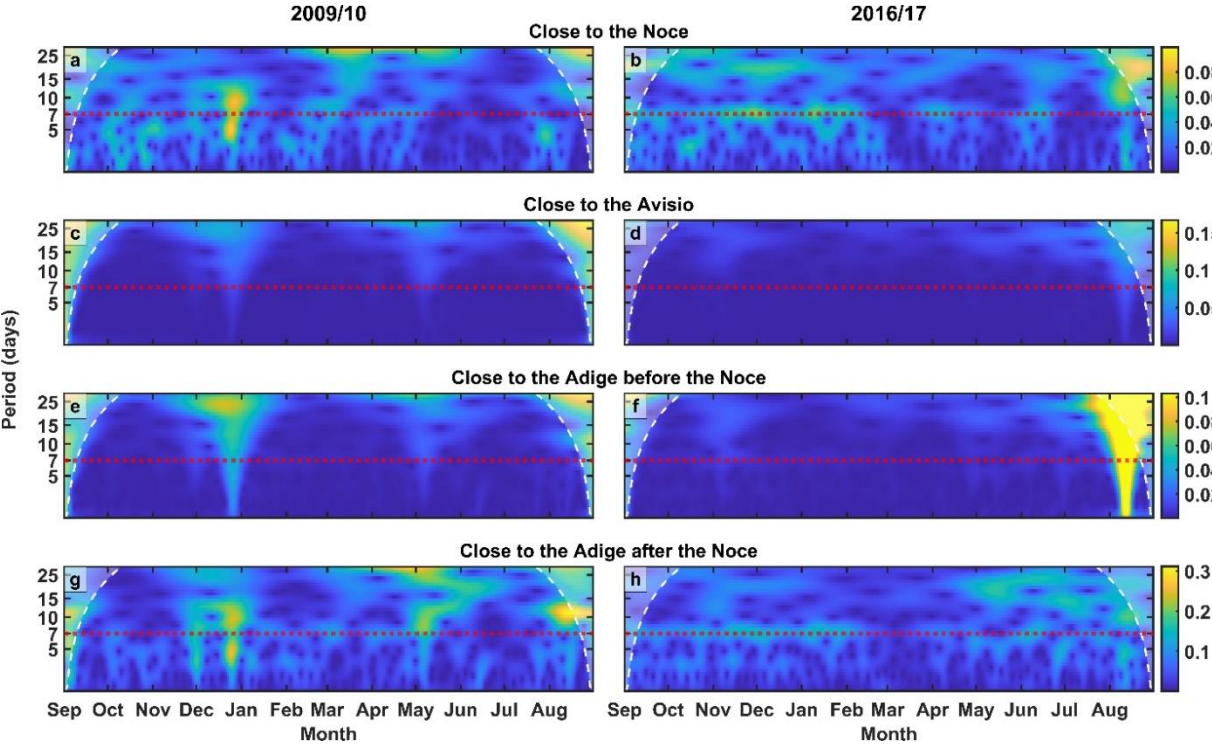
Figure 7.6: Continuous wavelet transform of the groundwater head time series at selected locations (see Figure 7.1c). Warmer color indicates times and periods of intense power. The white shaded areas show the cone of influence. The dashed red line along the period of 7 days identifies the temporal scale focus of the present study.

7.5.3 MAPS OF WAVELET SPECTRUM AND COHERENCE WAVELET BETWEEN RIVER STAGE AND GROUNDWATER HEADS

Figure 7.7 shows a map of the normalized time averaged wavelet spectrum value at the weekly period to extend the results obtained for the six observation points in Figure 7.5 to the entire study area. Here, higher values indicate that the 7-day averaged signal (understood as impact on the aquifer of the streamflow alteration due to

hydropower plant operations) is more intense for that specific location in comparison to other cells in the domain. In general, the power spectrum is lower in 2009/10 than in 2016/17, confirming that the impact of hydropeaking on the aquifer is more severe in a dry year than usual. Furthermore, the zones above the 75th percentile of the power spectrum intensity in each map are delimited with a dashed line to better identify the most influenced areas. In both years, we can consistently observe high values (above the 75th percentile) of the wavelet power close to the Noce River and close to the Adige after its confluence with the Noce. Notice that the results of the northern boundary condition are likely affected by the piezometer used to define the constant head boundary condition and therefore should be carefully interpreted (see Supporting Information, Text S1).

Figure 7.7: Map of the normalized time-averaged wavelet spectrum at a period of 7 days for the years 2009/10 and 2016/17. Warmer color indicates areas of higher power spectrum intensity. The dashed black lines show the area above the 75th percentile. Solid lines depict the rivers.

To quantify the area of the aquifer affected by surface water management, we calculate the time-averaged wavelet coherence between the simulated groundwater level and the river stage in the closest river cell at the period of 7 days as given in Eq. 7.6. The resulting maps are shown in Figure 7.8, where we observe high coherence between river stages and groundwater heads in both the hydrological years. High coherence values are distributed over a larger area for the year 2009/10 compared to that of 2016/17. This is because precipitation events affect both the river stage and the aquifer also in locations where there is no groundwater-surface water interaction. However, in both years, the highest coherence values occupy the portion of the aquifer closer to the rivers affected by hydropeaking.
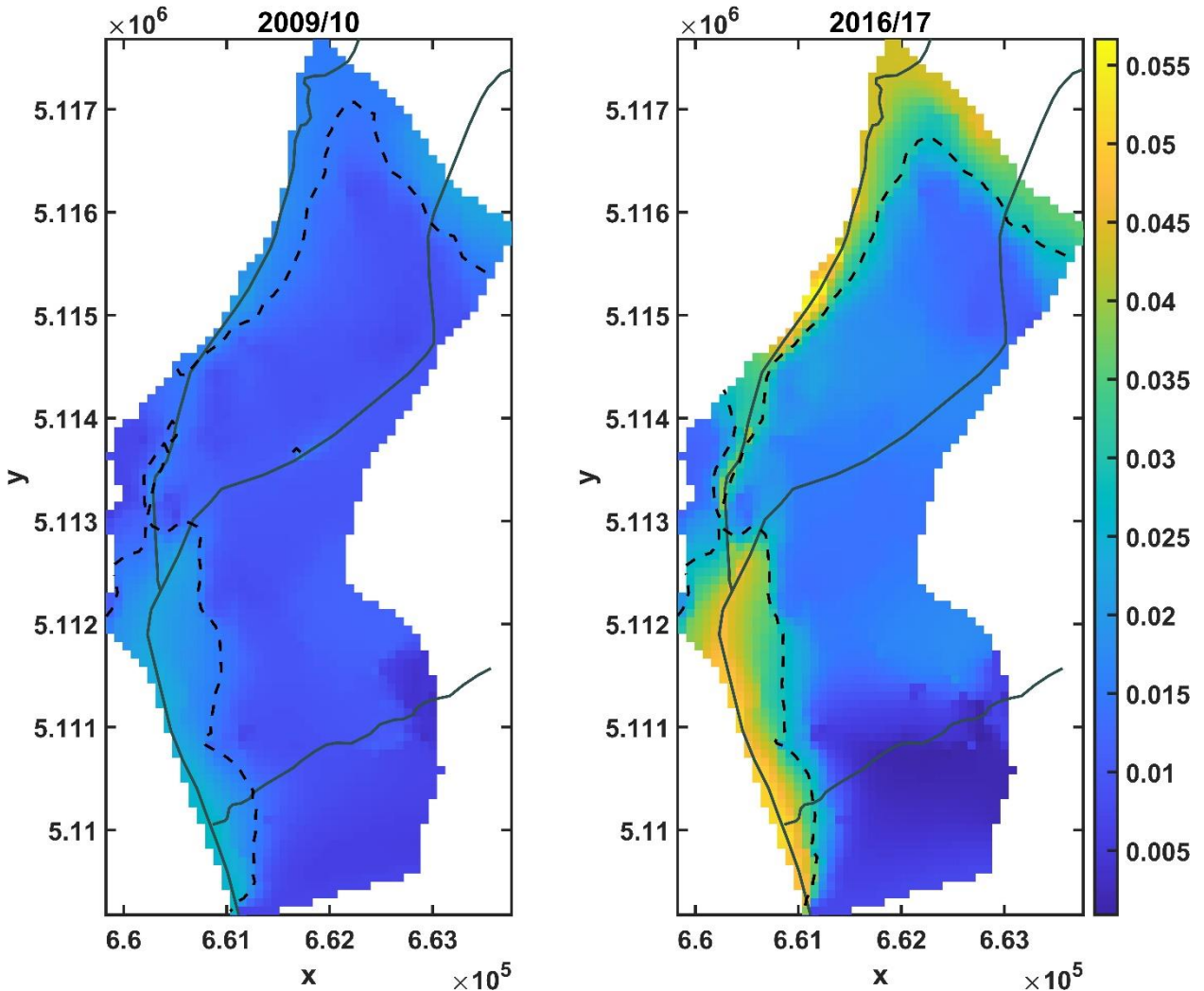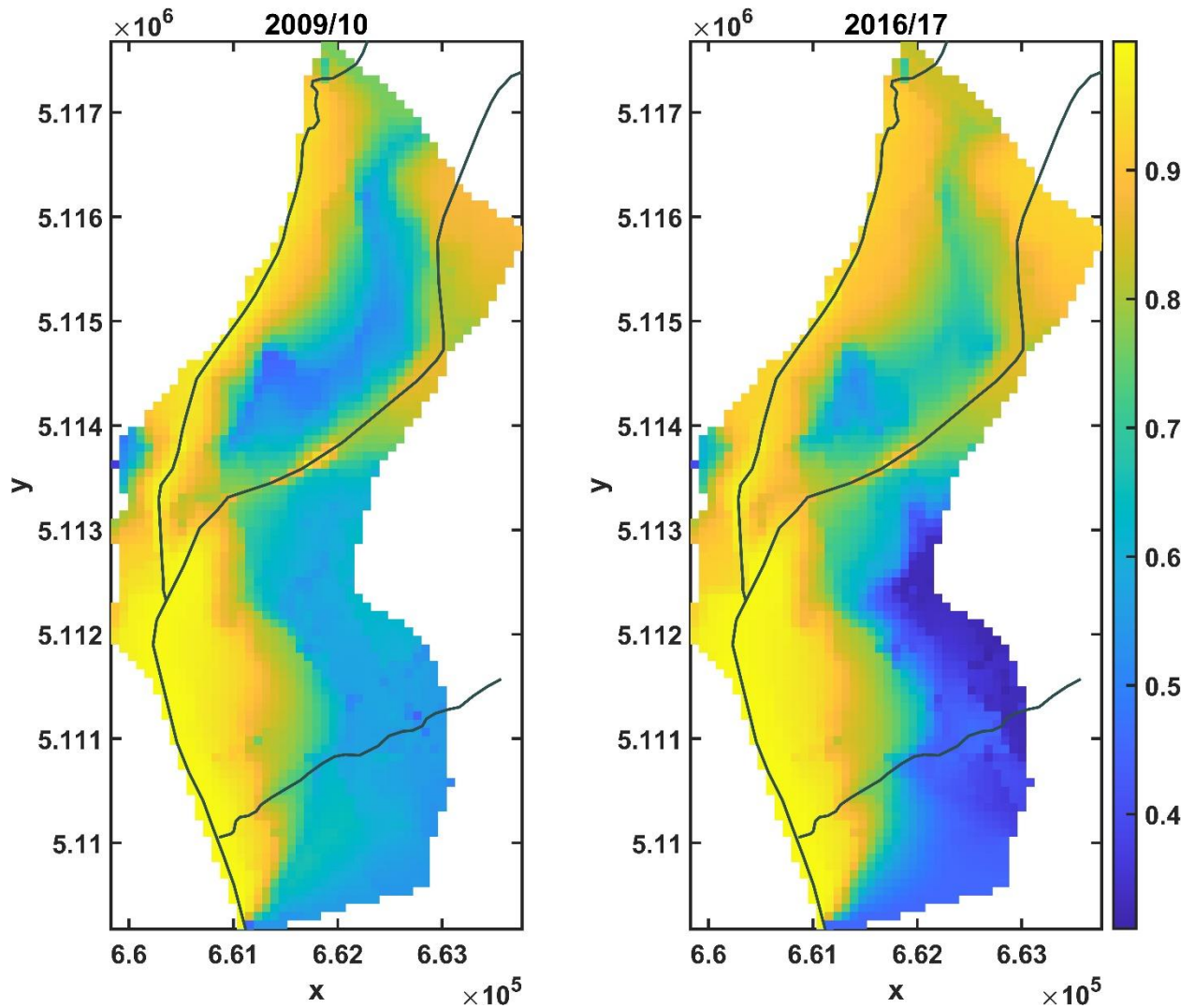
Figure 7.8: Map of the time-averaged coherence wavelet spectrum at a period of 7 days for the years 2009/10 and 2016/17. Warmer color indicates areas of higher coherence between the river stage and groundwater heads. Solid black lines depict the rivers.

The intensity of the signal and the extension of the impacted area depend on landscape attributes such as hydraulic conductivity, saturated thickness of the aquifer and specific yield. However, a systematic analysis is difficult to be performed in a real case study like the one considered in this study since the hydraulic conductivity field is heterogeneous in all three spatial dimensions and this influences the wave propagation in a non-trivial way. Moreover, the presence of the ditches can dampen the propagation of the signal, in particular during the wet periods when they can receive more water from the aquifer since the water exchange is proportional to the groundwater head. However, as we can observe by comparing Figure 7.1c and Figure 7.8, high coherence values also appear beyond the area occupied by the ditches. Furthermore, groundwater abstraction may also have a local effect on the analysis although it is of minor importance. In fact, the pumping rate of the wells does not occur with a specific temporal frequency that could interfere with the river signal and the pumping rates only affect areas which are small compared to the grid area of the model (80 x 80m).

7.5.4 EXCHANGE FLUXES BETWEEN RIVERS AND THE GROUNDWATER

Finally, we analyze the flux exchanged between the river reaches and the underlying groundwater cells. We calculate with the Software Zonebudget (Harbaugh 1990) and the Python-package FloPy (Bakker et al. 2016) the

water budget over the area surrounding the rivers (3 cells to the right and 3 to the left of each river cell corresponding to 240 m in each direction) considering separately the Adige River before merging with the Noce, the Adige River after merging with the Noce, the Noce River and the Avisio River. The Noce River mostly feeds the aquifer without strong seasonal patterns, although the exchanged water volume is lower in the dryer year (Figures 7.9a-b). The Avisio River is always feeding the aquifer, with clear peaks during the raining events of 2009 (Figures 7.9c-d). In Figure 7.9e, we observe that before the confluence with the Noce, the aquifer mainly feeds the Adige River until end April for the year 2009/10; then, the river has intermittent time intervals, in which it feeds the aquifer, in particular those associated with precipitation events. In the year 2016/17, the behavior of water exchange for the same reach is similar, although peak of water going to the aquifer is lower (Figure 7.9f). After the Adige merges with the Noce, the groundwater predominately feeds the river (Figures 7.9g-h), and while at intermittent time intervals, the water flux changes direction, the amount of water going from the river to the aquifer is much lower than that before the confluence with the Noce.

To analyze the periodicity of the exchange fluxes, we estimate the normalized time-averaged power spectrum of the difference between the water entering and leaving the system for each river (Figure 7.10). For the year 2009/10 we observe a clear peak around 4-days period along the Adige and the Noce Rivers. This peak is also associated to water management operations (Perez Ciria et al., 2019) and is characteristic for high flow condition during five working days and low flow conditions over the weekend. The 4-days peak also appears in the year 2016/17; however, that year displays an additional and dominating peak around the weekly period. This shows that although the volume of exchanged water does not significantly change in dry and wet years (Figure 7.9), the temporal dynamics of these exchanges is affected and may therefore impact solute and thermal transport.
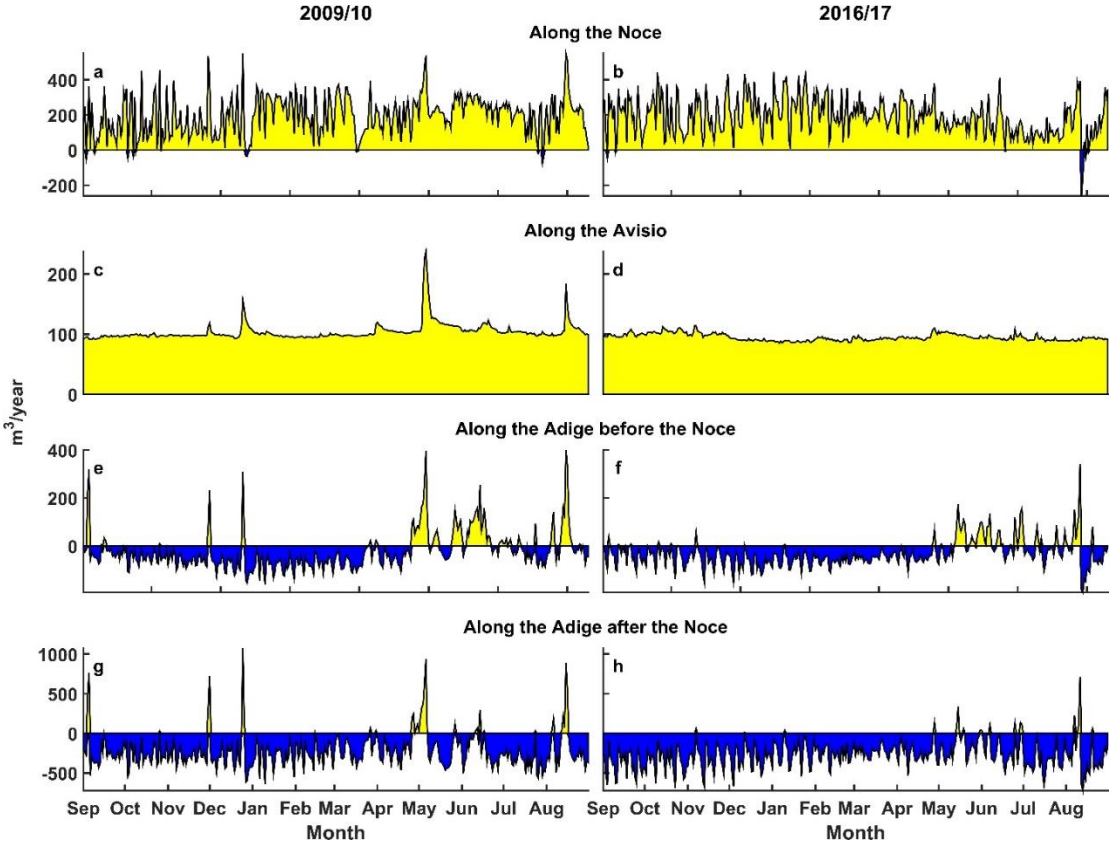
Figure 7.9: Water budget along the Noce, the Avisio, the Adige before the Noce and the Adige after the Noce. Negative values (blue areas) mean that the aquifer is feeding the river, positive values (yellow areas) mean that the river is feeding the aquifer.
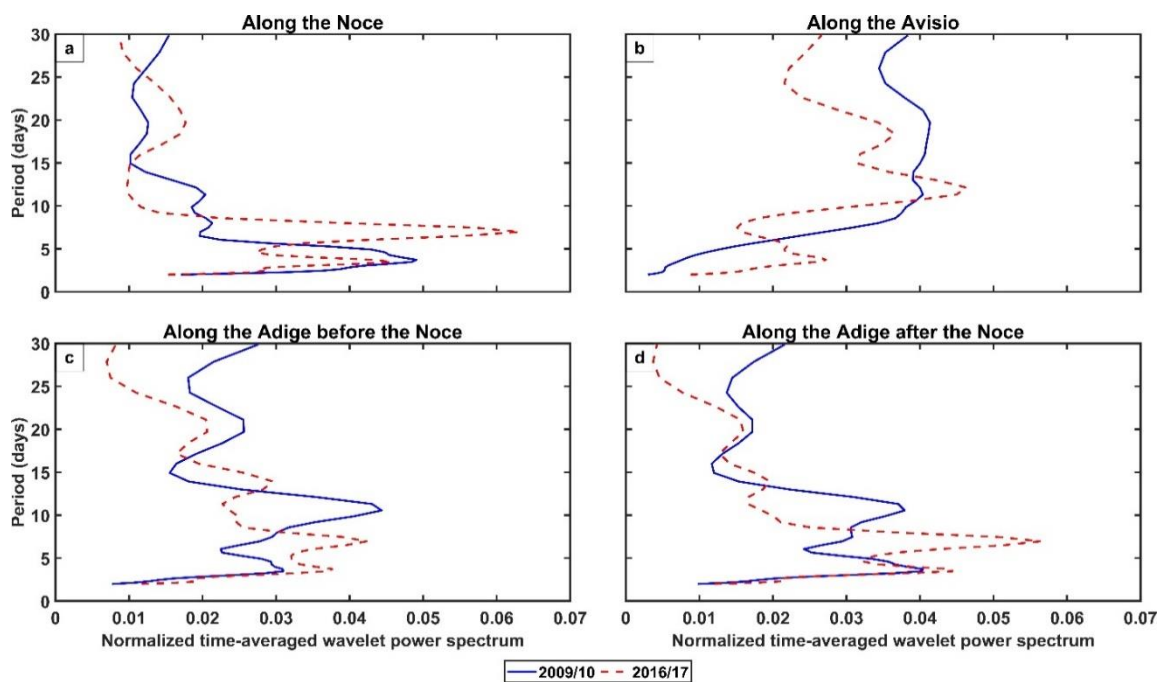
Figure 7.10: Normalized time-averaged power spectrum of the water budget along Adige, the Avisio and the Noce.

7.6 DISCUSSION

7.6.1 WAVELET ANALYSIS FOR UNDERSTANDING HIGHLY MANAGED RIVER SYSTEMS

The specific study area of this paper includes four river reaches differently influenced by hydropower plant operations. As shown in Figure 7.3, despite the similar hydrometeorological and climatic conditions, the composition of the river signal shows a strong difference, highlighting the dominant impact of water management on streamflow. Furthermore, thanks to the peculiarity of the investigated region, we are able to analyze the aquifer's response in two different years (2009/10 and 2016/17) with different hydrological and surface water management conditions. When we apply continuous and coherence wavelet analysis to study groundwater-surface water interactions, we observe a stronger impact of the river weekly signal on the aquifer during dry periods than during wet periods. Our findings are in line with the outcomes of Song et al. (2018) for the Columbia River and its underlying aquifer, as well as Li & Pasternack (2021), who analyzed several rivers in the state of California, most of them originating in Sierra Nevada and with a summer base flow controlled by snowmelt. Both authors pointed out that drought conditions can lead to stronger impacts from hydropeaking. However, while Song et al. (2018) focused on the hyporheic exchange, Li & Pasternack (2021) analyzed the river regimes. They concluded that the annual frequency of hydropeaking was higher in the dry season and in dry years compared to the wet season and wet years because of changes in the operation of hydropower plants (i.e., hydropower facilities generate electricity constantly since there is sufficient water). In our study, we observe that changes in the groundwater level fluctuations observed during the drier year 2016/17 respond to both the aquifer recharge (depending on meteorological conditions and soil properties) and to the surface water fluctuations, in particular in areas closer to the rivers. Since the surface water fluctuations come from river stage measurements, they already account for both precipitation events and, if it is the case, for changes in the operation of hydropower plants.

The continuous wavelet analysis (Figure 7.3) and the normalized time-averaged wavelet power spectrum analysis (Figure 7.5) show no significant signal at the 7-days periodicity in the aquifer close to the Avisio River, which is not affected by dam operations. In contrast, the signal is clearly visible in rivers affected by dam operations, such as the Noce River, and is more evident in low flow conditions, such as winter months or dry years. The groundwater close to these rivers shows a similar behavior (Figures 7.6a-b and 7.6g-h), indicating how the management of hydropower plants, especially in dry years, can affect the aquifer. The continuous wavelet analysis does not display any strong weekly signal at the observation point close to the Adige before the Noce (Figures 7.6e-f), even though the signal is present in the river stage fluctuations of the Adige in its proximity (Figures 7.3e-f). Two factors may explain this behavior: first, the signal in the river is weaker than the one observed after the confluence with the Noce River or in the Noce itself. Second, the porous material of the aquifer acts as a filter for the propagation of the fluctuations For instance, in a heterogeneous aquifer the signal of a fluctuating river dampens closer to the river in areas of low hydraulic conductivity (Merchán-Rivera et al. 2022), as occurs in the aquifer area corresponding to the upstream reach of the Adige River. Moreover, other factors such as the specific yield and aquifer thickness also play a role in the propagation of the signal into the aquifer (Sawyer et al. 2009).

Finally, we would like to highlight the importance of weekly fluctuations to study the aquifer at the regional scale. As mentioned in the Section 7.3, the operation of hydropower plants in the Adige catchment also happens at the subdaily scale, with important implications to the ecological and physical-chemical characteristics of the rivers (Zolezzi et al. 2011; Bruno et al. 2013), and eventually to the transport of contaminants in the underlying aquifer (Basilio Hazas & Chiogna 2022). However, higher frequencies have a shorter propagation distance in the aquifer (Sawyer et al., 2009; Merchán-Rivera et al. 2022; Rizzo et al. 2020) and therefore would have less impact at the scale considered in this work.

7.6.2 EFFECT OF HYDROLOGICAL CONDITIONS ON WEEKLY AQUIFER FLUCTUATIONS

In both years, the aquifer shows stronger 7-days fluctuations close to the Noce River and the Adige River after the confluence with the Noce River (Figure 7.7). However, the difference in intensity between wet and dry years evidences the hydrological control on the propagation of streamflow alterations in the aquifer system. The time-averaged wavelet coherence on the period of 7-days displayed in Figure 7.8 is generally higher and distributed on a smaller range for the year 2009/10, when the aquifer is more influenced by the precipitation. The fact that the values in areas far from the rivers or in the Avisio have similar values to the areas close to the Noce and to the Adige after the confluence with the Noce, shows that specific conditions of a hydrological year, such as snow melting or precipitation, can have a larger influence in a wet year over the entire aquifer, blurring the effect of fluctuations due to dam operations. As precipitation and temperature seasonality have the most impact on aquifer recharge (Moeck et al. 2020), in the studied area, precipitation events affect both river discharge and aquifer recharge, and lead to a coherent signal between river stage fluctuations and the groundwater hydraulic head even for aquifer regions not influenced by surface water - groundwater interaction. However, it appears that the extension of the total area displaying coherence values larger than 0.8 is very similar between the two contrasting hydrological situations (around 8 Km^2 in 2009/10, 7 Km^2 in 2016/17). Therefore, while hydrological conditions (wet/dry year) control the intensity (i.e. power) of the period of 7 days, the extension of the aquifer affected by surface water management does not seem to be very sensitive to the same hydrological drivers. These observations indicate that the portion of the aquifer influenced by the river fluctuations is strongly related to their periodicity and the aquifer characteristics itself, which is in accordance with the analytical solution for the head response presented in Singh (2004) and Sawyer et al. (2009).

7.6.3 IMPACT OF SURFACE WATER MANAGEMENT ON SURFACE WATER-GROUNDWATER EXCHANGE FLUXES

The management of the hydropower plants also influences the frequencies of the interactions between river and aquifer, as it is shown in Figure 7.10 with the normalized time-averaged wavelet power spectrum of the water budget along the four different reaches. Strong peaks at the 7-days frequency are visible along the Noce River and along the Adige River for the period 2016/17 (Figures 7.10a, c-d), suggesting that dry years may trigger changes in the frequency of the water exchange. In fact, the exchange between surface water and groundwater is controlled by the hydraulic gradient between the two water bodies. Therefore, if the groundwater level is below the average value during dry years, the fluctuations of the surface water bodies have a stronger effect since the minimum head in the river is prescribed by law through the ecological flow (European Comission 2016), which often depends on habitat suitability index for different species and on economic activities (e.g., (Carolli et al. 2017). As the changes are observed in rivers differently affected by hydropower management, these findings highlight the relevance to the weekly-period associated with streamflow alteration.

Altered streamflow conditions can either decrease or increase the residence times of the water and solute in the subsurface (Gomez-Velez et al. 2017; Merchán-Rivera et al. 2021; Singh et al. 2019). This is primarily dependent on the specific characteristics of the shape and intensity of the alterations and on geomorphological conditions. Our results further highlight that the seasonal meteorological conditions in a specific hydrological year affect not only surface water management but also surface water-groundwater interaction. Drought conditions induce stronger signal at the periodicity of 7 days, indicating a potential change in the transport of energy, solutes and even contaminants into the aquifer. This change may have implication for the transport of DOC and therefore affect biochemical reactions such as denitrification (Hinton et al. 1997; Inamdar et al. 2004). Apart from biogeochemical implications, surface water management also affects the river-aquifer systems from a thermodynamics point of view as fluctuations in the river stage alter the thermal spatial and temporal patterns in the subsurface (e.g., Song et al. 2018). This effect can be even stronger considering that rivers affected by hydropeaking are also affected by sudden fluctuations in temperature (Choi and Choi 2018; Zolezzi et al. 2011). The unregulated dam operations can be thus detrimental to the ecological health status of the river-aquifer systems. Water regulatory agencies should plan the monitoring of dam operations taking precipitation events and groundwater response into account. This would help to better manage the overall ecosystem functioning. In addition, special attention should be placed when contaminated sites are near regulated rivers, as surface water fluctuations can affect the transport of contaminants and mixing in the subsurface, either along the river corridors (Rizzo et al. 2020; Zachara et al. 2016) or in the underlying aquifer (Ziliotto et al. 2021).

7.7 CONCLUSIONS

In this paper, we have presented a new methodology to assess the impact of surface water management on aquifers based on continuous wavelet and wavelet coherence analysis. The method takes advantage of a 7-days periodicity present in the stage of rivers impacted by hydropower production and tracks the propagation of the signal into the aquifer. The implementation of wavelet maps opens the application of the methodology for the spatio-temporal analysis of surface water - groundwater interactions and allows us to clearly delineate also in complex heterogeneous aquifers the area affected by surface water management.

Moreover, the proposed wavelet analysis shows that the 7-days periodic fluctuations in river stage have a stronger impact on the aquifer during low flow conditions, such as in winter or in dry years than in wet periods. This variability also modifies the frequency of the water exchange between river and aquifer. The consequent changes in the groundwater - surface water interactions can have chemical and biochemical implications and can cause physical variations in the transport and residence times of solutes, including contaminants.

Our study area is representative of several similar catchments in the Alpine aquifers and it allows us to test the methodology considering rivers differently affected by surface water management under similar hydrogeological and meteorological conditions. As a next step, it will be important to include also the typical uncertainty affecting the hydraulic conductivity field and how it propagates on the generated maps, as recently proposed by Merchán-Rivera et al. (2022b) in the case of groundwater flooding. Moreover, one might investigate the sensitivity of these maps considering the variability in the riverbed hydraulic conductivity and other uncertain model parameters (e.g., uncertain recharge rates, propagation of the errors in the computed river head from the hydraulic model) or the impact of the interacting 7-days fluctuations at the confluence between two rivers strongly affected by dam operations. Another possibility would be to consider longer time series to investigate the impact of reservoir management on flood events and the change of water management policies.

Overall, this manuscript shows that the effects of surface water management can significantly affect aquifers, with consequences for the water, solute and energy fluxes between surface and subsurface water. In this sense, water regulatory agencies should monitor aquifers affected by surface water management considering this increased dynamic behavior in comparison to aquifers that display a lower temporal variability. In our view, this would provide fundamental information useful to improve the management of the ecosystem's functioning.

CHAPTER 8

CONCLUSIONS

This dissertation studied groundwater flow and mixing processes under highly transient boundary conditions at three different spatial scales: laboratory, field and regional scale. The highly transient boundary conditions were inspired by the case of hydropeaking, specifically by the Adige Valley, an Alpine valley in the north of Italy that is affected by multiple managed rivers. In accordance with hypothesis 1, this multi-scale approach helped to have a better overview and understanding of the effects of highly transient boundary conditions on porous media. The findings may improve the modeling of dissolved solutes in the groundwater, in particular near hydropeaked rivers and other fluctuating surface water bodies. They may also help decision-makers dealing with the management of hydropower plants, or have applications in other areas of science and engineering.

The laboratory-scale investigation focused on process understanding, considering a homogeneous porous media to isolate the effects of the transient boundary conditions. Flow-through laboratory experiments were performed in a setup representative of a cross-section traversed by two rivers affected by hydropeaking. The experiments were modeled using a non-linear velocity dependent parametrization of the hydrodynamic dispersion tensor. In general, we confirmed hypothesis 2 in that the experiments and their model-based interpretation allowed us to analyze at high spatio-temporal resolutions the evolution of a solute plume moving across the chamber. For both the experiment and the simulations, solute transport was studied with metrics such as the breakthrough curves, spreading, dilution index, and plume perimeter and area. The analyses helped to test hypothesis 3, related to mixing enhancement mechanisms due to transient conditions in the SW-GW interface. For instance, the dilution index displayed higher values under the transient flows, confirming that transient boundary conditions similar to hydropeaking can lead to mixing enhancement in homogeneous porous media. However, although river fluctuations lead to the plume's folding and stretching, and such deformation contributes to the observed enhancement, internal dispersion and diffusive process also played a significant role in dilution, in particular at lower velocities. Moreover, the flow field analysis revealed dynamic areas of higher shearing and stretching forces, particularly closer to the SW-GW interface. Finally, it was possible to experimentally show a link between flow topology and mixing, as it was observed that the effective Okubo-Weiss parameter was coherent with the rate of increase of the entropy of the plume.

The field-scale investigation incorporated the heterogeneous nature of the subsurface to the transient boundary conditions. Two studies were carried out at this scale: the first consisted of a cross-section of the Adige Valley, where we placed two solute plumes near the rivers and quantified mixing in terms of the dilution index. The second was a synthetic scenario, where we analyzed the Okubo-Weiss field. These studies helped to test hypothesis 4, related to the interaction between transient boundary conditions and heterogeneity, and their effect on mixing. In the cross-section, different hydraulic scenarios (i.e., varying riverbed conductance) and time resolutions (hourly and daily) showed a complex interplay between the river fluctuations, the river conductance and the hydraulic conductivity that affected solute transport. Mixing processes were controlled by the local hydraulic conductivity, by the river dynamics or by a combination of both depending on the investigated scenario. In addition, the characteristics of the SW-GW interface influenced the capacity for the solute plume finding or not preferential flow paths in the aquifer. In the second study, we compared the effect of different hydropeaking waves in the flow field. Here, while the hydraulic conductivity controlled the spatial distribution of the Okubo-Weiss field, the shape of the waves affected the propagation of the fluctuating signal into the aquifer and the temporal variability of the Okubo-Weiss values. In addition, the stochastic framework considering uncertainties in the hydropeaking waves helped to test hypothesis 5. Such approach revealed that the shape of the hydropeaking wave influenced the sensitivity of the stochastic parameters (i. e., amplitude and phase) to the

signal propagation and affected the probability density functions of the propagated signal at a specific moment. However, the mean values of the groundwater head did not significantly change in comparison with the deterministic scenarios due to the significant influence of the hydraulic conductivity.

The study at regional scale consisted of a model of the Adige Valley, which is traversed by multiple rivers differently affected by hydropeaking. At this scale, transport simulations with a refined grid became computationally too expensive. Since it was a three-dimensional model, it was impossible to use the Okubo-Weiss field following Equations 1.14 and 1.15, which are well-known for two-dimensional flow fields. Therefore, hypothesis 6 was tested by applying wavelet analysis techniques to study the impact of hydropeaking in the aquifer. One novelty of this work was the introduction of wavelet maps to delineate the zones most affected by the operation of hydropower plants. In general, we focused on the weekly periodicity of the fluctuations and compared two different hydrological years (wet and dry conditions). Results showed that drought conditions had a stronger impact on the groundwater heads, although the extension of the affected area was similar in both cases. Drought conditions also played a role in the frequency of the water exchanged between the river and the aquifer.

Overall, highly transient boundary conditions such as those generated by hydropeaking modify the flow topology and enhance mixing processes in the subsurface farther from the SW-GW interface. Table 8.1 summarizes the key findings structured according to the specific research questions from Table 1.1. Concluding ideas are deeper developed in the next subsections, following the research storyline established in section 1.2 and thus presented according to the multi spatial analysis: laboratory scale (Section 8.1), field scale (Section 8.2), and regional scale (Section 8.3).

Specific research question	Answer
Can hydropeaking enhance plume mixing in the underlying aquifer?	Hydropeaking can contribute to folding and stretching of a solute plume passing below the rivers.
	A plume in a transient field generated by hydropeaking-like boundary conditions can reach higher values of the dilution index, associated thus with mixing enhancement.
Which are the main mechanisms for mixing enhancement under highly transient boundary conditions (i.e., hydropeaking)?	Transverse dispersion contributed to most of the mixing enhancement in the studied setup.
	Though the plume deformation participates in mixing enhancement, particularly at higher velocities, internal dispersion and diffusive processes within the plume can dominate at certain moments.
What is the relation between flow topology and mixing under transient flow fields?	Transient boundary conditions generate spatio-temporal variable flow fields in a homogeneous porous medium, leading to dynamic areas of higher shearing and stretching forces.
	The rate of entropy and the effective Okubo-Weiss parameter can be coherent, in particular when the centroid of the plume is between the transient boundaries for the studied setup.
How does hydropeaking affect flow and mixing in a heterogeneous aquifer?	The transient boundary conditions, the hydraulic conductivity field, and the riverbed conductance interact in complex ways, and thus mixing processes may be controlled by one or more of these factors.
	The river fluctuations can help a solute plume to find preferential flow paths in the aquifer.

How do uncertainties in the boundary conditions affect the flow field and mixing?	Although the heterogeneities of the aquifer control the Okubo-Weiss field, the shape of the hydropeaking wave plays an important role in its temporal variability.
	The effect of the uncertainties in the amplitude and phase of hydropeaking events depends on the shape of the wave.
How does hydropeaking affect the aquifer at large scale?	The weekly signal of hydropeaking has a stronger impact on the aquifer during drought conditions, although there is little variation of the aquifer's area affected.
	The frequency of water exchanged between the river and the aquifer is more affected during drought conditions.

Table 8.1: Summary of specific research questions and respective answers.

8.1 MIXING ENHANCEMENT MECHANISMS UNDER HIGHLY TRANSIENT BOUNDARY CONDITIONS

The highly transient boundary conditions in the studied setup were able to deform the plume, in particular at higher velocities, when advection forces were dominating. The deformation was detected in the experiments and the simulations, in which it was possible to see the plume squeezing, folding and stretching. Additional evidence was observed in the breakthrough curves, which displayed multi-modal shapes only under the transient flows. While these observations were qualitative, the dilution index confirmed that mixing enhancement occurred in the transient flows of the investigated setup, pointing towards the hypothesis that hydropeaking can enhance mixing processes beyond the SW-GW interface.

The experimental results revealed fluctuations of the plume spreading in the transverse direction under the transient boundary conditions. Even if spreading cannot fully describe mixing (Rolle et al. 2009), this hinted a link between spreading in the vertical direction and mixing enhancement. Once the numerical simulations were completed, the local dispersion and solute flux showed that although the longitudinal dispersion coefficient was one order of magnitude larger than the transverse one, the dispersive flux was of the same order of magnitude in both directions. Moreover, the enhancement of dispersive fluxes in the transverse direction was stronger and thus contributed the most to the enhancement of the dilution index.

The analysis of the geometrical descriptors helped to investigate the mixing mechanisms further. For instance, the perimeter stopped increasing after a certain time, suggesting some limit in the enhancement of dispersion processes in the boundaries of the plume. In contrast, the plume area experienced a monotonic increase. Moreover, the ratio between the normalized dilution index and the normalized perimeter was close to one at higher velocities, while the dilution was more relevant at lower velocities. Therefore, when advection dominates, the plume deformation participates in mixing enhancement, and dispersion processes are strong at the fringes of the plume. At lower velocities, dispersion processes within the plume were dominant, driven partly by local concentration gradients and the local velocity. This observation is important for a general understanding of mixing processes in porous media, as it shows that the mass transfer occurring inside the plume can also contribute to dilution. Results also showed a relationship with the dilution index expressed as $E/E_0 = A/A_0$. This relatioship has two implications. First, it offers experimental evidence that the dilution index is indeed a measure related to the spatial dimension of a solute plume. Second, the area can be used as a proxy of dilution when concentration gradients are not available.

Complex flow fields have often been associated with heterogeneities and anisotropies in the hydraulic conductivity field. However, the model-based interpretation of the experiments allowed us to see how transient boundaries can generate flow fields with spatio-temporal variations in a homogenous porous media. Depending

on the water level of the reservoirs, the horizontal components of the velocity field could increase or decrease. The flow field in the vertical direction experienced changes in magnitude and, in some regions, also flow reversals. These reversals may be representative of a river changing between losing and gaining conditions, which means changing from being a source or a sink term for the aquifer.

The computed Okubo-Weiss parameter in the experimental setup was mainly positive, showing that shearing and stretching forces dominated in a homogeneous porous medium. However, it is worth noting that the higher values of the Okubo-Weiss were near the rivers, implying that the velocity contrasts (and not higher magnitudes) were the controlling factor for the stretching of the plume. Concerning flow topology and mixing, the effective Okubo-Weiss parameter and the rate of increase of the entropy were coherent, in particular when the centroid of the plume was between the reservoirs. In fact, this area experienced most of the mixing enhancement. Furthermore, when the effect of the hydrodynamic local dispersion was eliminated (by using an equivalent pore diffusion coefficient), neither the entropy rate nor the effective Okubo-Weiss parameter were significantly affected. This confirmed that mixing was controlled by the flow topology (i. e., Okubo-Weiss field).

8.2 INTERPLAY BETWEEN HIGHLY TRANSIENT BOUNDARY CONDITIONS AND HETEROGENEOUS AQUIFERS

The interplay between the transient boundary conditions and the heterogeneous field added additional complexity to the mixing dynamics. For instance, the transport of any solute plume in an aquifer may be controlled either by the river dynamics or by the local hydraulic conductivity, as shown by the dilution index of the modeled scenarios. Interestingly, while the daily resolution was able to highlight the role of the local hydraulic conductivity, the importance of river dynamics was detected only by the hourly resolution. In the studied cross-section, the combination of the river fluctuations and the riverbed conductance influenced the fact that the solute plume reached or did not reach preferential flow paths, as well in the amount of water exchanged between the river and the aquifer, and in the occurrence of flow reversals. The flow reversals would then lead to changes in the direction of the plume, which may also influence its fate and transport.

An interesting observation of the cross-section in the Adige Valley was the link to the studies at laboratory scale. In fact, on the side of the Noce river it was possible to see a slight stretching and folding of the plume. This happened in the scenarios with higher riverbed conductance and was partly identified by two local maxima in the concentration of the plume. When comparing one of the transient scenarios with its steady counterpart, the plume had a single maximum, confirming that the observed additional deformation was caused by the transient boundary conditions and not by just the hydraulic head imposed by the river.

The comparison of different-shaped hydropeaking waves showed that the hydraulic conductivity field controlled the spatial distribution of the Okubo-Weiss field and areas with high hydraulic conductivity contrast were more likely to display mixing hotspots. Nevertheless, the transient boundary conditions played a role in the temporal behavior of the Okubo-Weiss field. For instance, the shape, amplitude and periodicity of the hydropeaking wave influenced the intensity of the absolute value of the Okubo-Weiss, and depending on the phase of the fluctuation, it switch from positive to negative values (and viceversa) in a specific location. The shape of the hydropeaking wave also influenced the sensitivity of the uncertain parameters (i.e., amplitude and phase) and their impact on the propagation of the groundwater heads. However, the mean values did not significantly change in comparison with the deterministic scenarios due to the control exerted by hydraulic conductivity. Large uncertainties in the Okubo-Weiss appeared in areas of high contrast and large hydraulic conductivity, but transient conditions influenced the magnitude and temporal dominance of either vorticity, or shear and stretching forces, which changed following periodic patterns.

8.3 SURFACE WATER – GROUNDWATER INTERACTION AT REGIONAL SCALE

The continuous wavelet and the normalized time-averaged wavelet power spectrum analysis displayed a clear signal in the rivers affected by hydropeaking at the weekly periodicity, and a weak signal in the less affected rivers. Similar behavior was observed in the time series of the groundwater heads. As mentioned earlier, the weekly periodicity is useful because lower frequencies can penetrate further into the aquifer and thus be more relevant a larger scales. The signal of wavelet analysis was stronger during the low flow conditions, suggesting that hydropeaking can have a more significant impact on the groundwater during drought seasons. However, it is important to consider that the measured river discharges can be affected by changes in the operation of the hydropower plants in response to the low flow conditions, and thus the impact on the groundwater may be due to a combined effect of the meteorological and hydrological conditions (including alterations in aquifer recharge) and adaptations of water management.

The wavelet maps helped to analyze the influence of SW-GW interactions into que aquifer and revealed a large area impacted by the weekly fluctuations. The size of such area was similar for both wet and dry years, however the magnitude of the impact was also stronger during the drought conditions. The little variation in shape and size of both years may also be related to other factors involved in the propagation of the river fluctuations into the aquifer, such as the hydraulic conductivity, the specific yield, and the aquifer thickness.

When focusing on the SW-GW interface, the drought conditions revealed changes in the frequency of the water exchanged between the river and the aquifer, which in turn can affect biogeochemical and thermodynamic processes and contaminant transport. This provides evidence that the seasonal meteorological conditions may not only affect surface water bodies, but also surface water-groundwater interactions.

8.4 OUTLOOK

In this dissertation, the laboratory scale investigation was performed in a homogeneous porous medium, while heterogeneities in the hydraulic conductivity were introduced at the field and regional scales. Therefore, a possibility for other experimental setups would be to include heterogeneities and anisotropies in flow-through chambers to analyze how they interact with the dynamic boundaries. Furthermore, other scenarios with highly transient boundary conditions other than hydropeaking can be considered in subsequent studies. For instance, engineered pumping systems based on the work of Neupauer et al. (2014) are starting to be tested in the laboratory, and future works considering density-driven flows are envisioned. Moreover, since mixing-controlled reactions are common in porous media, future research could investigate reactive solute transport in transient flows combining laboratory and model-based interpretations. Lagrangian frameworks could be also implemented to analyze mixing, using for example Lyapunov exponents or Poincaré maps, which have been applied to study reactive transport in porous media (Wright et al. 2017; Engdahl et al. 2014) and chaotic structures in natural groundwater systems (Wu et al. 2020; Trefry et al. 2019). In general, a better understanding of mixing mechanisms in the subsurface under highly transient boundary conditions is relevant for modeling the fate and transport of contaminants and for implementing remediation strategies. Nonetheless, the results of this dissertation can have applications in other areas of science and engineering, such as in chemical engineering with the use of packed bed reactors.

Computation and numerical methods are another direction for improvement. In fact, solving the flow equation under highly transient boundary conditions was computationally expensive and the solver parameters had to be constantly adjusted in order to reach convergence and conserve the mass water balance. This challenge was reinforced by the fine grid needed to capture the transport features observed in the laboratory and eliminate numerical dispersion, not only in the simulations, but also in the computation of the Okubo-Weiss field. In fact,

results were not accurate when this topological metric was calculated with up to six significant numbers (based on the array reading formats of MODFLOW). Thus, the computation had to use the double-precision floating-point format, which was also expensive in terms of memory and computational time. Therefore, future work could focus on robust numerical methods especially designed for highly transient flows, and the optimization of data postprocessing. These applications could be helpful in modeling flow and transport across different scales.

The presented investigations in the Adige Valley were based on piezometer measurements from the years 2009, 2010, 2016 and 2017. However, new piezometers have been installed since 2017, and a multiparameter probe was placed in the Noce River in 2021. The new time series of groundwater heads open the possibility of improving model calibration, modeling other cross-sections closer to the river confluence, studying longer time series, or focusing on extreme hydrological seasons, as the droughts registered in the summer 2022. Since the equipment is also monitoring temperature and electrical conductivity, further studies could also focus on transport phenomena between the river and the groundwater. In fact, thermopeaking is a problem well-known in the Noce River (Zolezzi et al. 2011); thus, it may be worth analyzing its impact on the groundwater.

Uncertainty analysis could be implemented in the field and regional models. For instance, as the Adige and the Noce rivers have different hydropeaking regimes, the propagation of uncertainties would be different on each side of the aquifer. In addition, the riverbed conductance may be another source of uncertainty to be considered for future research. The link between flow topology and solute transport could be analyzed within a stochastic framework; in fact, the transport of the plume was more sensitive to changes in the riverbed conductance than the gorundwater head. Moreover, it may be interesting to explore the sensitivity of the wavelet maps to the variability of the river fluctuations, the hydraulic conductivity, or other uncertain model parameters.

Finally, despite the advantages of hydropower production, unregulated dam operations can have negative impacts on the ecological status of river-aquifer systems. Therefore, water regulatory agencies should monitor dam operations considering the groundwater response to river fluctuations, precipitation, and other meteorological conditions. Moreover, since hydropeaking and other fluctuating surface water bodies can affect the transport and mixing of contaminants, special attention should be placed when a contaminated site is near such boundaries. Overall, if decision-makers and practitioners are more aware of the implications of transient boundaries on solute transport, they may establish better water management practices that ultimately benefit both the ecosystem and the humankind.

Appendix

Supporting information to Chapter 3 – Relation between

mixing and plume geometry in porous media

Introduction

In this Supporting Information, Text S1 describes the comparison between the linear and the non-linear velocity-dependent hydrodynamic model for a continuous injection (steady-state plume) and a pulse injection (transient plume) under steady flow conditions. The parameters used for the comparison are reported in Table S1. Figures S1 and S2 show the concentration maps and vertical spatial profiles of the numerical simulations for the continuous injection. Figures S3 and S4 present the concentration maps and breakthrough curves at the outlet for the transient plume, respectively; while the dilution index, mass and plume's moments are displayed in Figure S5. Table 2 contains the fixed parameters used in the groundwater flow model. The calibrated parameters and their range of variability are given in Table S3. Text S2 comments on the model performance and Table S.4 presents the RMSE between the flow-through experiments and the numerical simulations. Concentration distributions, breakthrough curves and vertical profiles of the steady flow experiments and numerical simulations are presented in Figures S6-S9.

Text S1. Comparison between the linear and the non-linear hydrodynamic transport models

To verify the numerical code implementation of the non-linear velocity-dependent dispersion parameterization, we compare the proposed approach with the non-modified MT3D-USGS model for two different transport cases under uniform flow conditions. Under such conditions it is possible to modify the dispersivities to obtain equivalent hydrodynamic dispersion. Note that this is no more valid under spatially variable and/or transient flow.

The first test is performed under steady-state transport conditions considering a continuous injection, while the second one was performed considering transient transport conditions. We used a transverse dispersivity coefficient for the linear velocity-dependent model so that the transverse dispersion would be the same as in the non-linear velocity-dependent model. Further information of the flow and transport model is provided Table S1.

The concentration map and the vertical profiles of the continuous injection (Figures S1-S2), as well as the concentration distribution, breakthrough curves, and plume metrics of the point injection (Figures S3-S5) show a good match between the linear and the non-linear solutions. This allows us to verify the correct implementation of the non-linear transport model that was used to simulate the flow-through experiments. We note that introducing a non-linear parameterization of local transverse dispersion is relevant not only at the laboratory

scale (Chiogna et al. 2010; Sprocati et al. 2021) but also for larger scale applications (Chiogna et al. 2011; Cirpka et al. 2011; Rizzo et al. 2020).

TEXT S2. MODEL PERFORMANCE

In general, we observe that the model captures the location and the shape of the solute plume (Figures 4 and 6, RMSE<17 mg/L) and the breakthrough curves in Figures 5 and 6 show a good agreement between the model and the experiment. In fact, the RMSE values between the modeled BTCs and the BTC from the image analysis and the spectroscopy measurements are <35 mg/L and <27 mg/L, respectively. These values are less than 12% of the initial concentration. The perimeter was well reproduced in all cases with an RMSE<3.3 cm, which is within the experimental uncertainty (about 10% or less of the plume perimeter). The RMSE of the dilution index was below 8 cm^3 for most experiments, which is less than 10% of the estimated initial dilution index. Only in the transient flow simulation at 14 m/d the RMSE was larger than 10% of the initial dilution (RMSE=15 cm^3), however this may be because the modeled dilution index was slightly underestimated [Figure 7(a-b)]. The RMSE of the area was less than 3 cm^2 for v=5m/d, which less than 10% of the initial plume area. At v=14 m/d the RMSE was about 13 cm^2 and 24 cm^2 for the steady and transient flow, respectively. The higher value in the RMSE of the transient flow may be due to the underestimation of the model seen in Figure 3.7(f), however the evolution of the area follows a comparable trend with the experiment. The complete set of RMSE values is shown in Table S3.

SUPPORTING FIGURES
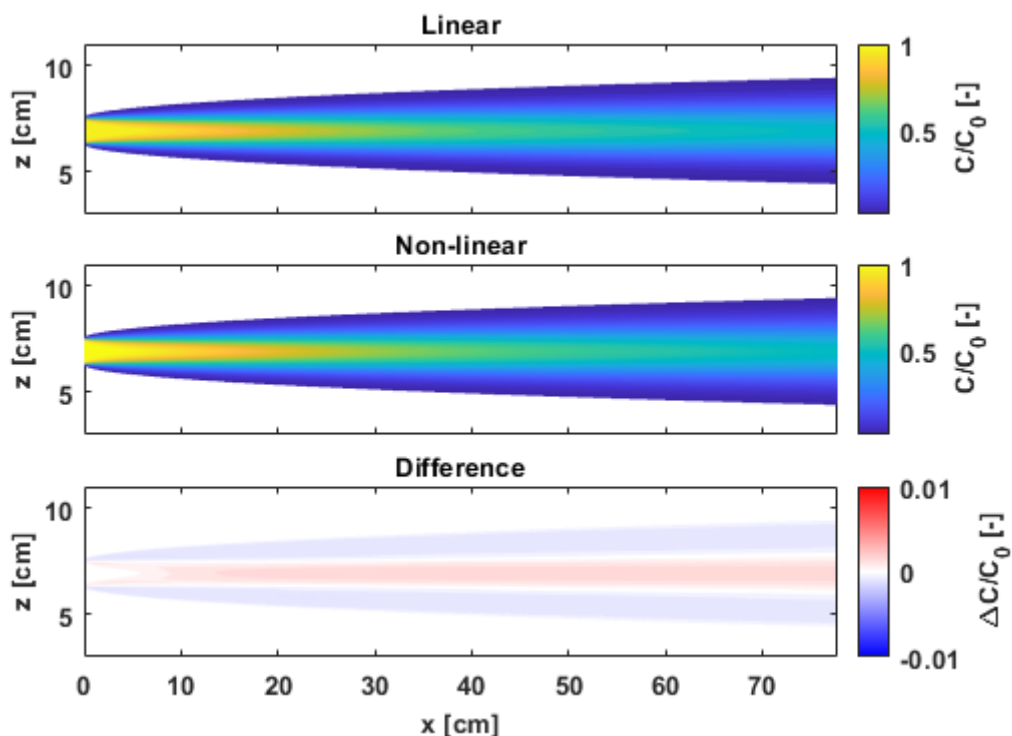
Figure S1: Comparison of concentration distribution between linear and non-linear numerical solutions for a continuous injection.
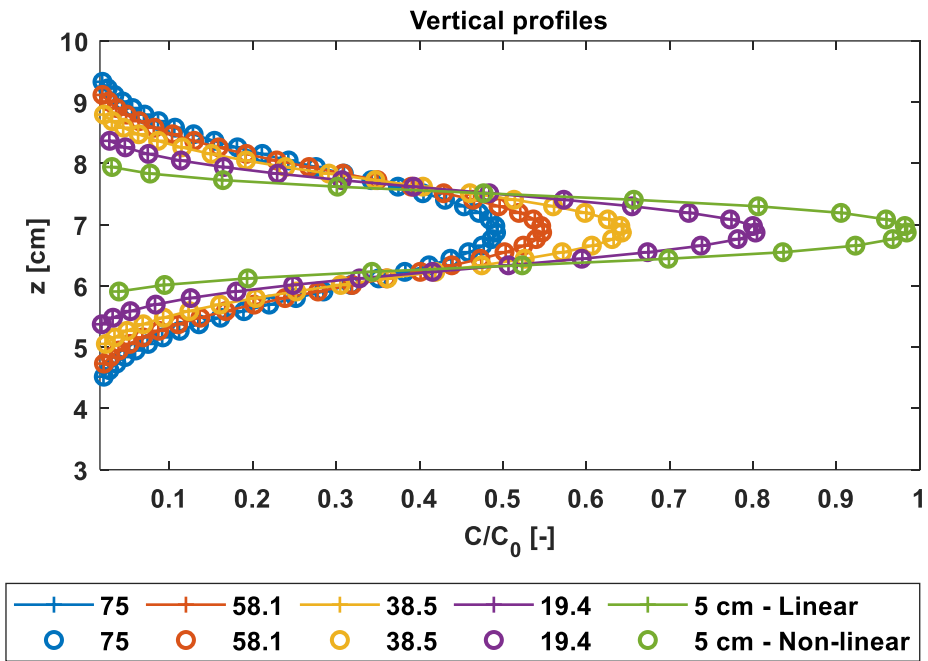
Figure S2: Vertical breakthrough curves at different distance from the continuous injection source. Comparison between linear and non-linear transverse dispersion parameterizations in the numerical model.
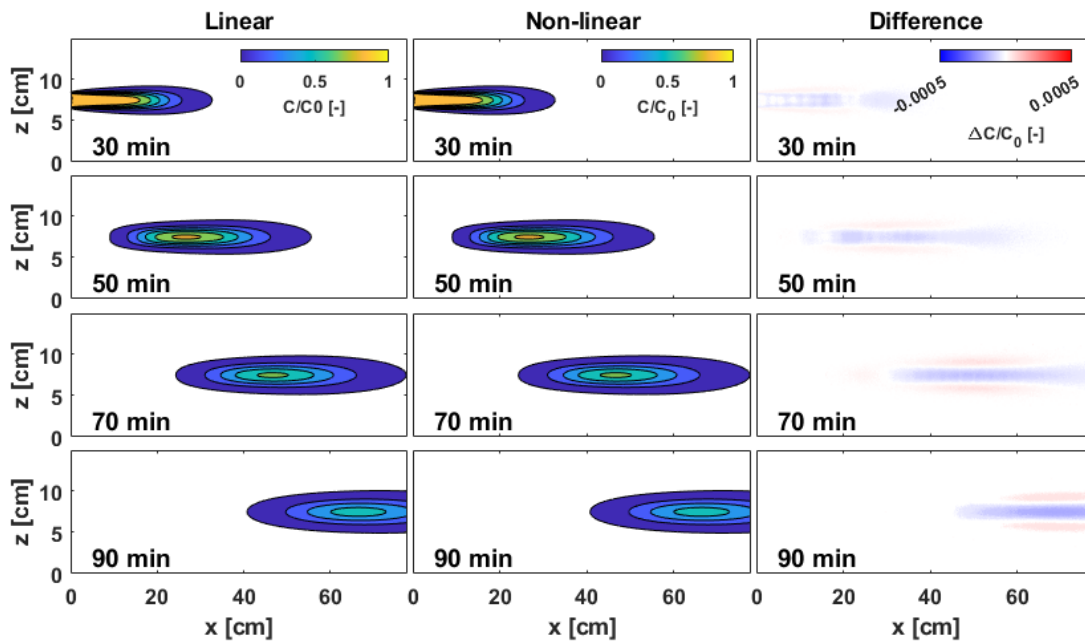
Figure S3: Comparison between linear and non-linear transverse dispersion parameterization in the numerical model for a pulse injection over a line source in steady flow system.
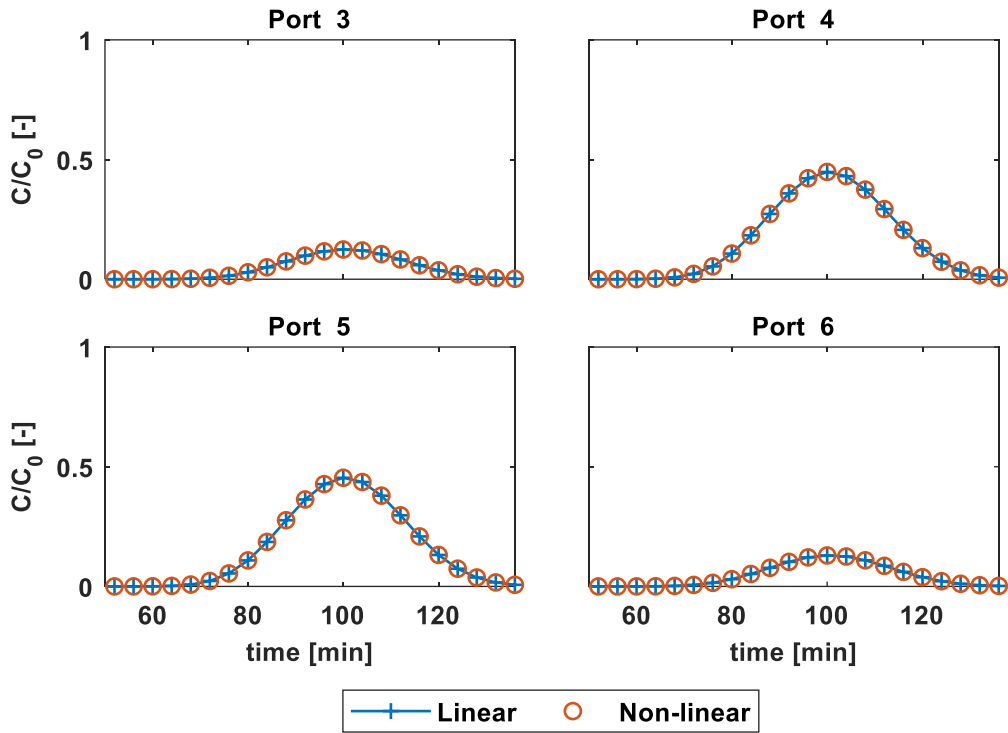
Figure S4: Breakthrough curves comparing the numerical simulations considering linear and nonlinear transverse dispersion parameterizations for a pulse injection over a line source in a steady flow.
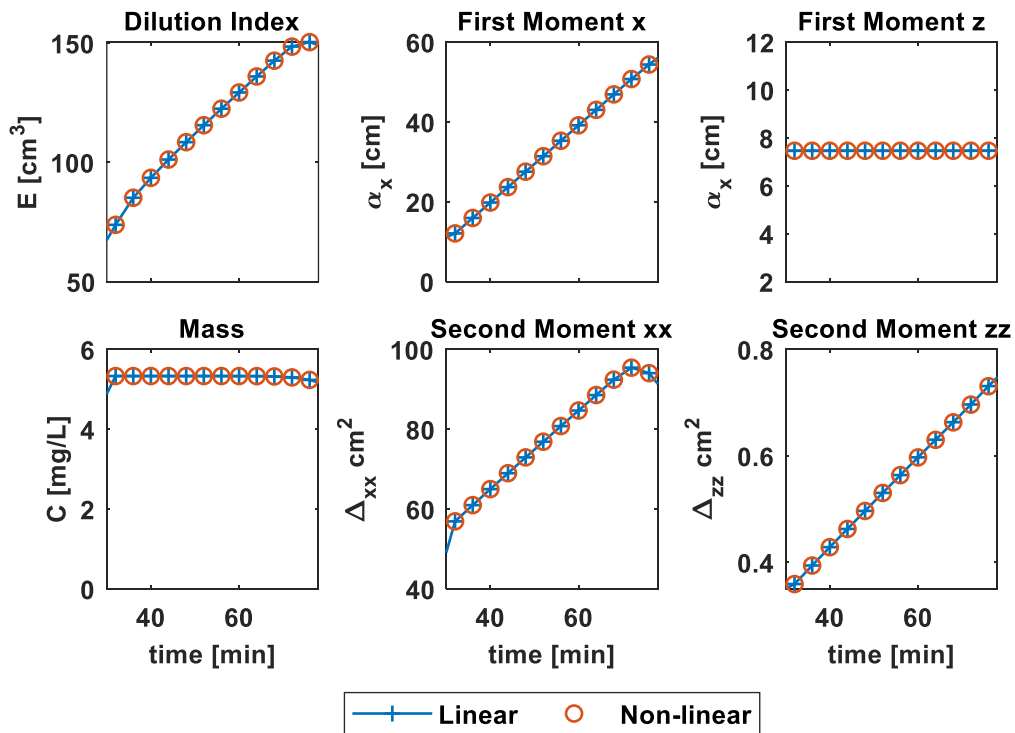
Figure S5: Dilution index, mass and moments of the plume for a pulse injection comparing linear and nonlinear dispersion parameterizations.
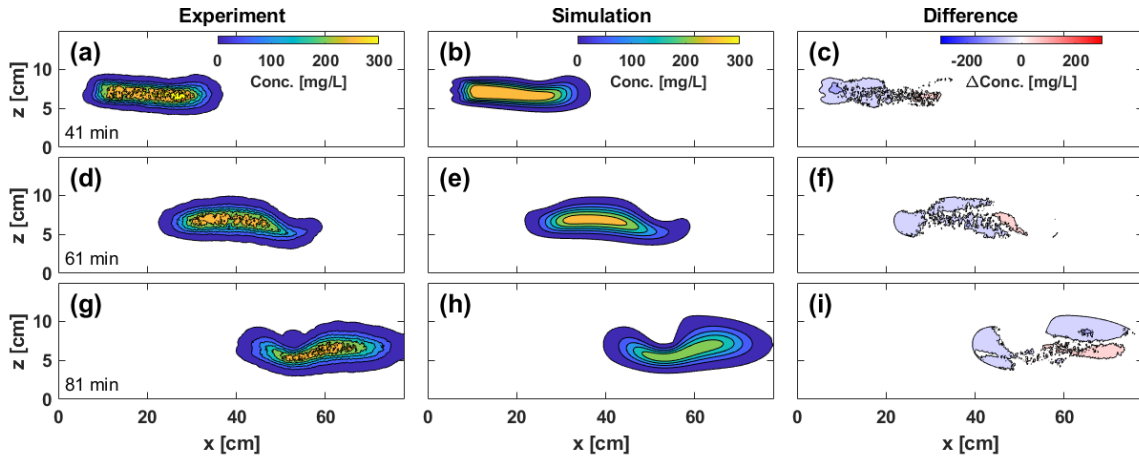
Figure S6: (**a**-**i**) Concentration distribution of the tracer plume under steady flow conditions at 14 m/d. The columns correspond to the experimental images (left), simulation (center) and difference (right). The rows correspond to 41 (top), 61 (center) and 81 (bottom) minutes.
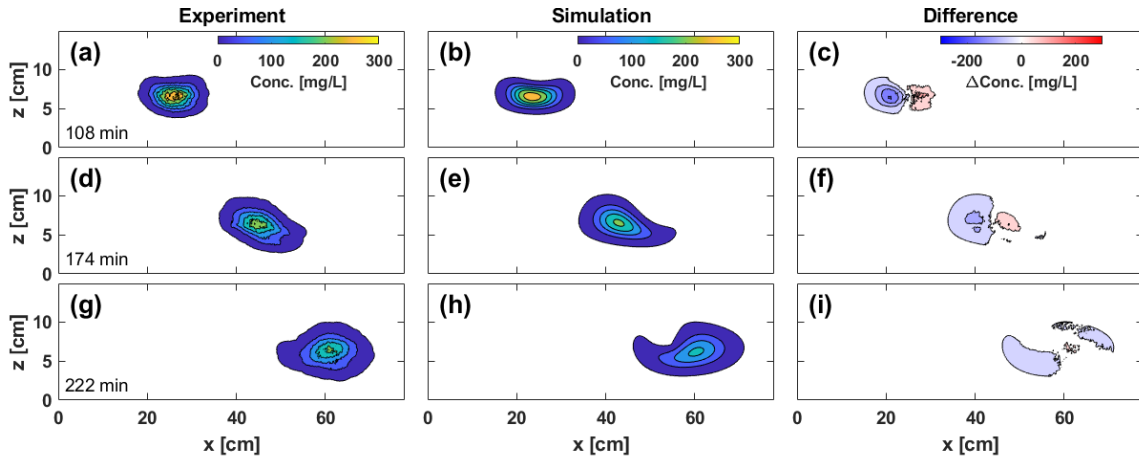
Figure S7: (**a**-**i**) Concentration distribution of the tracer plume under steady flow conditions at 5 m/d. The columns correspond to the experimental images (left), simulation (center) and difference (right). The rows correspond to 110 (top), 166 (center) and 200 (bottom) minutes.
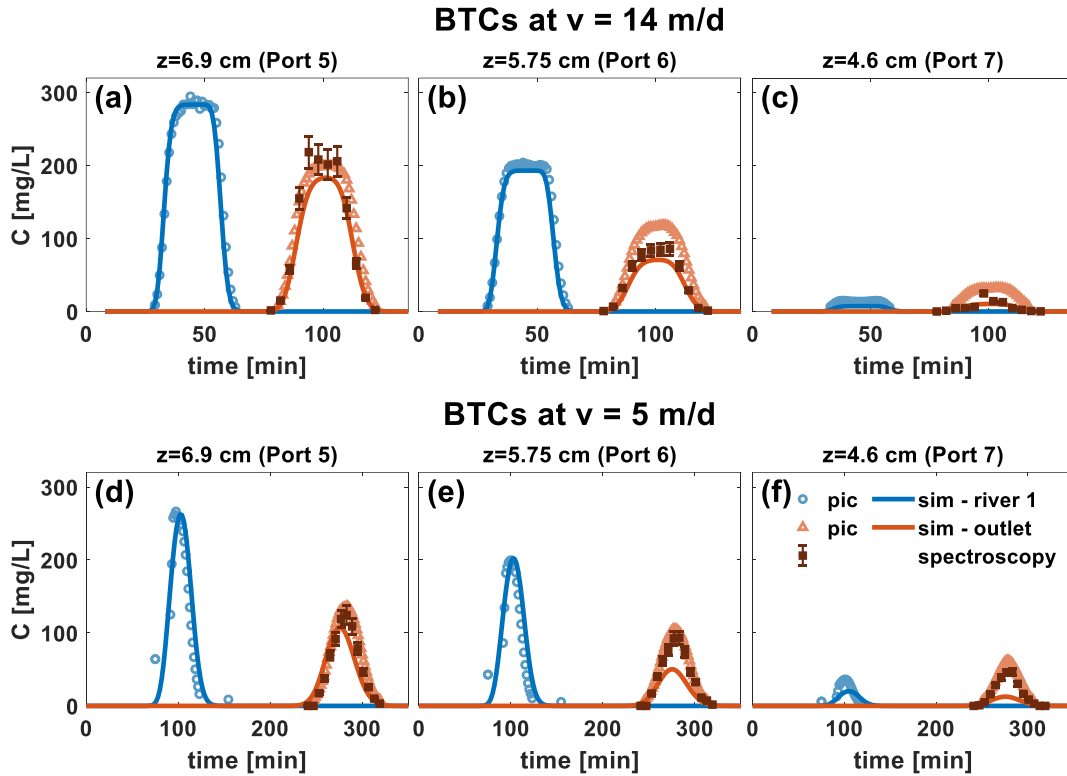
Figure S8. Breakthrough curves for the steady flow experiments (darker, marked line) and the corresponding simulations (lighter, continuous line) at 14 (a-c) and 5 (d-f) m/d.
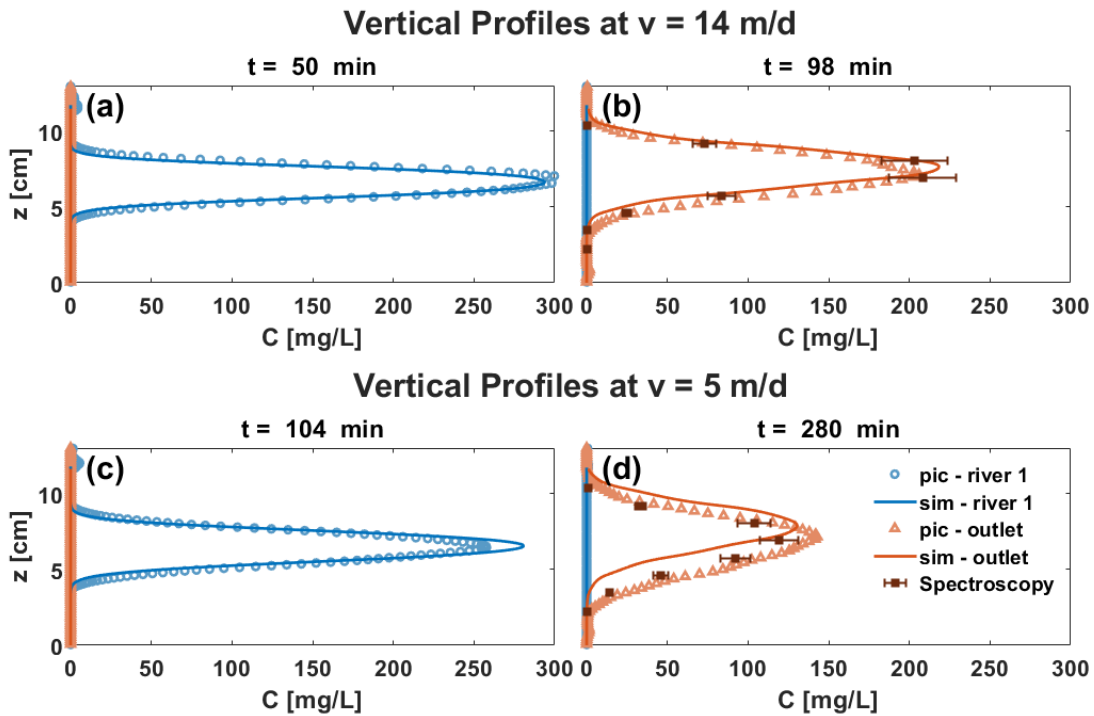
Figure S9. Vertical profiles for the experiment (symbols) and the model (lines) under steady flow conditions at 14 (a,c) and 5 (b,d) m/d.

SUPPORTING TABLES

Model parameter	Value
Pore velocity, v [m/d]	14
Initial concentration, C_0 [mg/L]	300
Source width w [cm]	1.18
D_T [m^2/ s]	8.12x 10^{-9}
D_L [m^2/ s]	1.01 x 10^{-7}
Duration injection, t_0 [min]	8

Table S1. Model parameters for the comparison of the linear and non-linear codes in MT3D-USGS.

Porous media characteristics	Value
Grain size [mm], glass beads	1-1.5
Grain size [mm], sand	0.5-0.8
Measured parameters	**Value**
Hydraulic conductivity [m/s], glass beads	1.27 x 10^{-2}
Porosity [-]	0.4
Aqueous diffusion coefficient at T=20°C [m^2/s]	3.6×10^{-10}

Table S2. Porous media characteristics and measured parameters of the groundwater flow model.

Calibrated parameters	Distribution	Value
Hydraulic conductivity [m/s], sand	$\mathcal{U}$ (5.00 x 10^{-4}, 1.25 x 10^{-3})	9.17 x 10^{-4}
Specific storage [1/m]	$\mathcal{U}$ (6.36 x 10^{-4}, 9.83 x 10^{-4})	9.83 x 10^{-4}
Specific yield [-]	$\mathcal{U}$ (0.1,0.4)	0.4
Vertical anisotropy [-], glass beads	$\mathcal{U}$ (1,10)	2.5
Vertical anisotropy [-], sand	$\mathcal{U}$ (1,10)	3.2
Pumping rate multiplier [-]		
Steady flow, v=14 m/d		1.04
Transient flow, v=14 m/d	$\mathcal{U}$ (0.9,1.1)	1.01
Steady flow, v=5 m/d		1.06
Transient flow, v=5 m/d		1.06
Riverbed conductance [m^2/s], left river		
v=14 m/d	$\mathcal{U}$ (ln(3.33 x 10^{-8}), ln(5.00x 10^{-7}))	8.55 x 10^{-8}
v=5 m/d		4.50 x 10^{-8}
Riverbed conductance [m^2/s], right river		
v=14 m/d	$\mathcal{U}$ (ln(8.33 x 10^{-9}), ln(4.17x 10^{-7}))	8.55 x 10^{-8}
v=5 m/d		1.67 x 10^{-8}
River head addend [cm], left river		
Steady flow, v=14 m/d		-0.3
Transient flow, v=14 m/d	$\mathcal{U}$ (-2,2)	0
Steady flow, v=5 m/d		-0.1
Transient flow, v=5 m/d		1.5
River head addend [cm], right river		
Steady flow, v=14 m/d		-0.3
Transient flow, v=14 m/d	$\mathcal{U}$ (-2,2)	0
Steady flow, v=5 m/d		0
Transient flow, v=5 m/d		-0.5

Table S3. Calibrated parameters of the groundwater flow model.

RMSE	Steady flow, 14 m/d	Transient flow, 14 m/d	Steady flow, 5 m/d	Transient flow, 5 m/d
Concentration distribution [mg/L]	8.71	16.97	8.94	7.38
Breakthrough curves [mg/L]	18.36	34.72	33.00	32.44
Breakthrough curves, spectroscopy [mg/L]	13.25	12.42	17.23	26.44
Dilution index [cm^3]	7.01	14.76	1.64	1.82
Perimeter [cm]	3.29	2.61	1.10	1.85
Area [cm^2]	13.39	23.73	2.79	2.93
Longitudinal 1st moment [cm]	0.17	0.83	1.64	0.98
Transversal 1st moment [cm]	0.03	0.35	0.12	0.27
Longitudinal 2nd moment [cm^2]	1.67	9.74	3.81	3.75
Transversal 2nd moment [cm^2]	0.06	0.38	0.23	0.29

Table S4. Root mean square error (RMSE) for concentration distribution of the tracer, breakthrough curves (image analysis and spectroscopy), dilution index, perimeter, area and moments of the plume. Concentration distributions are at 41, 61 and 81 min at v=14 m/d, and at 110, 166 and 200 at v=5m/d. The BTCs are along the whole experiment. The rest of the RMSE values correspond to the times when the plume is completely inside the flow-through chamber (39-72 min at 14 m/d, and 58-210 min at 5 m/d).

REFERENCES

3BMeteo (2022): Meteo mese, storico di San Michele All'adige 2017. Available online at https://www.3bmeteo.com/meteo/san+michele+alladige/storico, checked on 2022.

Agarwal, A.; Maheswaran, R.; Kurths, J.; Khosa, R. (2016a): Wavelet Spectrum and Self-Organizing Maps-Based Approach for Hydrologic Regionalization -a Case Study in the Western United States. In *Water Resour Manage* 30 (12), pp. 4399–4413. DOI: 10.1007/s11269-016-1428-1.

Agarwal, A.; Maheswaran, R.; Sehgal, V.; Khosa, R.; Sivakumar, B.; Bernhofer, C. (2016b): Hydrologic regionalization using wavelet-based multiscale entropy method. In *Journal of Hydrology* 538, pp. 22–32. DOI: 10.1016/j.jhydrol.2016.03.023.

Ahmadi, Navid; Acocella, Michela; Fries, Elisabeth; Mosthaf, Klaus; Rolle, Massimo (2022): Oxygen Propagation Fronts in Porous Media Under Evaporative Conditions at the Soil/Atmosphere Interface: Lab-Scale Experiments and Model-Based Interpretation. In *Water Resources Research* 58 (6). DOI: 10.1029/2021WR031668.

Anderson, Mary P.; Woessner, William W.; Hunt, R. J. (2015): Applied groundwater modeling. Simulation of flow and advective transport. Second edition. London, San Diego CA: Academic Press.

Aref, Hassan; Blake, John R.; Budišić, Marko; Cardoso, Silvana S. S.; Cartwright, Julyan H. E.; Clercx, Herman J. H. et al. (2017): Frontiers of chaotic advection. In *Rev. Mod. Phys.* 89 (2). DOI: 10.1103/RevModPhys.89.025007.

Arntzen, Evan V.; Geist, David R.; Dresel, P. Evan (2006): Effects of fluctuating river flow on groundwater/surface water mixing in the hyporheic zone of a regulated, large cobble bed river. In *River Res. Applic.* 22 (8), pp. 937–946. DOI: 10.1002/rra.947.

Autorità di bacini distrentualle delle Alpi Orientali (2010): Piano di gestione dei bacini idrografici delle alpi orientali–Bacino del fiume adige. Available online at http://www.alpiorientali.it/direttiva-2000-60/piano-di-gestione-acque-2010-2015/piano-approvato.html.

Autorità di Bacino del Fiume Adige (2007): Periodico trimestrale a cura dell'Autoritá Di Bacino del Fiume Adige. Edited by Provincia Autonoma di Trento.

Bagtzoglou, Amvrossios C.; Oates, Peter M. (2007): Chaotic Advection and Enhanced Groundwater Remediation. In *J. Mater. Civ. Eng.* 19 (1), pp. 75–83. DOI: 10.1061/(ASCE)0899-1561(2007)19:1(75).

Bakker, M.; Post, V.; Langevin, C. D.; Hughes, J. D.; White, J. T.; Starn, J. J.; Fienen, M. N. (2016): Scripting MODFLOW Model Development Using Python and FloPy. In *Ground water* 54 (5), pp. 733–739. DOI: 10.1111/gwat.12413.

Bakker, Mark; Hemker, Kick (2002): A Dupuit formulation for flow in layered, anisotropic aquifers. In *Advances in Water Resources* 25 (7), pp. 747–754. DOI: 10.1016/S0309-1708(02)00074-X.

Ballarini, E.; Bauer, S.; Eberhardt, C.; Beyer, C. (2014): Evaluation of the role of heterogeneities on transverse mixing in bench-scale tank experiments by numerical modeling. In *Ground water* 52 (3), pp. 368–377. DOI: 10.1111/gwat.12066.

Bandopadhyay, Aditya; Davy, Philippe; Le Borgne, Tanguy (2018): Shear Flows Accelerate Mixing Dynamics in Hyporheic Zones and Hillslopes. In *Geophys. Res. Lett.* 45 (21), 11,659-11,668. DOI: 10.1029/2018GL079914.

Basilio Hazas, Mónica; Chiogna, Gabriele (2022): Effects of highly transient boundary conditions on groundwater solute transport. In Miguel Ortega-Sánchez (Ed.): Proceedings of the 39th IAHR World Congress From Snow to Sea, 19/06/2022 - 24/06/2022. Spain: International Association for Hydro-Environment Engineering and Research (IAHR), pp. 3832–3840.

Basilio Hazas, Mónica; Marcolini, Giorgia; Castagna, Marta; Galli, Matteo; Singh, Tanu; Wohlmuth, Barbara; Chiogna, Gabriele (2022a): Drought Conditions Enhance Groundwater Table Fluctuations caused by Hydropower Plant Management. In *Water Resources Research*. DOI: 10.1029/2022WR032712.

Basilio Hazas, Mónica; Ziliotto, Francesca; Rolle, Massimo; Chiogna, Gabriele (2022b): Linking mixing and flow topology in porous media: An experimental proof. In *Phys. Rev. E* 105 (3). DOI: 10.1103/PhysRevE.105.035105.

Bauer, Robert D.; Rolle, Massimo; Bauer, Sebastian; Eberhardt, Christina; Grathwohl, Peter; Kolditz, Olaf et al. (2009): Enhanced biodegradation by hydraulic heterogeneities in petroleum hydrocarbon plumes. In *Journal of contaminant hydrology* 105 (1-2), pp. 56–68. DOI: 10.1016/j.jconhyd.2008.11.004.

Bear, Jacob (1979): Hydraulics of groundwater, McGraw-Hill series in water resources and environmental engineering. New York: McGraw-Hill International Book Co, London.

Bear, Jacob; Cheng, Alexander H.-D. (2010): Modeling Under Uncertainty. In Jacob Bear, Alexander H.-D. Cheng (Eds.): Modeling Groundwater Flow and Contaminant Transport. Dordrecht: Springer Netherlands, pp. 637–693.

Bedekar, Vivek; Morway, Eric D.; Langevin, Christian D.; Tonkin, Matthew J. D. (2016a): MT3D-USGS version 1: A U.S. Geological Survey release of MT3DMS updated with new and expanded transport capabilities for use with MODFLOW. Edited by U.S. Geological Survey Techniques and Methods 6-A53.

Bedekar, Vivek; Morway, Eric D.; Langevin, Christian D.; Tonkin, Matthew J. D. (2016b): MT3D-USGS: Groundwater Solute Transport Simulator for MODFLOW. U.S. Geological Survey Software Release: U.S. Geological Survey.

Béjar, M.; Vericat, D.; Batalla, R. J.; Gibbins, C. N. (2018): Variation in flow and suspended sediment transport in a montane river affected by hydropeaking and instream mining. In *Geomorphology* 310, pp. 69–83. DOI: 10.1016/j.geomorph.2018.03.001.

Bejarano, María D.; Jansson, Roland; Nilsson, Christer (2018): The effects of hydropeaking on riverine plants: a review. In *Biological reviews of the Cambridge Philosophical Society* 93 (1), pp. 658–673. DOI: 10.1111/brv.12362.

Beretta, G. P. (2011): Progetto per la definizione strumenti gestionali delle acque sotterranee con L'ausilio di modelli idrogeologici. Edited by Provincia Autonoma di Trento. Trento, Italy.

Beven, Keith; Binley, Andrew (2014): GLUE: 20 years on. In *Hydrological Processes* 28 (24), pp. 5897–5918. DOI: 10.1002/hyp.10082.

Bittner, Daniel; Narany, Tahoora Sheikhy; Kohl, Bernhard; Disse, Markus; Chiogna, Gabriele (2018): Modeling the hydrological impact of land use change in a dolomite-dominated karst system. In *Journal of Hydrology* 567, pp. 267–279. DOI: 10.1016/j.jhydrol.2018.10.017.

Blanch-Mercader, C.; Yashunsky, V.; Garcia, S.; Duclos, G.; Giomi, L.; Silberzan, P. (2018): Turbulent Dynamics of Epithelial Cell Cultures. In *Physical review letters* 120 (20), p. 208101. DOI: 10.1103/PhysRevLett.120.208101.

Boano, F.; Harvey, J. W.; Marion, A.; Packman, A. I.; Revelli, R.; Ridolfi, Luca; Wörman, Anders (2014): Hyporheic flow and transport processes: Mechanisms, models, and biogeochemical implications. In *Rev. Geophys.* 52 (4), pp. 603–679. DOI: 10.1002/2012RG000417.

Boisson, A.; de Anna, Pietro; Bour, O.; Le Borgne, T.; Labasque, T.; Aquilina, L. (2013): Reaction chain modeling of denitrification reactions during a push-pull test. In *Journal of contaminant hydrology* 148, pp. 1–11. DOI: 10.1016/j.jconhyd.2013.02.006.

Bolster, Diogo; Dentz, Marco; Carrera, Jesús (2009): Effective two-phase flow in heterogeneous media under temporal pressure fluctuations. In *Water Resour. Res.* 45 (5). DOI: 10.1029/2008WR007460.

Boufadel, Michel C.; Suidan, Makram T.; Venosa, Albert D. (2006): Tracer Studies in Laboratory Beach Simulating Tidal Influences. In *J. Environ. Eng.* 132 (6), pp. 616–623. DOI: 10.1061/(ASCE)0733-9372(2006)132:6(616).

Boutt, David F.; Fleming, Brandon J. (2009): Implications of anthropogenic river stage fluctuations on mass transport in a valley fill aquifer. In *Water Resour. Res.* 45 (4). DOI: 10.1029/2007WR006526.

Boving, Thomas B.; Grathwohl, Peter (2001): Tracer diffusion coefficients in sedimentary rocks: correlation to porosity and hydraulic conductivity. In *Journal of contaminant hydrology* 53 (1-2), pp. 85–100. DOI: 10.1016/S0169-7722(01)00138-3.

Boyce, Scott E. (2020): MODFLOW One-Water Hydrologic Flow Model (MF-OWHM) Conjunctive Use and Integrated Hydrologic Flow Modeling Software: U.S. Geological Survey.

Boyce, Scott E. (2022): MODFLOW One-Water Hydrologic Flow Model (MF-OWHM) Conjunctive Use and Integrated Hydrologic Flow Modeling Software, version 2.2.0: U.S. Geological Survey Software Release.

Boyce, Scott E.; Hanson, R. T.; Ferguson, I.; Schmid, W.; Henson, W.; Reimann, T. et al. (2020): One-Water Hydrologic Flow Model: A MODFLOW based conjunctive-use simulation software. In *U.S. Geological Survey Techniques and Methods 6–A60*. DOI: 10.3133/tm6A60.

Brau, Fabian; Schuszter, G.; de Wit, Anne (2017): Flow Control of A+B→C Fronts by Radial Injection. In *Physical review letters* 118 (13), p. 134101. DOI: 10.1103/PhysRevLett.118.134101.

Bresciani, Etienne; Kang, Peter K.; Lee, Seunghak (2019): Theoretical Analysis of Groundwater Flow Patterns Near Stagnation Points. In *Water Resources Research* 55 (2), pp. 1624–1650. DOI: 10.1029/2018WR023508.

Bruno, Maria Cristina; Maiolini, Bruno; Carolli, Mauro; Silveri, Luana (2009): Impact of hydropeaking on hyporheic invertebrates in an Alpine stream (Trentino, Italy). In *Ann. Limnol. - Int. J. Lim.* 45 (3), pp. 157–170. DOI: 10.1051/limn/2009018.

Bruno, Maria Cristina; Siviglia, Annunziato; Carolli, Mauro; Maiolini, Bruno (2013): Multiple drift responses of benthic invertebrates to interacting hydropeaking and thermopeaking waves. In *Ecohydrol.* 6 (4), pp. 511–522. DOI: 10.1002/eco.1275.

Budroni, M. A.; Upadhyay, V.; Rongy, L. (2019): Making a Simple A+B→C Reaction Oscillate by Coupling to Hydrodynamic Effect. In *Physical review letters* 122 (24), p. 244502. DOI: 10.1103/PhysRevLett.122.244502.

Cameron, R. H.; Martin, W. T. (1947): The Orthogonal Development of Non-Linear Functionals in Series of Fourier-Hermite Functionals. In *The Annals of Mathematics* 48 (2), p. 385. DOI: 10.2307/1969178.

Cardenas, M. Bayani; Wilson, John L.; Zlotnik, V. A. (2004): Impact of heterogeneity, bed forms, and stream curvature on subchannel hyporheic exchange. In *Water Resour. Res.* 40 (8). DOI: 10.1029/2004WR003008.

Carolli, Mauro; Geneletti, Davide; Zolezzi, Guido (2017): Assessing the impacts of water abstractions on river ecosystem services: an eco-hydraulic modelling approach. In *Environmental Impact Assessment Review* 63, pp. 136–146. DOI: 10.1016/j.eiar.2016.12.005.

Casas-Mulet, Roser; Alfredsen, Knut; Hamududu, Byman; Timalsina, Netra Prasad (2015): The effects of hydropeaking on hyporheic interactions based on field experiments. In *Hydrol. Process.* 29 (6), pp. 1370–1384. DOI: 10.1002/hyp.10264.

Casas-Mulet, Roser; Matthews, Emily; Geist, Juergen; Durance, Isabelle; Cable, Jo (2021): Negative effects of parasite exposure and variable thermal stress on brown trout (Salmo trutta) under future climatic and hydropower production scenarios. In *Climate Change Ecology* 2, p. 100039. DOI: 10.1016/j.ecochg.2021.100039.

Casella, Elisa; Molcard, Anne; Provenzale, Antonello (2011): Mesoscale vortices in the Ligurian Sea and their effect on coastal upwelling processes. In *Journal of Marine Systems* 88 (1), pp. 12–19. DOI: 10.1016/j.jmarsys.2011.02.019.

Castagna, Marta (2017): Raccolta ed elaborazione di dati dinamici della parte settentrionale della Valle dell'Adige. Trento, Italy.

Castagna, Marta; Bellin, Alberto; Chiogna, Gabriele (2015): Uncertainty Estimation and Evaluation of Shallow Aquifers' Exploitability: The Case Study of the Adige Valley Aquifer (Italy). In *Water* 7 (12), pp. 3367–3395. DOI: 10.3390/w7073367.

Castro-Alcalá, Eduardo; Fernàndez-Garcia, Daniel; Carrera, Jesús; Bolster, Diogo (2012): Visualization of mixing processes in a heterogeneous sand box aquifer. In *Environmental science & technology* 46 (6), pp. 3228–3235. DOI: 10.1021/es201779p.

Chang, Sun Woo; Clement, T. Prabhakar (2012): Experimental and numerical investigation of saltwater intrusion dynamics in flux-controlled groundwater systems. In *Water Resources Research* 48 (9). DOI: 10.1029/2012WR012134.

Chen, Kewei; Chen, Xingyuan; Song, Xuehang; Briggs, Martin A.; Jiang, Peishi; Shuai, Pin et al. (2022): Using Ensemble Data Assimilation to Estimate Transient Hydrologic Exchange Flow Under Highly Dynamic Flow Conditions. In *Water Resources Research* 58 (5). DOI: 10.1029/2021WR030735.

Cheng, Alexander H.-D.; Cheng, Daisy T. (2005): Heritage and early history of the boundary element method. In *Engineering Analysis with Boundary Elements* 29 (3), pp. 268–302. DOI: 10.1016/j.enganabound.2004.12.001.

Chiogna, Gabriele; Cirpka, Olaf A.; Grathwohl, Peter; Rolle, Massimo (2011): Transverse mixing of conservative and reactive tracers in porous media: Quantification through the concepts of flux-related and critical dilution indices. In *Water Resour. Res.* 47 (2). DOI: 10.1029/2010WR009608.

Chiogna, Gabriele; Cirpka, Olaf A.; Rolle, Massimo; Bellin, Alberto (2015): Helical flow in three-dimensional nonstationary anisotropic heterogeneous porous media. In *Water Resour. Res.* 51 (1), pp. 261–280. DOI: 10.1002/2014WR015330.

Chiogna, Gabriele; Eberhardt, Christina; Grathwohl, Peter; Cirpka, Olaf A.; Rolle, Massimo (2010): Evidence of compound-dependent hydrodynamic and mechanical transverse dispersion by multitracer laboratory experiments. In *Environmental science & technology* 44 (2), pp. 688–693. DOI: 10.1021/es9023964.

Chiogna, Gabriele; Hochstetler, David L.; Bellin, Alberto; Kitanidis, Peter K.; Rolle, Massimo (2012): Mixing, entropy and reactive solute transport. In *Geophys. Res. Lett.* 39 (20). DOI: 10.1029/2012gl053295.

Chiogna, Gabriele; Majone, Bruno; Cano Paoli, Karina; Diamantini, Elena; Stella, Elisa; Mallucci, Stefano et al. (2016): A review of hydrological and chemical stressors in the Adige catchment and its ecological status. In *The Science of the total environment* 540, pp. 429–443. DOI: 10.1016/j.scitotenv.2015.06.149.

Chiogna, Gabriele; Marcolini, Giorgia; Liu, Wanying; Pérez Ciria, Teresa; Tuo, Ye (2018a): Coupling hydrological modeling and support vector regression to model hydropeaking in alpine catchments. In *The Science of the total environment* 633, pp. 220–229. DOI: 10.1016/j.scitotenv.2018.03.162.

Chiogna, Gabriele; Rolle, Massimo; Bellin, Alberto; Cirpka, Olaf A. (2014): Helicity and flow topology in three-dimensional anisotropic porous media. In *Advances in Water Resources* 73, pp. 134–143. DOI: 10.1016/j.advwatres.2014.06.017.

Chiogna, Gabriele; Skrobanek, Patrick; Narany, Tahoora Sheikhy; Ludwig, Ralf; Stumpp, Christine (2018b): Effects of the 2017 drought on isotopic and geochemical gradients in the Adige catchment, Italy. In *The Science of the total environment* 645, pp. 924–936. DOI: 10.1016/j.scitotenv.2018.07.176.

Cho, Michelle S.; Solano, Felipe; Thomson, Neil R.; Trefry, Michael G.; Lester, Daniel R.; Metcalfe, Guy (2019): Field Trials of Chaotic Advection to Enhance Reagent Delivery. In *Groundwater Monit R* 39 (3), pp. 23–39. DOI: 10.1111/gwmr.12339.

Choi, Byungwoong; Choi, Sung-Uk (2018): Impacts of hydropeaking and thermopeaking on the downstream habitat in the Dal River, Korea. In *Ecological Informatics* 43, pp. 1–11. DOI: 10.1016/j.ecoinf.2017.10.016.

Cil, Mehmet B.; Xie, Minwei; Packman, Aaron I.; Buscarnera, Giuseppe (2017): Solute mixing regulates heterogeneity of mineral precipitation in porous media. In *Geophys. Res. Lett.* 44 (13), pp. 6658–6666. DOI: 10.1002/2017GL073999.

Cirpka, Olaf A.; Attinger, Sabine (2003): Effective dispersion in heterogeneous media under random transient flow conditions. In *Water Resour. Res.* 39 (9). DOI: 10.1029/2002WR001931.

Cirpka, Olaf A.; Barros, Felipe P. J. de; Chiogna, Gabriele; Rolle, Massimo; Nowak, Wolfgang (2011): Stochastic flux-related analysis of transverse mixing in two-dimensional heterogeneous porous media. In *Water Resour. Res.* 47 (6). DOI: 10.1029/2010WR010279.

Cirpka, Olaf A.; Chiogna, Gabriele; Rolle, Massimo; Bellin, Alberto (2015): Transverse mixing in three-dimensional nonstationary anisotropic heterogeneous porous media. In *Water Resour. Res.* 51 (1), pp. 241–260. DOI: 10.1002/2014WR015331.

Clemente, R.; Sastre, F.; Barrero-Gil, A.; Velazquez, A. (2019): Mixing downstream of a moving square cylinder in the confined laminar regime: Influence of different motion laws. In *Experimental Thermal and Fluid Science* 109, p. 109846. DOI: 10.1016/j.expthermflusci.2019.109846.

Coduto, D. P. (1999): Geotechnical engineering: principles and practices. Upper Saddle River, NJ: Prentice Hall.

Comolli, Alessandro; de Wit, Anne; Brau, Fabian (2019): Dynamics of A+B → C reaction fronts under radial advection in three dimensions. In *Physical review. E* 100 (5-1), p. 52213. DOI: 10.1103/PhysRevE.100.052213.

Cremer, Clemens J.M.; Neuweiler, Insa (2019): How Dynamic Boundary Conditions Induce Solute Trapping and Quasi-stagnant Zones in Laboratory Experiments Comprising Unsaturated Heterogeneous Porous Media. In *Water Resour. Res.* 55 (12), pp. 10765–10780. DOI: 10.1029/2018WR024470.

Cremer, Clemens J.M.; Neuweiler, Insa; Bechtold, Michel; Vanderborght, Jan (2016): Solute Transport in Heterogeneous Soil with Time-Dependent Boundary Conditions. In *Vadose Zone Journal* 15 (6), vzj2015.11.0144. DOI: 10.2136/vzj2015.11.0144.

Danish, Mohammad; Suman, Sawan; Girimaji, Sharath S. (2016): Influence of flow topology and dilatation on scalar mixing in compressible turbulence. In *J. Fluid Mech.* 793, pp. 633–655. DOI: 10.1017/jfm.2016.145.

de Anna, Pietro; Dentz, Marco; Tartakovsky, Alexandre M.; Le Borgne, Tanguy (2014): The filamentary structure of mixing fronts and its control on reaction kinetics in porous media flows. In *Geophys. Res. Lett.* 41 (13), pp. 4586–4593. DOI: 10.1002/2014GL060068.

de Anna, Pietro; Le Borgne, Tanguy; Dentz, Marco; Tartakovsky, Alexandre M.; Bolster, Diogo; Davy, Philippe (2013): Flow intermittency, dispersion, and correlated continuous time random walks in porous media. In *Physical review letters* 110 (18), p. 184502. DOI: 10.1103/PhysRevLett.110.184502.

de Barros, Felipe P. J.; Dentz, Marco; Koch, Jonas; Nowak, Wolfgang (2012): Flow topology and scalar mixing in spatially heterogeneous flow fields. In *Geophys. Res. Lett.* 39 (8), L08404. DOI: 10.1029/2012GL051302.

de Dreuzy, J.-R.; Carrera, Jesús; Dentz, Marco; Le Borgne, Tanguy (2012): Asymptotic dispersion for two-dimensional highly heterogeneous permeability fields under temporally fluctuating flow. In *Water Resour. Res.* 48 (1). DOI: 10.1029/2011WR011129.

Delgado, J.M.P.Q. (2006): A critical review of dispersion in packed beds. In *Heat Mass Transfer* 42 (4), pp. 279–310. DOI: 10.1007/s00231-005-0019-0.

Dentz, Marco; Carrera, Jesús (2003): Effective dispersion in temporally fluctuating flow through a heterogeneous medium. In *Physical review. E, Statistical, nonlinear, and soft matter physics* 68 (3 Pt 2), p. 36310. DOI: 10.1103/PhysRevE.68.036310.

Dentz, Marco; Carrera, Jesús (2005): Effective solute transport in temporally fluctuating flow through heterogeneous media. In *Water Resour. Res.* 41 (8). DOI: 10.1029/2004WR003571.

Dentz, Marco; Hidalgo, Juan J.; Lester, Daniel (2022): Mixing in Porous Media: Concepts and Approaches Across Scales. In *Transp Porous Med*. DOI: 10.1007/s11242-022-01852-x.

Dentz, Marco; Le Borgne, Tanguy; Englert, Andreas; Bijeljic, Branko (2011): Mixing, spreading and reaction in heterogeneous media: a brief review. In *Journal of contaminant hydrology* 120-121, pp. 1–17. DOI: 10.1016/j.jconhyd.2010.05.002.

Dentz, Marco; Lester, Daniel R.; Le Borgne, Tanguy; de Barros, Felipe P. J. (2016): Coupled continuous-time random walks for fluid stretching in two-dimensional heterogeneous media. In *Physical review. E* 94 (6-1), p. 61102. DOI: 10.1103/PhysRevE.94.061102.

Derx, J.; Blaschke, A. P.; Blöschl, G. (2010): Three-dimensional flow patterns at the river–aquifer interface — a case study at the Danube. In *Advances in Water Resources* 33 (11), pp. 1375–1387. DOI: 10.1016/j.advwatres.2010.04.013.

Di Dato, Mariaines; de Barros, Felipe P. J.; Fiori, Aldo; Bellin, Alberto (2018): Improving the Efficiency of 3-D Hydrogeological Mixers: Dilution Enhancement Via Coupled Engineering-Induced Transient Flows and Spatial Heterogeneity. In *Water Resour. Res.* 54 (3), pp. 2095–2111. DOI: 10.1002/2017WR022116.

Dountcheva, Iordanka; Sanz, David; Cassiraga, Eduardo; Galabov, Vassil; Gómez-Alday, Juan José (2020): Identifying non-stationary and long-term river–aquifer interactions as a response to large climatic patterns and anthropogenic pressures using wavelet analysis (Mancha Oriental Aquifer, Spain). In *Hydrological Processes* 34 (25), pp. 5134–5145. DOI: 10.1002/hyp.13934.

Dudley-Southern, Marina; Binley, Andrew (2015): Temporal responses of groundwater-surface water exchange to successive storm events. In *Water Resour. Res.* 51 (2), pp. 1112–1126. DOI: 10.1002/2014WR016623.

Engdahl, Nicholas B.; Benson, David A.; Bolster, Diogo (2014): Predicting the enhancement of mixing-driven reactions in nonuniform flows using measures of flow topology. In *Physical review. E, Statistical, nonlinear, and soft matter physics* 90 (5-1), p. 51001. DOI: 10.1103/PhysRevE.90.051001.

Epting, Jannis; Huggenberger, Peter; Radny, Dirk; Hammes, Frederik; Hollender, Juliane; Page, Rebecca M. et al. (2018): Spatiotemporal scales of river-groundwater interaction - The role of local interaction processes and regional groundwater regimes. In *The Science of the total environment* 618, pp. 1224–1243. DOI: 10.1016/j.scitotenv.2017.09.219.

European Comission (2016): Common implementation strategy for the Water Framework Directive (2000/60/EC): Guidance document No. 31. Ecological flows in the implementation of the Water Framework Directive: Technical Report -2015 – 86. Edited by Publications Office. Luxembourg.

Ferencz, Stephen B.; Cardenas, M. Bayani; Neilson, Bethany T. (2019): Analysis of the Effects of Dam Release Properties and Ambient Groundwater Flow on Surface Water-Groundwater Exchange Over a 100-km-Long Reach. In *Water Resour. Res.* 55 (11), pp. 8526–8546. DOI: 10.1029/2019WR025210.

Fette, Markus Wolfgang (2005): Tracer Studies of River-Groundwater Interaction under Hydropeaking Conditions. Doctoral Thesis. SWISS FEDERAL INSTITUTE OF TECHNOLOGY ZURICH, Switzerland.

Fette, Markus Wolfgang; Weber, C.; Peter, Armin; Wehrli, B. (2007): Hydropower production and river rehabilitation: A case study on an alpine river. In *Environ Model Assess* 12 (4), pp. 257–267. DOI: 10.1007/s10666-006-9061-7.

Francis, Blair A.; Francis, Luke K.; Cardenas, M. Bayani (2010): Water table dynamics and groundwater-surface water interaction during filling and draining of a large fluvial island due to dam-induced river stage fluctuations. In *Water Resour. Res.* 46 (7). DOI: 10.1029/2009WR008694.

Freeman, Herbert (1961): On the Encoding of Arbitrary Geometric Configurations. In *IEEE Trans. Electron. Comput.* EC-10 (2), pp. 260–268. DOI: 10.1109/TEC.1961.5219197.

Fu, Jianlin; Jaime Gómez-Hernández, J. (2009): Uncertainty assessment and data worth in groundwater flow and mass transport modeling using a blocking Markov chain Monte Carlo method. In *Journal of Hydrology* 364 (3-4), pp. 328–341. DOI: 10.1016/j.jhydrol.2008.11.014.

Galli, Matteo (2019): Effect of hydropeaking on groundwater flow in the Adige aquifer (Italy). Master's thesis. Technical University of Munich.

Geng, Xiaolong; Michael, Holly A.; Boufadel, Michel C.; Molz, Fred J.; Gerges, Firas; Lee, Kenneth (2020): Heterogeneity Affects Intertidal Flow Topology in Coastal Beach Aquifers. In *Geophys. Res. Lett.* 47 (17). DOI: 10.1029/2020GL089612.

Gillespie, Ben R.; Desmet, Simon; Kay, Paul; Tillotson, Martin R.; Brown, Lee E. (2015): A critical analysis of regulated river ecosystem responses to managed environmental flows from reservoirs. In *Freshw Biol* 60 (2), pp. 410–425. DOI: 10.1111/fwb.12506.

Golub, Gene H.; Welsch, John H. (1969): Calculation of Gauss quadrature rules. In *Math. Comp.* 23 (106), pp. 221–230. DOI: 10.1090/S0025-5718-69-99647-1.

Gomez-Velez, Jesus D.; Krause, Stefan; Wilson, John L. (2014): Effect of low-permeability layers on spatial patterns of hyporheic exchange and groundwater upwelling. In *Water Resour. Res.* 50 (6), pp. 5196–5215. DOI: 10.1002/2013WR015054.

Gomez-Velez, Jesus D.; Wilson, John L.; Cardenas, M. Bayani; Harvey, J. W. (2017): Flow and Residence Times of Dynamic River Bank Storage and Sinuosity-Driven Hyporheic Exchange. In *Water Resour. Res.* 53 (10), pp. 8572–8595. DOI: 10.1002/2017WR021362.

Goode, Daniel J.; Konikow, Leonard F. (1990): Apparent dispersion in transient groundwater flow. In *Water Resour. Res.* 26 (10), pp. 2339–2351. DOI: 10.1029/WR026i010p02339.

Graham, Emily B.; Stegen, James C.; Huang, Maoyi; Chen, Xingyuan; Scheibe, Timothy D. (2019): Subsurface biogeochemistry is a missing link between ecology and hydrology in dam-impacted river corridors. In *The Science of the total environment* 657, pp. 435–445. DOI: 10.1016/j.scitotenv.2018.11.414.

Grathwohl, Peter (1998): Diffusion in Natural Porous Media: Contaminant Transport, Sorption/Desorption and Dissolution Kinetics. Boston, MA: Springer US (Topics in Environmental Fluid Mechanics, 1).

Grinsted, A.; Moore, J. C.; Jevrejeva, S. (2004): Application of the cross wavelet transform and wavelet coherence to geophysical time series. In *Nonlin. Processes Geophys.* 11 (5/6), pp. 561–566. DOI: 10.5194/npg-11-561-2004.

Gu, Chuanhui; Anderson, William; Maggi, Federico (2012): Riparian biogeochemical hot moments induced by stream fluctuations. In *Water Resour. Res.* 48 (9). DOI: 10.1029/2011WR011720.

Gu, Chuanhui; Hornberger, George M.; Herman, Janet S.; Mills, Aaron L. (2008): Influence of stream-groundwater interactions in the streambed sediments on NO 3− flux to a low-relief coastal stream. In *Water Resour. Res.* 44 (11). DOI: 10.1029/2007WR006739.

Guedes de Carvalho, J.R.F.; Delgado, J.M.P.Q. (2005): Overall map and correlation of dispersion data for flow through granular packed beds. In *Chemical Engineering Science* 60 (2), pp. 365–375. DOI: 10.1016/j.ces.2004.07.121.

Guérin, Adrien; Devauchelle, Olivier; Robert, Vincent; Kitou, Thierry; Dessert, Céline; Quiquerez, Amélie et al. (2019): Stream-Discharge Surges Generated by Groundwater Flow. In *Geophys. Res. Lett.* 46 (13), pp. 7447–7455. DOI: 10.1029/2019GL082291.

Haberer, Christina M.; Muniruzzaman, Muhammad; Grathwohl, Peter; Rolle, Massimo (2015): Diffusive-Dispersive and Reactive Fronts in Porous Media: Iron(II) Oxidation at the Unsaturated-Saturated Interface. In *Vadose Zone Journal* 14 (5), vzj2014.07.0091. DOI: 10.2136/vzj2014.07.0091.

Haberer, Christina M.; Rolle, Massimo; Cirpka, Olaf A.; Grathwohl, Peter (2012): Oxygen Transfer in a Fluctuating Capillary Fringe. In *Vadose Zone Journal* 11 (3), vzj2011.0056. DOI: 10.2136/vzj2011.0056.

Haberer, Christina M.; Rolle, Massimo; Liu, Sanheng; Cirpka, Olaf A.; Grathwohl, Peter (2011): A high-resolution non-invasive approach to quantify oxygen transport across the capillary fringe and within the underlying groundwater. In *Journal of contaminant hydrology* 122 (1-4), pp. 26–39. DOI: 10.1016/j.jconhyd.2010.10.006.

Harbaugh, Arlen W. (1990): A computer program for calculating subregional water budgets using results from the U.S. Geological Survey modular three-dimensional ground-water flow model. In *U.S. Geological Survey Open-File Report 90–392* 46. DOI: 10.3133/ofr90392.

Harbaugh, Arlen W. (2005): MODFLOW-2005, the US Geological Survey modular groundwater model: the groundwater flow process. Edited by US Department of the Interior, US Geological Survey Reston, VA.

Harbaugh, Arlen W.; Banta, Edward R.; Hill, Mary C.; McDonald, Michael G. (2000): MODFLOW-2000, The U.S. Geological Survey modular ground-water model: User guide to modularization concepts and the ground-water flow process. With assistance of U.S. Geological Survey (Open-File Report, 00-92). Available online at http://pubs.er.usgs.gov/publication/ofr200092.

Hauer, Christoph; Holzapfel, Patrick; Leitner, P.; Graf, W. (2017a): Longitudinal assessment of hydropeaking impacts on various scales for an improved process understanding and the design of mitigation measures. In *The Science of the total environment* 575, pp. 1503–1514. DOI: 10.1016/j.scitotenv.2016.10.031.

Hauer, Christoph; Holzapfel, Patrick; Tonolla, Diego; Habersack, Helmut; Zolezzi, Guido (2019): In situ measurements of fine sediment infiltration (FSI) in gravel-bed rivers with a hydropeaking flow regime. In *Earth Surf. Process. Landforms* 44 (2), pp. 433–448. DOI: 10.1002/esp.4505.

Hauer, Christoph; Siviglia, Annunziato; Zolezzi, Guido (2017b): Hydropeaking in regulated rivers - From process understanding to design of mitigation measures. In *The Science of the total environment* 579, pp. 22–26. DOI: 10.1016/j.scitotenv.2016.11.028.

Hernandez-Aguirre, Alberto; Hernandez-Martinez, Eliseo; López-Isunza, Felipe; Castillo, Carlos O. (2022): Framing a novel approach for pseudo continuous modeling using Direct Numerical Simulations (DNS): Fluid dynamics in a packed bed reactor. In *Chemical Engineering Journal* 429, p. 132061. DOI: 10.1016/j.cej.2021.132061.

Hester, Erich T.; Cardenas, M. Bayani; Haggerty, Roy; Apte, Sourabh V. (2017): The importance and challenge of hyporheic mixing. In *Water Resour. Res.* 53 (5), pp. 3565–3575. DOI: 10.1002/2016WR020005.

Hester, Erich T.; Santizo, Katherine Y.; Nida, Abenezer A.; Widdowson, Mark A. (2021): Hyporheic transverse mixing zones and dispersivity: Laboratory and numerical experiments of hydraulic controls. In *Journal of contaminant hydrology* 243, p. 103885. DOI: 10.1016/j.jconhyd.2021.103885.

Heyman, Joris; Lester, Daniel R.; Turuban, Régis; Méheust, Yves; Le Borgne, Tanguy (2020): Stretching and folding sustain microscale chemical gradients in porous media. In *Proceedings of the National Academy of Sciences of the United States of America* 117 (24), pp. 13359–13365. DOI: 10.1073/pnas.2002858117.

Hidalgo, Juan J.; Fe, Jaime; Cueto-Felgueroso, Luis; Juanes, Ruben (2012): Scaling of convective mixing in porous media. In *Physical review letters* 109 (26), p. 264503. DOI: 10.1103/PhysRevLett.109.264503.

Hinton, M. J.; Schiff, S. L.; English, M. C. (1997). In *Biogeochemistry* 36 (1), pp. 67–88. DOI: 10.1023/A:1005779711821.

Hochstetler, David L.; Kitanidis, Peter K. (2013): The behavior of effective rate constants for bimolecular reactions in an asymptotic transport regime. In *Journal of contaminant hydrology* 144 (1), pp. 88–98. DOI: 10.1016/j.jconhyd.2012.10.002.

Hochstetler, David L.; Rolle, Massimo; Chiogna, Gabriele; Haberer, Christina M.; Grathwohl, Peter; Kitanidis, Peter K. (2013): Effects of compound-specific transverse mixing on steady-state reactive plumes: Insights from

pore-scale simulations and Darcy-scale experiments. In *Advances in Water Resources* 54, pp. 1–10. DOI: 10.1016/j.advwatres.2012.12.007.

Hosseiny, Seyedeh Habibbeh; Bozorg-Haddad, Omid; Bocchiola, Daniele (2021): Water, culture, civilization, and history. In : Economical, Political, and Social Issues in Water Resources: Elsevier, pp. 189–216.

Huntington, Justin L.; Niswonger, Richard G. (2012): Role of surface-water and groundwater interactions on projected summertime streamflow in snow dominated regions: An integrated modeling approach. In *Water Resour. Res.* 48 (11). DOI: 10.1029/2012WR012319.

Hurst, N. C.; Danielson, J. R.; Dubin, D. H. E.; Surko, C. M. (2016): Evolution of a Vortex in a Strain Flow. In *Physical review letters* 117 (23), p. 235001. DOI: 10.1103/PhysRevLett.117.235001.

Impey, Chris (2022): Life beyond Earth: How will it first be detected? In *Acta Astronautica* 197, pp. 387–398. DOI: 10.1016/j.actaastro.2022.03.019.

Inamdar, Shreeram P.; Christopher, Sheila F.; Mitchell, Myron J. (2004): Export mechanisms for dissolved organic carbon and nitrate during summer storm events in a glaciated forested catchment in New York, USA. In *Hydrological Processes* 18 (14), pp. 2651–2661. DOI: 10.1002/hyp.5572.

Jaeger, Stefanie; Ehni, Markus; Eberhardt, Christina; Rolle, Massimo; Grathwohl, Peter; Gauglitz, Guenter (2009): CCD camera image analysis for mapping solute concentrations in saturated porous media. In *Analytical and bioanalytical chemistry* 395 (6), pp. 1867–1876. DOI: 10.1007/s00216-009-2978-3.

Jakeman, Anthony J.; Barreteau, Olivier; Hunt, Randall J.; Rinaudo, Jean-Daniel; Ross, Andrew (Eds.) (2016): Integrated Groundwater Management. Concepts, Approaches and Challenges. 1st ed. 2016. Cham: Springer International Publishing; Imprint: Springer.

Jiménez-Martínez, Joaquín; de Anna, Pietro; Tabuteau, Hervé; Turuban, Régis; Le Borgne, Tanguy; Méheust, Yves (2015): Pore-scale mechanisms for the enhancement of mixing in unsaturated porous media and implications for chemical reactions. In *Geophys. Res. Lett.* 42 (13), pp. 5316–5324. DOI: 10.1002/2015GL064513.

Jiménez-Martínez, Joaquín; Le Borgne, Tanguy; Tabuteau, Hervé; Méheust, Yves (2017): Impact of saturation on dispersion and mixing in porous media: Photobleaching pulse injection experiments and shear-enhanced mixing model. In *Water Resources Research* 53 (2), pp. 1457–1472. DOI: 10.1002/2016WR019849.

Jiménez-Martínez, Joaquín; Porter, Mark L.; Hyman, Jeffrey D.; Carey, J. William; Viswanathan, Hari S. (2016): Mixing in a three-phase system: Enhanced production of oil-wet reservoirs by CO 2 injection. In *Geophys. Res. Lett.* 43 (1), pp. 196–205. DOI: 10.1002/2015GL066787.

Kadoch, B.; Del-Castillo-Negrete, D.; Bos, W. J. T.; Schneider, K. (2011): Lagrangian statistics and flow topology in forced two-dimensional turbulence. In *Physical review. E, Statistical, nonlinear, and soft matter physics* 83 (3 Pt 2), p. 36314. DOI: 10.1103/PhysRevE.83.036314.

Kahler, David M.; Kabala, Zbigniew J. (2016): Acceleration of groundwater remediation by deep sweeps and vortex ejections induced by rapidly pulsed pumping. In *Water Resources Research* 52 (5), pp. 3930–3940. DOI: 10.1002/2015WR017157.

Kang, Peter K.; Bresciani, Etienne; An, Seongnam; Lee, Seunghak (2019): Potential impact of pore-scale incomplete mixing on biodegradation in aquifers: From batch experiment to field-scale modeling. In *Advances in Water Resources* 123, pp. 1–11. DOI: 10.1016/j.advwatres.2018.10.026.

Kinzelbach, Wolfgang; Ackerer, Philippe (1986): Modélisation de la propagation d'un contaminant dans un champ d'écoulement transitoire. In *Hydrogéologie* (2), pp. 197–206.

Kitanidis, Peter K. (1986): Parameter Uncertainty in Estimation of Spatial Functions: Bayesian Analysis. In *Water Resour. Res.* 22 (4), pp. 499–507. DOI: 10.1029/WR022i004p00499.

Kitanidis, Peter K. (1994): The concept of the Dilution Index. In *Water Resour. Res.* 30 (7), pp. 2011–2026. DOI: 10.1029/94WR00762.

Laio, F.; Porporato, Amilcare; Ridolfi, Luca; Rodriguez-Iturbe, I. (2001): Plants in water-controlled ecosystems: active role in hydrologic processes and response to water stress. In *Advances in Water Resources* 24 (7), pp. 707–723. DOI: 10.1016/S0309-1708(01)00005-7.

Le Borgne, Tanguy; Dentz, Marco; Davy, Philippe; Bolster, Diogo; Carrera, Jesús; Dreuzy, Jean-Raynald de; Bour, Olivier (2011): Persistence of incomplete mixing: a key to anomalous transport. In *Physical review. E, Statistical, nonlinear, and soft matter physics* 84 (1 Pt 2), p. 15301. DOI: 10.1103/PhysRevE.84.015301.

Le Borgne, Tanguy; Dentz, Marco; Villermaux, Emmanuel (2013): Stretching, coalescence, and mixing in porous media. In *Physical review letters* 110 (20), p. 204501. DOI: 10.1103/PhysRevLett.110.204501.

Lee, Sang H.; Kang, Peter K. (2020): Three-Dimensional Vortex-Induced Reaction Hot Spots at Flow Intersections. In *Physical review letters* 124 (14), p. 144501. DOI: 10.1103/PhysRevLett.124.144501.

Lester, Daniel R.; Dentz, Marco; Le Borgne, Tanguy (2016): Chaotic mixing in three-dimensional porous media. In *J. Fluid Mech.* 803, pp. 144–174. DOI: 10.1017/jfm.2016.486.

Lester, Daniel R.; Dentz, Marco; Le Borgne, Tanguy; de Barros, Felipe P. J. (2018): Fluid Deformation in Random Steady Three Dimensional Flow. In *J. Fluid Mech.* 855, pp. 770–803. DOI: 10.1017/jfm.2018.654.

Lester, Daniel R.; Metcalfe, Guy; Trefry, Michael G. (2013): Is chaotic advection inherent to porous media flow? In *Physical review letters* 111 (17), p. 174101. DOI: 10.1103/PhysRevLett.111.174101.

Levanon, Elad; Gvirtzman, Haim; Yechieli, Yoseph; Oz, Imri; Ben-Zur, Elad; Shalev, Eyal (2019): The Dynamics of Sea Tide-Induced Fluctuations of Groundwater Level and Freshwater-Saltwater Interface in Coastal Aquifers: Laboratory Experiments and Numerical Modeling. In *Geofluids* 2019, pp. 1–9. DOI: 10.1155/2019/6193134.

Li, Fei; Liu, Junjie; Ren, Jianlin; Cao, Xiaodong; Zhu, Yifang (2016): Numerical investigation of airborne contaminant transport under different vortex structures in the aircraft cabin. In *International journal of heat and mass transfer* 96, pp. 287–295. DOI: 10.1016/j.ijheatmasstransfer.2016.01.004.

Li, Tingyu; Pasternack, Gregory B. (2021): Revealing the diversity of hydropeaking flow regimes. In *Journal of Hydrology* 598, p. 126392. DOI: 10.1016/j.jhydrol.2021.126392.

Lu, Mengqian; Tippett, Michael; Lall, Upmanu (2015): Changes in the seasonality of tornado and favorable genesis conditions in the central United States. In *Geophys. Res. Lett.* 42 (10), pp. 4224–4231. DOI: 10.1002/2015GL063968.

Lykkegaard, Mikkel B.; Dodwell, Tim J.; Moxey, David (2021): Accelerating uncertainty quantification of groundwater flow modelling using a deep neural network proxy. In *Computer Methods in Applied Mechanics and Engineering* 383, p. 113895. DOI: 10.1016/j.cma.2021.113895.

Maavara, Taylor; Chen, Qiuwen; van Meter, Kimberly; Brown, Lee E.; Zhang, Jianyun; Ni, Jinren; Zarfl, Christiane (2020): River dam impacts on biogeochemical cycling. In *Nat Rev Earth Environ* 1 (2), pp. 103–116. DOI: 10.1038/s43017-019-0019-0.

Magill, Clayton R.; Ashley, Gail M.; Domínguez-Rodrigo, Manuel; Freeman, Katherine H. (2016): Dietary options and behavior suggested by plant biomarker evidence in an early human habitat. In *Proceedings of the National Academy of Sciences of the United States of America* 113 (11), pp. 2874–2879. DOI: 10.1073/pnas.1507055113.

Majone, Bruno; Villa, Francesca; Deidda, Roberto; Bellin, Alberto (2016): Impact of climate change and water use policies on hydropower potential in the south-eastern Alpine region. In *The Science of the total environment* 543 (Pt B), pp. 965–980. DOI: 10.1016/j.scitotenv.2015.05.009.

Marçais, Jean; Derry, Louis A.; Guillaumot, Luca; Aquilina, Luc; Dreuzy, Jean-Raynald de (2022): Dynamic Contributions of Stratified Groundwater to Streams Controls Seasonal Variations of Streamwater Transit Times. In *Water Resour. Res.* 58 (3). DOI: 10.1029/2021WR029659.

Mattis, Steven A.; Butler, T. D.; Dawson, C. N.; Estep, D.; Vesselinov, V. V. (2015): Parameter estimation and prediction for groundwater contamination based on measure theory. In *Water Resour. Res.* 51 (9), pp. 7608–7629. DOI: 10.1002/2015WR017295.

Mays, David C.; Neupauer, Roseanna M. (2012): Plume spreading in groundwater by stretching and folding. In *Water Resour. Res.* 48 (7). DOI: 10.1029/2011WR011567.

McCallum, James L.; Shanafield, Margaret (2016): Residence times of stream-groundwater exchanges due to transient stream stage fluctuations. In *Water Resour. Res.* 52 (3), pp. 2059–2073. DOI: 10.1002/2015WR017441.

McCarty, Perry L.; Criddle, Craig S. (2012): Chemical and Biological Processes: The Need for Mixing. In Peter K. Kitanidis, Perry L. McCarty (Eds.): Delivery and Mixing in the Subsurface, vol. 4. New York, NY: Springer New York (SERDP/ESTCP Environmental Remediation Technology), pp. 7–52.

McDonald, Michael G.; Harbaugh, Arlen W. (1988): A modular three-dimensional finite-difference ground-water flow model. -. With assistance of U.S. G.P.O. (Techniques of Water-Resources Investigations, 06-A1). Available online at http://pubs.er.usgs.gov/publication/twri06A1.

Meile, T.; Boillat, J.-L.; Schleiss, A. J. (2011): Hydropeaking indicators for characterization of the Upper-Rhone River in Switzerland. In *Aquat Sci* 73 (1), pp. 171–182. DOI: 10.1007/s00027-010-0154-7.

Merchán-Rivera, Pablo (2022): Uncertainties due to river boundary conditions during extreme events. Technical University of Munich, Germany.

Merchán-Rivera, Pablo; Basilio Hazas, Mónica; Marcolini, Giorgia; Chiogna, Gabriele (2022a): Propagation of hydropeaking waves in heterogeneous aquifers: effects on flow topology and uncertainty quantification. In *Int J Geomath* 13 (1). DOI: 10.1007/s13137-022-00202-9.

Merchán-Rivera, Pablo; Geist, Alexandra; Disse, Markus; Huang, Jingshui; Chiogna, Gabriele (2022b): A Bayesian framework to assess and create risk maps of groundwater flooding. In *Journal of Hydrology* 610, p. 127797. DOI: 10.1016/j.jhydrol.2022.127797.

Merchán-Rivera, Pablo; Wohlmuth, B.; Chiogna, Gabriele (2021): Identifying Stagnation Zones and Reverse Flow Caused by River-Aquifer Interaction: An Approach Based on Polynomial Chaos Expansions. In *Water Resour. Res.* 57 (12). DOI: 10.1029/2021WR029824.

Meteotrentino (2022): Stazioni Meteorologiche T0408 Mezzolombardo (Maso Delle Part). Available online at http://storico.meteotrentino.it/web.htm?ppbm=T0408&rs&1&df, checked on 2022.

Miller, K. L.; Berg, S. J.; Davison, J. H.; Sudicky, E. A.; Forsyth, P. A. (2018): Efficient uncertainty quantification in fully-integrated surface and subsurface hydrologic simulations. In *Advances in Water Resources* 111, pp. 381–394. DOI: 10.1016/j.advwatres.2017.10.023.

Moeck, Christian; Grech-Cumbo, Nicolas; Podgorski, Joel; Bretzler, Anja; Gurdak, Jason J.; Berg, Michael; Schirmer, Mario (2020): A global-scale dataset of direct natural groundwater recharge rates: A review of variables, processes and relationships. In *The Science of the total environment* 717, p. 137042. DOI: 10.1016/j.scitotenv.2020.137042.

Montanari, Alberto; Bahr, Jean; Blöschl, Günter; Cai, Ximing; Mackay, D. Scott; Michalak, Anna M. et al. (2015): Fifty years of Water Resources Research : Legacy and perspectives for the science of hydrology. In *Water Resour. Res.* 51 (9), pp. 6797–6803. DOI: 10.1002/2015WR017998.

Moslehi, Mahsa; Barros, Felipe P. J. de (2017): Uncertainty quantification of environmental performance metrics in heterogeneous aquifers with long-range correlations. In *Journal of contaminant hydrology* 196, pp. 21–29. DOI: 10.1016/j.jconhyd.2016.12.002.

Muniruzzaman, Muhammad; Haberer, Christina M.; Grathwohl, Peter; Rolle, Massimo (2014): Multicomponent ionic dispersion during transport of electrolytes in heterogeneous porous media: Experiments and model-based interpretation. In *Geochimica et Cosmochimica Acta* 141, pp. 656–669. DOI: 10.1016/j.gca.2014.06.020.

Muniruzzaman, Muhammad; Rolle, Massimo (2015): Impact of multicomponent ionic transport on pH fronts propagation in saturated porous media. In *Water Resour. Res.* 51 (8), pp. 6739–6755. DOI: 10.1002/2015WR017134.

Muniruzzaman, Muhammad; Rolle, Massimo (2017): Experimental investigation of the impact of compound-specific dispersion and electrostatic interactions on transient transport and solute breakthrough. In *Water Resour. Res.* 53 (2), pp. 1189–1209. DOI: 10.1002/2016WR019727.

Neupauer, Roseanna M.; Meiss, James D.; Mays, David C. (2014): Chaotic advection and reaction during engineered injection and extraction in heterogeneous porous media. In *Water Resour. Res.* 50 (2), pp. 1433–1447. DOI: 10.1002/2013WR014057.

Neupauer, Roseanna M.; Sather, Lauren J.; Mays, David C.; Crimaldi, John P.; Roth, Eric J. (2020): Contributions of Pore-Scale Mixing and Mechanical Dispersion to Reaction During Active Spreading by Radial Groundwater Flow. In *Water Resour. Res.* 56 (7). DOI: 10.1029/2019WR026276.

Nissan, Alon; Dror, Ishai; Berkowitz, Brian (2017): Time-dependent velocity-field controls on anomalous chemical transport in porous media. In *Water Resour. Res.* 53 (5), pp. 3760–3769. DOI: 10.1002/2016WR020143.

Niswonger, Richard G.; Panday, Sorab; Ibaraki, Motomu (2011): MODFLOW-NWT, A Newton formulation for MODFLOW-2005. In *U.S. Geological Survey Techniques and Methods 6–A37*.

Nowak, W.; Barros, F. P. J. de; Rubin, Y. (2010): Bayesian geostatistical design: Task-driven optimal site investigation when the geostatistical model is uncertain. In *Water Resour. Res.* 46 (3). DOI: 10.1029/2009WR008312.

Okubo, Akira (1970): Horizontal dispersion of floatable particles in the vicinity of velocity singularities such as convergences. In *Deep Sea Research and Oceanographic Abstracts* 17 (3), pp. 445–454. DOI: 10.1016/0011-7471(70)90059-8.

Ortega-Casanova, J.; Lai, C.-H. (2018): CFD study on laminar mixing at a very low Reynolds number by pitching and heaving a square cylinder. In *Computers & Fluids* 168, pp. 318–327. DOI: 10.1016/j.compfluid.2018.03.068.

Ottino, J. M. (1990): Mixing, Chaotic Advection, and Turbulence. In *Annu. Rev. Fluid Mech.* 22 (1), pp. 207–254. DOI: 10.1146/annurev.fl.22.010190.001231.

Pauloo, Richard A.; Fogg, Graham E.; Guo, Zhilin; Harter, Thomas (2021): Anthropogenic basin closure and groundwater salinization (ABCSAL). In *Journal of Hydrology* 593, p. 125787. DOI: 10.1016/j.jhydrol.2020.125787.

Pérez Ciria, Teresa; Chiogna, Gabriele (2020): Intra-catchment comparison and classification of long-term streamflow variability in the Alps using wavelet analysis. In *Journal of Hydrology* 587, p. 124927. DOI: 10.1016/j.jhydrol.2020.124927.

Pérez Ciria, Teresa; Labat, David; Chiogna, Gabriele (2019): Detection and interpretation of recent and historical streamflow alterations caused by river damming and hydropower production in the Adige and Inn river basins using continuous, discrete and multiresolution wavelet analysis. In *Journal of Hydrology* 578, p. 124021. DOI: 10.1016/j.jhydrol.2019.124021.

Pérez Ciria, Teresa; Puspitarini, H. D.; Chiogna, Gabriele; François, B.; Borga, M. (2020): Multi-temporal scale analysis of complementarity between hydro and solar power along an alpine transect. In *The Science of the total environment* 741, p. 140179. DOI: 10.1016/j.scitotenv.2020.140179.

Perlekar, Prasad; Ray, Samriddhi Sankar; Mitra, Dhrubaditya; Pandit, Rahul (2011): Persistence problem in two-dimensional fluid turbulence. In *Physical review letters* 106 (5), p. 54501. DOI: 10.1103/PhysRevLett.106.054501.

Person, Émilie (2013): Impact of Hydropeaking on Fish and their Habitat. École Polytechnique Fédérale de Lausanne, Switzerland.

Phelan, Frederick R.; Hughes, Nicholas R.; Pathak, Jai A. (2008): Chaotic mixing in microfluidic devices driven by oscillatory cross flow. In *Physics of Fluids* 20 (2), p. 23101. DOI: 10.1063/1.2830550.

Pianosi, Francesca; Beven, Keith; Freer, Jim; Hall, Jim W.; Rougier, Jonathan; Stephenson, David B.; Wagener, Thorsten (2016): Sensitivity analysis of environmental models: A systematic review with practical workflow. In *Environmental Modelling & Software* 79, pp. 214–232. DOI: 10.1016/j.envsoft.2016.02.008.

Pinay, Gilles; Peiffer, Stefan; Dreuzy, Jean-Raynald de; Krause, Stefan; Hannah, David M.; Fleckenstein, Jan H. et al. (2015): Upscaling Nitrogen Removal Capacity from Local Hotspots to Low Stream Orders' Drainage Basins. In *Ecosystems* 18 (6), pp. 1101–1120. DOI: 10.1007/s10021-015-9878-5.

Piscopo, Amy N.; Neupauer, Roseanna M.; Mays, David C. (2013): Engineered injection and extraction to enhance reaction for improved in situ remediation. In *Water Resour. Res.* 49 (6), pp. 3618–3625. DOI: 10.1002/wrcr.20209.

Podgorski, Joel; Berg, Michael (2020): Global threat of arsenic in groundwater. In *Science (New York, N.Y.)* 368 (6493), pp. 845–850. DOI: 10.1126/science.aba1510.

Provincia Autonoma di Trento - Ufficio Dighe (2017): Dati della rete di monitoraggio dell'Ufficio Dighe – Servizio Prevenzione rischi della Provincia Autonoma di Trento. Available online at https://www.floods.it/public/DatiLive.php.

Pulg, Ulrich; Vollset, Knut Wiik; Velle, Gaute; Stranzl, Sebastian (2016): First observations of saturopeaking: Characteristics and implications. In *The Science of the total environment* 573, pp. 1615–1621. DOI: 10.1016/j.scitotenv.2016.09.143.

Rehfeldt, Kenneth R.; Gelhar, Lynn W. (1992): Stochastic analysis of dispersion in unsteady flow in heterogeneous aquifers. In *Water Resour. Res.* 28 (8), pp. 2085–2099. DOI: 10.1029/92WR00750.

Reising, L. J. (2018): Effects of active and Ppassive spreading on mixing and reaction during groundwater remediation by engineered injection and extraction. University of Colorado at Boulder. Civil engineering Graduate theses & Dissertations.

Rizzo, Calogero B.; Song, Xuehang; de Barros, Felipe P. J.; Chen, Xingyuan (2020): Temporal flow variations interact with spatial physical heterogeneity to impact solute transport in managed river corridors. In *Journal of contaminant hydrology* 235, p. 103713. DOI: 10.1016/j.jconhyd.2020.103713.

Robinson, J.; Rahmat-Samii, Y. (2004): Particle Swarm Optimization in Electromagnetics. In *IEEE Trans. Antennas Propagat.* 52 (2), pp. 397–407. DOI: 10.1109/TAP.2004.823969.

Rodell, M.; Famiglietti, J. S.; Wiese, D. N.; Reager, J. T.; Beaudoing, H. K.; Landerer, F. W.; Lo, M-H (2018): Emerging trends in global freshwater availability. In *Nature* 557 (7707), pp. 651–659. DOI: 10.1038/s41586-018-0123-1.

Rodríguez-Escales, P.; Fernàndez-Garcia, Daniel; Drechsel, J.; Folch, A.; Sanchez-Vila, X. (2017): Improving degradation of emerging organic compounds by applying chaotic advection in Managed Aquifer Recharge in randomly heterogeneous porous media. In *Water Resour. Res.* 53 (5), pp. 4376–4392. DOI: 10.1002/2016WR020333.

Rodriguez-Iturbe, I.; Porporato, Amilcare; Laio, F.; Ridolfi, Luca (2001): Plants in water-controlled ecosystems: active role in hydrologic processes and response to water stress. In *Advances in Water Resources* 24 (7), pp. 695–705. DOI: 10.1016/S0309-1708(01)00004-5.

Rolle, Massimo; Chiogna, Gabriele; Hochstetler, David L.; Kitanidis, Peter K. (2013): On the importance of diffusion and compound-specific mixing for groundwater transport: an investigation from pore to field scale. In *Journal of contaminant hydrology* 153, pp. 51–68. DOI: 10.1016/j.jconhyd.2013.07.006.

Rolle, Massimo; Eberhardt, Christina; Chiogna, Gabriele; Cirpka, Olaf A.; Grathwohl, Peter (2009): Enhancement of dilution and transverse reactive mixing in porous media: experiments and model-based interpretation. In *Journal of contaminant hydrology* 110 (3-4), pp. 130–142. DOI: 10.1016/j.jconhyd.2009.10.003.

Rolle, Massimo; Hochstetler, David L.; Chiogna, Gabriele; Kitanidis, Peter K.; Grathwohl, Peter (2012): Experimental Investigation and Pore-Scale Modeling Interpretation of Compound-Specific Transverse Dispersion in Porous Media. In *Transp Porous Med* 93 (3), pp. 347–362. DOI: 10.1007/s11242-012-9953-8.

Rolle, Massimo; Kitanidis, Peter K. (2014): Effects of compound-specific dilution on transient transport and solute breakthrough: A pore-scale analysis. In *Advances in Water Resources* 71, pp. 186–199. DOI: 10.1016/j.advwatres.2014.06.012.

Rolle, Massimo; Le Borgne, Tanguy (2019): Mixing and Reactive Fronts in the Subsurface. In *Reviews in Mineralogy and Geochemistry* 85 (1), pp. 111–142. DOI: 10.2138/rmg.2018.85.5.

Roullet, Guillaume; Klein, Patrice (2010): Cyclone-anticyclone asymmetry in geophysical turbulence. In *Physical review letters* 104 (21), p. 218501. DOI: 10.1103/PhysRevLett.104.218501.

Santizo, Katherine Y.; Widdowson, Mark A.; Hester, Erich T. (2020): Abiotic Mixing-Dependent Reaction in a Laboratory Simulated Hyporheic Zone. In *Water Resour. Res.* 56 (9). DOI: 10.1029/2020WR027090.

Sawyer, Audrey Hucks; Cardenas, M. Bayani; Bomar, Ashleigh; Mackey, Meredith (2009): Impact of dam operations on hyporheic exchange in the riparian zone of a regulated river. In *Hydrol. Process.* 23 (15), pp. 2129–2137. DOI: 10.1002/hyp.7324.

Scarborough, V. L.; Gallopin, G. G. (1991): A water storage adaptation in the maya lowlands. In *Science (New York, N.Y.)* 251 (4994), pp. 658–662. DOI: 10.1126/science.251.4994.658.

Schaefli, B.; Maraun, D.; Holschneider, M. (2007): What drives high flow events in the Swiss Alps? Recent developments in wavelet spectral analysis and their application to hydrology. In *Advances in Water Resources* 30 (12), pp. 2511–2525. DOI: 10.1016/j.advwatres.2007.06.004.

Scheidegger, Adrian E. (1954): Statistical Hydrodynamics in Porous Media. In *Journal of Applied Physics* 25 (8), pp. 994–1001. DOI: 10.1063/1.1721815.

Schmadel, Noah M.; Ward, Adam S.; Lowry, Christopher S.; Malzone, Jonathan M. (2016): Hyporheic exchange controlled by dynamic hydrologic boundary conditions. In *Geophys. Res. Lett.* 43 (9), pp. 4408–4417. DOI: 10.1002/2016GL068286.

Schmadel, Noah M.; Ward, Adam S.; Wondzell, Steven M. (2017): Hydrologic controls on hyporheic exchange in a headwater mountain stream. In *Water Resour. Res.* 53 (7), pp. 6260–6278. DOI: 10.1002/2017WR020576.

Sen, Sabyasachi; Singh, Prajwal; Heyman, Joris; Le Borgne, Tanguy; Bandopadhyay, Aditya (2020): The impact of stretching-enhanced mixing and coalescence on reactivity in mixing-limited reactive flows. In *Physics of Fluids* 32 (10), p. 106602. DOI: 10.1063/5.0022798.

Serra, Jean Paul (1982): Image analysis and mathematical morphology. London, New York: Academic Press.

Shang, Xiaopeng; Huang, Xiaoyang; Yang, Chun (2015): Mixing enhancement by the vortex in a microfluidic mixer with actuation. In *Experimental Thermal and Fluid Science* 67, pp. 57–61. DOI: 10.1016/j.expthermflusci.2014.10.017.

Shivamoggi, B. K.; van Heijst, G. J. F.; Kamp, L. P. J. (2022): The Okubo–Weiss criterion in hydrodynamic flows: geometric aspects and further extension. In *Fluid Dyn. Res.* 54 (1), p. 15505. DOI: 10.1088/1873-7005/ac495d.

Shuai, Pin; Chen, Xingyuan; Song, Xuehang; Hammond, Glenn E.; Zachara, John M.; Royer, Patrick et al. (2019): Dam Operations and Subsurface Hydrogeology Control Dynamics of Hydrologic Exchange Flows in a Regulated River Reach. In *Water Resour. Res.* 55 (4), pp. 2593–2612. DOI: 10.1029/2018WR024193.

Siebert, S.; Burke, J.; Faures, J. M.; Frenken, K.; Hoogeveen, J.; Döll, P.; Portmann, F. T. (2010): Groundwater use for irrigation – a global inventory. In *Hydrol. Earth Syst. Sci.* 14 (10), pp. 1863–1880. DOI: 10.5194/hess-14-1863-2010.

Simmons, C. T.; Pierini, M. L.; Hutson, J. L. (2002). In *Transp Porous Med* 47 (2), pp. 215–244. DOI: 10.1023/A:1015568724369.

Simms, Stephanie R.; Parker, Evan; Bey, George J.; Negrón, Tomás Gallareta (2012): Evidence from Escalera al Cielo: Abandonment of a Terminal Classic Puuc Maya hill complex in Yucatán, Mexico. In *Journal of Field Archaeology* 37 (4), pp. 270–288. DOI: 10.1179/0093469012Z.00000000025.

Singh, Sushil K. (2004): Aquifer Response to Sinusoidal or Arbitrary Stage of Semipervious Stream. In *J. Hydraul. Eng.* 130 (11), pp. 1108–1118. DOI: 10.1061/(ASCE)0733-9429(2004)130:11(1108).

Singh, Tanu; Gomez-Velez, Jesus D.; Wu, Liwen; Wörman, Anders; Hannah, David M.; Krause, Stefan (2020): Effects of Successive Peak Flow Events on Hyporheic Exchange and Residence Times. In *Water Resour. Res.* 56 (8). DOI: 10.1029/2020WR027113.

Singh, Tanu; Wu, Liwen; Gomez-Velez, Jesus D.; Lewandowski, Jörg; Hannah, David M.; Krause, Stefan (2019): Dynamic Hyporheic Zones: Exploring the Role of Peak Flow Events on Bedform-Induced Hyporheic Exchange. In *Water Resour. Res.* 55 (1), pp. 218–235. DOI: 10.1029/2018WR022993.

Smith, R. C. (2013): Uncertainty Quantification: Theory, Implementation, and Applications, Computational Science and Engineering.: SIAM.

Sole-Mari, Guillem; Fernàndez-Garcia, Daniel; Sanchez-Vila, Xavier; Bolster, Diogo (2020): Lagrangian Modeling of Mixing-Limited Reactive Transport in Porous Media: Multirate Interaction by Exchange With the Mean. In *Water Resources Research* 56 (8). DOI: 10.1029/2019WR026993.

Song, Xuehang; Chen, Xingyuan; Stegen, James; Hammond, Glenn E.; Song, Hyun-Seob; Dai, Heng et al. (2018): Drought Conditions Maximize the Impact of High-Frequency Flow Variations on Thermal Regimes and Biogeochemical Function in the Hyporheic Zone. In *Water Resour. Res.* 54 (10), pp. 7361–7382. DOI: 10.1029/2018WR022586.

Song, Xuehang; Chen, Xingyuan; Zachara, John M.; Gomez-Velez, Jesus D.; Shuai, Pin; Ren, Huiying; Hammond, Glenn E. (2020): River Dynamics Control Transit Time Distributions and Biogeochemical Reactions in a Dam-Regulated River Corridor. In *Water Resour. Res.* 56 (9). DOI: 10.1029/2019WR026470.

Souzy, M.; Lhuissier, H.; Méheust, Yves; Le Borgne, Tanguy; Metzger, B. (2020): Velocity distributions, dispersion and stretching in three-dimensional porous media. In *J. Fluid Mech.* 891. DOI: 10.1017/jfm.2020.113.

Speth, John D. (1987): Early hominid subsistence strategies in seasonal habitats. In *Journal of Archaeological Science* 14 (1), pp. 13–29. DOI: 10.1016/S0305-4403(87)80003-1.

Sposito, Garrison (2006): Chaotic solute advection by unsteady groundwater flow. In *Water Resour. Res.* 42 (6). DOI: 10.1029/2005WR004518.

Sprocati, Riccardo; Gallo, Andrea; Sethi, Rajandrea; Rolle, Massimo (2021): Electrokinetic Delivery of Reactants: Pore Water Chemistry Controls Transport, Mixing, and Degradation. In *Environmental science & technology* 55 (1), pp. 719–729. DOI: 10.1021/acs.est.0c06054.

Stroock, Abraham D.; Dertinger, Stephan K. W.; Ajdari, Armand; Mezić, Igor; Stone, Howard A.; Whitesides, George M. (2002): Chaotic mixer for microchannels. In *Science (New York, N.Y.)* 295 (5555), pp. 647–651. DOI: 10.1126/science.1066238.

Sudret, Bruno (2008): Global sensitivity analysis using polynomial chaos expansions. In *Reliability Engineering & System Safety* 93 (7), pp. 964–979. DOI: 10.1016/j.ress.2007.04.002.

Sundararajan, Pavithra; Stroock, Abraham D. (2012): Transport phenomena in chaotic laminar flows. In *Annual review of chemical and biomolecular engineering* 3, pp. 473–496. DOI: 10.1146/annurev-chembioeng-062011-081000.

Tang, Q.; Kurtz, W.; Brunner, P.; Vereecken, H.; Hendricks Franssen, H.-J. (2015): Characterisation of river–aquifer exchange fluxes: The role of spatial patterns of riverbed hydraulic conductivities. In *Journal of Hydrology* 531, pp. 111–123. DOI: 10.1016/j.jhydrol.2015.08.019.

Teixeira Parente, Mario; Bittner, Daniel; Mattis, Steven A.; Chiogna, Gabriele; Wohlmuth, Barbara (2019): Bayesian Calibration and Sensitivity Analysis for a Karst Aquifer Model Using Active Subspaces. In *Water Resources Research* 55 (8), pp. 7086–7107. DOI: 10.1029/2019WR024739.

Tenorio-Fernandez, L.; Zavala-Hidalgo, J.; Olvera-Prado, E. R. (2019): Seasonal variations of river and tidal flow interactions in a tropical estuarine system. In *Continental Shelf Research* 188, p. 103965. DOI: 10.1016/j.csr.2019.103965.

Toonder, Jaap den; Bos, Femke; Broer, Dick; Filippini, Laura; Gillies, Murray; de Goede, Judith et al. (2008): Artificial cilia for active micro-fluidic mixing. In *Lab on a Chip* 8 (4), pp. 533–541. DOI: 10.1039/B717681C.

Torrence, Christopher; Compo, Gilbert P. (1998): A Practical Guide to Wavelet Analysis. In *Bull. Amer. Meteor. Soc.* 79 (1), pp. 61–78. DOI: 10.1175/1520-0477(1998)079<0061:APGTWA>2.0.CO;2.

Torrence, Christopher; Webster, Peter J. (1999): Interdecadal Changes in the ENSO–Monsoon System. In *J. Climate* 12 (8), pp. 2679–2690. DOI: 10.1175/1520-0442(1999)012<2679:ICITEM>2.0.CO;2.

Townley, Lloyd R. (1995): The response of aquifers to periodic forcing. In *Advances in Water Resources* 18 (3), pp. 125–146. DOI: 10.1016/0309-1708(95)00008-7.

Trefry, Michael G.; Lester, Daniel R.; Metcalfe, Guy; Wu, J. (2019): Temporal Fluctuations and Poroelasticity Can Generate Chaotic Advection in Natural Groundwater Systems. In *Water Resour. Res.* 55 (4), pp. 3347–3374. DOI: 10.1029/2018WR023864.

Turuban, Régis; Lester, Daniel R.; Heyman, Joris; Le Borgne, Tanguy; Méheust, Yves (2019): Chaotic mixing in crystalline granular media. In *J. Fluid Mech.* 871, pp. 562–594. DOI: 10.1017/jfm.2019.245.

Turuban, Régis; Lester, Daniel R.; Le Borgne, Tanguy; Méheust, Yves (2018): Space-Group Symmetries Generate Chaotic Fluid Advection in Crystalline Granular Media. In *Physical review letters* 120 (2), p. 24501. DOI: 10.1103/PhysRevLett.120.024501.

U. S. Army Corps of Engineers (2016): HEC-RAS river analysis system user manual.

United Nations General Assembly (2018): UNGA 72/128, UNGA. In : The human rights to safe drinking water and sanitation.

Valocchi, Albert J.; Bolster, Diogo; Werth, Charles J. (2019): Mixing-Limited Reactions in Porous Media. In *Transp Porous Med* 130 (1), pp. 157–182. DOI: 10.1007/s11242-018-1204-1.

Viesi, D.; Crema, L.; Zanetti, A.; Galgaro, A.; Scotton, P. (2016): Geoscambio nella Provincia Autonoma di Trento.

Villermaux, E.; Stroock, Abraham D.; Stone, Howard A. (2008): Bridging kinematics and concentration content in a chaotic micromixer. In *Physical review. E, Statistical, nonlinear, and soft matter physics* 77 (1 Pt 2), p. 15301. DOI: 10.1103/PhysRevE.77.015301.

Vrugt, Jasper A.; ter Braak, Cajo J. F.; Clark, Martyn P.; Hyman, James M.; Robinson, Bruce A. (2008): Treatment of input uncertainty in hydrologic modeling: Doing hydrology backward with Markov chain Monte Carlo simulation. In *Water Resour. Res.* 44 (12). DOI: 10.1029/2007WR006720.

Wagner, Beatrice; Hauer, Christoph; Schoder, Angelika; Habersack, Helmut (2015): A review of hydropower in Austria: Past, present and future development. In *Renewable and Sustainable Energy Reviews* 50, pp. 304–314. DOI: 10.1016/j.rser.2015.04.169.

Wallace, Corey D.; Sawyer, Audrey Hucks; Soltanian, Mohamad Reza; Barnes, Rebecca T. (2020): Nitrate Removal Within Heterogeneous Riparian Aquifers Under Tidal Influence. In *Geophys. Res. Lett.* 47 (10). DOI: 10.1029/2019GL085699.

Waltham, David (2019): Is Earth special? In *Earth-Science Reviews* 192, pp. 445–470. DOI: 10.1016/j.earscirev.2019.02.008.

Weiss, John (1991): The dynamics of enstrophy transfer in two-dimensional hydrodynamics. In *Physica D: Nonlinear Phenomena* 48 (2-3), pp. 273–294. DOI: 10.1016/0167-2789(91)90088-Q.

Welch, Chani; Cook, Peter G.; Harrington, Glenn A.; Robinson, Neville I. (2013): Propagation of solutes and pressure into aquifers following river stage rise. In *Water Resour. Res.* 49 (9), pp. 5246–5259. DOI: 10.1002/wrcr.20408.

Werner, Adrian D.; Bakker, Mark; Post, Vincent E.A.; Vandenbohede, Alexander; Lu, Chunhui; Ataie-Ashtiani, Behzad et al. (2013): Seawater intrusion processes, investigation and management: Recent advances and future challenges. In *Advances in Water Resources* 51, pp. 3–26. DOI: 10.1016/j.advwatres.2012.03.004.

Werth, Charles J.; Cirpka, Olaf A.; Grathwohl, Peter (2006): Enhanced mixing and reaction through flow focusing in heterogeneous porous media. In *Water Resour. Res.* 42 (12). DOI: 10.1029/2005WR004511.

Wilson, Andrew I. (2012): Hydraulic Engineering and Water Supply. In John Peter Oleson (Ed.): The Oxford handbook of engineering and technology in the classical world. Oxford: Oxford University Press (Oxford handbooks).

Wright, Elise E.; Richter, David H.; Bolster, Diogo (2017): Effects of incomplete mixing on reactive transport in flows through heterogeneous porous media. In *Phys. Rev. Fluids* 2 (11). DOI: 10.1103/PhysRevFluids.2.114501.

Wu, Hongjing; Chen, Bing (2015): Evaluating uncertainty estimates in distributed hydrological modeling for the Wenjing River watershed in China by GLUE, SUFI-2, and ParaSol methods. In *Ecological Engineering* 76, pp. 110–121. DOI: 10.1016/j.ecoleng.2014.05.014.

Wu, J.; Lester, Daniel R.; Trefry, Michael G.; Metcalfe, Guy (2020): When Do Complex Transport Dynamics Arise in Natural Groundwater Systems? In *Water Resour. Res.* 56 (2). DOI: 10.1029/2019WR025982.

Wu, Liwen; Singh, Tanu; Gomez-Velez, Jesus D.; Nützmann, Gunnar; Wörman, Anders; Krause, Stefan; Lewandowski, Jörg (2018): Impact of Dynamically Changing Discharge on Hyporheic Exchange Processes Under Gaining and Losing Groundwater Conditions. In *Water Resour. Res.* 54 (12). DOI: 10.1029/2018WR023185.

Xiu, Dongbin (2010): Numerical methods for stochastic computations: a spectral method approach. Princeton, N.J.: Princeton University Press.

Xiu, Dongbin; Karniadakis, George Em (2002): The Wiener—Askey Polynomial Chaos for Stochastic Differential Equations. In *SIAM J. Sci. Comput.* 24 (2), pp. 619–644. DOI: 10.1137/S1064827501387826.

Xu, Tianfang; Valocchi, Albert J.; Ye, Ming; Liang, Feng; Lin, Yu-Feng (2017): Bayesian calibration of groundwater models with input data uncertainty. In *Water Resources Research* 53 (4), pp. 3224–3245. DOI: 10.1002/2016WR019512.

Ye, Yu; Chiogna, Gabriele; Cirpka, Olaf A.; Grathwohl, Peter; Rolle, Massimo (2015a): Enhancement of plume dilution in two-dimensional and three-dimensional porous media by flow focusing in high-permeability inclusions. In *Water Resour. Res.* 51 (7), pp. 5582–5602. DOI: 10.1002/2015WR016962.

Ye, Yu; Chiogna, Gabriele; Cirpka, Olaf A.; Grathwohl, Peter; Rolle, Massimo (2015b): Experimental Evidence of Helical Flow in Porous Media. In *Physical review letters* 115 (19), p. 194502. DOI: 10.1103/PhysRevLett.115.194502.

Ye, Yu; Chiogna, Gabriele; Cirpka, Olaf A.; Grathwohl, Peter; Rolle, Massimo (2015c): Experimental investigation of compound-specific dilution of solute plumes in saturated porous media: 2-D vs. 3-D flow-through systems. In *Journal of contaminant hydrology* 172, pp. 33–47. DOI: 10.1016/j.jconhyd.2014.11.002.

Ye, Yu; Chiogna, Gabriele; Cirpka, Olaf A.; Grathwohl, Peter; Rolle, Massimo (2016): Experimental investigation of transverse mixing in porous media under helical flow conditions. In *Physical review. E* 94 (1-1), p. 13113. DOI: 10.1103/PhysRevE.94.013113.

Ye, Yu; Chiogna, Gabriele; Lu, Chunhui; Rolle, Massimo (2018): Effect of Anisotropy Structure on Plume Entropy and Reactive Mixing in Helical Flows. In *Transp Porous Med* 121 (2), pp. 315–332. DOI: 10.1007/s11242-017-0964-3.

Ye, Yu; Chiogna, Gabriele; Lu, Chunhui; Rolle, Massimo (2020): Plume deformation, mixing, and reaction kinetics: An analysis of interacting helical flows in three-dimensional porous media. In *Physical review. E* 102 (1-1), p. 13110. DOI: 10.1103/PhysRevE.102.013110.

Yellen, B.; Boutt, D. F. (2015): Hydropeaking induces losses from a river reach: observations at multiple spatial scales. In *Hydrol. Process.* 29 (15), pp. 3261–3275. DOI: 10.1002/hyp.10438.

Yoon, Seonkyoo; Dentz, Marco; Kang, Peter K. (2021): Optimal fluid stretching for mixing-limited reactions in rough channel flows. In *J. Fluid Mech.* 916. DOI: 10.1017/jfm.2021.208.

Zachara, John M.; Chen, Xingyuan; Murray, Chris; Hammond, Glenn E. (2016): River stage influences on uranium transport in a hydrologically dynamic groundwater-surface water transition zone. In *Water Resour. Res.* 52 (3), pp. 1568–1590. DOI: 10.1002/2015WR018009.

Zachara, John M.; Chen, Xingyuan; Song, Xuehang; Shuai, Pin; Murray, Chris; Resch, C. Tom (2020): Kilometer-Scale Hydrologic Exchange Flows in a Gravel Bed River Corridor and Their Implications to Solute Migration. In *Water Resources Research* 56 (2). DOI: 10.1029/2019WR025258.

Zachara, John M.; Long, Philip E.; Bargar, John; Davis, James A.; Fox, Patricia; Fredrickson, Jim K. et al. (2013): Persistence of uranium groundwater plumes: contrasting mechanisms at two DOE sites in the groundwater-river interaction zone. In *Journal of contaminant hydrology* 147, pp. 45–72. DOI: 10.1016/j.jconhyd.2013.02.001.

Zaremehrjardy, Majid; Victor, Justin; Park, Seonggyu; Smerdon, Brian; Alessi, Daniel S.; Faramarzi, Monireh (2022): Assessment of snowmelt and groundwater-surface water dynamics in mountains, foothills, and plains regions in northern latitudes. In *Journal of Hydrology* 606, p. 127449. DOI: 10.1016/j.jhydrol.2022.127449.

Zhang, Changyong; Dehoff, Karl; Hess, Nancy; Oostrom, Mart; Wietsma, Thomas W.; Valocchi, Albert J. et al. (2010): Pore-Scale Study of Transverse Mixing Induced CaCO $_3$ Precipitation and Permeability Reduction in a Model Subsurface Sedimentary System. In *Environmental science & technology* 44 (20), pp. 7833–7838. DOI: 10.1021/es1019788.

Zhang, Pengfei; Devries, Stephanie L.; Dathe, Annette; Bagtzoglou, Amvrossios C. (2009): Enhanced mixing and plume containment in porous media under time-dependent oscillatory flow. In *Environmental science & technology* 43 (16), pp. 6283–6288. DOI: 10.1021/es900854r.

Ziliotto, Francesca; Basilio Hazas, Mónica; Rolle, Massimo; Chiogna, Gabriele (2021): Mixing Enhancement Mechanisms in Aquifers Affected by Hydropeaking: Insights From Flow-Through Laboratory Experiments. In *Geophys. Res. Lett.* 48 (21). DOI: 10.1029/2021GL095336.

Zolezzi, Guido; Siviglia, Annunziato; Toffolon, Marco; Maiolini, Bruno (2011): Thermopeaking in Alpine streams: event characterization and time scales. In *Ecohydrol.* 4 (4), pp. 564–576. DOI: 10.1002/eco.132.